University of Liverpool

School of Engineering

Lattice-Boltzmann studies on the effect of the morphological properties of porous medium in immiscible displacements

Author: Han Zhang

May 2023

Abstract

Immiscible two-phase flow in the porous medium is unquestionably of great significance in numerous natural and industrial processes. It has been well established and accepted that in addition to the fluid properties, the morphology of the porous medium also plays a significant role in the final volumetric throughput of a particular fluid. Especially topological features of the pore structures have been found to exert a strong influence on the hydrodynamic behaviour of two-phase flows as they express a measure of pore space and consequently flow path connectivity and availability.

The current study investigates the effect of the pore space connectivity, expressed through the Euler characteristic, on the hydrodynamic behaviour of a water-wet, oil-water two-phase system under three different states: transient state, steady-state, and low driving forces. Two-dimensional simulations are conducted in an artificially generated porous medium with the same grain size and grain density using a multi-relaxation time multi-component multiphase lattice-Boltzmann model. The transient study showed that the wetting phase saturation and the degree of pore network homogeneity have a significant impact on the dynamic evolution of wetting and non-wetting phase topology, which is governed by a series of coalescence and snap-off events. It is also observed that the macroscopic steady-state of the velocity field does not imply topological steadiness, which can be a significant element in designing artificial filters to reach certain requests. The impact of the pore space morphology on the transient dynamics of the two-phase flow is monitored and quantified through a series of hydrodynamic and topological parameters that signify the underlying flow transport processes. After the immiscible two-phase flow is relaxed to steady-state, the topological features of the porous medium are shown to significantly affect the macroscale capillary pressure and relative permeability curves for drainage and imbibition but in different ways. It is also demonstrated that pore space connectivity has a strong influence on the fluid phase distribution and fragmentation patterns in the

porous structure depending on the displacement process. Understanding the fluid phase connectivity transformation is important in the petroleum extraction process to optimise operations. In the case of immiscible displacements under low driving force in the porous medium, it is shown that as the driving force decrease, the flow processes enter the low capillary region. The low capillary region commonly appears in gravity-driven flows such as groundwater permeation and storage of oil and gas under the surface. Pore structures with different Euler characteristics behave differently in the low capillary region which can be observed through the non-linear region of relative permeability and capillary number. In addition, the pore network homogeneity is also crucial in phase connectivity development under low driving forces.

The current study is focused on the effect of pore space connectivity on immiscible two-phase flows in two-dimension. However, a complete description of the morphological properties of the porous medium effect in immiscible displacements can not be accomplished. For future work, the effect of higher viscosity ratios and other geometrical properties of the porous medium can be considered. Moreover, this study can be expanded to three-dimensional to investigate the impact of curvature.

Keywords: *Porous Medium, Euler Characteristic, Two-Phase Flow, Transient Analysis, steady-state Analysis, Low Capillary Number, Drainage, Imbibition*

Contents

Abstract **I**

List of Figure **V**

List of Table **XIII**

Acknowledgement **XV**

Nomenclature **XVII**

1 Introduction **1**

1.1 Multiphase flows in porous medium 1

1.2 Thesis subject 6

1.3 Elements of novelty 7

1.4 Progress of research 7

1.5 Outline of the Thesis 8

2 Literature review **11**

2.1 Multiphase flows 11

2.2 Flow in porous medium 12

2.2.1 Single phase flow in porous media 12

2.2.2 Immiscible multiphase flows in porous media 14

2.3 Critical gaps and research questions 24

3 Methodology **27**

3.1 The lattice-Boltzmann modelling (LBM) 27

3.2 Shan-Chen Method 29

3.3 Multi-relaxation time Lattice-Boltzmann model 31

3.4 Boundary Condition 33
3.5 Validation 34

4 Transient state study **41**
4.1 Artificial porous medium 41
4.2 Model set-up 45
4.3 Drainage 47
4.4 Imbibition 62
4.5 Summary 77

5 Steady-state study **79**
5.1 Artificial porous medium 79
5.2 Drainage and imbibition 81
5.3 Summary 94

6 Low driving forces study **97**
6.1 Drainage 97
6.2 Imbibition 110
6.3 Summary 122

7 Conclusion **123**
7.1 Research summary 123
7.2 Recommendations for future works 127

Bibliography **128**

Appendix A: Representative elementary volume **141**

Appendix B: Contour and vector plots for transient state study **143**

List of Figures

1.1 Coalesce and snap-off behavior in multiphase flow, a) coalesce, b) snap-off (Ashgriz, 2011). 3

1.2 Examples of porous medium, a) sandstone, b) ceramics c) bone (Bear, 2018). 4

2.1 Snapshot of the four flow regimes: a) large-ganglion dynamics (LGD), b) small-ganglion dynamics (SGD), c) drop-traffic flow (DTF), d) connected pathway flow (CPF)Avraam and Payatakes (1995). 15

2.2 The two-phase distribution at different saturation ($S_w = 0.3, 0.5, 0.7$) for different wettability, Left column is the neutral wetting cases ($\theta = 90^o$); right column is strong wetting cases($\theta = 168.57^o$)(Zhao et al., 2017). 17

2.3 Ganglion Dynamics: snap-o and coalescence events result in continuously changing phase connectivity at fixed saturation (Armstrong et al., 2016). . 18

2.4 Permeation behavior of water and oil emulsions through a fibrous filter with a constant porosity, x_f=82.1%, and contact angle, $\theta = 135^o$, for different fiber diameters, d_f=(a) 4 and (b) 16 μm. Panels (a3) and (b3) display the velocity contours corresponding to panels (a2) and (b2), respectively (Mino et al., 2018). 20

2.5 The water infiltration for the four porous mediums at different instantaneous times (Ju et al., 2020). 22

2.6 Interfacial surfaces and curvatures (magnitude indicated by colour bar) for the three-phase system (air-water-oil) Paustian et al. (2021). 23

3.1 The directional vectors and the weighting factors of the D2Q9 model. . . 28

3.2 Classification of solids in a porous medium: black nodes are surface (boundary) solids; grey checker nodes are interior (isolated) solids. 33

3.3 Solid boundary bounces back scheme. 33

3.4 Schematic of the two-phase flow between two parallel plates employed to validate the MCMP LBM model. 35

3.5 (a)Velocity profile of an oil-water two-phase system flowing between two parallel plates obtained using the MCMP-LBM model and the analytical solution for $M = 1.04$, $S_w = 0.5$ and $G = 5 \times 10^{-6}$. (b) Predicted relative permeability values obtained using the MCMP-LBM model and the analytical solution for the wetting and non-wetting phases for the flow of an oil-water system between two parallel plates for $M = 1.04$ and $G = 5 \times 10^{-6}$. 36

3.6 Droplet 'bag' breakup for $We = 38.7$. The flow direction is from left to right. 37

3.7 Temporal snapshots of the bounding contour line of the droplet after impact on a solid flat surface (Re=95.2, We=2.86, M=1.04). 38

3.8 Time evolution of the non-dimensional spread factor (Re=95.2, We=2.86, M=1.04). 39

4.1 Grain and pore space distributions of the artificially generated porous medium characterised by $\chi_0 = -680$ (structure 1) in (a) and $\chi_0 = -920$ (structure 7) in (b). 42

4.2 Pore size and pore throat distributions for the porous medium structures 1-7. In (a) pore size distribution, (b) cumulative distribution of pore sizes, (c) pore throat distribution and (d) cumulative distribution of pore throats. 45

4.3 Initial and boundary conditions for the simulation of the two-phase flow. . 46

4.4 Volume fraction contour plots of the temporal evolution of the displacement of the wetting phase by the injected non-wetting phase for an Euler characteristic of $\chi_0 = -800$ and a steady-state wetting phase saturation rate of 0.7. In terms of lattice units $t = 5 \times 10^4$ in (a), $t = 1 \times 10^5$ in in (b), $t = 2 \times 10^5$ in (c), $t = 2.5 \times 10^5$ in (d), $t = 3 \times 10^5$ in (e), $t = 3.5 \times 10^5$ in (f), $t = 4 \times 10^5$ in (g), t=4.5×10^5 in (h), $t = 5 \times 10^5$ in (i), $t = 5.5 \times 10^5$ in, (j) $t = 6 \times 10^5$ in (k), and $t = 7 \times 10^5$ in (l). 48

4.5 Variation of the saturation rate of the wetting phase with the number of time steps for the final constant values of in (a) $S_w = 0.91$, in (b) $S_w = 0.7$, in (c) $S_w = 0.49$, in (d) $S_w = 0.32$ and in (e) $S_w = 0.2$. The vertical red dashed line indicates the time at which steady saturation is reached. 50

4.6 Variation in the average velocity in the x direction of the wetting (dashed lines) and non-wetting (solid lines) phases with the number of time steps for final constant values of in (a) S_w=0.91, in (b) S_w=0.7, in (c) S_w=0.49, in (d) S_w=0.32 and in (e) S_w=0.2. The vertical red dashed line indicates the time at which the macroscopic steady-state is reached. 52

4.7 Temporal evolution of the capillary pressure for in (a) S_w=0.91, in (b) S_w=0.7, in (c) S_w=0.49, in (d) S_w=0.32 and in (e) S_w=0.2. 53

4.8 Variation of the Euler characteristic of the wetting phase χ_w with the number of time steps for in (a) S_w=0.91, in (b) S_w=0.7, in (c) S_w=0.49, in (d) S_w=0.32 and in (e) S_w=0.2. 55

4.9 Temporal evolution of the Euler characteristic of the wetting and non-wetting phases per unit average grain, ξ_w and ξ_{nw}, for in (a) S_w=0.91, in (b) S_w=0.7, in (c) S_w=0.49, in (d) S_w=0.32, in (e) S_w=0.2. 56

4.10 Temporal evolution of the interface length represented by the non-dimensional variable ζ for in (a) S_w=0.91, in (b) S_w=0.7 in (c) S_w=0.49, in (d) S_w=0.32 and in (e) S_w=0.2. 60

4.11 Temporal evolution of the interface length as represented by the non-dimensional variables ζ_w and ζ_{nw} for in (a) S_w=0.91, in (b) S_w=0.7, in (c) S_w=0.49, in (d) S_w=0.32 and in (e) S_w=0.2. 61

4.12 Volume fraction contour plots of the temporal evolution of the displacement of the non-wetting phase by the injected wetting phase for an Euler characteristic of $\chi_0 = -800$ and a steady-state wetting phase saturation rate of 0.3. In terms of lattice units $t = 7 \times 10^4$ in (a), $t = 1.4 \times 10^5$ in (b), $t = 2.1 \times 10^5$ in (c), $t = 2.8 \times 10^5$ in (d), $t = 3.5 \times 10^5$ in (e), $t = 4.2 \times 10^5$ in (f), $t = 4.9 \times 10^5$ in (g), $t = 5.6 \times 10^5$ in (h), $t = 6.3 \times 10^5$ in (i), $t = 7 \times 10^5$ in (j) and $t = 7.7 \times 10^5$ in (k). 63

4.13 Variation of the saturation rate of the wetting phase with the number of time steps for the final constant values of in (a) $S_w = 0.09$, in (b) $S_w = 0.3$, in (c) $S_w = 0.45$, in (d) $S_w = 0.6$ and in (e) $S_w = 0.85$. The vertical red dashed line indicates the time at which steady saturation is reached. 65

4.14 Variation in the average velocity in the x direction of the wetting (dashed lines) and non-wetting (solid lines) phases with the number of time steps for final constant values of in (a) $S_w = 0.09$, in (b) $S_w = 0.3$, in (c) $S_w = 0.45$, in (d) $S_w = 0.6$ and in (e) $S_w = 0.85$. The vertical red dashed line indicates the time at which the macroscopic steady-state is reached. 66

4.15 Temporal evolution of the capillary pressure for in (a) $S_w = 0.09$, in (b) $S_w = 0.3$, in (c) $S_w = 0.45$, in (d) $S_w = 0.6$ and in (e) $S_w = 0.85$. 68

4.16 Variation of the Euler characteristic of the wetting phase, χ_w, with the number of time steps for in (a) $S_w = 0.09$, in (b) $S_w = 0.3$, in (c) $S_w = 0.45$, in (d) $S_w = 0.6$ and in (e) $S_w = 0.85$. 70

4.17 Temporal evolution of the Euler characteristic of the wetting phase per unit grain ξ_w and of the non-wetting phase per unit grain ξ_{nw} for in (a) $S_w = 0.09$, in (b) $S_w = 0.3$, in (c) $S_w = 0.45$, in (d) $S_w = 0.6$ and in (e) $S_w = 0.85$. . . 71

4.18 Temporal evolution of the interface length represented by the nondimensional variable ζ for in (a) $S_w = 0.09$, in (b) $S_w = 0.3$, in (c) $S_w = 0.45$, in (d) $S_w = 0.6$ and in (e) $S_w = 0.85$. 75

4.19 Temporal evolution of the interface length as represented by the nondimensional variables ζ_w and ζ_{nw} for in (a) $S_w = 0.09$, in (b) $S_w = 0.3$, in (c) $S_w = 0.45$, in (d) $S_w = 0.6$ and in (e) $S_w = 0.85$. 76

5.1 Grain and pore space configurations of the artificially generated porous medium for in (a) structure 1, $\chi_0 = -680$ and in (b) structure 7, $\chi_0 = -930$. 80

5.2 Pore size and pore throat distributions for the porous medium structures 1-7; (a) pore size distribution, (b) cumulative distribution of pore sizes, (c) pore throat distribution and (d) cumulative distribution of pore throats. . 80

5.3 Predicted steady-state two-phase flow distribution patterns for imbibition on the top and drainage on the bottom for structure 4 and with $S_w = 0.15$ in (a) and (d), $S_w = 0.55$ in (b) and (e), and $S_w = 0.85$ in (c) and (f). The wetting phase is shown in blue, the non-wetting phase in yellow, and the solid phase in black. 82

5.4 Variation of the steady-state relative permeability of the wetting phase (dashed lines) and the non-wetting phase (solid lines) with wetting phase saturation during (a) drainage and (b) imbibition. 83

5.5 Steady state variation of the capillary pressure with wetting phase saturation during drainage (solid lines) and imbibition (dashed lines). 85

5.6 Variation at steady-state of the fluid-fluid interface length (as represented by the non-dimensional variable ζ) with wetting phase saturation during (a) drainage and in (b) imbibition. 86

5.7 Variation at steady-state of ζ_w (solid lines) and ζ_{nw} (dashed lines) with wetting phase saturation during (a) drainage and (b) imbibition. 87

5.8 Variation at steady-state of the Euler characteristic of the wetting phase with wetting phase saturation during (a) drainage and (b) imbibition. . . . 89

5.9 Major points of large cluster formation of non-wetting (upper - yellow colour) and wetting (lower - blue colour) phase clusters during the transient through $\chi_w = 0$, for structure 6. 90

5.10 Variation at steady-state of the average pore size of the wetting phase (dotted lines) and the non-wetting phase (solid lines) against the wetting phase saturation during (a) drainage and (b) imbibition. 93

6.1 Predicted steady-state two-phase flow distribution patterns for drainage for structure 4 ($\chi_0 = 800$) at $S_w = 0.7$ and with a different driving force, $G = 5 \times 10^{-6}$ in (a), $G = 2 \times 10^{-6}$ in (b), $G = 1 \times 10^{-6}$ in (c), and $G = 5 \times 10^{-7}$ in (d). The wetting phase is shown in blue, the non-wetting phase in yellow, and the solid phase in black. 98

6.2 Variation of relative permeability of the wetting phase (dashed lines)and non-wetting phase (solid lines) with body force for the final constant values of in (a) S_w=0.91, in (b) S_w=0.7 in (c) S_w=0.49, in (d) S_w=0.32 in (e) S_w=0.2.100

6.3 Variation of capillary number with body force for the final constant values of in (a) S_w=0.91, in (b) S_w=0.7 in (c) S_w=0.49, in (d) S_w=0.32 in (e) S_w=0.2.102

6.4 Variation of the Euler characteristic of the wetting phase χ_w with body force for the final constant values of in (a) S_w=0.91, in (b) S_w=0.7 in (c) S_w=0.49, in (d) S_w=0.32 in (e) S_w=0.2. 104

6.5 Variation of the Euler characteristic of the wetting and non-wetting phases per unit average grain, ξ_w and ξ_{nw} with body force for the final constant values of in (a) S_w=0.91, in (b) S_w=0.7 in (c) S_w=0.49, in (d) S_w=0.32 in (e) S_w=0.2. 105

6.6 Variation of the interface length represented by the non-dimensional variable ζ with body force for the final constant values of in (a) S_w=0.91, in (b) S_w=0.7 in (c) S_w=0.49, in (d) S_w=0.32 in (e) S_w=0.2. 108

6.7 Variation of the interface length as represented by the non-dimensional variables ζ_w and ζ_{nw} with body force for the final constant values of in (a) S_w=0.91, in (b) S_w=0.7 in (c) S_w=0.49, in (d) S_w=0.32 in (e) S_w=0.2. . . 109

6.8 Predicted steady-state two-phase flow distribution patterns for imbibition for structure 4 ($\chi_0 = 800$) at $S_w = 0.3$ and with the different driving force, $G = 5 \times 10^{-6}$ in (a), $G = 2 \times 10^{-6}$ in (b), $G = 1 \times 10^{-6}$ in (c), and $G = 5 \times 10^{-7}$ in (d). The wetting phase is shown in blue, the non-wetting phase in yellow, and the solid phase in black. 111

6.9 Variation of relative permeability of the wetting phase and non-wetting phase with body force for the final constant values of in (a) S_w=0.09, in (b) S_w=0.3 in (c) S_w=0.45, in (d) S_w=0.6 in (e) S_w=0.85. 112

6.10 Variation of capillary number with body force (per unit area) for the final constant values of in (a) S_w=0.09, in (b) S_w=0.3, in (c) S_w=0.45, in (d) S_w=0.6 in (e) S_w=0.85. 113

6.11 Variation of the Euler characteristic of the wetting phase χ_w with body force for the final constant values of in (a) S_w=0.09, in (b) S_w=0.3, in (c) S_w=0.45, in (d) S_w=0.6 in (e) S_w=0.85. 116

6.12 Variation of the Euler characteristic of the wetting and non-wetting phases per unit average grain, ξ_w and ξ_{nw} with body force for the final constant values of in (a) S_w=0.09, in (b) S_w=0.3, in (c) S_w=0.45, in (d) S_w=0.6 in (e) S_w=0.85. 117

6.13 Variation of the interface length represented by the non-dimensional variable ζ with body force for the final constant values of in (a) S_w=0.09, in (b) S_w=0.3, in (c) S_w=0.45, in (d) S_w=0.6 in (e) S_w=0.85. 119

6.14 Variation of the interface length as represented by the non-dimensional variables ζ_w and ζ_{nw} with body force for the final constant values of in (a) S_w=0.09, in (b) S_w=0.3, in (c) S_w=0.45, in (d) S_w=0.6, in (e) S_w=0.85. . . 120

A1 Representative elementary volume determination through testing (a) porosity and (b) permeability values. 142

B1 Volume fraction contour plots of the temporal evolution of the injection of the nonwetting phase (yellow) into the wetting phase (blue) for a steady state saturation rate of wetting phase of 0.91 and Euler characteristic $\chi_0 = -800$. In terms of lattice units $t = 5 \times 10^4$ in (a), $t = 1 \times 10^5$ in (b), $t = 1.5 \times 10^5$ in (c), $t = 2 \times 10^5$ in (d), $t = 2.5 \times 10^5$ in (e), $t = 3 \times 10^5$ in (f), $t = 3.5 \times 10^5$ in (g), $t = 4 \times 10^5$ in (h), $t = 4.5 \times 10^5$ in (i) and $t = 5 \times 10^5$ in (j). 144

B2 Volume fraction contour plots of the temporal evolution of the injection of the nonwetting phase (yellow) into the wetting phase for a steady state saturation rate of the wetting phase of 0.49 and Euler characteristic of $\chi_0 = -800$. In terms of lattice units $t = 6 \times 10^4$ in (a), $t = 1.2 \times 10^5$ in (b), $t = 1.8 \times 10^5$ in (c), $t = 2.4 \times 10^5$ in (d), $t = 3 \times 10^5$ in (e), $t = 3.6 \times 10^5$ in (f), $t = 4.2 \times 10^5$ in (g), $t = 4.8 \times 10^5$ in (h), $t = 5.4 \times 10^5$ in (i), $t = 6 \times 10^5$ in (j), $t = 6.6 \times 10^5$ in (k), $t = 7.2 \times 10^5$ in (l), $t = 7.8 \times 10^5$ in (m) and $t = 8.4 \times 10^5$ in (n). 145

B3 Volume fraction contour plots of the temporal evolution of the injection of the nonwetting phase (yellow) into the wetting phase (blue) for the steady saturation rate of the wetting phase of 0.32 and Euler characteristic of $\chi_0 = -800$. In terms of lattice units $t = 6 \times 10^4$ in (a), $t = 1.2 \times 10^5$ in (b), $t = 1.8 \times 10^5$ in (c), $t = 2.4 \times 10^5$ in (d), $t = 3 \times 10^5$ in (e), $t = 3.6 \times 10^5$ in (f), $t = 4.2 \times 10^5$ in (g), $t = 4.8 \times 10^5$ in (h), $t = 5.4 \times 10^5$ in (i), $t = 6 \times 10^5$ in (j), $t = 6.6 \times 10^5$ in (k), $t = 7.2 \times 10^5$ in (l), $t = 7.8 \times 10^5$ in (m) and $t = 8.4 \times 10^5$ in (n). 146

B4 Volume fraction contour plots of the temporal evolution of the injection of the nonwetting phase (yellow) in the wetting phase (blue) for the steady saturation rate of the wetting phase of 0.2 and an Euler characteristic of $\chi_0 = -800$. In terms of lattice units $t = 7 \times 10^4$ in (a), $t = 1.4 \times 10^5$ in (b), $t = 2.1 \times 10^5$ in (c), $t = 2.8 \times 10^5$ in (d), $t = 3.5 \times 10^5$ in (e), $t = 4.2 \times 10^5$in (f), $t = 4.9 \times 10^5$ in (g), $t = 5.6 \times 10^5$ in (h), $t = 6.3 \times 10^5$ in (i), $t = 7 \times 10^5$ in (j), $t = 7.7 \times 10^5$ in (k), $t = 8.4 \times 10^5$ in (l), $t = 9.1 \times 10^5$ in (m) and $t = 9.8 \times 10^5$ in (n). 147

B5 Volume fraction contour plots of the temporal evolution of the injection of the wetting phase (blue) into the non-wetting phase (yellow) for a steady state saturation rate of wetting phase of 0.09 and Euler characteristic $\chi_0 = -800$. In terms of lattice units $t = 5 \times 10^4$ in (a), $t = 1 \times 10^5$ in (b), $t = 1.5 \times 10^5$ in (c), $t = 2 \times 10^5$ in (d), $t = 2.5 \times 10^5$ in (e), $t = 3 \times 10^5$ in (f), $t = 4 \times 10^5$ in (g), $t = 4.5 \times 10^5$ in (h) and $t = 5 \times 10^5$ in (i). 148

B6 Volume fraction contour plots of the temporal evolution of the injection of the wetting phase (blue) into the non-wetting phase (yellow) for a steady state saturation rate of the wetting phase of 0.45 and Euler characteristic of $\chi_0 = -800$. In terms of lattice units $t = 7.2 \times 10^4$ in (a), $t = 1.44 \times 10^5$ in (b), $t = 2.16 \times 10^5$ in (c), $t = 2.88 \times 10^5$ in (d), $t = 3.6 \times 10^5$ in (e), $t = 4.32 \times 10^5$ in (f), $t = 5.04 \times 10^5$ in (g), $t = 5.76 \times 10^5$ in (h), $t = 6.48 \times 10^5$ in (i), $t = 7.2 \times 10^5$ in (j) and $t = 7.92 \times 10^5$ in (k). 149

B7 Volume fraction contour plots of the temporal evolution of the injection of the wetting phase (blue) into the non-wetting phase (yellow) for the steady saturation rate of the wetting phase of 0.6 and Euler characteristic of $\chi_0 = -800$. In terms of lattice units $t = 7.5 \times 10^4$ in (a), $t = 1.5 \times 10^5$ in (b), $t = 2.25 \times 10^5$ in (c), $t = 3 \times 10^5$ in (d), $t = 3.75 \times 10^5$ in (e), $t = 4.5 \times 10^5$ in (f), $t = 5.25 \times 10^5$ in (g), $t = 6 \times 10^5$ in (h), $t = 6.75 \times 10^5$ in (i), $t = 7.5 \times 10^5$ in (j) and $t = 8.25 \times 10^5$ in (k). 150

B8 Volume fraction contour plots of the temporal evolution of the injection of the wetting phase (blue) in the non-wetting phase (yellow) for the steady saturation rate of the wetting phase of 0.85 and an Euler characteristic of $\chi_0 = -800$. In terms of lattice units $t = 8.5 \times 10^4$ in (a), $t = 1.7 \times 10^5$ in (b), $t = 2.55 \times 10^5$ in (c), $t = 3.4 \times 10^5$ in (d), $t = 4.25 \times 10^5$ in (e), $t = 5.1 \times 10^5$ in (f), $t = 5.95 \times 10^5$ in (g), $t = 6.8 \times 10^5$ in (h), $t = 7.65 \times 10^5$ in (i), $t = 8.5 \times 10^5$ in (j) and $t = 9.35 \times 10^5$ in (k). 151

B9 Velocity magnitude vector plot on selected areas (for flow demonstration purposes only). 152

List of Tables

2.1 Main researches and research focuses 24

4.1 The effective Minkowski functionals (ϕ_0, L_0, $\overline{\chi}_0$), the average pore coordination number of the porous medium C_p, the hydraulic tortuosity T, the average pore size $\overline{d}_P$ and the average pore throat $\overline{d}_T$, for the seven artificial structures considered in this work. 43

5.1 The values of the effective Minkowski functionals (ϕ_0, L_0, $\bar{\chi}_0$), the average pore coordination number of the porous medium C_p, the hydraulic tortuosity T, the average pore size $\bar{d}_P$, and the average pore throat $\bar{d}_T$ for the seven artificial structures. 81

Acknowledgement

I would like to thank the department of civil engineering at Xi'an Jiaotong-University and the department of Engineering at the University of Liverpool for giving me this opportunity for PhD study and providing me with great academic and computational resources for the implementation of this project. I would also like to thank my supervisors Dr K. Papadiki and Dr S. Shaw for their guidance and encouragement whenever I had problems and doubts. I would like to thank my parents for their love and support. I was not an easy child growing up, but they always believed in me, endure me, and tried to understand me. Thank you for everything. Finally, I would like to express my gratitude to Mr Xu for staying with me through all pleasant and tough times, for believing in me and for supporting me for the years of my PhD life.

Nomenclature

Latin symbols

Symbol	Description
a	distance between centreline to interface
A	area
b	volumetric parameter
c_s	speed of sound
C	contour length
C_p	pore coordination number
$\bar{d_T}$	average pore throat
$\bar{d_p}$	average pore size
D	spreading droplet diameter
$D*$	the maximum spread factor
D_0	initial droplet diameter
e_i	direction factor
f_i^σ	density distribution function
$f_i^{\sigma,eq}$	equilibrium distribution function
F_σ	force factor
$F_{c,\sigma}$	fluid-fluid cohesion force
$F_{ads,\sigma}$	fluid-solid adhesion force
G	body force
G_c	fluid-fluid cohesion parameter
$G_{ads,\sigma}$	fluid-solid adhesion parameter
i^{th}	direction

k_κ	effective permeability of the κ phase
k_i	intrinsic permeability
$k_{r,\kappa}$	relative permeability of the κ phase
$k_{r,w}$	relative permeability of wetting phase
$k_{r,nw}$	relative permeability of non-wetting phase
l	length of porous medium
L	distance between centreline to soild wall
L_0	effective contour length
m_i^κ	the moment of phase density distribution function
$m_i^{\kappa,eq}$	the moment of phase density equilibrium function
M	viscosity ratio
$\mathbf{M}$	the orthogonal transformation matrix
n	grain density
N_i	node in interface
N_w	node in wetting phase
N_s	node in solid phase
N_{nw}	node in non-wetting phase
N_{tot}	node in total void phase
O	number of liquid phase
p_c	critical pressure
P_c	capillary pressure
P_w	fluid pressure of the wetting phase
P_{nw}	fluid pressure of the non-wetting phase
r	grain size
S	number of isolated solid objects
S_w	saturation rate of the wetting phase
S_{nw}	saturation rate of the non-wetting phase
$\mathbf{S}$	the diagonal matrix
t	the number of the time step

T	tortuosity
T_c	critical temperature
u'	common velocity
u_0	droplet velocity
u_x	velocity in x-direction
$u_{x,w}$	average velocity of wetting phase in x-direction
$u_{x,nw}$	average velocity of non-wetting phase in x-direction
u_σ^{eq}	macroscopic velocity
w_i	weighting factor
Z	grains

Greek symbols

Symbol	**Description**
α	attraction parameter
Δt	time scale
ζ	the interface length
ζ_w	the interface length per unit wetting phase
ζ_{nw}	the interface length per unit non-wetting phase
θ_{eq}	equilibrium contact angle
κ	wetting or non-wetting phase
μ_w	dynamic viscosity of wetting phase
μ_{nw}	dynamic viscosity of non-wetting phase
ν_w	kinematic viscosity of wetting phase
ν_{nw}	kinematic viscosity of non-wetting phase
ξ_w	Euler characteristic of the wetting phase per unit grain enclosed by the wetting phase
ξ_{nw}	Euler characteristic of the wetting phase per unit grain enclosed by the non-wetting phase

ρ	density
ρ_w	density of wetting phase
ρ_{nw}	density of non-wetting phase
τ	relation time
ϕ_0	effective solid phase fraction
χ_w	Euler characteristic of wetting phase
χ_{nw}	Euler characteristic of non-wetting phase
$\bar{\chi}_0$	effective Euler characteristic
$\psi(\rho)$	effective mass
$\mathbf{\Omega}$	collision matrix

Abbreviations

Symbol	**Description**
APS	average pore size
APT	average pore throat
BGK	Bhatnagar-Gross-Krook model
Ca	capillary number
CFD	computational fluid dynamic
CPF	connected pathway flow
DTF	drop-traffic flow
LBM	Lattice-Boltzmann model
LGD	large-ganglion dynamics
MCMP	multicomponent multiphase
MRT	muiti-relaxation time
Oh	the Ohnesorge number
REV	representative elementary volume
Re	the Reynolds number
SCMC	Shan-Chen Multicomponent
SGD	small-ganglion dynamics
We	the Weber number

Chapter 1

Introduction

This chapter gives a brief introduction to the background in multiphase flow through porous medium and developments of numerical methods (lattice-Boltzmann model). Followed by the subject of this thesis and finished with the thesis outline.

1.1 Multiphase flows in porous medium

Multiphase flow is a common phenomenon that appeared in everyday life, both in nature and in industrial processes, for instance, oil and gas fields, geological sequestration of carbon dioxide, power plants, etc. Multiphase flow study is critically important in petroleum related fields not only in extraction but also in the petrochemical engineering process. Most of the oil wells ultimately produce both oil and gas from the formation and in some cases produce water as well. Studies showed that in China, with only the exploitation rate of 18.5% for oil, and 9.2% for gas in the ocean, the development potential is quite high, and multiphase flow technologies is one of the key points to overcome the difficulty of drilling and exploration under deep ocean (Li, 2014). Engineers need to accurately understand and predict the physical behaviours of multiphase flow to optimise operations. Considering that drilling and exploration are costly and risky operations and expenditure associated are usually valued at millions of dollars just to trace the hydrocarbons (Tanoh, 2016). During the first stage of exploitation, the field with high content of oil and gas can be collected easily by natural flow from the reservoir. With further exploitation, the production changes from flowing to pumping. As the storage of oil and gas under surface become lower and lower, the phase transform from connected pathways to ganglion dy-

namics, in other words, trapped as immobile clusters(Rücker et al., 2015). The oil and gas that remain underground at this stage can be very difficult to exploit. The problem can only be solved by increasing pressure or injecting acid, however, these procedures can be highly costly and risk to contaminate soil and groundwater. To avoid these situations and solve the problem to exploit oil and gas under low storage, the understanding of multiphase flow becomes crucial. In addition, in the process industry, it is a common problem to deal with multiphase phenomenons, for instants, chemical reactors, liquid-vapour separators. etc (Wang, 2016). Another important application of multiphase study is water treatment, such as groundwater treatment, and wastewater treatment. Groundwater is the primary source of drinking water and irrigation water in many parts of the world, the current situation is not optimistic showed by reports(Zhang, 2021). Since 2015, over 30 billion funds have been invested in prevention and reparation from the government (Liu, 2015). Development of the multiphase separating system can help treat wastewater with oil content and other immiscible contaminants (Wang et al., 2010), for instance, when oil leaks or spills in the ocean. Moreover, one way to improve the water quality of rivers and lakes is aeration which can increase oxygen content and decrease ammonia content (COMSOL, 2018). Simulation of multiphase flow can help design such systems. Multiphase studies can help reduce the source of pollution and contamination, and also treat the water supplies. Moreover to optimise these processes, improve efficiency, and ensure safety for our future. Therefore, multiphase studies are significant both in nature and the industrial field.

Any fluid flow containing more than one phase can be considered as multiphase flow. The term phase is a thermodynamic definition that refers to the state of matter (Yadigaroglu and Hewitt, 2017). It can be gas, liquid or solid. The layers between fluid phases are called interfaces. Within a multiphase system, the distribution of the fluids and the geometry of the interfaces cannot be predicted a priori. Bubbles can be distributed uniformly through the domain, or coalescence and snap-off can happen due to different impacts and conditions as shown in Fig.1.1 (Ashgriz, 2011). Fluids properties of engineering significance such as phase velocity, pressure drop, etc. cannot be determined without understanding the situations and behaviour of the multiphase flow. The phase distribution and flow patterns of multiphase flow depend on the structure properties, for instance, the morphology of the structures, wettability, etc., and the fluid properties, such as density, viscosity ratios, etc., as well as flow conditions, such as driving forces, initial phase saturations, etc.

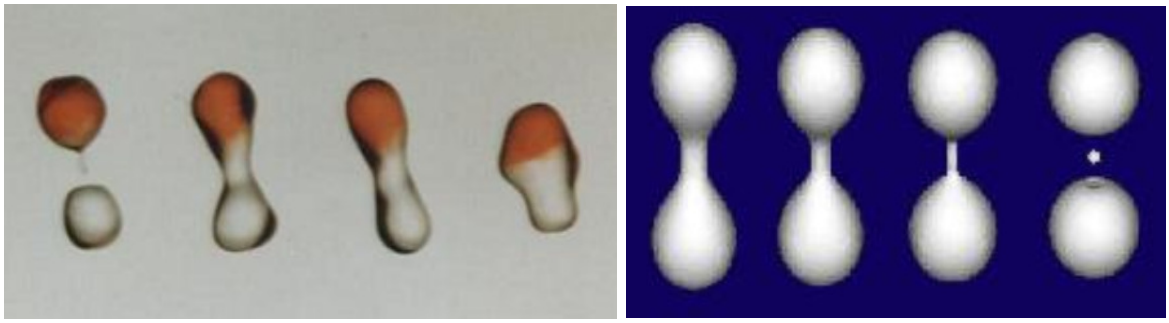

(a) (b)

Figure 1.1: Coalesce and snap-off behavior in multiphase flow, a) coalesce, b) snap-off (Ashgriz, 2011).

A porous medium can naturally occur, e.g. sand and fissured rocks; manufactured, e.g. ceramics and filter, or organic, e.g. lungs and bones are shown in Fig. 1.2. A porous medium domain in common contains two parts, one occupied with solid phase and the remaining part is a void space (Bear, 2018). The solid phase here represents a wider range compared to the strict definition. For instance, soft materials such as rubber and organic tissue can also be referred to as 'solid' in a porous medium. The void space is normally occupied by one or multiple gas or liquid. The pore space is not necessarily interconnected. However, in consideration of fluid flow within a porous medium, at least one part of the void phase needs to be interconnected. Porous structures are normally divided into two types: the unconsolidated and consolidated medium (Huinink, 2016). The unconsolidated materials consist particles that are separated from each other, such as all kinds of soils. While consolidated materials, the solid matrix forms a spanning phase, such as bones and concrete.

In most cases, the geometry of a porous medium is highly complicated. The nature of a porous medium is very different depending on the size, shape, connectivity and organisation of the void structures within it. Flow and transport properties of pore structures depend on their morphology which can be estimated by experimental or computational methods. In order to describe the morphology of a porous medium, Minkowski functionals can be used. There are three independent Minkowski functionals in 2-dimensions, area, perimeter, and the Euler characteristic. In 3-dimensions, there are four, volume, surface

area, curvature, and the Euler characteristic. The Euler characteristic as the main parameter for this study, is the topological characteristic of a structure based on the relationship between the number of void space components and the number of isolated solid clusters, which describe the connectivity of a porous medium. However, Minkowski functionals are not a complete description of a porous medium. There are also other properties that affect the structure of a porous medium, fluid distribution, and interface geometry.

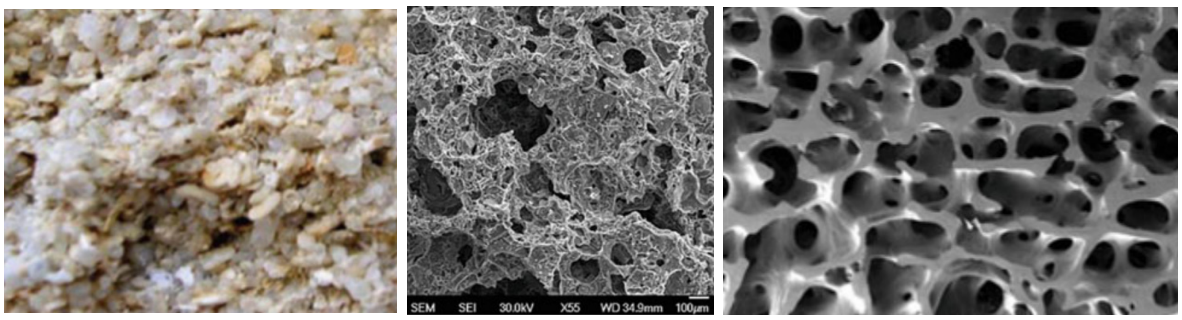

(a) (b) (c)

Figure 1.2: Examples of porous medium, a) sandstone, b) ceramics c) bone (Bear, 2018).

The determination of the macroscopic characteristics of a porous medium, such as the topology, geometry, and overall morphology of the pore structures, together with how a fluid, possibly composed of multiple components, transports through this void structure can help understand numerous biological, industrial and engineering applications. When the domain is large and multiple channels and cavities with varying size and distance occur in the field, the volume averaging and global measurements such as conductivity and permeability become useful in describing the flow condition and simplify the description (Nield et al., 2006). In industrial applications, the key point is not only to describe the properties of a porous medium but also to optimize the flow condition and assemble the results, in order to improve the efficiency of the process. Fluid flow in the porous medium can be affected by various forces. The relationship between pressures/energy drop and flow rate is one of the most important problems in both single and multiphase studies. For example, in the process of oil-gas flow in the petroleum industrial field, the distribution of pressure, the magnitude of energy and the amount of production are highly related to fluid phase distribution and velocity field development.

There are many important properties of flow in a porous medium, such as permeability,

energy loss and pressure drop in packed beds. Permeability is defined as the ability to convey fluids. It is a correlation between structure characteristics, for instance, porosity and surface area and flow properties discovered by Darcy (Blackwell, 1975). In the low Reynolds number regime, the permeability is governed by Darcy's law (Darcy, 1856) that links the discharge per unit area, with the applied pressure gradient, by the linear relation. The theory was then further developed and extended to the multiphase area, where each phase moves through its channel within the void spaced bound by the solid matrix. The pressure drop for laminar fluid flow through a randomly packed structure can also be calculated using the Carman–Kozeny equation, which taken into account of the measure of the pore space connectivity (J. Kozeny, 1927; Carman, 1937). The energy loss along the length of the material bed due to friction can be described by the Ergun equation. Using an extensive set of experimental data which covered a wide range of particle sizes and shapes, Ergun (1952) presented a general equation to calculate the pressure drop in a porous medium for both laminar and turbulent flow conditions. However, none of these previous theories is a complete explanation of relative permeability (Muskat and Meres, 1936). They only take into account the phase saturation without considering the effect of viscous coupling between two phases. However, relative permeability can be affected by the geometry properties of pore structures, fluid phase wettability, capillary number, viscosity ratio, flow process, etc. (Sahimi and Tsotsis, 1997; Li et al., 2005; Zhang, 2011; Ramstad et al., 2012).

Studies of multiphase flow in the porous medium can be done in both experimentally and numerically. Due to the vast growth of computational resources in recent years, artificial pore structures with well-defined geometrical and topological properties can be constructed, and the fluid behaviour can be computed and studied numerically (Blunt et al., 2013). Advantages of numerical study include lower cost, the ability to simulate complicated systems and ideal conditions and reduce the amount of heavy workload and time from experimental works. The numerical solution of multiphase flows normally starts from the general conservation laws of mass, momentum and energy expressed by partial differential equations. Depending on the method of solutions, the computational domain needs to be separated into volume, grids, or elements so that the velocity and pressure of each point in the domain can be stored in every node or averaged over a finite volume. The set of equations can be completed by including the necessary constitutive laws, for example, the equation of state

which governs the physical properties of the subject; general laws of nature which describe the natural behaviours under an idealized or simplified situation; the relationship of parameters such as heat transfer coefficients, friction factors, etc (Yadigaroglu and Hewitt, 2017). In addition, the boundary condition needs to be defined according to the physical understanding of the problem. In multiphase flow cases, the descriptions of the evolution in time for each phase such as pressure, velocity, and temperature are required, along with the geometry of the interfaces.

1.2 Thesis subject

The subject of this thesis is to study the effect of the morphological properties of the porous medium on immiscible two-phase flows during the drainage and imbibition process. The numerical investigations are performed using the multi-component multiphase (MCMP) lattice-Boltzmann model which is capable of simulating multi-phase flows in complex domains. The porous mediums are 2D and generated randomly using the Boolean model. These artificial pore structures are generated with specific predetermined values of Minkowski functionals. The codes for generating porous medium and LBM simulation are developed with MATLAB.

The main task of this thesis, to study immiscible two-phase flows is separated into three parts, under transient state, under steady-state, and low driving forces. The impact of pore space connectivity, as expressed through the Euler characteristic on the chemically inert, thermodynamically stable, immiscible two-phase flow through the connected pore structure are studied under these conditions by using lattice-Boltzmann methods. The oil-water like system was chosen for this thesis, where the water is the wetting phase and the oil is the non-wetting phase. Seven different artificial pore structures are generated based on the random distribution of overlapping circles with similar values of porosity and contour length, and different Euler characteristics, with the same grain size and grain density for each condition (same structures are used for the transient study and low driving forces study). This thesis focuses on analysing the relative permeability, interface length, Euler characteristic of the wetting and non-wetting phases, and the capillary pressure for imbibition and drainage at different saturation rates. The impact of the variable Euler characteristic on the average pore coordination number, pore size and pore throat distribution are also taken into account

for a more complete geometrical and topological picture of the observed porous medium.

1.3 Elements of novelty

Multiphase studies of both experimental and numerical on the macroscopic behaviour of immiscible two-phase flows in the porous medium have been done in the past literature to understand the impact of fluid phase topology (Armstrong et al., 2018; Ramstad et al., 2012; Hussain et al., 2014; Zhang et al., 2016; McClure et al., 2020; Ott et al., 2020). As a relatively new method, the lattice-Boltzmann modelling (LBM) has been used to study flows in porous mediums in recent years due to its advantage in the treatment of interphase dynamics and complex boundaries condition. However, most of these past studies focused on the relationship between relative permeability and viscosity ratio, wetting angle, etc. **To the best of the author's knowledge, systematic investigations on the impact of the pore space morphology, and more specifically connectivity have not received the same level of attention**. The impact of pore space morphology of immiscible two-phase flows remains largely unexplored. In the current work, a two-dimensional MCMP LBM is used to study the impact of the morphological properties of the porous medium on immiscible two-phase flows during the drainage and imbibition process. The pore structures with different geometrical properties are artificially generated, and the dependence of various fluid properties at different saturation rates on the morphological properties of the porous medium is analysed.

1.4 Progress of research

The research started with reviewing past studies on multiphase flows using lattice-Boltzmann models, and porous medium. By studying the lattice-Boltzmann models and discovering their native advantages, the code was first developed for single-phase flow for me to study LBM from the basic. The pore structures were generated after studying the Minkowski functionals which are used to capture the mathematical properties of a porous medium. The artificial pore structures that were generated with specific predetermined values of Minkowski functionals were tested with the LBM code for single-phase flow to study the effect of porosity, contour length, and Euler characteristics. The results showed that the pore space topology, as expressed through the Euler characteristic is the most interesting

parameter to study. The following step was to generate 7 structures with similar porosity and contour length, and different Euler characteristics used for two-phase studies and calculate the average pore coordination number, pore size and pore throat distribution for further analysis.

Moving into the two-phase flow stage, the first step was code development for two-phase flows. The original Shan-Chen method was used and improved with the multi-relaxation time LBM. Then, it was validated using two immiscible viscous fluids of Poiseuillie flow between two parallel plates to test the accuracy in the prediction of fluid properties. Another validation was done to show the model can qualitatively capture the topological change during the drainage/imbibition process by simulating a droplet breakup pattern for a selected Weber number. The two-phase system was chosen to be an oil-water like system, thus the research outcome can be more useful and related to the industry. The first project of this thesis was the steady-state condition study taken place during the second year. For the second part of this thesis, the transient study, droplet impacting on a flat surface to calculate the maximum spread factor was performed to validate the ability of the model in capturing the transient development of immiscible two-phase flows. The third and final part of this thesis was immiscible two-phase flows at low driving forces. For all three conditions, fluid properties such as relative permeability, velocity field, and morphology of the phases such as interface area, and Euler characteristic of each phase, were studied to identify the impact of pore space topology.

1.5 Outline of the Thesis

This thesis includes 7 main chapters.

The first chapter gives a brief introduction to the background of multiphase flow through a porous medium, including the importance of studying multiphase flows and the definition of a porous medium. In addition, introduces the developments of numerical methods (lattice-Boltzmann model) for multiphase flows, followed by the thesis subject and elements of the novelty of this current research. This chapter finishes with a description of the thesis outline.

The second chapter presents an in depth review of the state-of-the-art development in the field focusing on computational models, multiphase flows, and porous medium. Specifically,

the use of lattice-Boltzmann modelling for multiphase flow is reviewed. Both experimental and numerical studies are involved in this chapter.

The third chapter briefly introduces the numerical methods of this project, the pseudo potential Shan and Chen method, which is a multi-component multiphase (MCMP) lattice-Boltzmann model (LBM). Starts from the basics of LBM, and moves into the Shan-Chen Method where two sets of density distribution functions are used for two-phase flows, and the Multi-relaxation time model Chapter 3 concludes with 3 validations for the current model.

The fourth chapter gives detailed information on the immiscible two-phase flow under transient state conditions. Including the porous medium generation and morphology, the model set-up, and the results and discussions of both drainage and imbibition process, which include saturation rate, velocity fields, capillary pressure, Euler characteristic, and interface length of each phase.

The fifth chapter provides a detailed analysis of immiscible two-phase flow under steady-state conditions. Including the porous medium morphology (different porous medium compare to chapter four), and the simulation results of both drainage and imbibition process, which include relative permeability, capillary pressure, Euler characteristic, interface length, and average pore size of each phase.

The sixth chapter presents a detailed analysis of immiscible two-phase flow at low driving forces. Including the results and discussions of both drainage and imbibition processes (the porous medium and model set-up are the same as Chapter 4), which include relative permeability, capillary number, Euler characteristic, and interface length of each phase.

Chapter seven gives a general summary of this thesis, includes important conclusions from this research, and recommended works for the future.

In addition, one appendix can be seen at the end of this thesis.

Appendix A The representative elementary volume.

Appendix B Contour and vector plots for transient state study.

Chapter 2

Literature review

This chapter reviews the previous studies of multiphase flows in the porous medium. Specifically past investigations that used lattice-Boltzmann modelling for immiscible two-phase flow including both experimental and numerical studies.

2.1 Multiphase flows

Studies of multiphase flow, heat and mass transfer covered a wide range of problems, for instance, bubble or droplet translation, propellant burning, smoke formation, gas in liquids, sedimentation. (Oran and Boris, 2002). All these subjects have their own distinguishing characteristics, and different formulations, approximations, and different measurement methods were used to study these systems in the past. There is no one set of equations and supporting assumptions that fit every multiphase situation as each system is unique. In general, it is assumed that each phase is in its thermodynamic equilibrium state, however, the different phases are not necessarily in equilibrium with each other (Oran and Boris, 2002). Therefore, it is necessary to calculate the rates of transfer of mass, momentum, and energy among the phases in order to solve the problem. Multiphase flow models can be developed in three ways: experimentally(Zhang et al., 2015; Yang and Zhang, 2022; Liu et al., 2023), theoretically (Hatta et al., 1998; Raghavan, 2009; Nazeer et al., 2022), and computationally(Farokhipour et al., 2020; Yang et al., 2020; Afzali et al., 2022).

Multiphase flows in porous media are one of the most important and common scenarios in both natural and industrial processes. Generally, multiphase flows in pores structures

can be driven by gravitational, capillary and viscous forces (Wang, 1998). Gravity move phases in the direction of the gravitational field. It commonly appears in injecting steam for enhanced oil recovery, where the injected phase tends to rise to the top of the existing phase and causes premature breakthrough of steam within the production wells (Kumar Singh and Priyadarshini Nayak, 2023). Capillary forces play important roles in forming the phase distribution in heterogeneous porous media (Zakirov and Khramchenkov, 2020). Viscous forces influence phase motion relatively between fluids with higher and lower viscosity, where the process of fluids with different viscosity displacing one another can be inherently unstable and causes fingering of phase interfaces (Singh et al., 2021). In the past, due to the complicated properties of porous media and the inherent nonlinearities of multiphase flow problems, studies were limited to small scare, lower dimensions and simplifying assumptions(Eshgarf et al., 2023). In order to solve these problems which involve gravity, capillarity and phase change, many numerical algorithms, for example, the Buckley–Leverett equation (Buckley and Leverett, 1942), the McWhorter and Sunada equation (MSE) (McWhorter and Sunada, 1990) and approximate models, for instance, the unsaturated flow theory by Morel-Seytoux (1989) were proposed. For immiscible flows and transport in porous media, another difficulty lies in the presence of the irregular phase interfaces separating the phases. For such multi-region problems, the moving interfaces need to be tracked to better understand the physical relationship between them, thus complex mapping and numerical remeshing are required (Wang, 1998).

2.2 Flow in porous medium

2.2.1 Single phase flow in porous media

In the past decades, several theoretical (Bachmat and Bear, 1986; Whitaker, 1986; Gray, 1999; Cai et al., 2012), experimental (Avraam and Payatakes, 1995; Tsakiroglou et al., 2003, 2005; Aggelopoulos and Tsakiroglou, 2008; Aidun and Clausen, 2010) and numerical approaches (Gunstensen and Rothman, 1993; Sahimi and Tsotsis, 1997; Ghassemzadeh and Sahimi, 2004; Li et al., 2005; Zhang, 2011) have been developed to describe the flow and transport behaviour in porous media.

Koponen et al. (1997) used the lattice-gas method in a 2-dimensional porous substance

of randomly placed equal-size rectangles to investigate the correlation between the specific surface, tortuosity, effective porosity, permeability, and porosity of the model porous structure. The study revealed some of the limitations of the originally proposed Kozeny equation, whilst a modification of it which includes the effective porosity and tortuosity of the porous medium was proposed.

Vogel and Roth (2001) conducted network simulations to investigate the effect of porous media topology on water flow and solute transport through the determination of the pore size distribution and the definition of a spatial, pore space connectivity function based on the 3D Euler number. Comparing the simulation results to independent measurements in the same soil material, it was concluded that the pore size distribution and connectivity can provide good estimations of the hydraulic properties of porous media. Similarly, Vogel (2000) also investigated the effect of the pore structure on water retention and solute transport using a pore network model. It was shown that the pore topology can be adjusted in a way that different pore size distributions can lead to identical water retention curves, while the hydraulic conductivity and solute dispersion through the porous medium is dependent on the water retention curve and not on specific combinations of pore size distribution and topology. However, a pore network that is based on image analysis could potentially oversimplify the real geometry. In this way, the flow through an idealized shape capillary can be significantly different from a real irregular pore with the same mean diameter.

Lehmann et al. (2008) used the LBM to investigate the impact of the geometrical properties on the permeability and the fluid phase distribution in porous media. The effects of volume, surface, curvature and connectivity (the four Minkowski functionals) on the hydraulic conductivity and the water retention curve were studied. It was found that the permeability was significantly more sensitive to the surface and volume than the curvature and the connectivity. Moreover, it was identified that the description of porous media using Minkowski functionals should be coupled with the characterization of the pore sizes for a more complete description of its geometrical properties.

Scholz et al. (2012b) used the LBM and experiments to investigate the relationship between the porous medium permeability and the Euler characteristic. The 2-dimensional study proposed a replacement of the porosity based term, as described by Archie's law in the Katz-Thompson model (Katz and Thompson, 1986), with a mathematical form that relies on the topology of the pore space through the Euler characteristic. The proposed relation allows for permeability predictions over a wide range of porosities without prior knowledge

of the structure's percolation threshold.

Yang et al.(2017) studied the impact of randomness of the porous structure, particle size level and particle shape on flow characteristics, and concluded that randomness has a significant effect on the permeability of porous media with the same number of grains, and that the permeability is enhanced with spherical particles rather than cubical ones.

Decreases in the porous medium permeability with increasing mass flow rate due to the laminar inertial effect was studied by Arabjamaloei and Ruth (2017). A new empirical correlation was proposed to fit the scale permeability - mass flow rate relationship. However, the effective properties must be included in order to accurately predict the permeability in a complicated porous medium. Eshghinejadfard et al.

2.2.2 Immiscible multiphase flows in porous media

In the past decades, studies of multiphase flow in the porous medium have been done from both experimental (Avraam and Payatakes, 1995; Tsakiroglou et al., 2003, 2005; Aggelopoulos and Tsakiroglou, 2008; Aidun and Clausen, 2010) and numerical approaches (Gunstensen and Rothman, 1993; Sahimi and Tsotsis, 1997; Ghassemzadeh and Sahimi, 2004; Li et al., 2005; Zhang, 2011). Many experimental, theoretical and numerical studies in recent years have provided strong evidence for the importance of the pore structure topology and morphology of the interface on multiphase flows through a porous medium (Ramstad et al., 2012; Hussain et al., 2014). Therefore, many fluid properties such as relative permeability and capillary pressure of each phase are depends not only on the saturation, but also on the morphological properties geometry of the pore structure, and flow properties like the capillary number, viscosity ratio, the wetting angle and the flow process itself (drainage, imbibition, infiltration)(Spanne et al., 1994; Langaas and Papatzacos, 2001; Xu and Liu, 2018), invariant saturation rate, interface area, and capillary pressure (Erpelding et al., 2013). At the pore level, coalesce and snap-off of one fluid phase relative to the other also needs to be accounted for. In the field of two immiscible fluids through the porous medium, many authors have studied such factors affecting quantities.

Avraam and Payatakes (1995) used a model pore network of chamber-and-throat type in glass to study the steady-state water-oil two-phase flow in the porous medium. Moreover, relative permeability affected by the four flow regimes the large-ganglion dynamics

(LGD), small-ganglion dynamics (SGD), drop-traffic flow (DTF) and connected pathway flow (CPF) are shown in Fig.2.1. Observations and macroscopic measurements results showed that the relative permeability of both oil and water correlate strongly with flow regimes, and increased from ganglion dynamics to connected pathway flow as the flow mechanisms changed. In addition, this study suggested that the relative permeability is not only related to saturation rate, but also to capillary number, wettability, and other parameters. Thus, the conventional flow theory needs to be revamped and new studies need to be conducted to better understand two-phase flow in the porous medium.

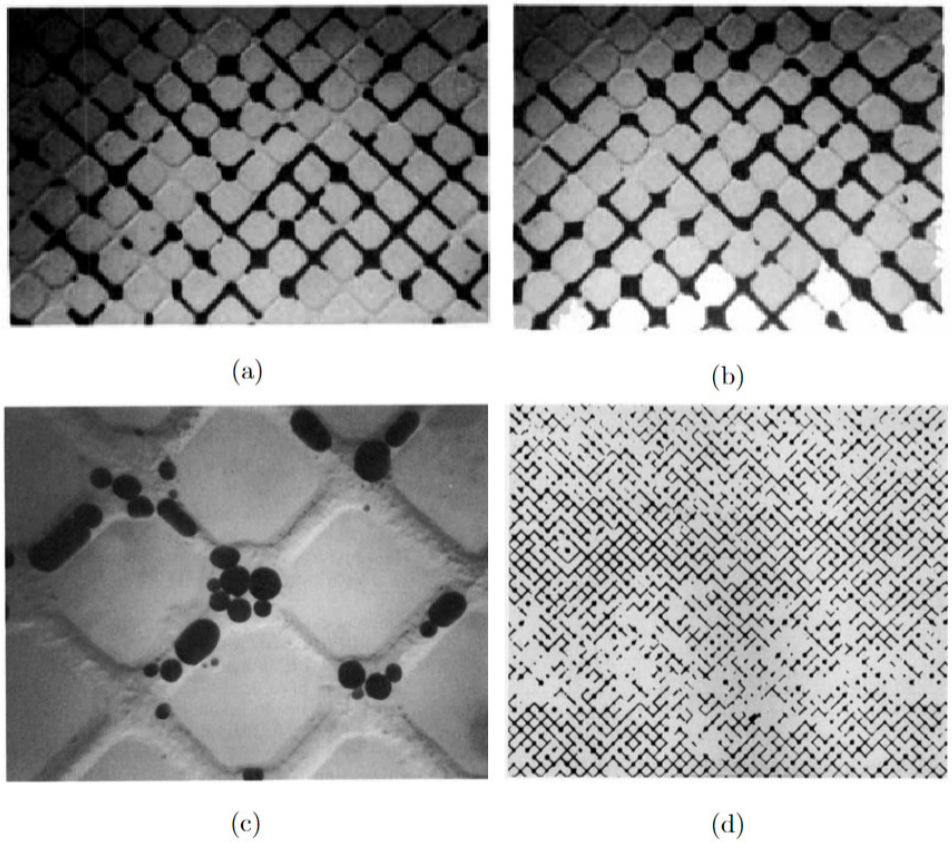

Figure 2.1: Snapshot of the four flow regimes: a) large-ganglion dynamics (LGD), b) small-ganglion dynamics (SGD), c) drop-traffic flow (DTF), d) connected pathway flow (CPF)Avraam and Payatakes (1995).

Li et al. (2005) investigate the viscous coupling effects between the two fluid phases in the porous medium using a three-dimensional LBM. Relative permeability was studied as a function of fluid viscosities, wettability, and capillary number. Strong correlations between the relative permeability and interfacial area were found from the simulation results which suggested that the interfacial area between two-phase is a key variable for multiphase

flow in porous medium and the existing flow theory can not provide adequate insight into multiphase flow processes in pore structures.

By studying the effects of reservoir wettability, pore shape geometry, and viscosity ratio of flowing fluids, Ghassemi and Pak (2011) found that the viscosity ratio has a negligible effect on the relative permeability of the wetting fluid, but has a substantive impact on the non-wetting phase, while the pore shape geometry has virtually no effect on the relative permeability of the wetting phase. However, the computational domain for this study was too small compared to the experimental model due to high computational costs. Also, the initial condition of the simulations was set to be randomly filled with two fluids to achieve the desired saturation, which can not represent the natural process of immiscible displacements.

Zhao et al. (2017) used a multicomponent multiphase pseudopotential lattice-Boltzmann model (MCMP-LBM) to study the effects of capillary number , viscosity ratio and wettability on the relative permeability curves. The two-phase distribution at different saturation for different wettability are shown in Fig.2.2, where the solid phase is in grey, the wetting phase is in blue, and the non-wetting phase is in red. It can be seen that the non-wetting phase occupies the middle of the mainstream path, and the wetting phase flows along the surface of the solid boundaries. The results implicated that the relative permeability of the non-wetting phase increases with increasing capillary number and viscosity ratio, while the wetting phase is insensitive to the viscosity ratio which confirmed Ghassemi and Pak's observations in the previous study (Ghassemi and Pak, 2011) and the effect of the capillary number depends on the wettability.

Applying the MCSC LBM, Dou and Zhou (2013) compared the results between homogeneous and heterogeneous porous medium, and determined that the variation of the relative permeability with the capillary number and viscosity ratio is strongly dependent on the heterogeneity of the pore structures. However, they did not investigate the effect of the properties of the heterogeneity of the porous medium and the porous medium was basic block represented which is too simple compared to any naturally occurring or manufactured pore structures.

Rücker et al. (2015) investigated the dynamic transient process of oil displacement (imbibition process) between the full oil phase connectivity and ganglion dynamics states within a sandstone rock. One of the major discoveries of this study was the indication of non-wetting (oil) phase mass transfer occurs through a series of correlated snap-off and

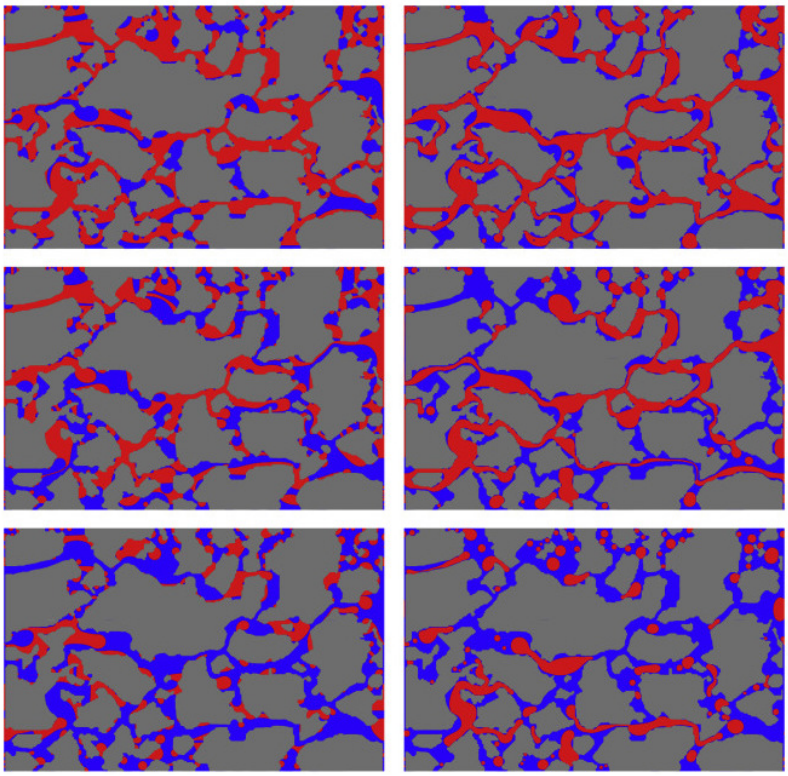

Figure 2.2: The two-phase distribution at different saturation ($S_w = 0.3, 0.5, 0.7$) for different wettability, Left column is the neutral wetting cases ($\theta = 90^o$); right column is strong wetting cases($\theta = 168.57^o$)(Zhao et al., 2017).

coalescence events, which gave rise to ganglia mobilisation patterns at macroscopic flow conditions that are insufficient to explain those events. However, this research did not consider the effect of the pore space topology on the underlying two-phase flow dynamics. Santiago et al. (2016) conducted a number of numerical experiments in 2-D, water-wet, porous geometry with a complex topology to evaluate the pore-scale dynamic processes during a secondary imbibition process of heavy oil using a finite volume approach at the pore-scale and the volume of the fluid method to properly capture interfaces. The simulations were conducted at three different temperature points and the pore-level events included the mobilisation of the oil ganglia, snap-off, coalescence and micro-fingering, in order to successfully capture the immiscible displacement of heavy oil. Although the key characteristics of the process were successfully captured and analysed in detail, the study made use of a single geometry with a limited characterisation of its morphology. Therefore, the impact of the porous medium morphology on the underlying dynamic processes can not be extracted from the conclusions.

The experimental results of two-fluid configurations during immiscible displacement ob-

served from fast x-ray microtomography were compared with the numerical simulation of LBM to investigate the mobilization of disconnected nonwetting phase clusters performed by Armstrong et al. (2016). This study demonstrated similar displacement patterns where the motion of the non-wetting phase disconnected clusters occurs through consecutive snap-off and coalescence events shown in Fig.2.3. Additionally, it showed that fluid phase topology is the controlling parameter for the relative permeability and that it can evolve at constant saturation, with macroscopic implications. The study provided great insights into the impact of fluid phase topology on fractional flow dynamics, however, the impact of the pore space connectivity and morphology was not taken into account.

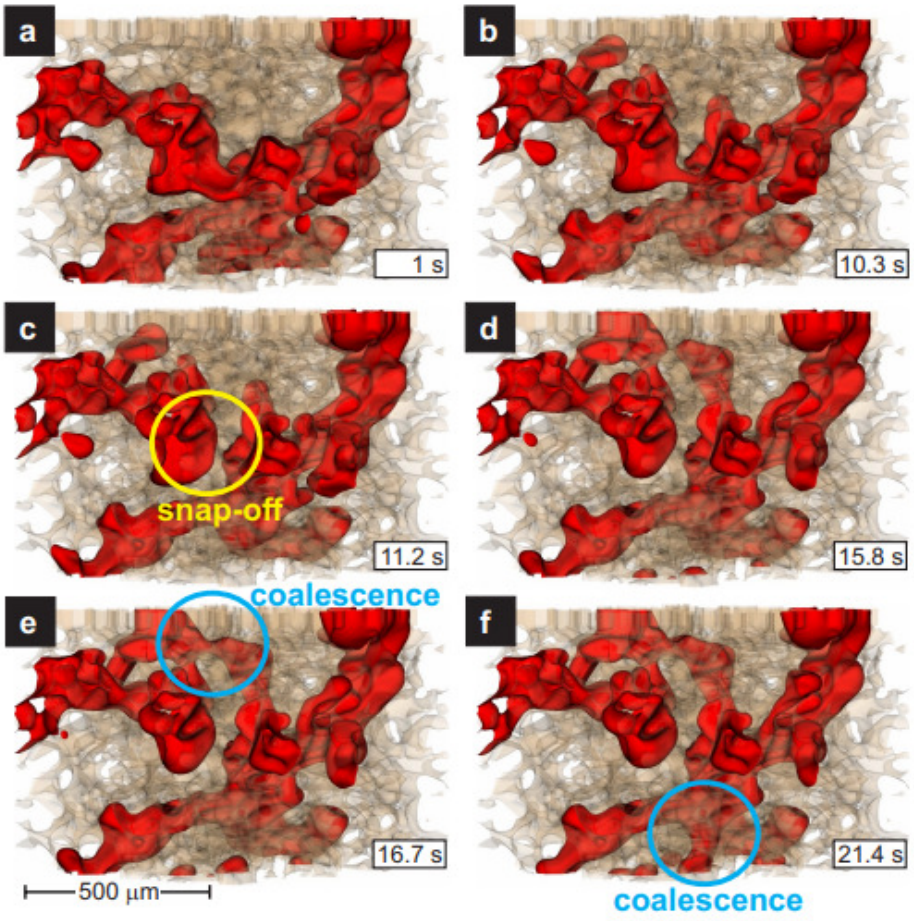

Figure 2.3: Ganglion Dynamics: snap-o and coalescence events result in continuously changing phase connectivity at fixed saturation (Armstrong et al., 2016).

Zhang et al. (2016) revealed that non-linear flow regions exist in different flow regimes (i.e., fully connected flow, partially connected flow), that are highly affected by the pore size distribution, porosity, solid phase connectivity and solid phase contour length. They also determined that the magnitude of the driving forces required to overcome the observed

non-linearities was highly dependent not only on the phase saturation but also on the morphological properties of the porous medium. Whereas, the initial conditions were set as one fluid randomly distribute within the other fluid to achieve different saturation rates, which can not represent the natural process of immiscible displacements.

Li et al. (2017) performed a simulation of steady-state two-phase flow using Shan-Chen multi-component lattice-Boltzmann model (SCMC-LBM) to study the effect of geometrical properties, such as wettability, adhesive force, pore size distribution, and specific surface area on fluid distribution. The results indicated that the thin wetting phase formed around the solid phase resulted in discrete wetting phase distribution and reduced the mobility of the wetting phase, however, did not affect non-wetting phase mobility. In addition, decreasing wettability, increasing average pore radius and improving fluid connectivity can reduce the effect of the capillary pressure in heterogeneous pores structures. The geometrical properties in this study were represented by pore size distribution. However, the geometrical properties of a porous medium are a much more complicated concept that pore size distribution can not fully describe.

Mino et al. (2018) investigated the effects of the filter porosity, wettability, and fibre diameter on the coalescing behaviours using the free-energy lattice-Boltzmann method of two-dimensional permeation simulations for the water and oil system through fibrous filters. Fig.2.4 shows the permeation behaviour of water and oil through fibrous filters with different fibre diameters and the velocity contour plot of each filter, where solid fibres are in grey, water is the wetting phase in blue and oil is the non-wetting phase in yellow. The simulation results demonstrated that filters with larger pore spacings can form larger droplets to pass through without coalescing. Based on the finding, the bilayer filters were designed to ensure the effectiveness of droplet coalescence.

Xu and Liu (2018) studied the effects of saturation, viscosity ratio, and contact angle on the steady-state fluid distributions, relative permeability, and the interface length within realistic Berea sandstone using a 2-dimensional colour-gradient LBM. The main findings are the interface lengths present an unsymmetrical behaviour with respect to the increasing saturation, whilst increasing viscosity ratios shifted both the intersection point of the relative permeability curves and the maximum interface length to lower saturations. However, the study is limited to 2D due to its computational efficiency, while the real-world physical problems are in 3D. Thus, the results from this study may not be quantitatively correct.

Khanamiri and Torsæter (2018) imaged the transient dynamics and topological evolution

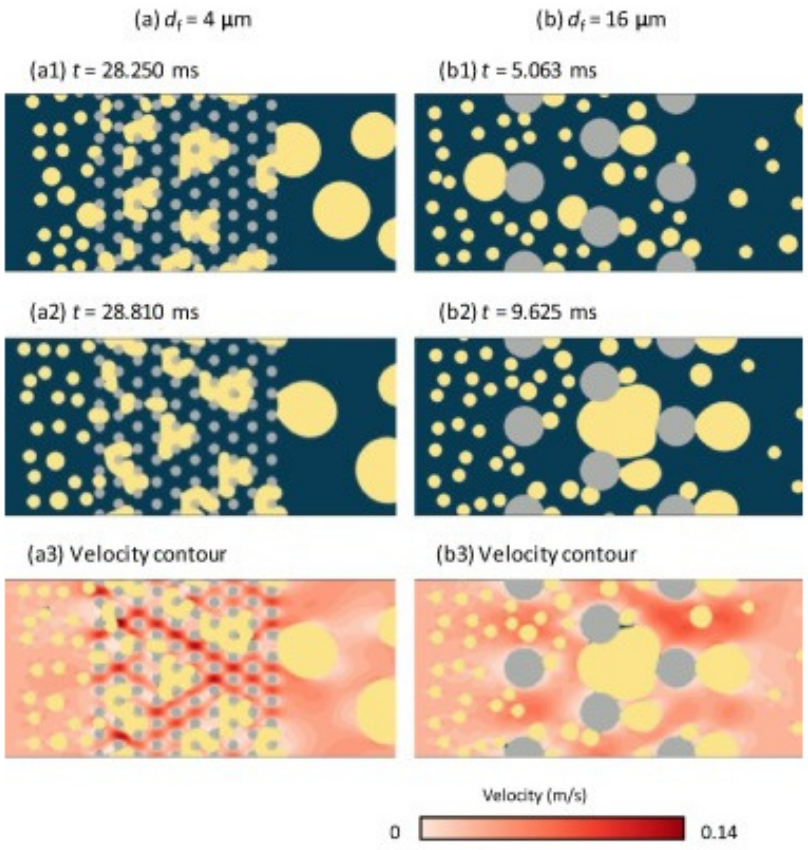

Figure 2.4: Permeation behavior of water and oil emulsions through a fibrous filter with a constant porosity, x_f=82.1%, and contact angle, $\theta = 135^o$, for different fiber diameters, d_f=(a) 4 and (b) 16 μm. Panels (a3) and (b3) display the velocity contours corresponding to panels (a2) and (b2), respectively (Mino et al., 2018).

of a two-phase flow using synchrotron X-ray computed microtomography for varying brine-oil compositions and saturation rates. From the experiential results, it was shown that a hysteresis pattern was present in the system during drainage and imbibition. Whereas, during drainage, a significant increase in the non-wetting phase (oil) Euler characteristic can be observed. In addition, it was shown that over time, mass and momentum exchange between ganglia and the non-wetting phase connected flow pathway resulted in a varying topological evolution pattern dependent on the interfacial properties of the two fluids and the brine injection rate. This study draws significant conclusions on the inter-dependency of fluid phase topology, the physical properties and injection flow rates of the system. However, it does not cover the entirety of the wetting phase saturation spectrum and is performed in a porous medium of specific morphology.

Li et al. (2019) studied the effect of the initial fluid distribution, saturation history and

magnitude of the hydraulic gradient on the steady-state interfacial area, capillary pressure and relative permeability using the MCMP-LBM. They found that the relative permeability is more sensitive to the magnitude of the hydraulic gradient compared to the initial fluid distribution or saturation history, because of the threshold hydraulic gradient. They also investigated the differences in interfacial area, capillary pressure and saturation surface at dynamic equilibrium in steady-state infiltration and at quasi-static equilibrium. The study also showed the importance of fluid distribution as a result of the flow pattern in describing the capillary pressure curve, and the relationship between interfacial area–capillary pressure and saturation rate.

Ju et al. (2020) studied the impact of the porous medium geometry on the transient imbibition patterns of a water-oil system using a multi-component colour-gradient LBM. Four porous structure models were modelled with different pore size distributions and pore shapes. The water infiltration for the four porous mediums at different instantaneous times can be seen in Fig.2.5. The porosities and topological skeletons of the porous structures remained invariant. The study showed that preferential water-oil pathways are formed based on the pore size distribution and pore geometry during imbibition. However, those preferential pathways remain unchanged due to the constant topological skeletons of the porous medium under consideration. Thus, the effect of the topological skeletons during the imbibition process remains unknown.

Aziz et al. (2020) used CFD simulations to evaluate the impact of the pore morphology, using two mediums of similar topology but different pore size distributions, on the two-phase flow dynamics under different wettability conditions (high and low salinity waterflooding) to study how wettability change impacts oil recovery. This study provided strong evidence that the effect of pore size distribution, as well as the intrinsic heterogeneity of the pore space in enhancing oil recovery. The impact of the pore space morphology was found to dominate the changes in the wettability and was identified as the primary performance indicator for oil ganglia remobilisation in the tertiary mode. However, similar to the previous study (Rücker et al., 2015), the effect of pore space connectivity and topology was not quantified and remained invariant in the investigation.

Paustian et al. (2021) performed a study on the behaviour of both two-phase flow (water-oil and water-air) and three-phase flow (air-water-oil) in a porous medium, Fig.2.6 shows the simulation results of the interfacial surfaces of the three-phase system (air-water-oil). The air-water interfacial area is very small because of the presence of oil layers between

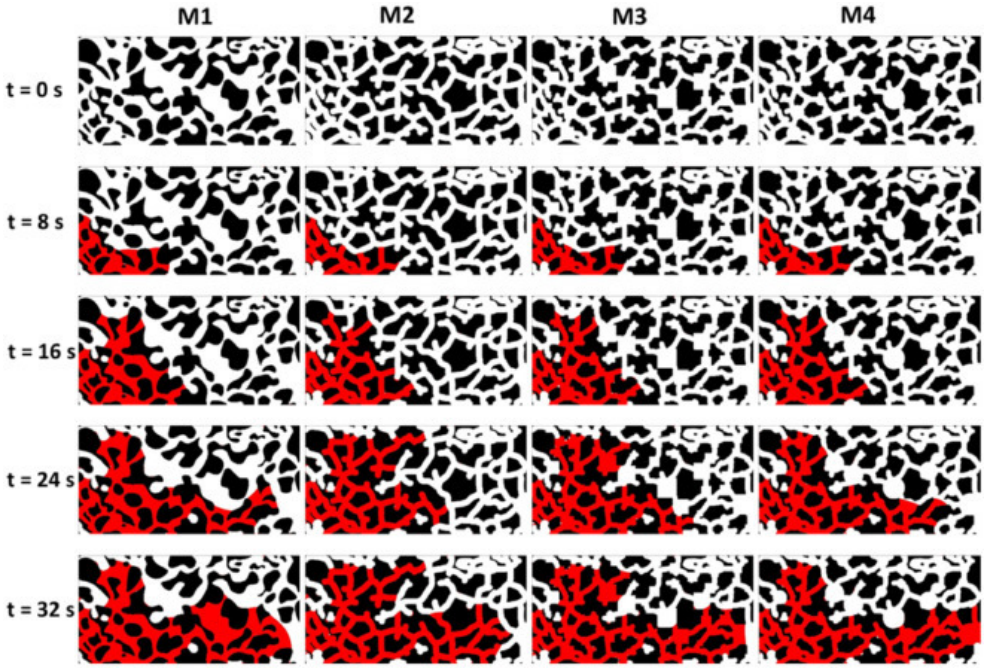

Figure 2.5: The water infiltration for the four porous mediums at different instantaneous times (Ju et al., 2020).

the air and water. The simulation results indicated a non-hysteretic relationship of capillary pressure, saturation and fluid-fluid interfacial area for both the oil-water and air-oil system while determining the three-phase system relationship was well described by the thermodynamics-based theory proposed by Majid Hassanizadeh and Gray (1993).

Nemer et al. (2021) investigated the impact of the wettability alteration, i.e. a gradual transition from oil-wet to water-wet fractional flow, and the domain geometry on the pore scale displacement of the phases. Two different types of porous medium were considered namely sphere-pack and rock slice domains. The improvements of the oil phase fractional flow were observed as the wettability state changed into a water-wet condition and were affected by structure geometry, capillary number, and phase saturation. Although this study indicated a strong dependency of the oil phase fractional flow with the saturation, wettability conditions, domain geometry, and the frequency of local pore-scale events, such as coalescence and snap-off, it did not systematically explore the relationship between the pore space topology and the fluid phase dynamics at either unsteady or steady-state conditions. This is because the effect of pore topology in the study was primarily considered in a qualitative rather than a quantified parametric form.

From a similar study, Bakhshian et al. (2020) investigated the coupled effects of wettability and pore geometry in the homogeneous and heterogeneous porous mediums and also showed

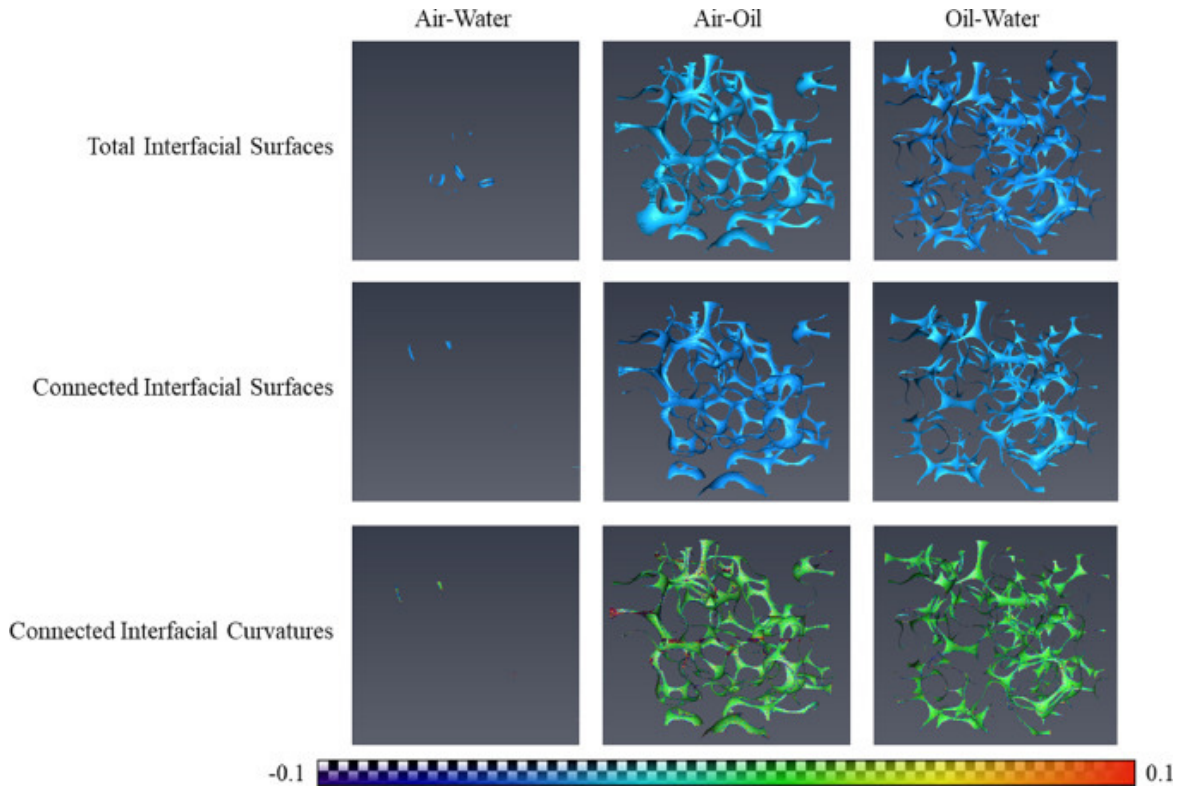

Figure 2.6: Interfacial surfaces and curvatures (magnitude indicated by colour bar) for the three-phase system (air-water-oil) Paustian et al. (2021).

that pore space homogeneity and heterogeneity is one of the major factors controlling immiscible two-phase flows, with burst flow being the dominant pore-scale displacement mechanism under drainage conditions. However, no systematic investigation was performed to further analyse the effect of pore structure morphology.

Wei et al. (2022) employed a Voronoi diagram approach to generate artificial porous mediums with varying morphology and study the effect of pore space heterogeneity on the enhanced oil recovery (drainage) process at low permeability. Moreover, capillary number and wettability effects on the fluid phase distribution and resulting dynamics were also investigated. One of the major findings of the study is that increased porous medium heterogeneity, as expressed through the pore connectivity rate, will reduce oil (non-wetting phase) recovery due to intense gas channelling. The larger probability of continuous wide pores, in this case, was identified to be the main cause of the observation, further evidencing the dependency of the two-phase drainage process on the porous domain topology.

To sum up, all these previously mentioned studies have revealed remarkable results for immiscible two-phase flows in the porous medium shown in Tab.2.1.

Table 2.1: Main researches and research focuses

Researches	**Research focuses**
Koponen et al. (1997); Vogel and Roth (2001); Lehmann et al. (2008); Scholz et al. (2012b); Yang et al. (2017)	Correlation between morphology and permeability for single phase flow
Avraam and Payatakes (1995); Li et al. (2005); Ghassemi and Pak (2011); Zhao et al. (2017); Li et al. (2017); Xu and Liu (2018)	Correlation between fluid properties and relative permeability
Dou and Zhou (2013);Zhang et al. (2016); Li et al. (2017); Mino et al. (2018); Ju et al. (2020); Aziz et al. (2020)	Correlation between morphology and relative permeability
Dou and Zhou (2013); Santiago et al. (2016) Paustian et al. (2021); Nemer et al. (2021) Wei et al. (2022)	Correlation between morphology and phase connectivity
Armstrong et al. (2018);Khanamiri and Torsæter (2018); Li et al. (2019)	Correlation between phase connectivity and relative permeability

2.3 Critical gaps and research questions

All these previously mentioned studies have revealed remarkable results for immiscible two-phase flows in the porous medium. However, most of these past studies focused on fluid properties such as the relationship between relative permeability, viscosity ratio, wettability, etc. Critical gaps in this research area can be seen as follow:

- There are no systematic investigations on the impact of the pore space morphology.
- The impact of pore space connectivity of immiscible two-phase flows remains largely unexplored.
- The relationship between pore space morphology and phase connectivity has not received the same level of attention compared to fluid properties.

Research questions of this thesis can be raised from the critical gaps. To systematically study the impact of the morphological properties of the porous medium on immiscible two-phase flows during the drainage and imbibition process under three different conditions using a two-dimensional MCMP LBM. The pore structures with different geometrical properties are artificially generated in 2D, and the dependence of various fluid properties at different saturation rates on the morphological properties of the porous medium is analysed. The study of an oil-water like system is separated into three parts, under transient state, under steady-state, and low driving forces. The impact of pore space connectivity, as expressed through the Euler characteristic on the chemically inert, thermodynamically stable, immiscible two-phase flow through the connected pore structure is studied under these conditions. This thesis focuses on analysing the relative permeability, interface length, Euler characteristic of the wetting and non-wetting phases, and the capillary pressure for imbibition and drainage at different saturation rates. The impact of the variable Euler characteristic on the average pore coordination number, pore size and pore throat distribution are also taken into account for a more complete geometrical and topological picture of the observed porous medium.

Chapter 3

Methodology

This chapter gives a brief distribution of the numerical methods of this project, the pseudo-potential Shan and Chen method, which is a multi-component multiphase (MCMP) LBM model. Followed by the validation of this current model.

3.1 The lattice-Boltzmann modelling (LBM)

The lattice-Boltzmann modelling (LBM) technique was introduced by McNamara and Zanetti in 1988 (Mohamad, 2011). It is a pseudo-molecular method that tracks the evolution of the particle distribution function, which is built upon microscopic models and mesoscopic kinetic equations. In the past 20 years, the LBM has become an attractive alternative for the numerical simulation of flows in porous medium with complex geometries (Kalaydjian, 1990; Qian et al., 1992; Avraam and Payatakes, 1995), due to its ability to solve equations in an arbitrary pore space geometry and topology rather than in simplified models of them (Joekar-Niasar et al., 2010). Compared to traditional CFD methods, by using Navier–Stokes equations to solve macroscopic variables such as velocity, pressure, and density (Luo, 1998; Inamuro et al., 2004), the fluids are replaced by fractious particles in LBM. The macroscopic variables are solved by these particles streaming along given directions and colliding at the lattice sites (Yadigaroglu and Hewitt, 2017). LBM is easy to apply for complex domains and treat multiphase and multicomponent flows without tracking/capturing/reconstructing the interfaces in between (Chen and Doolen, 1998). Due to these advantages in studying fluid flow applications involving interphase dynamics and complex boundaries condition. It was possible to perform detailed simulations of multi-

phase flow in artificially generated geometries (Narváez et al., 2010; Narváez and Harting, 2010). The streaming and collide express are shown as follows:

$$f_i(\mathbf{x}+\mathbf{e}_i\Delta t, t+\Delta t) = f_i(\mathbf{x},t) - \frac{\Delta t}{\tau}\left(f_i(\mathbf{x},t) - f_i^{eq}(\mathbf{x},t)\right), \quad i = 0,1,2,...,8, \tag{3.1}$$

where $f_i(\mathbf{x}+\mathbf{e}_i\Delta t, t+\Delta t) = f_i(\mathbf{x},t)$ is the streaming process and $\frac{\Delta t}{\tau}\left(f_i(\mathbf{x},t) - f_i^{eq}(\mathbf{x},t)\right)$ is the collision part, $f_i(\mathbf{x},t)$ is the density distribution function in the i^{th} direction, $\mathbf{e}_i$ is the directional vector in the i^{th} direction, τ is the relaxation time and Δt is the size of the time step.

The fluid particles collision is considered as a relaxation towards a local equilibrium and for the D2Q9 case, equilibrium distribution function f_i^{eq} can be expressed as:

$$f_i^{eq}(\mathbf{x},t) = \rho w_i \left[1 + \frac{\mathbf{e}_i\cdot\mathbf{u}}{c_s^2} + \frac{(\mathbf{e}_i\cdot\mathbf{u})^2}{2c_s^4} - \frac{\mathbf{u}\cdot\mathbf{u}}{2c_s^2}\right], \tag{3.2}$$

where ρ is the density, $c_s = c/\sqrt{3}$ is the lattice sound speed, and $c = \Delta x/\Delta t$ is the ratio of the lattice spacing Δx and time step Δt.

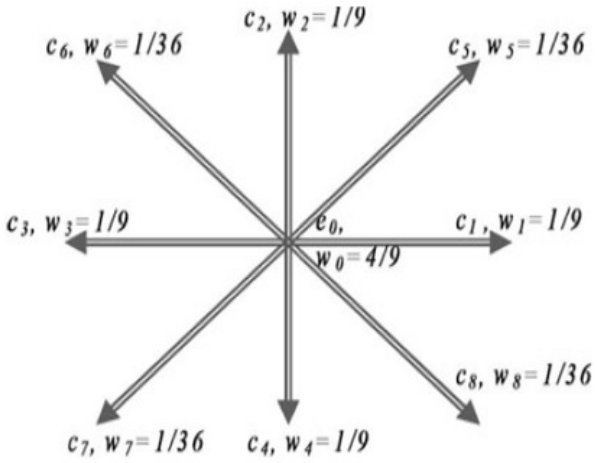

Figure 3.1: The directional vectors and the weighting factors of the D2Q9 model.

For this project, we used a D2Q9 model, which is convenient for the hydrodynamic and thermal analysis of fluid flows. D2Q9 model includes 2 dimensional and contains 9 velocities shown in Fig.3.1. The directional vectors, which are commonly referred to as the 'particle velocities' in LBM, and the weighting factors w_i are given by:

$$[\mathbf{e}_0,\mathbf{e}_1,\mathbf{e}_2,\mathbf{e}_3,\mathbf{e}_4,\mathbf{e}_5,\mathbf{e}_6,\mathbf{e}_7,\mathbf{e}_8] = \begin{bmatrix} 0 & 1 & 0 & -1 & 0 & 1 & -1 & -1 & 1 \\ 0 & 0 & 1 & 0 & -1 & 1 & 1 & -1 & -1 \end{bmatrix}. \tag{3.3}$$

$$w_i = \begin{cases} 4/9, & i = 0; \\ 1/9, & i = 1, 2, 3, 4; \\ 1/36, & i = 5, 6, 7, 8. \end{cases} \tag{3.4}$$

Because particle mass is uniform, these microscopic velocities and momenta are always effectively equivalent. The lattice unit (lu) is the fundamental measure of length in the LBM models and time steps (ts) are the time unit. For mass and momentum conservations, the macroscopic fluid density is represented by the summation of distribution functions at each lattice site:

$$\rho = \sum_{i=0}^{9} f_i. \tag{3.5}$$

The momentum is calculated as an average of the lattice (microscopic) velocities e_i weighted by the distribution function f_i:

$$\mathbf{u} = \frac{1}{\rho} \sum_{i=0}^{9} f_i \mathbf{e_i}. \tag{3.6}$$

3.2 Shan-Chen Method

For multiphase or multicomponent flow, several LBM model was developed in the past twenty years. For instants, Rothman–Keller (RK) LBM was proposed by Gunstensen et al. (1991) based on the lattice gas model, which used colour gradients to separate and simulate the interaction at the interfaces. Shan-Chen (SC) method was developed in 1993, which is a pseudo-potential model (Shan and Chen, 1993, 1994). And the free energy model proposed by Swift et al. (1996) describes an approach that in equilibrium the steady-state can be related to free energy. For this project, the SC-LBM model was chosen and applied to the present two-phase flow. The general idea of the SC model is to use an interaction force between particles to simulate microscopic interactions and separate the phase automatically. Such automatic phase separation becomes an attractive characteristic because the interface between phases is a post-processed quantity instead of a mathematical boundary that can be mortified by changing the phase densities and no explicit tracking and capturing of interface technique is needed (Chen et al., 2014). Hence, the SC model become one of the most popular LBM multiphase models because of its simplicity and versatility. For the current model, two sets of density distribution

functions are defined at each lattice node, one set for each phase, all of which satisfy the LBM equation. Constraining attention to two dimensions, the D2Q9 model is used for this study. Thus, for the i^{th} lattice node with position $\mathbf{x}(=(x,y))$, at time t, and for a single time relaxation scheme, defined as:

$$f_i^{\kappa}(\mathbf{x}+\mathbf{e}_i\Delta t, t+\Delta t) = f_i^{\kappa}(\mathbf{x},t) - \frac{\Delta t}{\tau_\kappa}\left(f_i^{\kappa}(\mathbf{x},t) - f_i^{\kappa,eq}(\mathbf{x},t)\right), \quad i=0,1,2,...,8, \tag{3.7}$$

where $f_i^{\kappa}(\mathbf{x},t)$ is the κ^{th} phase density distribution function in the i^{th} direction, and τ_κ is the relaxation time of the κ^{th} phase. Define the Maxwell-Boltzmann equilibrium distribution function $f_i^{\kappa,eq}(\mathbf{x},t)$ by

$$f_i^{\kappa,eq}(\mathbf{x},t) = \rho_\kappa w_i\left[1 + \frac{\mathbf{e}_i\cdot\mathbf{u}_\kappa^{eq}}{c_s^2} + \frac{(\mathbf{e}_i\cdot\mathbf{u}_\kappa^{eq})^2}{2c_s^4} - \frac{\mathbf{u}_\kappa^{eq}\cdot\mathbf{u}_\kappa^{eq}}{2c_s^2}\right], \tag{3.8}$$

where ρ_κ is the density of the κ^{th} phase. For each lattice node, the macroscopic average fluid velocity field of the multiphase flow, $\mathbf{u}'$, common to both phases, is defined as

$$\mathbf{u}'(\mathbf{x},t) = \frac{\sum_{\kappa=1}^{2}\left(\sum_{i=0}^{8}\frac{f_i^{\kappa}\mathbf{e}_i}{\tau_\kappa}\right)}{\sum_{\kappa=1}^{2}\frac{\rho_\kappa}{\tau_\kappa}}, \tag{3.9}$$

while the individual macroscopic velocity in each phase, at each lattice node, $\mathbf{u}_\kappa^{eq}$, has the form

$$\mathbf{u}_\kappa^{eq}(\mathbf{x},t) = \mathbf{u}' + \frac{\tau_\kappa\mathbf{F}_\kappa}{\rho_\kappa}. \tag{3.10}$$

The total force (per unit area) acting on each phase, at each lattice node, $\mathbf{F}_\kappa$, used in this work is given by

$$\mathbf{F}_\kappa(\mathbf{x},t) = \mathbf{F}_{c,\kappa} + \mathbf{F}_{ads,\kappa} + \mathbf{G}, \tag{3.11}$$

where $\mathbf{F}_{c,\kappa}$ is the fluid-fluid cohesion force (per unit area), $\mathbf{F}_{ads,\kappa}$ is the fluid-solid adhesion force (per unit area) and $\mathbf{G}$ is the body force (per unit area). The last term is used to drive the flow through the porous medium. The discretised forms of the fluid-fluid cohesion and fluid-solid adhesion forces are given respectively by

$$\mathbf{F}_{c,\kappa}(\mathbf{x},t) = -G_c\psi(\rho_\kappa(\mathbf{x},t))\sum_{i=1}^{8}\omega_i\psi(\rho_{\overline{\kappa}}(\mathbf{x}+\mathbf{e}_i\Delta t,t))\,\mathbf{e}_i, \tag{3.12}$$

and

$$\mathbf{F}_{ads,\kappa}(\mathbf{x},t) = -G_{ads,\kappa}\psi(\rho_\kappa(\mathbf{x},t))\sum_{i=1}^{8}\omega_i s(\mathbf{x}+\mathbf{e}_i\Delta t,t)\,\mathbf{e}_i, \tag{3.13}$$

where the parameter G_c is the strength of the cohesion force, while $G_{ads,\kappa}$ represents the interaction strength between the solid (pore) wall and each fluid. $G_{ads,\kappa}$ is negative for the wetting phase and positive for the non-wetting phase (Shan and Chen, 1993). The subscripts κ and $\overline{\kappa}$ denote the two respective fluid phases, while $\psi(\rho_\kappa(\mathbf{x},t))$ is the effective mass of the κth phase. The indicator functions $s(\mathbf{x}+\mathbf{e}_i\Delta t,t)$ in equation (3.13) is used to calculate whether a lattice node is in the solid or fluid domain. For a lattice node in the solid domain, the indicator function is set to 1 while for the fluid domain, it is set equal to 0.

For each phase, the macroscopic fluid pressure p_κ is related to the fluid effective mass $\psi(\rho_\kappa)$ by the LBM system equation of state

$$p_\kappa = c_s^2\rho_\kappa + \frac{c_0}{2}g[\psi(\rho_\kappa)]^2, \tag{3.14}$$

which on re-arranging gives

$$\psi(\rho_\kappa) = \sqrt{\frac{2(p_\kappa - c_s^2\rho_\kappa)}{c_0 g}}, \tag{3.15}$$

where the parameter $g = 9/2$ and for the D2Q9 model, $c_0 = 6.0$. By now choosing an appropriate thermodynamic equation of state for p_κ, the effective mass in each phase can be defined. Here we use the Carnahan-Starling equation, which provided critical temperature and pressure values are not approached, provides a good model for both oil and water. For each phase, this equation of state has the form(Yuan and Schaefer, 2006)

$$p_\kappa = \rho_\kappa RT\frac{1+b\rho_\kappa/4+(b\rho_\kappa/4)^2-(b\rho_\kappa/4)^3}{(1-b\rho_\kappa/4)^3} - a\rho_\kappa^2, \tag{3.16}$$

where $a = 0.4963R^2T_c^2/p_c$ is the attraction parameter, $b = 0.18727RT_c/p_c$ is the volumetric parameter and T_c and p_c are the respective critical temperature and critical pressure values (Zhang et al., 2016). Here we set $a = 0.5$, $b = 4$ and $R = 1$ (Gong and Cheng, 2012).

3.3 Multi-relaxation time Lattice-Boltzmann model

For the multi-relaxation time (MRT) LBM the phase density distribution function f_i^κ for the κ-th phase in the i-th direction has the form

$$f_i^\kappa(\mathbf{x}+\mathbf{e}_i\Delta t, t+\Delta t) = f_i^\kappa(\mathbf{x},t) - \mathbf{\Omega}[f_i^\kappa(\mathbf{x},t) - f_i^{\kappa,eq}(\mathbf{x},t)], \qquad i = 0,1,2,\cdots 8, \tag{3.17}$$

where the single relaxation timescale τ has been replaced by the collision matrix $\mathbf{\Omega}$ which accounts for a number of different relaxation timescales.

Defining instead the phase density distribution function in terms of the momentum space, Eq. (3.17) becomes

$$f_i^\kappa(\mathbf{x}+\mathbf{e}_i\Delta t, t+\Delta t) = f_i^\kappa(\mathbf{x},t) - \mathbf{M}^{-1}\cdot\mathbf{S}[\mathbf{m}^\kappa(\mathbf{x},t) - \mathbf{m}^{\kappa,eq}(\mathbf{x},t)], \tag{3.18}$$

where the moments m_i^κ and $m_i^{\kappa,eq}$ of the phase density distribution function f_i^κ and the equilibrium distribution $f_i^{\kappa,eq}$ are related through the matrix equations

$$\mathbf{m}^\kappa = \mathbf{M}\mathbf{f}^\kappa, \quad \mathbf{m}^{\kappa,eq} = \mathbf{M}\mathbf{f}^{\kappa,eq}. \tag{3.19}$$

The orthogonal transformation matrix, $\mathbf{M}$, for the D2Q9 model is

$$\mathbf{M} = \begin{bmatrix} 1 & 1 & 1 & 1 & 1 & 1 & 1 & 1 & 1 \\ -4 & -1 & -1 & -1 & -1 & 2 & 2 & 2 & 2 \\ 4 & -2 & -2 & -2 & -2 & 1 & 1 & 1 & 1 \\ 0 & 1 & 0 & -1 & 0 & 1 & -1 & -1 & 1 \\ 0 & -2 & 0 & 2 & 0 & 1 & -1 & -1 & 1 \\ 0 & 0 & 1 & 0 & -1 & 1 & 1 & -1 & -1 \\ 0 & 0 & -2 & 0 & 2 & 1 & 1 & -1 & -1 \\ 0 & 1 & -1 & 1 & -1 & 0 & 0 & 0 & 0 \\ 0 & 0 & 0 & 0 & 0 & 1 & -1 & 1 & -1 \end{bmatrix}. \tag{3.20}$$

while the inverse of $\mathbf{M}$ is given by

$$\mathbf{M}^{-1} = \frac{1}{36}\begin{bmatrix} 4 & -4 & 4 & 0 & 0 & 0 & 0 & 0 & 0 \\ 4 & -1 & -2 & 6 & -6 & 0 & 0 & 9 & 0 \\ 4 & -1 & -2 & 0 & 0 & 6 & -6 & -9 & 0 \\ 4 & -1 & -2 & -6 & 6 & 0 & 0 & 9 & 0 \\ 4 & -1 & -2 & 0 & 0 & -6 & 6 & -9 & 0 \\ 4 & 2 & 1 & 6 & 3 & 6 & 3 & 0 & 9 \\ 4 & 2 & 1 & -6 & -3 & 6 & 3 & 0 & -9 \\ 4 & 2 & 1 & -6 & -3 & -6 & -3 & 0 & 9 \\ 4 & 2 & 1 & 6 & 3 & -6 & -3 & 0 & -9 \end{bmatrix} \tag{3.21}$$

The diagonal matrix $\mathbf{S}$ of the transformed multi-relaxation time rates is given by

$$\mathbf{S} = \mathrm{diag}(\tau_\rho^{-1}, \tau_e^{-1}, \tau_\xi^{-1}, \tau_j^{-1}, \tau_q^{-1}, \tau_j^{-1}, \tau_q^{-1}, \tau_{w,\nu}^{-1}, \tau_{nw,\nu}^{-1}). \tag{3.22}$$

The kinematic viscosity for the κ-th phase in the multi-relaxation-time LBM is given by

$$\nu_\kappa = (\tau_{\kappa,\nu} - 1/2)c_s^2\Delta t. \tag{3.23}$$

3.4 Boundary Condition

For LBM, the inward distribution functions to the integration domain need to be defined at the boundaries. For this project, three types of boundaries are used, bounceback boundaries, periodic boundaries, and pressure boundaries.

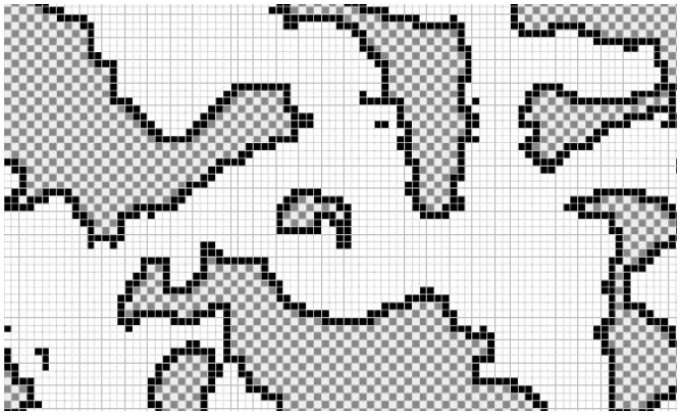

Figure 3.2: Classification of solids in a porous medium: black nodes are surface (boundary) solids; grey checker nodes are interior (isolated) solids.

Bounceback boundaries are particularly simple and important in making LBM popular among modellers interested in fluids simulation in domains filled with complex geometries, for instance, porous medium. The solid obstacles need to be designated into the particular node shown in Fig. 3.2. The solids are separated into boundary solids at the solid-fluid interface and isolated solids which have no contact with the fluid. An incoming fluid particle

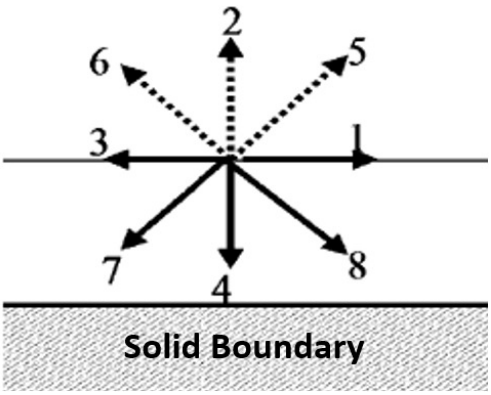

Figure 3.3: Solid boundary bounces back scheme.

moves towards the solid boundary, it bounces back into the flow domain shown in Fig.3.3. f_4, f_7, and f_8 are known from streaming process. It is assumed that, when these known distribution functions hit the wall, they bounce back to the solution domain. Therefore,

$f_5 = f_7$, $f_6 = f_8$, $f_2 = f_4$.

The periodic boundary condition is used for the open end of the structures. For this study, is the top and bottom sides of the porous medium. The distributions functions, f_4, f_7, and f_8 are unknown on the bottom and f_2, f_5, and f_6 are unknown on the top. The periodic boundary is as follows, $f_{2,bottom} = f_{2,top}$, $f_{5,bottom} = f_{5,top}$, $f_{6,bottom} = f_{6,top}$; and $f_{4,top} = f_{4,bottom}$, $f_{7,top} = f_{7,bottom}$, and $f_{8,top} = f_{8,bottom}$.

The pressure boundaries are applied on the inflow and outflow boundaries, which in this case are the left and right boundaries of the model. The two-phase flow in this study is driven by body force, and the inlet and outlet of the boundaries are set as constant pressure. A density ρ_0 is specified from which velocity is computed. The unknown distribution functions at each lattice node can be solved by maintaining the specified density at these lattice nodes.

3.5 Validation

For this study, three validations are performed. 1. Two immiscible viscous fluids of Poiseuillie flow between two parallel plates to calculate the relative permeability and compare with the analytical solution to test the accuracy of the current model in the prediction of fluid properties under steady-state. 2. A droplet breakup pattern for a selected Weber number to show the model can qualitatively capture the topological change during the drainage/imbibition process. 3. Droplet impacting on a flat surface to calculate the maximum spread factor to validate the ability of the model in capturing the transient development of immiscible two-phase flows.

A variant of Poiseuillie flow where the transport of two immiscible viscous fluids between two parallel plates is performed. In order to mimic the flow through a porous medium where the wetting phase is expected to be both attached and moving adjacent to the solid pore surface in a film layer, the set-up shown in Fig. 3.4, where the non-wetting phase is sandwiched between two wetting phase layers adjacent and in contact with the solid walls. The solid walls correspond to the top and bottom boundaries of the computational domain where non-slip boundary conditions are applied, and periodic boundary conditions

are applied to the inlet and outlet.

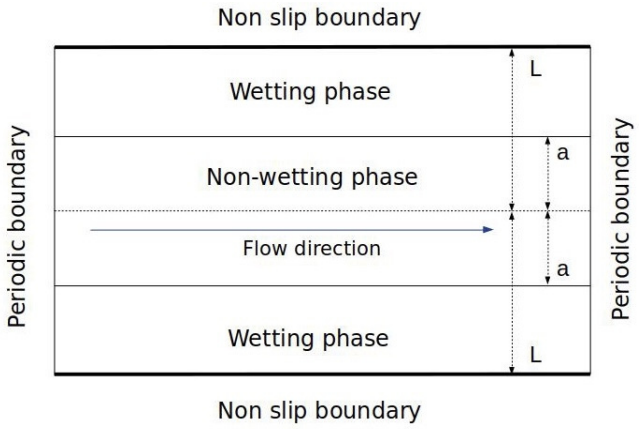

Figure 3.4: Schematic of the two-phase flow between two parallel plates employed to validate the MCMP LBM model.

For a pressure gradient of constant magnitude G applied across the computational domain in the horizontal direction, the analytical solution of the Navier-Stokes equation for this flow type yields the velocity field $(u_x, 0)$ can be calculated as

$$u_x = \begin{cases} \dfrac{G}{2\nu_w\rho_w}(L^2 - x^2), & a < |x| < L; \\ \\ \dfrac{G}{2\nu_w\rho_w}(L^2 - a^2) + \dfrac{G}{2\nu_{nw}\rho_{nw}}(a^2 - x^2), & 0 < |x| < a; \end{cases} \tag{3.24}$$

where $\nu_w, \nu_{nw}, \rho_w, \rho_{nw}$ are the respective kinematic viscosities and densities of the wetting and non-wetting phases, L is the distance between the centreline and each solid wall, while a is the distance between the centreline and each of the interfaces between the wetting and non-wetting phases. At a fixed saturation, the relative permeability in each phase is defined as the flow rate of phase i divided by the flow rate of phase i if it filled the whole channel of width $2L$. It can be shown that this reduces to evaluating (Yiotis et al., 2007)

$$k_{r,w} = \frac{\int_a^L u\,dx}{\int_0^L u_w\,dx}, \qquad k_{r,nw} = \frac{\int_0^a u\,dx}{\int_0^L u_{nw}\,dx}, \tag{3.25}$$

where $u \equiv u_x$ is defined by (3.24) while $u_i = G(L^2 - x^2)/(2\nu_i\rho_i)$ where i corresponds to the wetting and non-wetting phases, respectively. (3.25) corresponds to the superficial speed of the fluid particles across their respective cross-sections. Evaluating the integrals in (3.25) yields

$$k_{r,w} = \frac{1}{2}S_w^2(3 - S_w), \qquad k_{r,nw} = S_{nw}[\frac{3}{2}M + S_{nw}^2(1 - \frac{3}{2}M)], \tag{3.26}$$

where $S_w = 1 - a/L$, $S_{nw} = 1 - S_w = a/L$ and M is the dynamic viscosity ratio of the non-wetting to wetting phases, that is, μ_{nw}/μ_w $(=\rho_{nw}\nu_{nw}/(\rho_w\nu_w)$ (Yiotis et al., 2007). As observed by (Yiotis et al., 2007), the relative permeability of the wetting phase is only affected by the wetting phase saturation S_w, while for the non-wetting phase it is affected by both the non-wetting phase saturation S_{nw} and the dynamic viscosity ratio M.

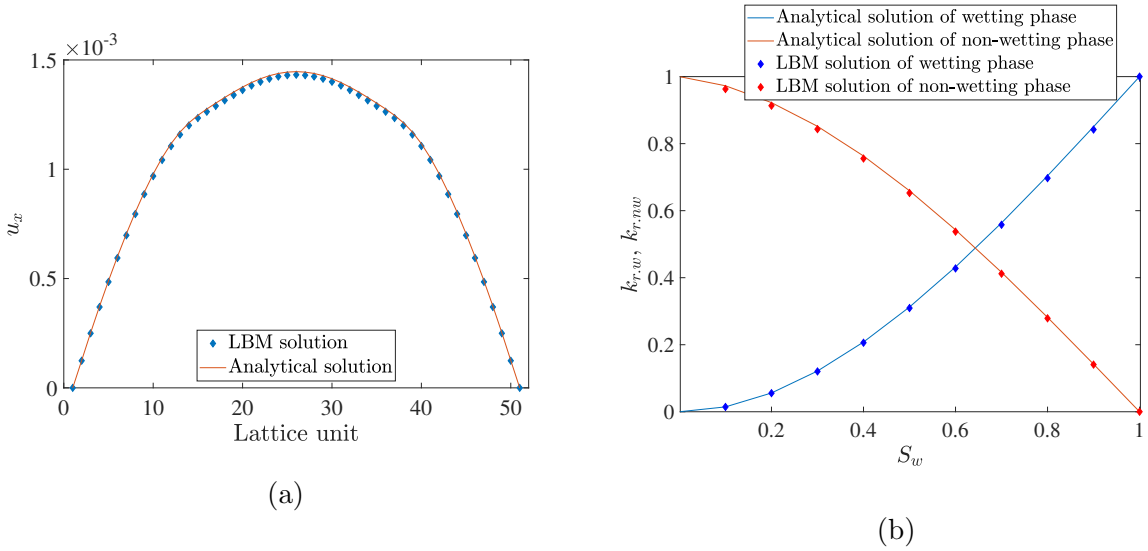

Figure 3.5: (a)Velocity profile of an oil-water two-phase system flowing between two parallel plates obtained using the MCMP-LBM model and the analytical solution for $M = 1.04$, $S_w = 0.5$ and $G = 5 \times 10^{-6}$. (b) Predicted relative permeability values obtained using the MCMP-LBM model and the analytical solution for the wetting and non-wetting phases for the flow of an oil-water system between two parallel plates for $M = 1.04$ and $G = 5 \times 10^{-6}$.

Here, the two-phase system is modelled as an oil-water system, where water is the wetting phase and oil is the non-wetting phase. Given the density ratio $\rho_{oil}/\rho_{water} = 0.8$ and the kinematic viscosity ratio $\nu_{oil}/\nu_{water} = 1.3$, the dynamic viscosity ratio, $M = 1.04$. Shows in Fig. 3.5a the predicted profile for the horizontal component of the velocity obtained using the MCMP-LBM model is compared against the analytical solution in a 100×51 lu^2 computational domain with $M = 1.04$, $S_w = 0.5$ and $G = 5 \times 10^{-6}$. Good agreement with the analytical solution can be clearly seen. A corresponding comparison of the relative permeability of the wetting and non-wetting phases with the wetting phase saturation is shown in Fig. 3.5b, where again a good agreement can be seen. Thus, both sets of results indicate that the employed MCMP-LBM can accurately predict the viscous coupling be-

tween the immiscible phases.

Figure 3.6: Droplet 'bag' breakup for $We = 38.7$. The flow direction is from left to right.

Additionally, we chose to qualitatively validate our model through the simulation of a droplet atomization pattern for a selected Weber number. Shows in Fig. 3.6, the breakup of an oil droplet in water for a Weber number of 38.7. The MCMP-LBM is able to qualitatively capture the 'bagging' breakup expected in the range of $20 < We < 50$ whereas a change in the topological state of the droplet (i.e. breakup) also occurs. It has to be noted that the observed droplet atomization pattern corresponds to the two-dimensional breakup analogue, whereas in three dimensions typically a nearly axisymmetric droplet bagging is observed before further atomization takes place.

The test case of a two-dimensional droplet of oil (non-wetting phase) in water (wetting phase) impacting on a flat surface is done. For the purposes of this test, we assume the density ratio $\rho_{oil}/\rho_{water} = 0.8$ and the kinematic viscosity ratio $\nu_{oil}/\nu_{water} = 1.3$, giving a value for the dynamic viscosity ratio, M, of 1.04. These parameter settings are also used in porous medium studies. The square computational domain of size $300 \times 300\,lu^2$ contain an oil droplet of diameter $D_0 = 100\,lu$ is placed in the middle of this domain and equilibrated over 20,000 lattice time steps. The solid surface is assumed to lie along the bottom boundary. Periodic boundary conditions are applied to the left and right boundaries while bounce-back boundary conditions are applied at the top and bottom boundaries. Initially, the oil droplet is assumed to be moving downwards with uniform speed u_0 towards the solid boundary. On impact with the solid boundary, the oil droplet will then undergo 'spreading' which is normally characterised in terms of the three non-dimensional parameters, the Weber number, We, the Reynolds number, Re, and the Ohnesorge number, Oh, which we define here respectively by

$$We = \frac{\rho_{oil} D_0 u_0^2}{\sigma}, \qquad Re = \frac{\rho_{oil} D_0 u_0}{\mu_{oil}}, \qquad Oh = \frac{\sqrt{We}}{Re}, \tag{3.27}$$

where μ_{oil} represents the dynamic viscosity of oil whilst σ denotes the interfacial surface tension between the two fluids.

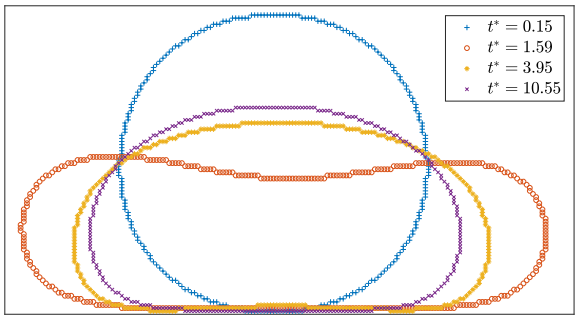

Figure 3.7: Temporal snapshots of the bounding contour line of the droplet after impact on a solid flat surface (Re=95.2, We=2.86, M=1.04).

Shows in Fig. 3.7, the shape of the oil droplet of four chosen times can be seen for Re=95.2, We=2.86, M=1.04 and an equilibrium contact angle of $\theta_{eq} = 135^o$. Here the non-dimensional time t^* is used where $t^* = tu_0/D_0$ and t is measured in lattice time step units. After impacting the solid surface, the oil droplet starts to spread as indicated by an increase in the diameter parallel to the solid surface and the oil droplet starts to assume an approximately elliptic shape ($t^* = 0.15$). As the remainder of the droplet continues to move downwards and spread outwards, the approximately elliptic shape becomes more pronounced achieving the maximum diameter parallel to the solid surface at $t^* = 1.59$, at which time it is also observed that the top of the oil droplet has involuted inwards. Interfacial surface tension now causes the sides of the oil droplet to retract and the top of the droplet to rebound as seen at $t^* = 3.95$ and the final equilibrium shape is achieved by $t^* = 10.55$.

In Fig. 3.8 the evolution of the non-dimensional spread factor D^* is shown where D^* is defined as the ratio of the spreading diameter D to the initial diameter D_0 of the oil droplet, that is, $D^* = D/D_0$. Therefore, the maximum spread factor, as determined by the LBM model is $D^*_{max} = 1.47$. To further validate our LBM implementation we compare this predicted value for D^*_{max} with corresponding values in the literature. Asai et al. (1993) offer the correlation formula $D^*_{max} = 1 + 0.48We^{0.5}\exp[-1.48We^{0.22}Re^{-0.21}]$, giving $D^*_{max} = 1.39$. The prediction equation of (Pasandideh-Fard et al., 1996), $D^*_{max} = ((We + 12)/[3(1 - \cos\theta_w) + 4We/\sqrt{Re}]^{0.5}$ (based on the energy conservation equation), yields $D^*_{max} = 1.62$, while the experimentally determined empirical formula of (Scheller

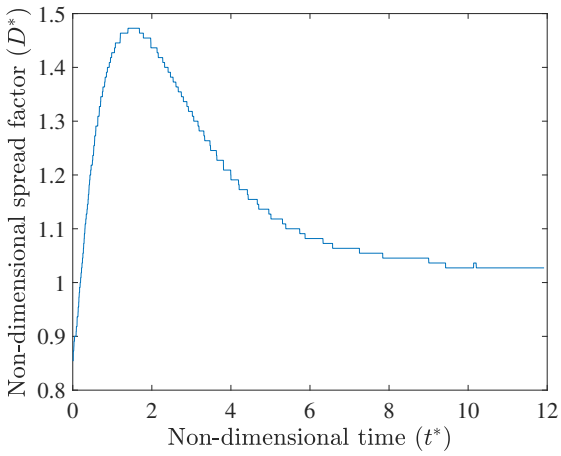

Figure 3.8: Time evolution of the non-dimensional spread factor (Re=95.2, We=2.86, M=1.04).

and Bousfield, 1995), $D^*_{max} = 0.61(Re^2Oh)^{0.166}$), predicts $D^*_{max} = 1.42$. Given the range of these predictions, the LBM simulations show good agreement.

Chapter 4

Transient state study

This chapter gives the detailed results and analysis of immiscible two-phase flow under transient state conditions of both drainage and imbibition. Starts from the porous medium generation and morphology follow by the model set-up, then moves into the results and discussions of both drainage and imbibition process, which include saturation rate, velocity fields, capillary pressure, Euler characteristic, and interface length of each phase.

4.1 Artificial porous medium

In this study, the artificially generated porous medium is considered to consist of two components, that is, a solid phase and a fluid phase, filling a square area l^2, where, l, is the linear dimension of the computational domain. In order to ensure the resultant pore distribution is not structured which would affect the theoretical definitions of quantities such as percolation thresholds, etc, a Boolean model is used to generate a random distribution of pores within the computational domain. The Boolean model consists of two simple steps. First, the 'germs', x_i, are randomly distributed within the computational domain's space using a standard randomisation function in MATLAB. Second, 'grains', Z_i, are grown on every randomly generated germ x_i. The resulting outcome of the Boolean model is the union set of all such germ-grain pairs:

$$Z = \bigcup_{i=1}^{\infty} (Z_i + x_i). \tag{4.1}$$

Uniform sized circular grains of radius 6 lattice units (lu) with a germ at their centre are used throughout the computational domain, for all the porous medium cases considered. In many cases, two or more circles overlap resulting in a more complex shaped grain which

has been created by multiple germs, the actual number corresponding to the number of overlapping circles. Examples of such grain 'clustering' can be seen in Fig. 4.1.

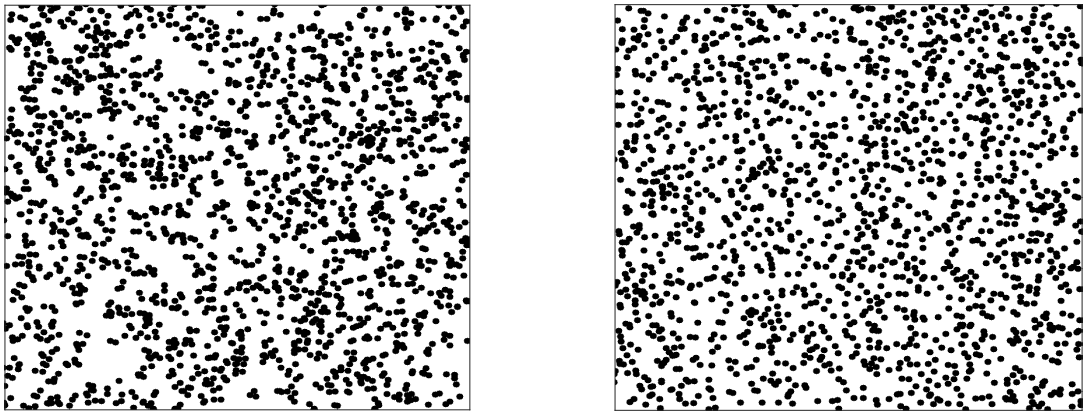

(a) (b)

Figure 4.1: Grain and pore space distributions of the artificially generated porous medium characterised by $\chi_0 = -680$ (structure 1) in (a) and $\chi_0 = -920$ (structure 7) in (b).

It should be stressed that the creation of the lattice node structure which uniformly fills the computational domain and the generation of the porous structure which is randomly distributed across the computational domain are independent processes which can be regarded as creating two separate computational layers. However, during the calculation phase, constant communication between the two layers provides the resultant predictions of fluid transport through a given pore structure.

A two-dimensional porous medium can be characterised by 3 (i.e. $d + 1$, where d is the dimensionality of the domain) Minkowski functionals, namely a representative area A, a representative contour length C, and the Euler characteristic χ (Armstrong et al., 2018). However, in this study, since the conducting (transport) phase is the pore space, then pertinent quantities need to be defined in terms of this space. The global morphology of the pore space can be determined by the corresponding Minkowski functionals per unit area, namely the porosity ϕ, the contour length to area ratio L, and the mean value of Euler characteristic, χ, given by the following equation

$$\chi = O - S, \tag{4.2}$$

where O is the number of void space components and S is the number of isolated solid clusters. The Euler characteristic per unit domain area is denoted as $\bar{\chi}$. The parameter S is determined by using an image processing function in MATLAB. To determine an appropriate computational grid size, a representative elementary volume (REV) analysis was conducted, and the domain size $800 \times 800\ lu^2$ is chosen as the REV for all results in this study (the detailed analysis shown in Appendix A). On constructing a given pore structure, it is possible that some pore space regions will be completely enclosed by the solid phase. Since the fluid can neither access nor be mobilised through such regions, then these void regions are discounted from the simulations. In order to exclude these inaccessible regions 'effective' Minkowski functionals (ϕ_0, L_0, $\bar{\chi}_0$) are employed instead to characterise the global morphology of each porous medium.

Table 4.1: The effective Minkowski functionals (ϕ_0, L_0, $\overline{\chi}_0$), the average pore coordination number of the porous medium C_p, the hydraulic tortuosity T, the average pore size $\overline{d}_P$ and the average pore throat $\overline{d}_T$, for the seven artificial structures considered in this work.

Structure	ϕ_0	L_0	$\bar{\chi}_0$ (χ_0)	C_p	T	$\overline{d}_P$	$\overline{d}_T$
1	0.756	0.0557	-0.00106 (-680)	3.289	1.211	23.58	11.71
2	0.757	0.0555	-0.00110 (-700)	3.372	1.205	23.09	11.69
3	0.756	0.0556	-0.00118 (-750)	3.376	1.215	23.08	11.41
4	0.758	0.0557	-0.00125 (-800)	3.392	1.237	22.63	11.09
5	0.759	0.0554	-0.00133 (-850)	3.390	1.192	22.18	11.12
6	0.757	0.0553	-0.00141 (-900)	3.394	1.212	22.04	10.97
7	0.758	0.0554	-0.00145 (-920)	3.365	1.208	21.47	11.15

In this study, seven artificial structures are employed in order to determine the effect of pore space connectivity on the transient flow of a water-wet, oil-water two-phase flow from initial injection to steady-state. The pertinent effective Minkowski functionals are displayed in Table 5.1. The changes in pore space connectivity are characterised through varying the effective Euler characteristic only, that is, the effective porosities and effective contour lengths are set approximately equal across the seven structures. Also, the grain size (discounting overlapping grains), and the grain density are also common to all porous

structures, $n = N/L^2$, where N is the total number of circular disks in the domain (1500), and L is the linear system dimension (Scholz et al., 2012a). The average porous medium pore coordination number (C_p), which is the average number of pore-throats per pore-body (Rabbani et al., 2014), is also calculated in order to investigate whether the variation of the Euler characteristic has an effect on the general coordination of the pore network. In addition, the geometric tortuosity (Blackwell, 1975) of each structure, the average pore size, $\bar{d_P}$, and the average pore throat, $\bar{d_T}$, are also shown in Table 5.1 for comparison.

In Table 5.1, the variations in these latter quantities can be seen to be 0.4% and 1.4%, respectively. The impact of varying the Euler characteristic on the average pore coordination number does not follow a monotonic trend but instead shows an increasing pattern for structures 1-4 and for the given porous structures peaks at $C_p = 3.394$ (structure 6). As the solid phase becomes increasingly disconnected (i.e. decreasing pore space: more negative $\bar{\chi}_0$), the number of average fluid-accessible paths around a pore tends to initially increase. However, further fragmentation of a given solid cluster into smaller ones or even individual grains, which will occur if the pore space $\bar{\chi}_0$ is reduced further, leads to a higher solid grain uniformity within the domain which will tend to lower the average number of throats connected to a pore body. In contrast to the average pore coordination number, the average pore body and pore throat sizes tend to decrease with the reduction of the pore space Euler characteristic due to the higher number of isolated solid clusters in the domain. However, small deviations from this general trend can be observed - for example, $\bar{d_T}$ of structure 5 is larger than that of structure 4 - due to the randomness of the porous medium generation process.

As χ_0 ($\overline{\chi}_0$) becomes less negative the grain distribution becomes increasingly less homogeneous with a marked increase in grain clustering and an increase in wider pore spaces. Conversely, as χ_0 ($\overline{\chi}_0$) becomes more negative both the grain distribution and the pore space become more uniform and less grain clustering is observed. In Figure 4.1, two of the employed structures are shown confirming these observations. These two structures correspond to the two extremes of the considered structures. In Figure 4.2 distributions of the pore body and pore throat size as variations in the lattice unit for the seven considered structures are shown together with the cumulative distributions. Although the general distribution pattern is similar for all structures, Figs. 4.2a - 4.2c indicate that for lower

pore space $\bar{\chi}_0$, the fraction of smaller pores and throats in the structure is generally higher. This is also partially reflected in the decreasing trend of their average values presented in Table 5.1.

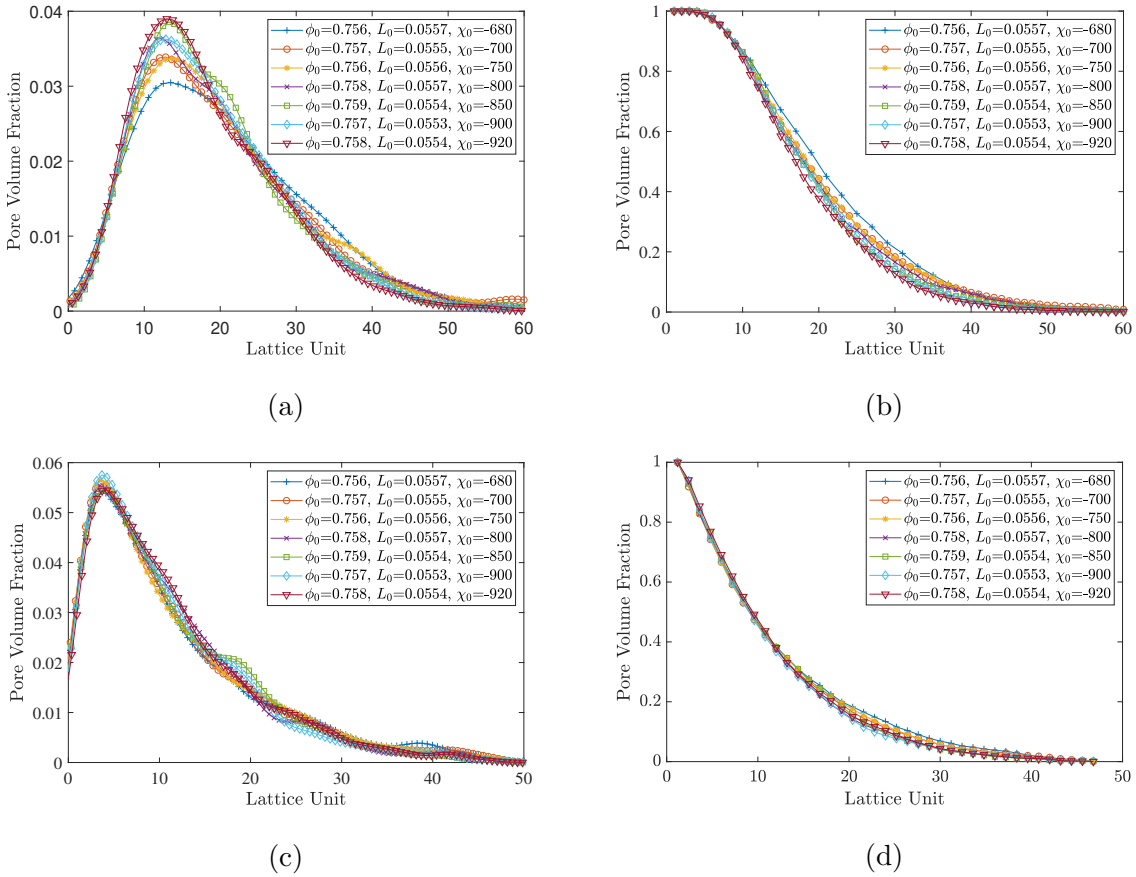

Figure 4.2: Pore size and pore throat distributions for the porous medium structures 1-7. In (a) pore size distribution, (b) cumulative distribution of pore sizes, (c) pore throat distribution and (d) cumulative distribution of pore throats.

4.2 Model set-up

Fig. 4.3 shows a general schematic of the model set-up. before all the simulations begin, for each of the structures considered, the conducting (pore) space is filled with the wetting phase fluid (water) only for drainage and the non-wetting phase fluid (oil) only for imbibition, that is, the pore structures are fully saturated fluid phase. At the macro level, the fluid is assumed to be stationary. At the time $t = 0$, injection begins with the non-wetting phase (oil) for drainage and the wetting phase (water) for imbibition moves into each of

the structures from the left-hand computational boundary whilst fluid can exit through the right-hand computational boundary. The thickness of the injecting phase (W_p), that is, the amount of fluid being injected into a given porous structure, is adjusted in order to produce the results desired steady-state ('constant') saturation value, after a finite time of evolution. The length of this time interval will depend on the required saturation level. On the left and right boundaries of the computational domain constant pressure boundary conditions are applied, as described by Zou and He (1997). The flow is driven in the horizontal direction by the application of a body force G (per unit area) at each lattice node in the conducting phase (Li et al. (2005); Zhang et al. (2016)) with magnitude $G = 5 \times 10^{-6}$. Periodic boundary conditions are applied at the top and bottom computational boundaries. Within the computational domain, no-slip boundary conditions are applied at all fluid-solid interfaces through the bounce-back boundary condition by which all particles colliding with a solid boundary are reflected back to their original position with their velocity reversed (Mohamad (2011)). In all simulations, the effects of gravity where neglected.

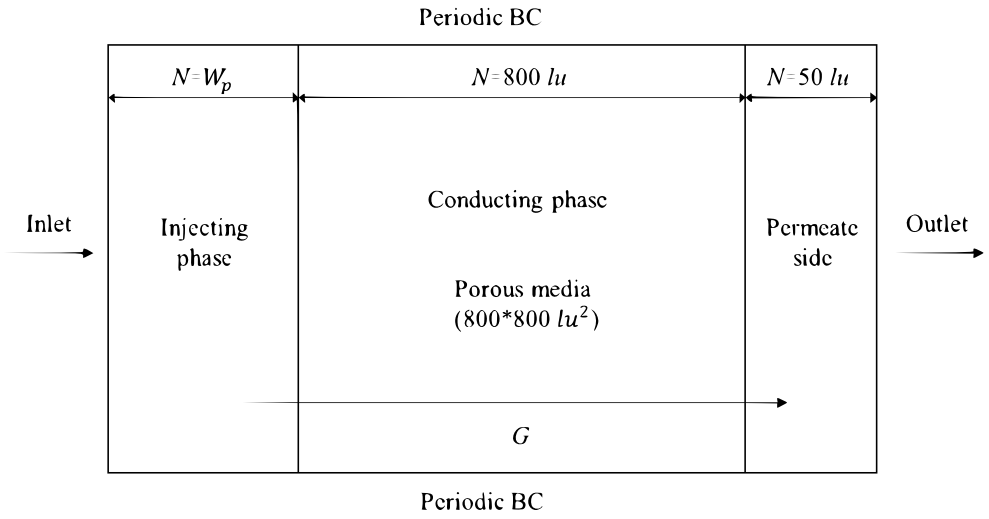

Figure 4.3: Initial and boundary conditions for the simulation of the two-phase flow.

For the water-wet, oil-water system the following set of physical parameters are used. For the respective kinematic viscosities, $\nu_w = 1.3 \times 10^{-6}\ m^2/s$, $\nu_{nw} = 1 \times 10^{-6}\ m^2/s$, while for the respective phase densities, $\rho_w = 1000\ kg/m^3$, $\rho_{nw} = 800\ kg/m^3$, giving the dynamic viscosity ratio $M = 1.04$. The equilibrium contact angle is assumed to be $\theta = 135^o$ (Al-Tamimi et al., 2021) while the interfacial fluid surface tension is set to $\sigma = 2.1\ mN/m$ for all simulations. In the MRT LBM, the fluid-solid adhesion interaction parameter and

the fluid-fluid cohesion parameter are set respectively to $G_{ads,\kappa} = \pm 0.5$ and $G_c = 0.8$. In terms of physical SI units, where the conversion equations of (Feng et al., 2007) have been employed, the uniform computational grid spacing is $\Delta x = \Delta y = 1 \times 10^{-5}\ m$ and the chosen time step is $\Delta t = 2.5 \times 10^{-6}\ s$.

The instantaneous saturation phase level is determined by the instantaneous phase densities ρ_κ at each lattice node. If $1 < \rho_\kappa < 1.2$ then the node is in the wetting phase (N_w), if $0.6 < \rho_\kappa < 0.8$ the node is the non-wetting phase (N_{nw}) and if $\rho_\kappa = 0$ the node is in the solid phase (N_s). Though the interface is expected to occupy a very small fraction of the saturation level, its inclusion ensures that the total saturation of the wetting phase and the non-wetting phase equals 1. Thus, if $0.8 < \rho_\kappa < 1.0$ the lattice node is assumed to be on the interface (N_i). The length of the fluid interface is calculated by summing N_i. For the phase macroscopic velocity, which is defined by (3.10), it is assumed a steady-state has been reached if the following condition is met

$$\frac{\sqrt{\sum_{\kappa=1}^{2}[u_\kappa^{eq}(\mathbf{x},t) - u_\kappa^{eq}(\mathbf{x},t-1000\Delta t)]^2}}{\sum_{\kappa=1}^{2} u_\kappa^{eq}(\mathbf{x},t)} < 5 \times 10^{-4}, \tag{4.3}$$

where u_κ^{eq} is the magnitude of the macroscopic phase velocity.

4.3 Drainage

This section presents results for drainage. For immiscible two-phase flow through a porous medium that the wetting phase has a stronger affinity for the solid walls and thus is more likely to be attached to the wall and flow in layers (thin films) adjacent to the wall, whilst the non-wetting phase is more likely to transport in the central parts of the pore spaces, away from the solid walls. These micro-level preferences together with the porous structure morphology clearly influence the resultant observed flow patterns and in turn, strongly influence observed macroscopic ensemble effects and measured quantities. Through the presented results, the evolution of a number of such macroscopic quantities from the initial injection of the non-wetting phase through to a given macroscopic steady-state are considered, for the seven topologically different structures defined in Table 5.1 which have different Euler characteristic. The simulations continue after the steady-state is reached

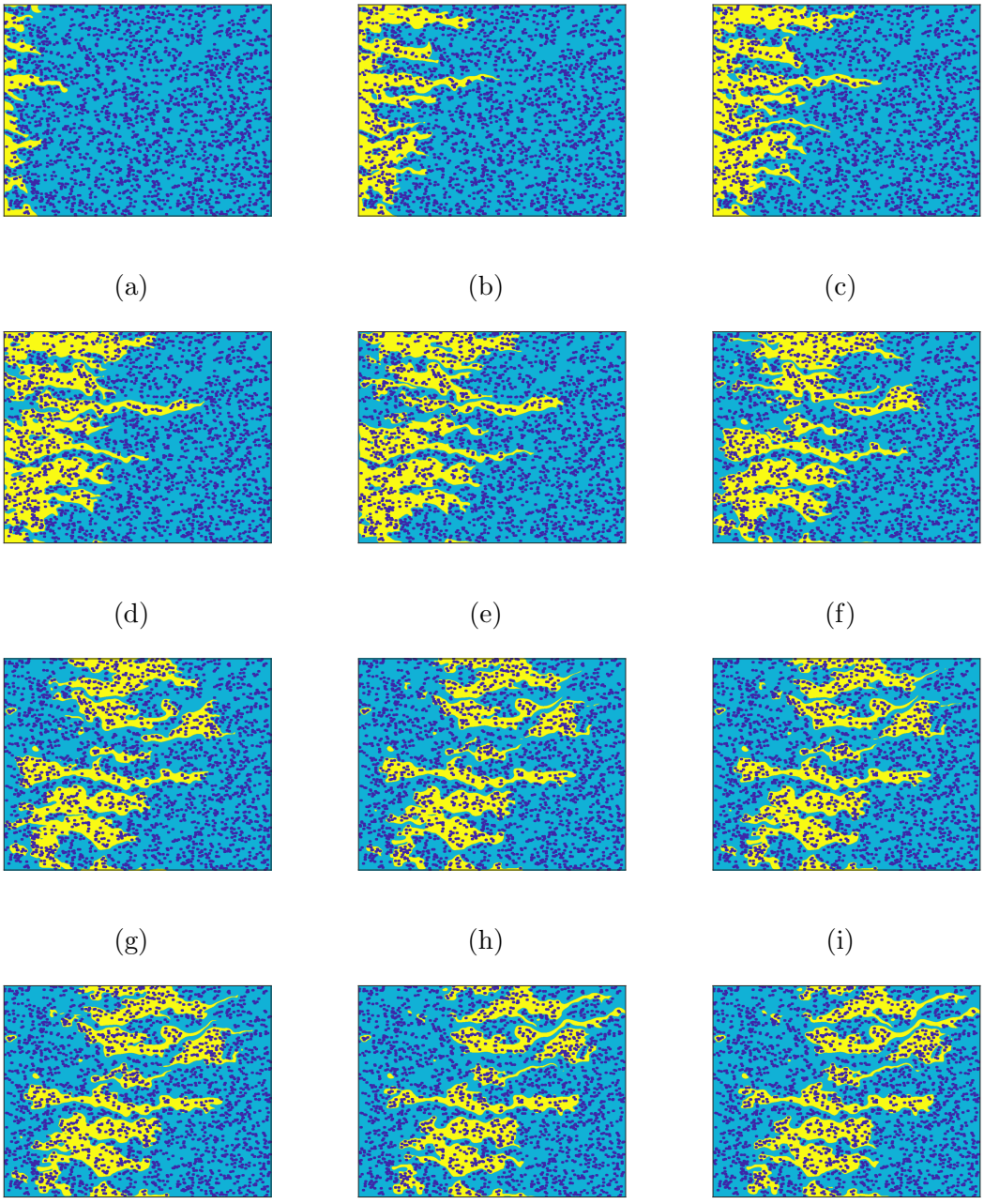

Figure 4.4: Volume fraction contour plots of the temporal evolution of the displacement of the wetting phase by the injected non-wetting phase for an Euler characteristic of $\chi_0 = -800$ and a steady-state wetting phase saturation rate of 0.7. In terms of lattice units $t = 5 \times 10^4$ in (a), $t = 1 \times 10^5$ in in (b), $t = 2 \times 10^5$ in (c), $t = 2.5 \times 10^5$ in (d), $t = 3 \times 10^5$ in (e), $t = 3.5 \times 10^5$ in (f), $t = 4 \times 10^5$ in (g), t=4.5 $\times 10^5$ in (h), $t = 5 \times 10^5$ in (i), $t = 5.5 \times 10^5$ in, (j) $t = 6 \times 10^5$ in (k), and $t = 7 \times 10^5$ in (l).

in order to understand resultant developments at the micro-level and show that the fluid continues to evolve in such a way as to maintain this macro-level steady-state.

Fig. 4.4 shows the contour plots of the volume fraction's transient evolution of the injected non-wetting phase (yellow) and the displaced wetting phase (light blue) for a pore space Euler characteristic of $\chi_0 = -800$ (structure 4) and a final steady-state wetting phase saturation of $S_w = 0.7$. (The contour plots of structure 4 and other saturation rate can be seen in Appendix B.) The porous structure is also visible in the presented contour plots as dark-coloured circles. This structure is the middle one of the considered structures while the two extremes are shown in Fig. 4.1. The progression of the non-wetting phase and consequential motion of the wetting phase is clearly tracked with many expected features seen, including fingers of the non-wetting phase protruding into the wetting phase and at later times a number of fragmentation/snap-off events. The wetting phase stays almost fully connected with occasional blobs being formed due to instantaneous bridging of the non-wetting phase around closely spaced solid grains; see for example the transitions in plots 4.4f to 4.4g, 4.4i to 4.4j, 4.4k to 4.4l, etc., in Fig. 4.4. The non-wetting phase, although initially appears fully connected locally, progresses to a highly disconnected state with a highly distorted blob geometry characterised by long fingers stretching to more than a third of the domain's length.

Fig. 4.5 shows the evolution of the wetting phase saturation to the final respective desired constant values of $S_w = 0.91, 0.7, 0.49, 0.32, 0.2$, for each of the considered porous structures. Nearly all of the displayed curves decrease monotonically to the final constant value with only a minor fluctuation seen for structure 1 in the case of $S_w = 0.91$, as the respective constant value is approached. Consistent with expectation, as S_w decreases, a longer time interval is required to achieve a given constant value since more non-wetting fluid needs to be injected into the given porous domain, though there is not much observable difference between the respective $S_w = 0.32$ and $S_w = 0.2$ results. For a given plot, as the pore space Euler characteristic χ_0 becomes more negative and thus the pore structure and pore space configuration becomes more homogeneous, the time interval to reach a constant value of S_w increases marginally, meaning the rate at which S_w changes decreases marginally. This observation could be associated with the decrease in the average pore body size in the porous medium as the pore space χ_0 becomes more negative. In such cases, the injected

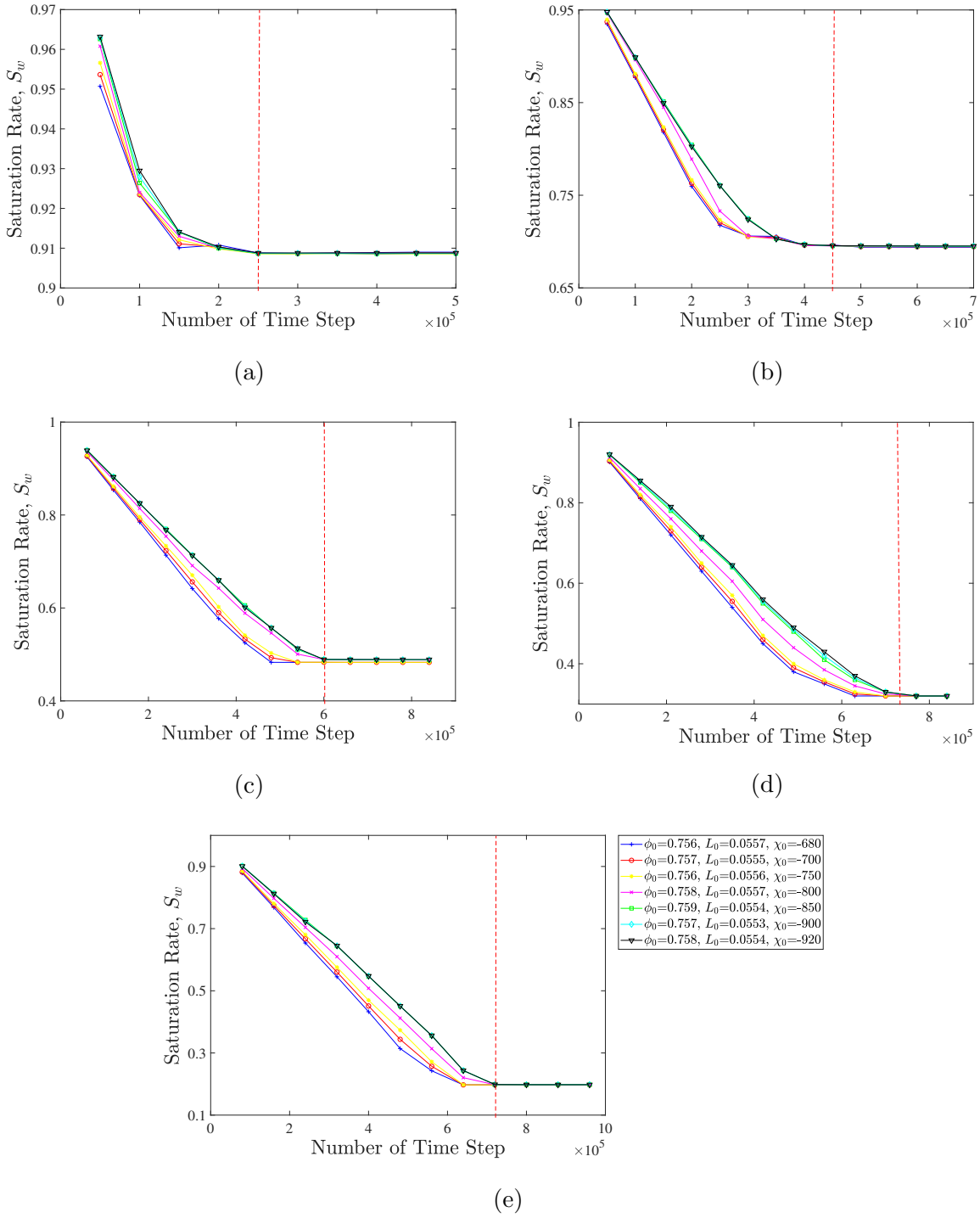

Figure 4.5: Variation of the saturation rate of the wetting phase with the number of time steps for the final constant values of in (a) $S_w = 0.91$, in (b) $S_w = 0.7$, in (c) $S_w = 0.49$, in (d) $S_w = 0.32$ and in (e) $S_w = 0.2$. The vertical red dashed line indicates the time at which steady saturation is reached.

non-wetting phase needs to penetrate smaller pores thus imposing a greater flow restriction which decreases the average transmission velocity through the porous medium and consequently increases the overall time needed to achieve a steady saturation degree.

The temporal evolution of the component of the average velocities of both phases in the x direction is shown in Fig. 4.6. The interpret two-phase fluid system steady-state at the macro-level if condition (Eq. 4.3) is met. The corresponding average velocity components in the y direction (not shown) were found to be most of the order of 10^{-5} or less. Therefore, the averaged fluid motion in each phase is dominated by their respective averaged components in the x direction (body force direction). Fig. 4.6 provides a good visual indication of when the macro-level steady-state has been achieved, that is, for times when $u_{x,\kappa}$ is constant on the scale of the plots. In comparing with Fig. 4.5, it is noted that for the middle values ($S_w = 0.7, 0.49, 0.32$) and in particular $S_w = 0.49$, though $u_{x,\kappa}$ is constant, some fluctuations in S_w is still observed before their respective constant values are reached at later times. In Fig. 4.6, for the $S_w = 0.9, 0.7$ plots, fluctuations are observed over early times as time steps increase, particularly for the wetting phase making trends harder to discern. As S_w decreases, more clear patterns can be seen. For $S_w = 0.32$ and $S_w = 0.2$, all the final constant values in $u_{x,nw}$ are larger than all the $u_{x,w}$ values, while at high $S_w = 0.91$, the steady-state $u_{x,nw}$ are smaller than $u_{x,w}$. For $S_w = 0.7, 0.49$, whether $u_{x,w} > u_{x,nw}$ for the final constant values is structure dependent. $u_{x,w}$ displays a curious dip before the respective constant values are achieved. In line with the observations of Fig. 4.5, average velocities for a less negative pore space χ_0, are higher than for a more negative pore space χ_0 (i.e. a more homogeneous pore network configuration). This is observed for both wetting and non-wetting phases although the relative magnitudes strongly depend on the corresponding saturation levels. As previously described, the negative impact of pore space homogeneity on the average pore size in the domain imposes certain flow restrictions that tend to slow down the fluid phase transmission through the porous medium. From a qualitative perspective, with a reference to the contour plots in Figs. 4.4f - 4.4h, a less negative pore space χ_0 tends to result in highly elongated non-wetting phase flow paths along the more loosely concentrated solid grain regions of the inhomogeneous domain. On the contrary, as the pore space χ_0 becomes more negative, the non-wetting phase front tends to become significantly more uniform and wider along the vertical direction indicating that the fluid does not follow preferential flow paths and spreads more evenly throughout the

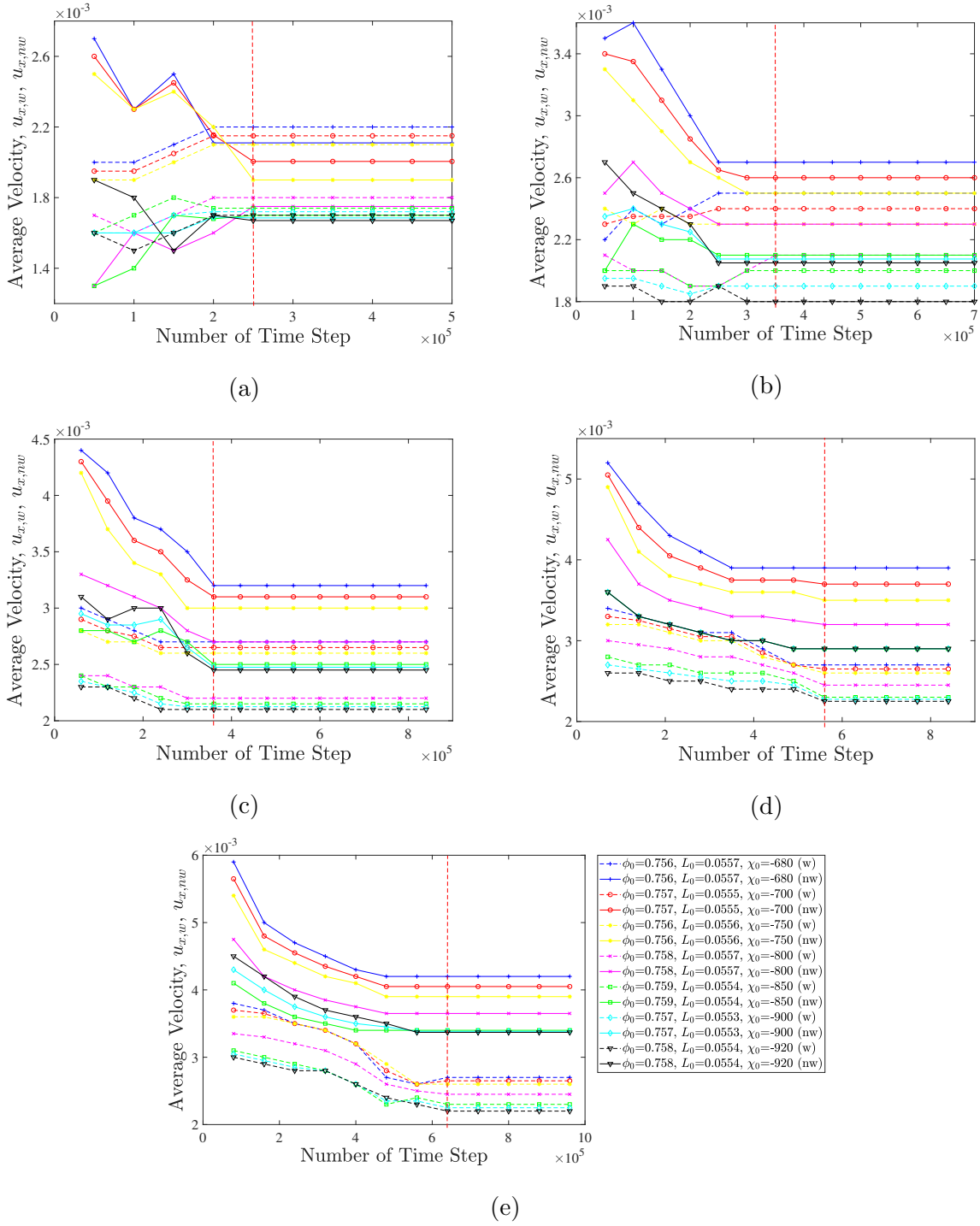

Figure 4.6: Variation in the average velocity in the x direction of the wetting (dashed lines) and non-wetting (solid lines) phases with the number of time steps for final constant values of in (a) S_w=0.91, in (b) S_w=0.7, in (c) S_w=0.49, in (d) S_w=0.32 and in (e) S_w=0.2. The vertical red dashed line indicates the time at which the macroscopic steady-state is reached.

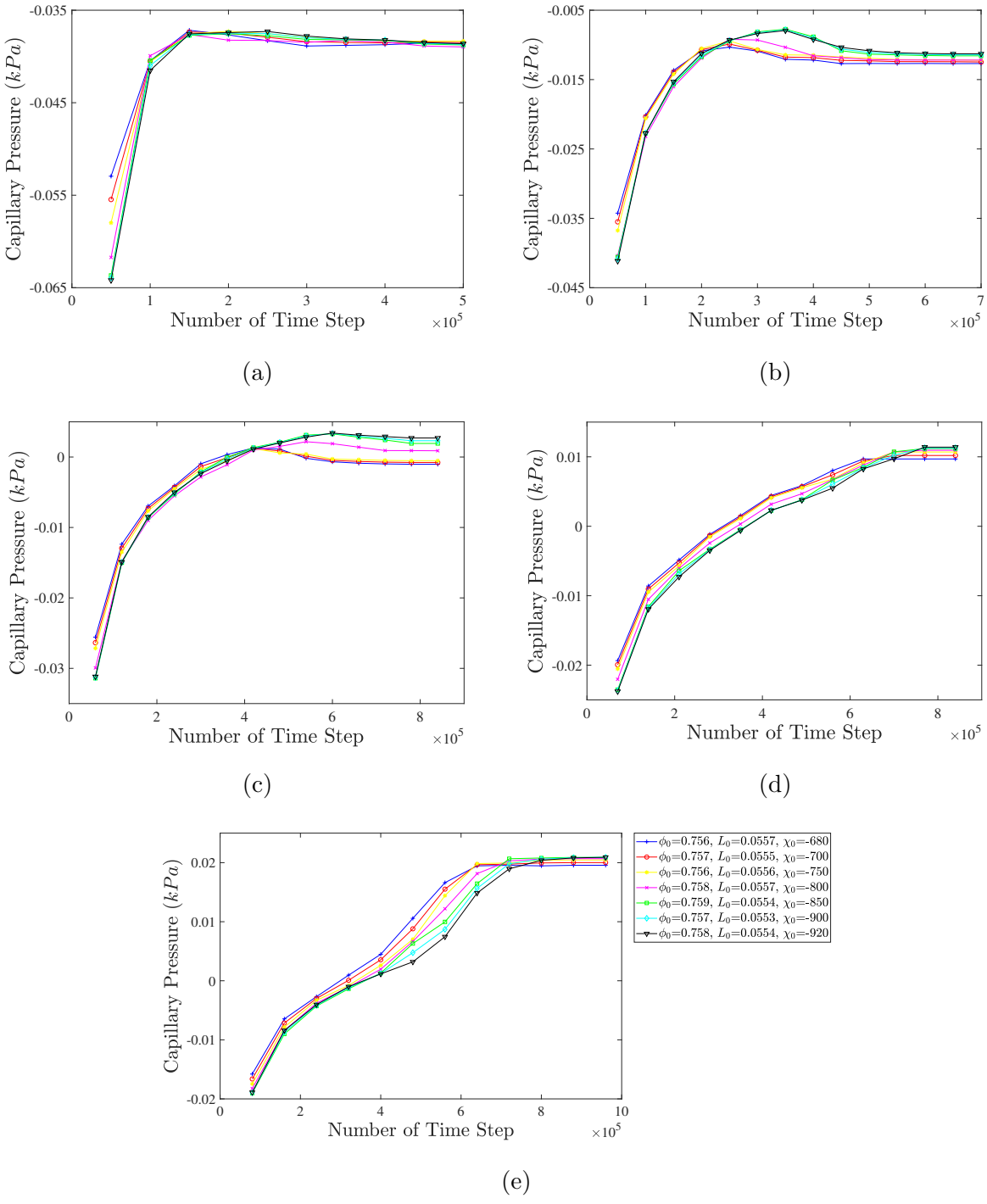

Figure 4.7: Temporal evolution of the capillary pressure for in (a) S_w=0.91, in (b) S_w=0.7, in (c) S_w=0.49, in (d) S_w=0.32 and in (e) S_w=0.2.

domain.

Fig. 4.7 shows the transient evolution of the capillary pressure in the system at different wetting phase saturation rates. It is evident that during transient flow conditions, for high wetting phase saturation $S_w = 0.91, 0.7$ (Figs. 4.7a and 4.7b), a lower degree of homogeneity in the porous medium results in a lower transient and final steady-state capillary pressure in the system. The reverse is observed close to the percolation threshold and beyond as lower homogeneity noticeably increases the transient capillary pressure. Hence, an interplay between saturation, which largely defines the regime of flow, and the porous medium morphology, dictate the overall transient behaviour of the fluid phases with respect to the pressure drop across the interface. Overall, it can be concluded that for wetting phase saturation values beyond its percolation threshold, lower pore space connectivity (i.e. less negative χ_0), favours the transport of non-wetting phase blobs across wider, preferential flow channels of lower hydrodynamic resistance. That is, non-wetting phase blobs generally prefer not to squeeze through densely packed regions of solid grains at these conditions. At wetting phase saturation values near the percolation threshold and below, lower pore space connectivity results in a greater pressure drop across the fluid phase interface. Due to higher interfacial curvatures since the non-wetting phase is forced to penetrate areas of high solid grain clustering until steady-state is achieved. However, this trend seems to change as steady-state conditions are reached and preferential flow channels become the main flow transmission pathways in the porous medium.

Back to the contour plots in Fig. 4.4, Fig. 4.4a to 4.4e correspond to the transition from the initial injection to macro-level steady-state as determined by condition (4.3). After this the injected phase is seen to continue transporting across the computational domain, as already noted, becomes increasingly disconnected with an increase in the number of isolated non-wetting phase blobs. Therefore, though at the macro-level the fluid system is assumed to be in a 'steady-state', this can be considered as a pseudo-state since at the micro-level the nature of the two-phase flow is still changing.

The transient fragmentation degree of the wetting/non-wetting phase can be quantified by monitoring the temporal evolution of the fluid phase Euler characteristic in the system. Fig. 4.8 captures this evolution for the wetting phase Euler characteristic, χ_w. The percola-

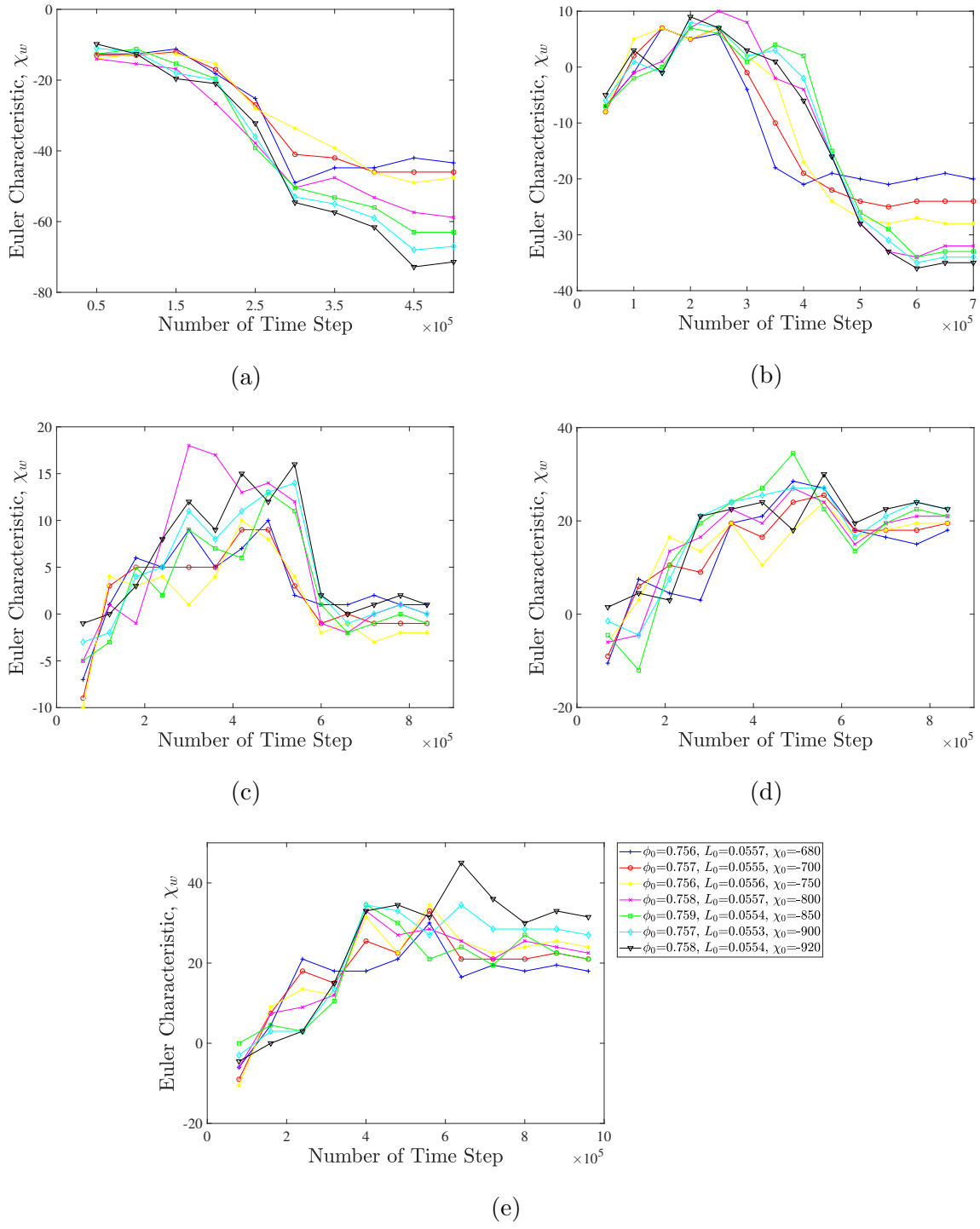

Figure 4.8: Variation of the Euler characteristic of the wetting phase χ_w with the number of time steps for in (a) S_w=0.91, in (b) S_w=0.7, in (c) S_w=0.49, in (d) S_w=0.32 and in (e) S_w=0.2.

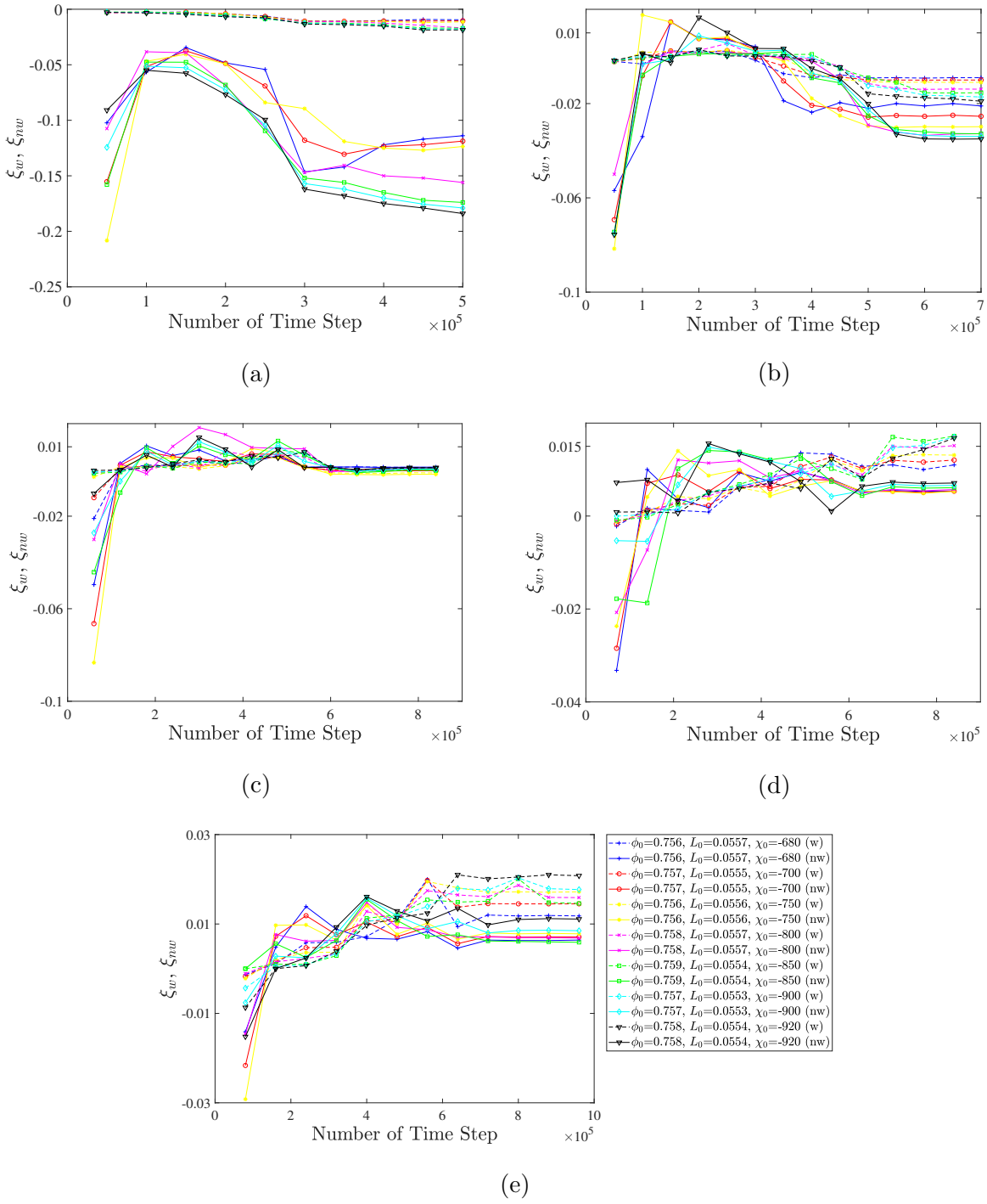

Figure 4.9: Temporal evolution of the Euler characteristic of the wetting and non-wetting phases per unit average grain, ξ_w and ξ_{nw}, for in (a) S_w=0.91, in (b) S_w=0.7, in (c) S_w=0.49, in (d) S_w=0.32, in (e) S_w=0.2.

tion threshold is referred to as either wetting or non-wetting phase changes from fragment to connected, and the phase Euler characteristic is close to zero. From a percolation theory perspective, a more positive χ_w represents a lower degree of wetting phase connectivity, whilst a more negative χ_w indicates a higher degree of wetting phase connectivity. The wetting and non-wetting phase connectivity levels can be considered as complementary since a high degree of wetting phase connectivity (that is, a more negative χ_w) signifies a high degree of non-wetting phase fragmentation (that is, a higher number of isolated non-wetting blobs in the domain). At $\chi_w = 0$, the system operates near its percolation threshold. In all the plots, for all the structures, the Euler characteristic undergoes a marked change, but after a sufficient time interval has elapsed, the rate of change reduces markedly, however, some variation is still occurring. As S_w decreases this levelling off takes longer to achieve. In the case of $S_w = 0.91$, the plots indicate a decrease in χ_w, whilst for $S_w = 0.7$ there is an initial increase with χ becoming positive, before a sharp decrease to a negative value. For $S_w = 0.49$ after the initial increase, there is a sharp decrease to a levelling off value in χ_w around $\chi_w = 0$. For lower values of S_w, after the progressively sharper increase, smaller decreases are seen before a levelling off. For both $S_w = 0.32$ and $S_w = 0.2$, the levelling off value for χ_w is positive. The above mentioned observations form a mosaic of simultaneously occurring processes which are linked to the final observed steady-state condition of the flow. More specifically and through a physical interpretation viewpoint, $S_w = 0.91$ corresponds to the ganglion dynamics regime and indicates that higher non-wetting phase fragmentation would be expected for pore structures with more negative χ_0 results in lower χ_w. It is also evident that even though a hydrodynamic macroscopic steady-state has been achieved (Figs 4.5,4.6), pore-scale processes, such as coalescence and snap-off continue to occur resulting in significant topological variations of the fluid phase. At $S_w = 0.7$, transient topological variations become more intense where an initially highly connected non-wetting phase gradually relaxes to a less connected state. The impact of the pore space χ_0 is similar to the $S_w = 0.91$ case. A similar transient behaviour can be observed for $S_w = 0.49$, however with a significant difference. The topological variation of χ_w relaxes at approximately zero, which means that the system operates very close to the percolation threshold. Physically, this indicates the large-scale connectivity of the non-wetting phase across the entirety of the domain. At this stage, the impact of the pore space χ_0 becomes largely indeterminate as the connection/fragmentation of the non-wetting phase is, in a way, counterbalanced by a corresponding fragmentation/connection

of the wetting phase. Lowering S_w beyond the percolation threshold saturation degree results in the inverse impact of the pore space χ_0 on phase connectivity. For both $S_w = 0.32$ and $S_w = 0.2$, intense coalescence of the non-wetting phase results in a positive χ_w which stabilises, although with noticeable fluctuations. It is worth noting that the impact of the pore space χ_0 is significantly higher in this regime for more negative χ_0. As mentioned previously, a more negative χ_0 minimises the preferential flow pathways, hence resulting in increased randomness/disorder in the flow which subsequently fragments to a greater number of blobs/droplets in the domain.

The temporal development of the non-dimensional variables $\xi_w = \chi_w/\bar{N}_w$ (Euler characteristic of the wetting phase per unit average grain enclosed by the wetting phase) and $\xi_{nw} = \chi_w/\bar{N_{nw}}$ (Euler characteristic of the wetting phase per unit average grain enclosed by the non-wetting phase) are shown in Fig 4.9. The aforementioned dimensionless variables provide information and an indication of the impact of solid grain clustering on the non-wetting and wetting phase blob formation. In a more general sense, they provide a measure of the phases' affinity to the solid matrix during snap-off and coalescence. Hence, a lower $\xi_\kappa = \chi_\kappa/\bar{N}_\kappa$ ratio, where κ represent either of the phases, would indicate that, on average, a fluid phase tends to surround a higher number of solid grains for a given pore space morphology. The inverse value of ξ_κ simply represents the number of average solid grains per blob in each phase. For higher saturation rates, $S_w = 0.91, 0.7$ the variation in ξ_w is much larger than that for ξ_{nw}. For all values of S_w, for latter times, the predicted values for ξ_w are larger than the corresponding ξ_{nw} values, except for $S_w = 0.49$ where both values, for all structures, tend to approximately zero on the scale of the plot (near the non-wetting phase percolation threshold region). In terms of the impact of the pore space morphology, the observed patterns are very similar to χ_w shown in Fig. 4.8. For $S_w = 0.91, 0.7$, the isolated blobs of both phases tend, on average, to form around a greater number of solid grains for a more negative χ_0, or for pore spaces with higher homogeneity. However, the reverse behaviour is observed for lower saturation levels, $S_w = 0.32, 0.2$ which corresponds to a hydrodynamic regime for which the non-wetting phase is fully connected in the domain, where a greater number of solid grains per blob is observed for less negative values of χ_0, or for pore spaces with lower homogeneity. This phenomenon can be linked to the nature of the drainage process itself. At higher fragmentation levels of the non-wetting phase ($S_w = 0.91, 0.7$) the formed ganglia tend to move along the flow

paths with lower resistance, that is, where there is a lower concentration of solid grains. In a highly homogeneous porous medium there is no preferential flow path, thus moving ganglia more uniformly surround the solid matrix resulting in a higher number of grains per blob. On the contrary, for saturation levels greater than the percolation threshold, the non-wetting phase is largely fully connected throughout the domain resulting in a greater number of wetting phase blobs. Hence, for a given pore space morphology, the wetting phase blobs will, on average, tend to adhere to the solid grain clusters more intensively in an inhomogeneous porous medium and less intensively in a homogeneous one.

In Figure 4.10, the dependence of the temporal evolution of the interface length, as characterised by the non-dimensional parameter ζ, with S_w for each considered structure is shown. The interface curves are defined as $\zeta = I_c\overline{d_T}/l^2$, where l^2 is the computational domain area, $\overline{d_T}$ is the average pore throat and I_c is the total length of the interface curves between two-phases. For all plots, ζ initially increases consistent with the non-wetting phase injection. For $S_w = 0.91, 0.7$ and 0.49, ζ continues to increase after the macro-level steady-state is achieved shown in Fig. 4.6. This is consistent with the observations that as the wetting phase transports, it fragments, with an associated increase in the number of non-wetting phase blobs. For later times this fragmentation reduces and almost constant values of ζ are achieved. Going from $S_w = 0.91$ to 0.7 the steady-state value of ζ increase significantly, with a larger variation seen between the structures. Not much difference can be seen between structures 6 and 7, but ζ increases as χ_0 become less negative for the other structures. Going from $S_w = 0.7$ to 0.49, the final value of ζ decreases for structures 6 and 7, but increases slightly for all the other structures. For $S_w = 0.32$ and 0.2, after achieving maximum values in ζ, all plots show a reduction in the parameter ζ until the levelling off occurs, consistent with the non-wetting phase increasingly replacing the wetting phase. Overall, it is evident from Fig. 4.10 that across the full spectrum of the saturation range of the wetting phase, the interface length between the two-phase is higher for a more inhomogeneous porous medium. This is in line with the previous observations in Figs. 4.8 and 4.9 with regard to preferential flow pathway formation and the more intensive wetting phase adhesion to solid grain clusters resulting in higher degrees of non-wetting/wetting phase blob distortions. In the porous medium with higher pore space homogeneity, the resulting blob geometry tends to minimise its interface contract length.

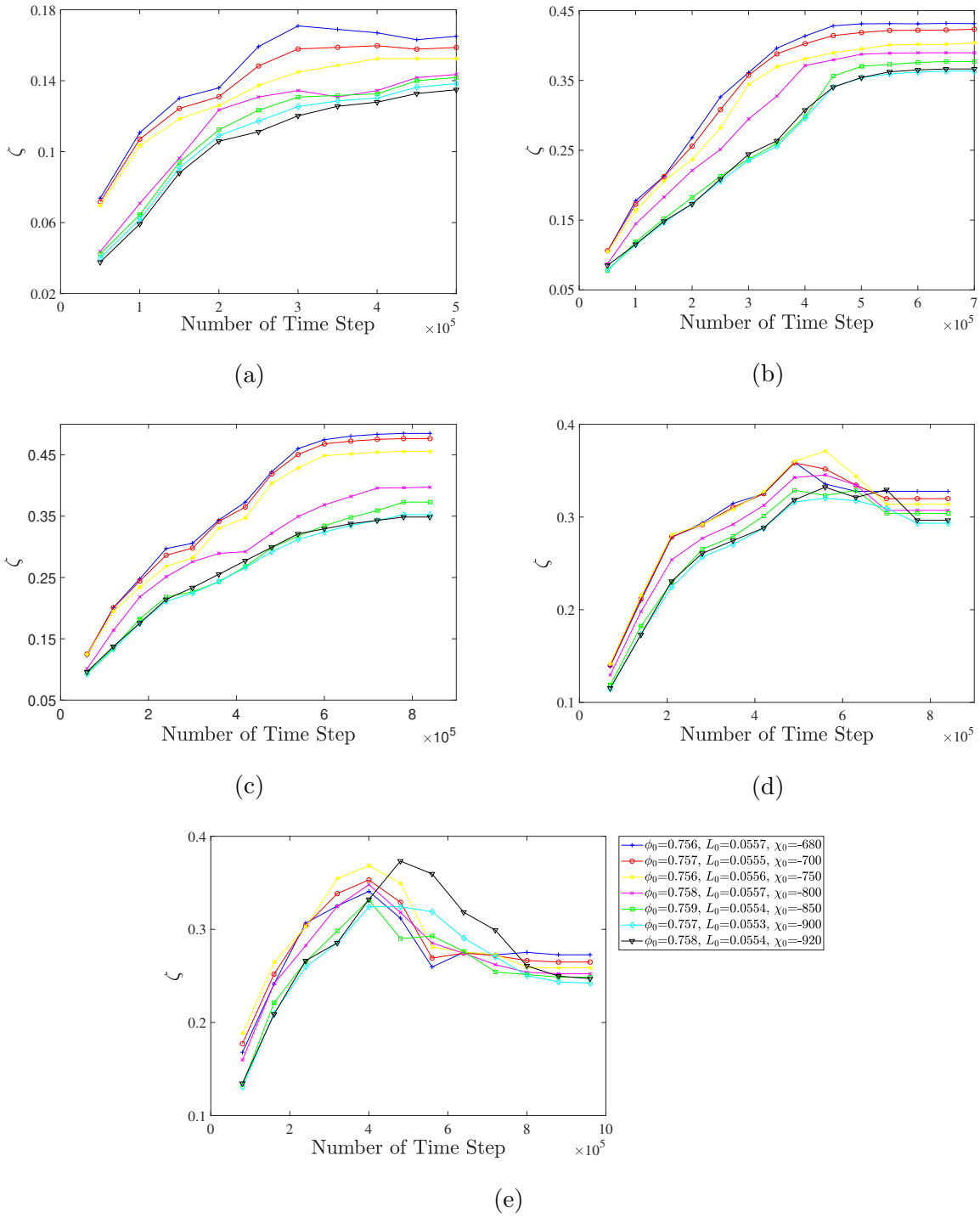

Figure 4.10: Temporal evolution of the interface length represented by the non-dimensional variable ζ for in (a) S_w=0.91, in (b) S_w=0.7 in (c) S_w=0.49, in (d) S_w=0.32 and in (e) S_w=0.2.

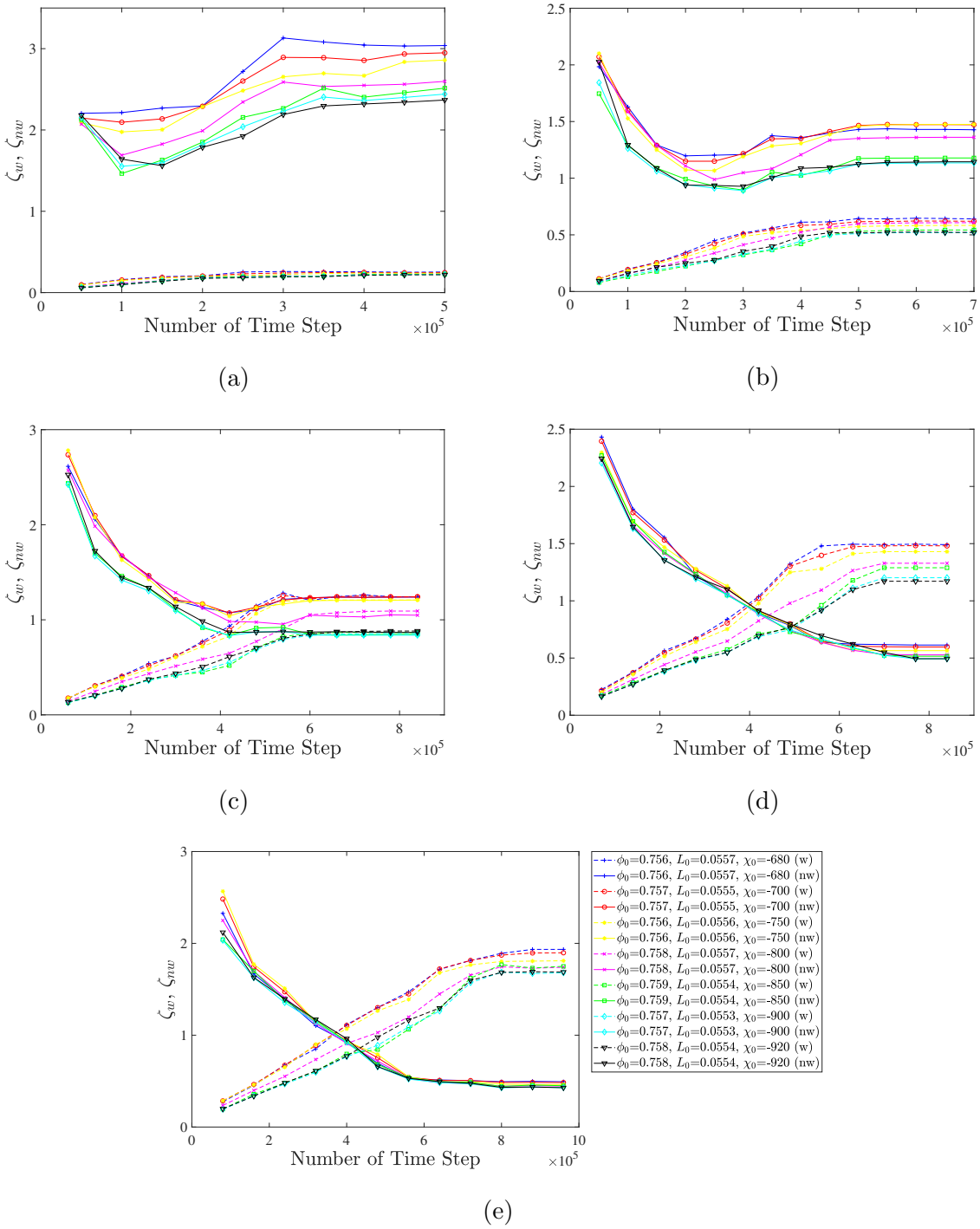

Figure 4.11: Temporal evolution of the interface length as represented by the non-dimensional variables ζ_w and ζ_{nw} for in (a) S_w=0.91, in (b) S_w=0.7, in (c) S_w=0.49, in (d) S_w=0.32 and in (e) S_w=0.2.

Fig. 4.11 plots of the interface length in terms of the nondimensional variables for wetting and non-wetting phase, $\zeta_w = I_c\overline{d_T}/l_w^2$ and $\zeta_{nw} = I_c\overline{d_T}/l_{nw}^2$. Mathematically, the quantities ζ_w and ζ_{nw} are a measure of the interface contact length per unit wetting/non-wetting phase area respectively. For $S_w = 0.49, 0.32, 0.2$ after sufficient time constant values are achieved but for $S_w = 0.91, 0.7$ small increases still appear to be occurring. Fig. 4.11 shows that for $S_w = 0.91, 0.7$ the increased inhomogeneity of the pore space generally results in a greater non-wetting phase interface length for a given volume fraction. The behaviour is similar for the wetting phase, however, the deviations are too small to be considered significant compared to the wetting phase.At $S_w = 0.49$, the general effect is also similar as for 0.91 and 0.7, however, structures 1-3 collapse onto the same curve, structure 4 is at a noticeably lower value and structures 5-7 also collapse onto the same curve at even lower magnitudes of ζ_{nw}. Physically, percolation threshold effects become evident for this specific case where the full connectivity of the non-wetting phase becomes dependent on the pore space topology. This becomes clearer that the behaviour of ζ_{nw} for $S_w = 0.32$ and 0.2, where all structures have collapsed onto a single curve, with minor deviations, at approximately a value of $\zeta_{nw} = 0.5$. Very similar behaviour is observed for ζ_w if one follows the plots and curves of Fig. 4.11 in the reverse direction (i.e. $S_w = 0.2 \rightarrow 0.91$).

4.4 Imbibition

Fig. 4.12 shows the numerically generated results of volume fraction plots of the evolution of the wetting phase (blue) and the displaced non-wetting phase (yellow) for a final constant saturation value of the wetting phase $S_w = 0.3$ and structure 4 ($\chi_0 = -800$). The randomly distributed pore structure is indicated by the dark-coloured circles. As the flow develops, a number of fingers of the wetting phase can be seen extending across the computational domain approximately in the x-direction, that is, in the direction of the body forcing. As time progresses the non-wetting phase remains almost fully connected - an isolated blob can be seen at the top of contour plots 4.12e and 4.12f and separately in 4.12i and 4.12k - while the wetting phase becomes increasingly disconnected, but with a number of markedly large blobs. Topologically, a complex transient profile is qualitatively observed in Figs 4.12a to 4.12k. Initially, the penetration of the wetting phase into the domain causes a noticeable fragmentation of the non-wetting phase, observed as oil ganglia contained within the larger wetting phase blobs (Figs 4.12d – 4.12g). However, a

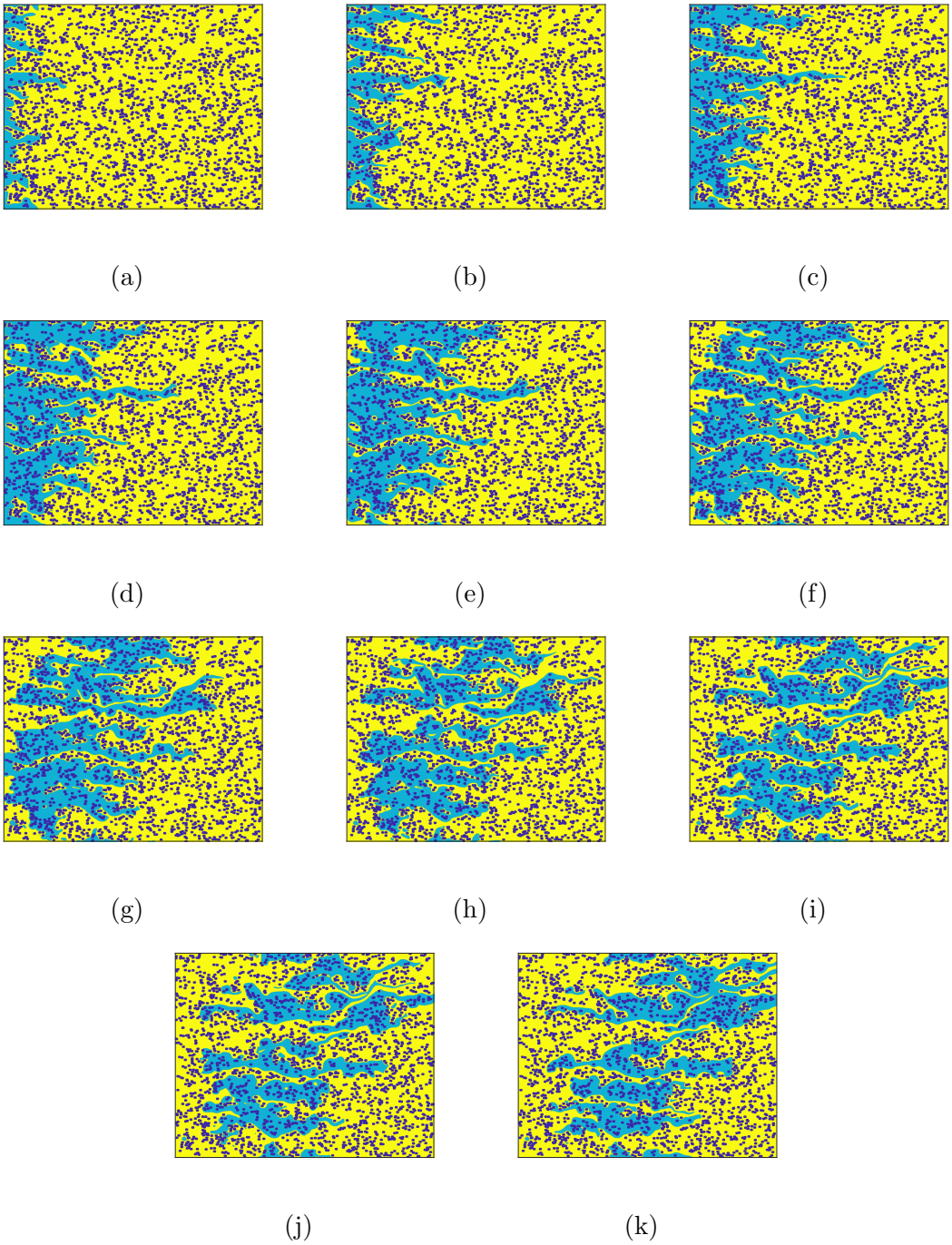

Figure 4.12: Volume fraction contour plots of the temporal evolution of the displacement of the non-wetting phase by the injected wetting phase for an Euler characteristic of $\chi_0 = -800$ and a steady-state wetting phase saturation rate of 0.3. In terms of lattice units $t = 7 \times 10^4$ in (a), $t = 1.4 \times 10^5$ in (b), $t = 2.1 \times 10^5$ in (c), $t = 2.8 \times 10^5$ in (d), $t = 3.5 \times 10^5$ in (e), $t = 4.2 \times 10^5$ in (f), $t = 4.9 \times 10^5$ in (g), $t = 5.6 \times 10^5$ in (h), $t = 6.3 \times 10^5$ in (i), $t = 7 \times 10^5$ in (j) and $t = 7.7 \times 10^5$ in (k).

marked decrease in these contained ganglia is observed as the flow moves towards its steady flow conditions (Figs 4.12h – 4.12k). Hence, a significant qualitative difference between drainage (Fig.4.4) and imbibition can be seen since the two displacement processes show almost inverse behavioural characteristics during their respective transient evolutions in the domain, that is, for a similar phase saturation ($S_{nw} = 0.3$ for drainage and $S_w = 0.3$ for imbibition) drainage results in an increased wetting phase connectivity whilst imbibition results in an increased wetting phase fragmentation.

The temporal developments of the instantaneous wetting phase saturation for the ultimate constant values are shown in Fig. 4.13, for the seven considered porous structures, whilst the corresponding evolution of the average fluid velocity in x direction of each phase is displayed in Fig. 4.14. Similar to drainage cases, the components of the respective averaged phase velocities in the y direction (not shown) were found to be mostly of $0(10^{-5})$, which is 100 times smaller than the corresponding components in the x direction, as shown in Fig. 4.14. Therefore Fig. 4.14 acts as a good visual aid in determining when steady-state is achieved. In general increasing trends of wetting phase saturation rate can be seen, though the rate of increase shows a degree of fluctuation for a number of the curves. In some cases, a small degree of overshoot (on the scale of the respective plots) is observed before a subsequent decrease to the final constant S_w values. As the desired S_w value is increased, a longer time interval is required to achieve these respective constant values. In general, these observations are to be expected given that a larger S_w requires more wetting phase injection. This is also consistent with the drainage displacement observations made in Section 4.3. As a general observation, when the connected pore space becomes more homogeneous, the time to reach the constant S_w value increases slightly, which is again similar to observations made in the context of drainage. However, based on Fig. 4.13a, the wetting phase droplet regime ($S_w = 0.09$) displays an exceptional character where the desired saturation level is reached faster for more homogeneous structures, though with noticeable fluctuations. This behaviour could be associated with the higher affinity of the wetting phase to the solid matrix, which, in turn, more effectively redistributes and reconfigures the continuous increase in the wetting phase droplets than an inhomogeneous domain with higher solid phase clustering.

The instantaneous domain averaged phase velocities $u_{x,w}$, $u_{x,nw}$ are also seen to converge

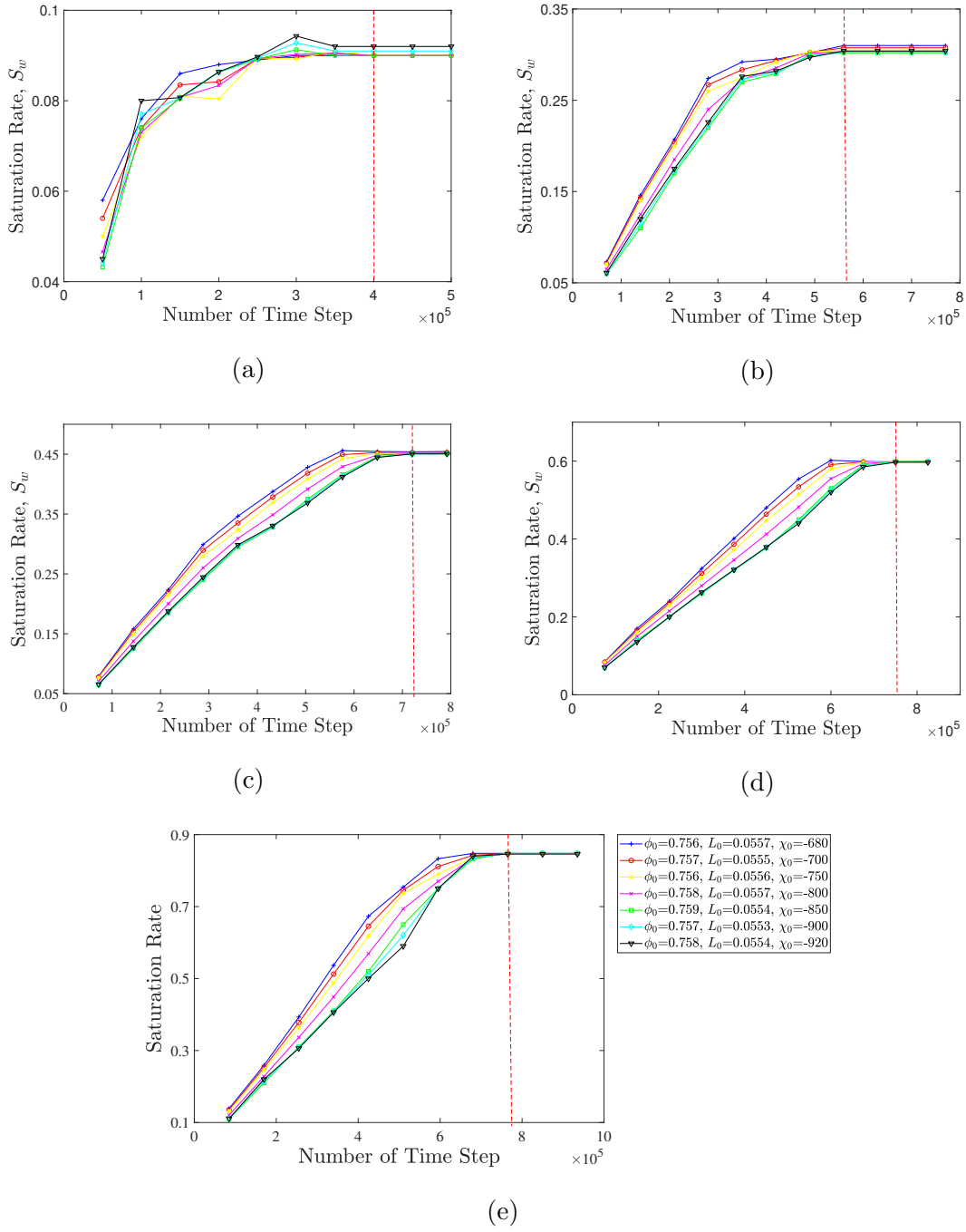

Figure 4.13: Variation of the saturation rate of the wetting phase with the number of time steps for the final constant values of in (a) $S_w = 0.09$, in (b) $S_w = 0.3$, in (c) $S_w = 0.45$, in (d) $S_w = 0.6$ and in (e) $S_w = 0.85$. The vertical red dashed line indicates the time at which steady saturation is reached.

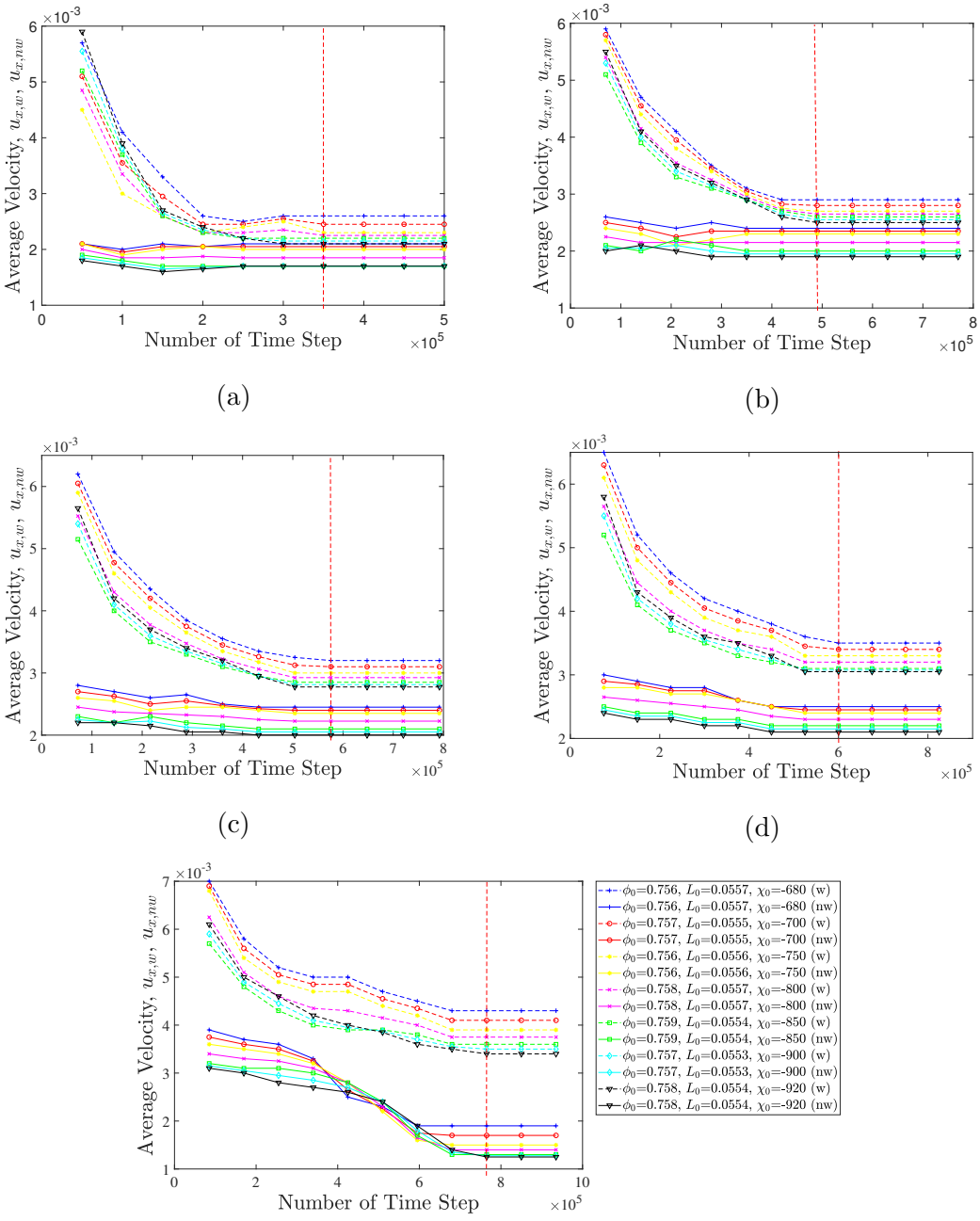

Figure 4.14: Variation in the average velocity in the x direction of the wetting (dashed lines) and non-wetting (solid lines) phases with the number of time steps for final constant values of in (a) $S_w = 0.09$, in (b) $S_w = 0.3$, in (c) $S_w = 0.45$, in (d) $S_w = 0.6$ and in (e) $S_w = 0.85$. The vertical red dashed line indicates the time at which the macroscopic steady-state is reached.

to respective constant values. For the $u_{x,w}$ curves, a mostly monotonic decrease to the final constant value is seen, though in some cases, some minor oscillations are observed just before the constant value is reached, for example, in Figs. 4.14a and 4.14e. The final constant values for $u_{x,w}$ decrease as the pore space χ_0 becomes more negative but initially ($t = 5 \times 10^4 \Delta t$) the $\chi_0 = -900, -920$ curves have larger than expected values, for example, for $S_w = 0.09$ these are the two largest values and are larger than the $\chi_0 = -800$ initial values for all the remaining plots. Relative to the wetting phase values, the non-wetting phase velocities $u_{x,nw}$ display less variation in all cases. The largest variations are seen for both $S_w = 0.6$ and $S_w = 0.85$ and a point of inflexion is observed for all χ_0 values around $t = 5 \times 10^5 \Delta t$. As S_w increase and the non-wetting phase become more and more disconnected and reaches the ganglion dynamics, where the non-wetting phase fragmentation get stuck within the pore bodies thus decreasing the averaged phase velocities. Both the initially shown values of $u_{x,nw}$ ($t = 5 \times 10^4 \Delta t$) and the final steady-state values decrease as the pore space Euler characteristic becomes more negative. It is also notable that all the steady-state wetting phase values of $u_{x,w}$ are larger than all the steady-state values of $u_{x,nw}$, for the same value of S_w. Compare to drainage, it is observed that during imbibition, lower pore space connectivity and higher solid grain clustering positively impact the phase transport velocity through the porous matrix. This can be associated with the impact of the solid phase clustering on the wetting and non-wetting phase configurations in the domain as the former will tend to flow over highly concentrated regions of solids, whereas the latter will tend to slide over it through the wider channels of the inhomogeneous domain.

Comparing the volume fraction contour plots in Fig. 4.12 with Fig. 4.14b, condition (Eq. 4.3) is reached by contour plot 4.12g, though there is only a small variation in $u_{x,nw}$ between contour plots 4.12f and 4.12i. After this, despite the two-phase system being in a macro-level steady-state, local variation is still occurring with the topology of the wetting phase blobs changing as they transport across the computational domain, although the number, in general, would appear to remain constant. Coalescence of some wetting phase blobs is observed between contour plots 4.12j and 4.12k (top right of the domain). The phenomenon of continuing snap-off and coalescence at steady-state has already been reported - see for example the numerical and experimental study of Armstrong et al. (2016) and the experimental observations of Khanamiri and Torsæter (2018) - and is consistent with observations in the context of drainage.

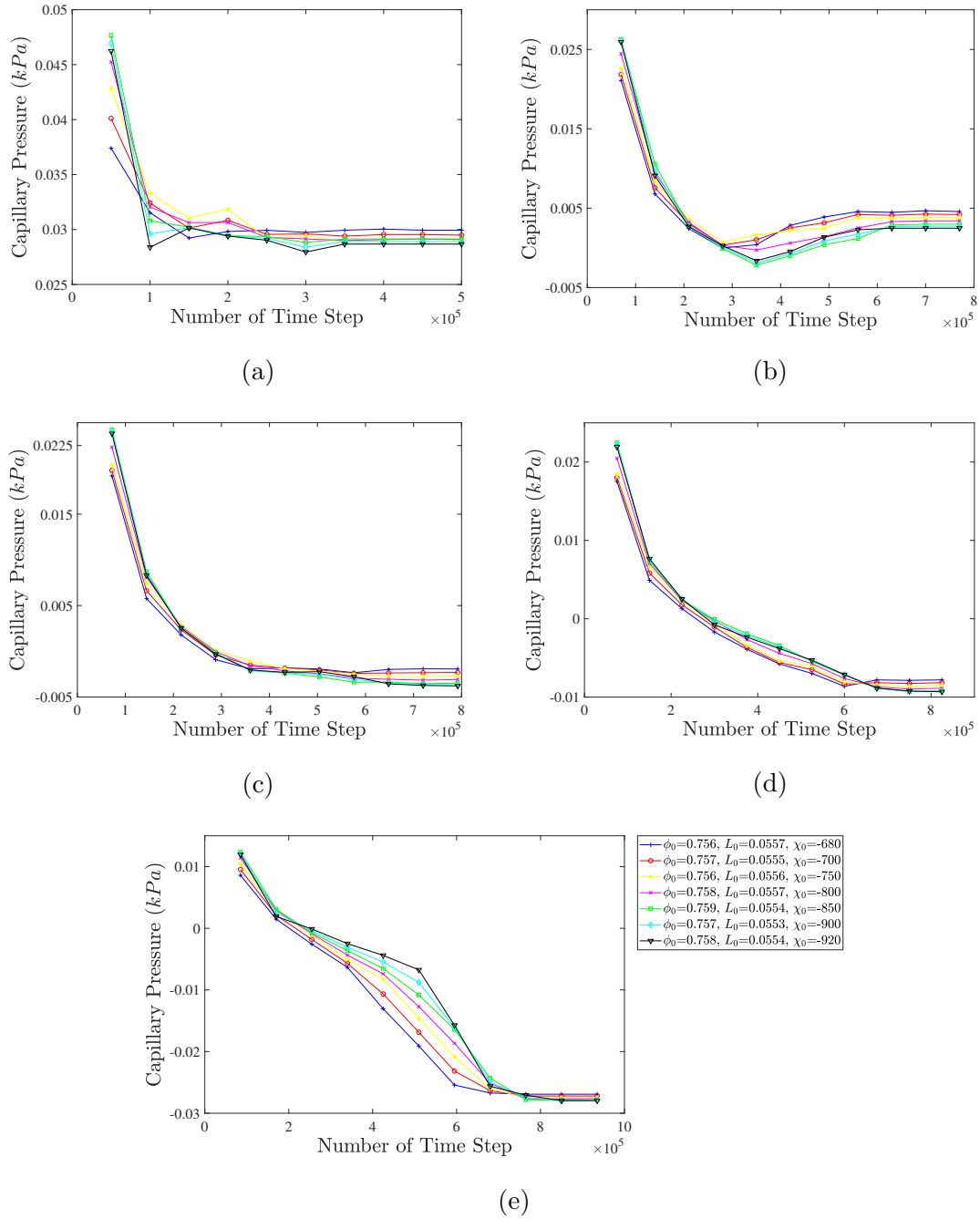

Figure 4.15: Temporal evolution of the capillary pressure for in (a) $S_w = 0.09$, in (b) $S_w = 0.3$, in (c) $S_w = 0.45$, in (d) $S_w = 0.6$ and in (e) $S_w = 0.85$.

Fig. 4.15 shows the impact of the pore space connectivity on the temporal evolution of the capillary pressure in the system for varying saturation. During imbibition, for all saturation values, initially high capillary pressures relax to lower values as the flow approaches a steady-state. In contrast to drainage, at steady-state conditions, the capillary pressure becomes lower for more homogeneous structures. This phenomenon can be associated with a lower interfacial curvature displacing the front as the wetting phase more uniformly attaches to the closely spaced solid grains. As also shown in Table 5.1, a more negative χ_0 also decreases the average pore size in the domain, which is indicative of a more closely spaced solid grain configuration. In addition, the evolution of the capillary pressure is also dependent on saturation. As S_w increases, the greatest interphase pressure drop in the porous medium gradually transitions from highly inhomogeneous structures to homogeneous ones. This is attributed to the effect of higher solid grain clustering on each phase's connectivity and the resulting interface geometry. It can be generally observed that for low wetting phase saturation, a more inhomogeneous domain tends to keep the capillary pressure at a high level indicative of higher fragmentation and droplet distortion patterns. This trend changes, however, as S_w increases and the flow transitions towards the ganglion dynamics regime (Fig. 4.15e), where more homogeneous medium further promotes non-wetting phase fragmentation, due to reduced channelisation, as the wetting phase is continuously injected into the domain.

The evolution of the Euler characteristic for the wetting phase, χ_w, for the seven porous structures and the five considered values of S_w, is shown in Fig. 4.16. As noted in drainage, the tracking of this parameter provides a means of the wetting phase fragmentation measurement over time. For $S_w = 0.09$, the wetting phase Euler characteristic increases to an approximately constant, positive final value with most curves showing oscillations in their gradient. For $S_w = 0.3$, all the curves seem to first decrease to respective (negative) minimum values before increasing to approximately constant, positive values. Fig. 4.14b indicate that the respective systems are approaching a macro-level steady-state for the times just after the respective curves achieve their minimum value. The minimum for $\chi_0 = -800$ corresponds to plot 4.12e, at which time the injected wetting phase would appear to be almost fully connected with some non-wetting phase blobs contained within it, but for later times an increased fragmentation of the wetting phase can be seen consistent

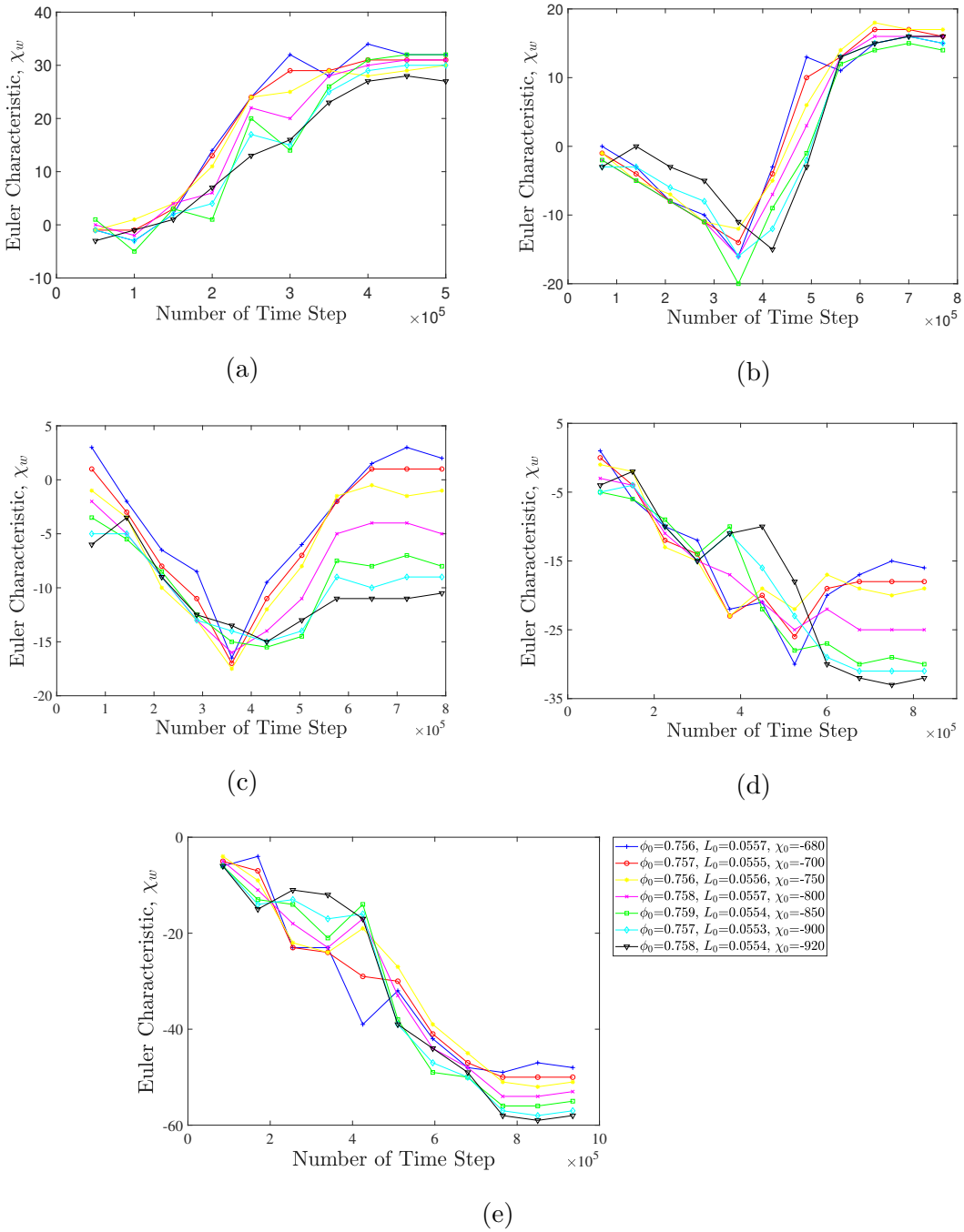

Figure 4.16: Variation of the Euler characteristic of the wetting phase, χ_w, with the number of time steps for in (a) $S_w = 0.09$, in (b) $S_w = 0.3$, in (c) $S_w = 0.45$, in (d) $S_w = 0.6$ and in (e) $S_w = 0.85$.

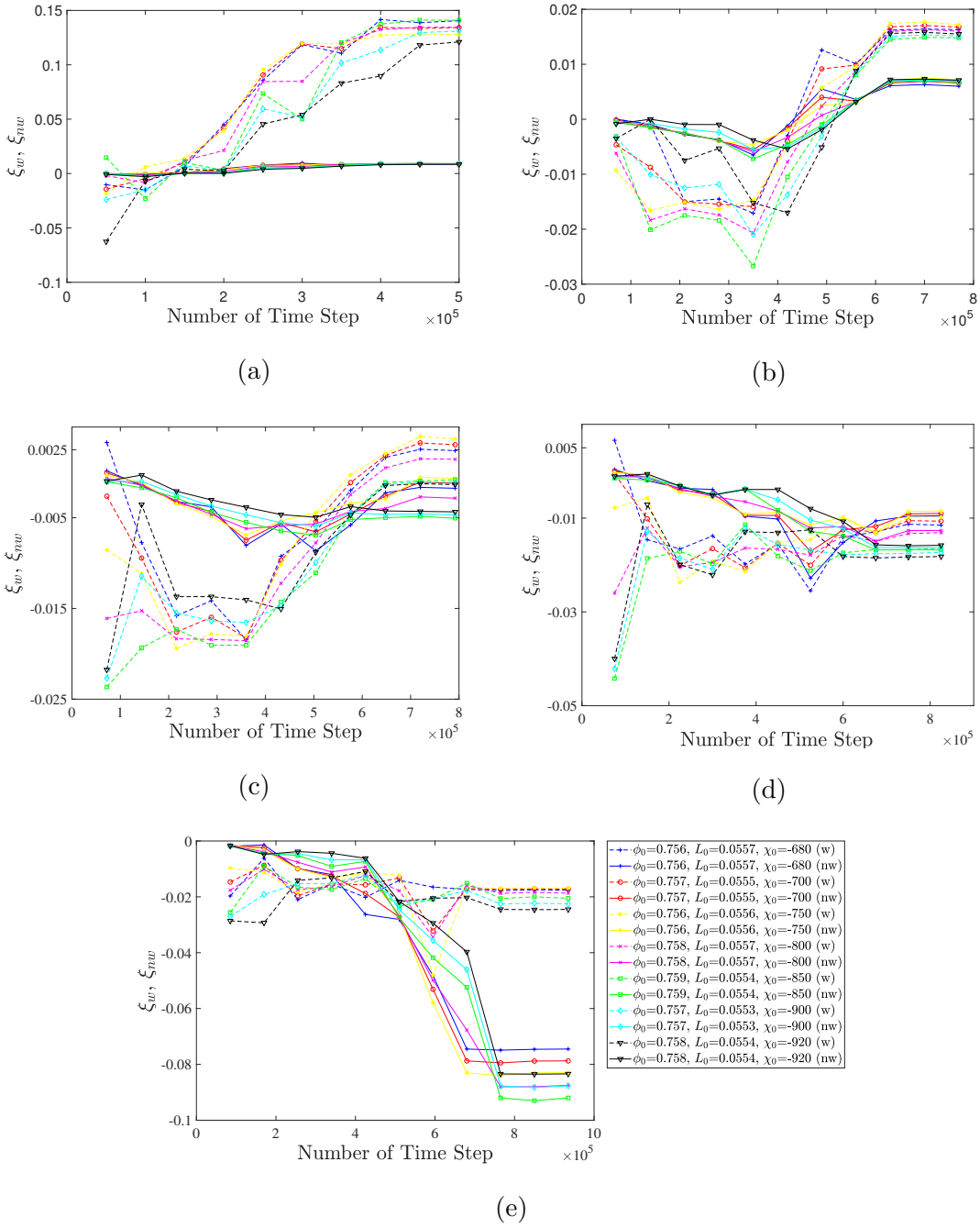

Figure 4.17: Temporal evolution of the Euler characteristic of the wetting phase per unit grain ξ_w and of the non-wetting phase per unit grain ξ_{nw} for in (a) $S_w = 0.09$, in (b) $S_w = 0.3$, in (c) $S_w = 0.45$, in (d) $S_w = 0.6$ and in (e) $S_w = 0.85$.

with the observations with regard to Fig. 4.16b. An interesting observation of this flow regime is that the transient topological behaviour of the wetting phase transitions from a highly connected state to an increasingly disconnected one as steady-state conditions are approached. Although there is no definite pattern on the impact of the pore space χ_0 on these transient patterns, it can generally be observed that lower pore space homogeneity results in lower wetting phase connectivity during this transitional stage. As mentioned, this phenomenon can be associated with the higher affinity of the wetting phase to closely packed solid grains, resulting in a greater number of isolated wetting phase blobs. The set of curves for $S_w = 0.45$ in Fig. 4.16c shows a similar pattern as $S_w = 0.3$, with the exception of the $\chi_0 = -920$ curve which first undergoes a small increase before decreasing to its minimum value. After the respective minimum values, all curves increase again to approximately constant final values, though as in the case of plot 4.16b, some small variations on the scale of the plot are still seen. A large spread in these final values is observed and the final values of χ_w decrease as χ_0 become more negative. The topological evolution of the wetting phase during imbibition at $S_w = 0.45$ is qualitatively similar to $S_w = 0.09$ and $S_w = 0.3$ for the pore space $\chi_0 = -680$ and $\chi_0 = -700$, with the exception that the steady-state χ_w value converges to approximately zero. This indicates that these two specific porous structures operate close to the wetting phase percolation threshold. This, however, is not the case for the rest of the structures, which all evolve to more negative values of χ_w, indicating that the wetting phase is well connected in the domain and beyond its percolation threshold. This also signifies the strong dependency of the percolating (wetting) phase on the pore space connectivity. For $S_w = 0.6$ and $S_w = 0.85$ shown in Fig. 4.16d and 4.16e, both decrease to the respective final, approximately constant, negative values in χ_w, whereas χ_0 becomes more negative, so does each of these final values. In Fig 4.16d, intermediate local maximum values would appear to increase (are less negative) as χ_0 becomes more negative. For the higher saturation values $S_w = 0.6$ and 0.85, there is a continuously increasing connectivity of the wetting phase (i.e. χ_w becomes more negative) but with an inverse impact of the pore space χ_0 on the transient state relative to the steady-state. It is observed that for the fully connected regime of the wetting phase, the higher homogeneity of the pore space tends to initially promote higher levels of wetting phase fragmentation but this trend is reversed as the flow gradually transitions to its final steady-state. As the domain becomes enriched by the continuous wetting phase injection, higher homogeneity favours higher wetting phase connectivity which results in a greater

number of non-wetting phase ganglia in the domain.

Fig. 4.17 shows the number of average solid grains per blob in the wetting and non-wetting phase. For $S_w = 0.09$ (Fig. 4.17a), both sets of curves display an increase over time, though, on the scale of the plot, changes in ξ_{nw} are minimal, achieving respective final, approximately constant values, just greater than zero. In contrast, plots for ξ_w display substantive increases with marked oscillations in gradient. In a number of cases, the initially displayed value for ξ_w is negative and the final, approximately constant, positive values in ξ_w are the largest values for all the shown S_w plots. In Fig. 4.17b ($S_w = 0.3$), the changes in ξ_w are noticeably smaller, therefore the variations in ξ_{nw} are easier to perceive but they are still smaller than the observed changes in ξ_w. Both sets of curves first decrease to negative values before transitioning to the final positive values. The respective minimum values would appear to correspond to the minimum values seen in Fig. 4.16b. For $S_w = 0.45$ (Fig. 4.17c) the observed variations have the smallest vertical range of the five saturation conditions, but even on this scale the respective curves for ξ_w still display larger variations than the corresponding ξ_{nw} curves. For the wetting phase curves, the distribution of the initially displayed points is interesting in that the three structures with more negative χ_0 correspond to the most negative values in ξ_w, with $\chi_0 = -850$ being the most negative, followed by $\chi_0 = -900$ and then $\chi_0 = -920$. For the other structures, as χ_0 becomes less negative, so does ξ_w. In Fig. 4.17d ($S_w = 0.6$), with the exception of the initial oscillations in ξ_w, for later times the variations in ξ_w and ξ_{nw} are comparable with the final approximately constant values also being comparable, though dependence on the χ_0 is clear. In the case of $S_w = 0.85$ (Fig. 4.17e) variations in ξ_{nw} are markedly larger. The non-wetting phase curves appear to originate at the same point on the scale of the plot and then become progressively more negative, with sharp gradients observed in the interval $5 \times 10^5 - 7.5 \times 10^5$, before final, approximately constant, negative values are achieved. To make a physical sense of Fig. 4.17, one has to observe the trend of each phase curve as they are approaching zero irrespective of their positive or negative values. Qualitatively, one can conclude that, during imbibition, the pore space χ_0 affects ξ_w and ξ_{nw} in a similar way, though with opposite trends across the complete saturation spectrum. For low wetting phase saturation ($S_w = 0.09,\ 0.30$) the more homogeneous the pore space becomes, the higher number of solid grains enclosed on average by each wetting phase blob, whilst the opposite is true for the non-wetting phase. However, at these low

wetting phase saturation levels, the impact of the pore space χ_0 on ξ_{nw} can be considered negligible. The same behaviour is also observed close to the percolation threshold of the wetting phase, ($S_w = 0.45$), although the impact of the pore space becomes significantly more noticeable for the non-wetting phase. The trend for the non-wetting phase is reversed and mimics the wetting phase trend for saturation values beyond the percolation threshold, ($S_w = 0.60,\ 0.85$), and is even clearer close to the ganglion dynamics regime. At this region, ξ_w and ξ_{nw} are closer to zero for pore spaces of higher inhomogeneity. Hence, at low S_w, wetting phase droplets tend to be more uniformly spread in a highly homogeneous medium, whilst preferential flow pathways over highly solid grain clustered regions form the backbone of the wetting phase topology evolution for saturation values beyond the percolation threshold.

In Fig. 4.18, the dependence of the evolution of the interface length defined in terms of the nondimensional parameter ζ is shown. For $S_w = 0.09, 0.3, 0.45, 0.6$, in general, the curves increase monotonically to final, approximately constant, values. For some of the curves, some minor oscillations in their gradient can be seen. As the χ_0 becomes more negative, for each of these values of S_w, ζ decreases. For the remaining value of S_w, that is $S_w = 0.85$ (plot 4.18e) a different behaviour pattern is observed. The interface length is first seen to rise to a maximum before decreasing to final, approximate constant values, though in one case ($\chi_0 = -680$) the curve reaches a local minimum before rising again to the final constant value. The timescale of the decrease corresponds to the period over which the inflectional behaviour was observed for $u_{x,nw}$ in Fig. 4.14e. In addition, an inversion in the respective sizes of ζ during this timescale with regard to χ_0. The largest values of ζ are observed for $S_w = 0.45$. The impact of the pore space connectivity on the interfacial length evolution during imbibition follows a similar pattern to drainage. Overall, as the wetting phase is continuously injected into the domain, across the full wetting phase saturation spectrum, lower levels of pore space homogeneity tend to increase the interface length between the two-phases. This is, again, in line with the previous observations related to the more intensive wetting phase adhesion to solid grain clusters resulting in higher degrees of non-wetting/wetting phase blob distortions. Fig. 4.18e, however, shows a very interesting, different, transient behaviour as the flow moves towards the ganglion dynamics regime (i.e. $S_w = 0.85$), where the continuous fragmentation of the non-wetting phase initially results in highly unsymmetrical blob geometries which eventually relax to more evenly shaped

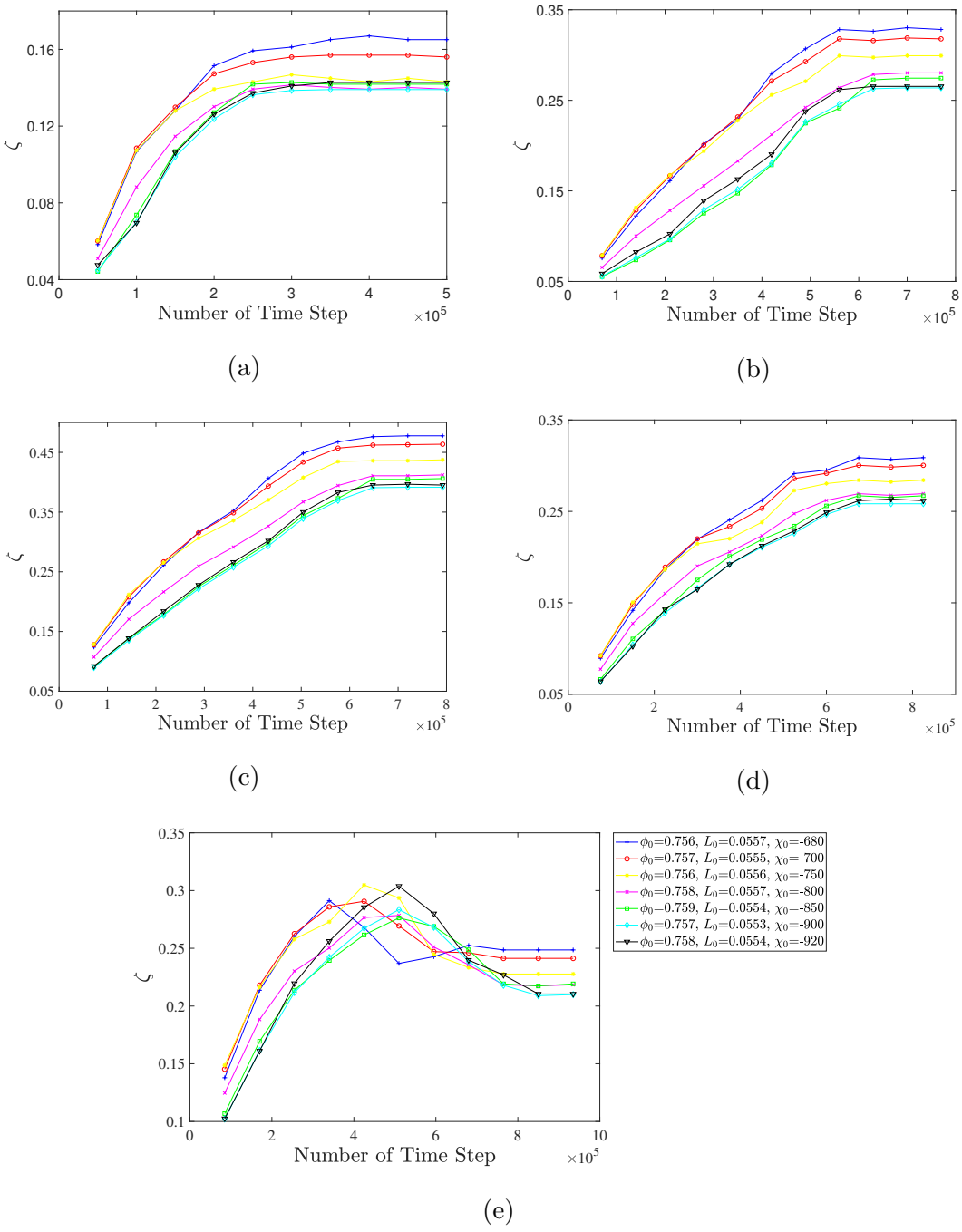

Figure 4.18: Temporal evolution of the interface length represented by the nondimensional variable ζ for in (a) $S_w = 0.09$, in (b) $S_w = 0.3$, in (c) $S_w = 0.45$, in (d) $S_w = 0.6$ and in (e) $S_w = 0.85$.

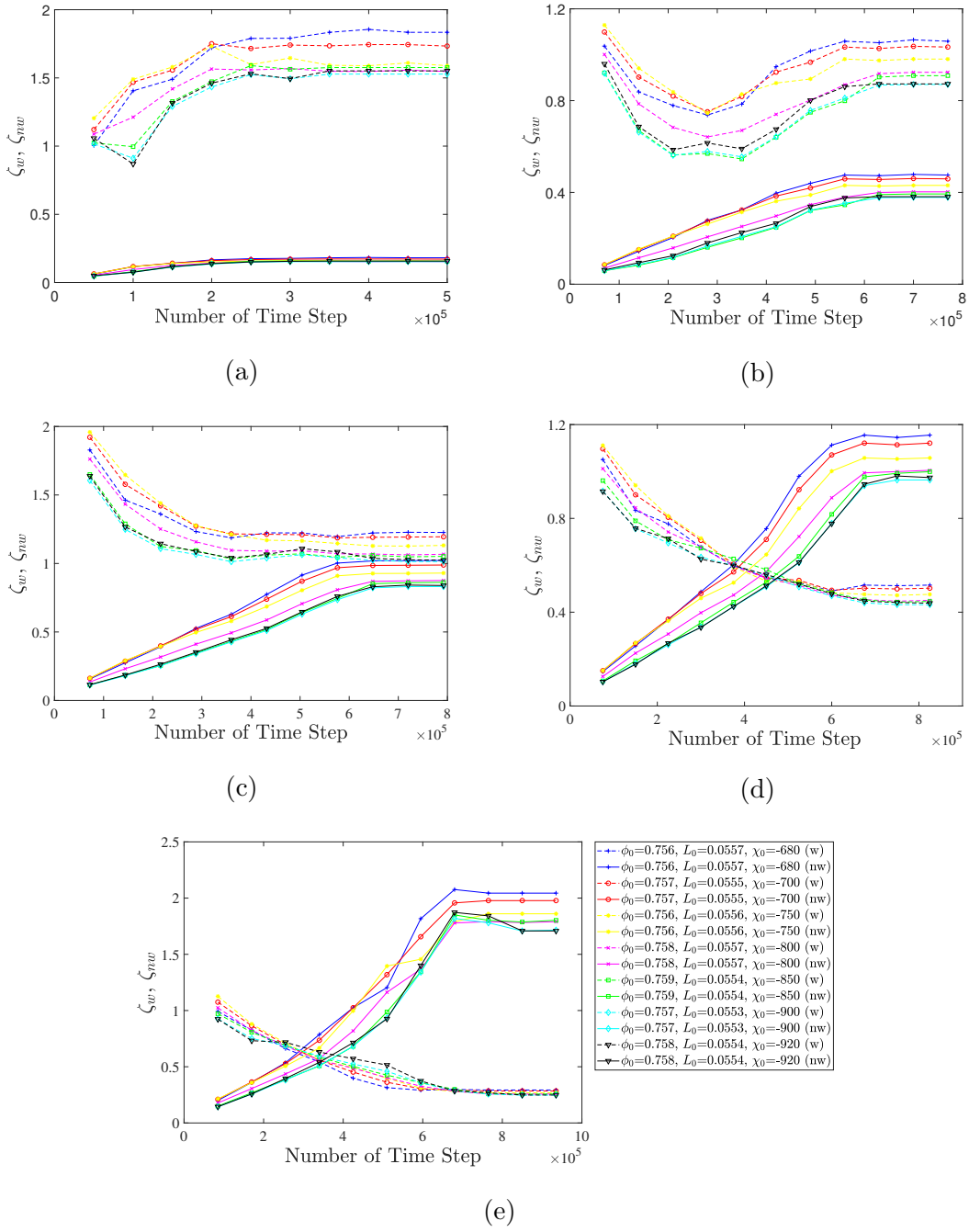

Figure 4.19: Temporal evolution of the interface length as represented by the nondimensional variables ζ_w and ζ_{nw} for in (a) $S_w = 0.09$, in (b) $S_w = 0.3$, in (c) $S_w = 0.45$, in (d) $S_w = 0.6$ and in (e) $S_w = 0.85$.

ganglia within the domain at steady-state.

In Figure 4.19 the evolution of the (total) length of the interface between the fluid phases scaled by the respective wetting/non-wetting phase areas is shown in terms of the nondimensional parameter. Fig. 4.19 shows that increased pore space homogeneity generally results in a lower wetting and non-wetting phase interface length for a given volume fraction occupied by the corresponding phase within the domain. For the low wetting phase saturation, a non-monotonic transient profile is observed, indicative of the initial connected state of the wetting phase that progressively transitions into highly fragmented droplets in the domain. The observed trends are similar for both phases and for both transient and steady-state regimes. The only noticeable exception occurs at $S_w = 0.85$ which corresponds to the ganglion dynamics regime. During the transient evolution of the interface length per unit phase area, it is observed that the highly homogeneous pore space gives rise to greater ζ_w values, a situation that is reversed when steady-state is achieved. This behaviour can be associated with the transient wetting phase fragmentation patterns (Fig. 4.16) due to reduced channelisation and hence lower connectivity. However, as the flow relaxes to its steady-state, the closely spaced solid grains result in a highly connected and uniform wetting phase network within the domain, minimising the overall interfacial length as opposed to a more inhomogeneous and highly irregular pore space.

4.5 Summary

To sum up, for the transient study, where the same body force G was applied to seven porous mediums with different χ_0 during the drainage and imbibition, and the flow properties such as saturation rate, velocity fields, capillary pressure, Euler characteristic, and interface length at different time steps from injection to steady-state were plotted and analyzed. It was found that the increasing levels of homogeneity in porous medium imposed greater flow restrictions which reduce the transmission velocities and extend the time interval needed to reach steady saturation. Capillary pressure decrease as the χ_0 becomes more negative. For both drainage and imbibition, as S_w increases, the non-wetting phase transited from fully connected to ganglion dynamic through its percolation threshold. During drainage, the degree of phase fragmentation/connectivity depended on the wetting phase saturation level, Where for low S_w, more homogeneous structures resulted in a higher value

of χ_w (higher wetting phase fragmentation), and for high S_w, more homogeneous structures resulted in lower value of χ_w, whilst an indeterminate state was observed near the non-wetting phase percolation threshold. During imbibition, the wetting phase transited from a highly connected state to a less connected one for low S_w, and more homogeneous structures resulted in a lower value of χ_w for all S_w. In addition, the was shown that the phase percolation threshold strongly relied on pore space topology. More homogeneous pore structures also resulted in higher levels of enclosed solid grains per phase blob for high S_w, and for low S_w the relationship inverted during drainage. As for imbibition, the wetting phase tended to enclose a higher number of solid grains, which resulted in a higher number of enclosed solid grains per phase blob for more homogeneous structures. For both drainage and imbibition, the interface length was higher for the inhomogeneous porous medium because of the higher degree of distortion of the corresponding blob geometries and flow channelisation.

Chapter 5

Steady-state study

This chapter provides a detailed analysis of immiscible two-phase flow under steady-state conditions. Starts from the porous medium generation and morphology (different porous medium compare to chapter four), follows by the results and discussions of both drainage and imbibition process, which include relative permeability, capillary pressure, Euler characteristic, interface length, and average pore size of each phase.

5.1 Artificial porous medium

The artificial pore structures generated for this chapter are different from the porous media shown in Chapter 4, with the same porosity, contour length and the Euler characteristic. In this study, seven artificial structures are generated with properties shown in Table 5.1. Two structures can be seen in Fig. 5.1 as examples.

In Figure 5.2 distributions of the pore body and pore throat size as variations in the lattice unit for the seven considered structures are shown together with the cumulative distributions. The displayed distributions are very similar to the corresponding plots shown in Section 4.1. Given the random process used to generate the porous structures each time a new structure is created, even for exactly the same Euler characteristic value, local, micro-level variations will occur. However, the similarity of Figure 5.2 with the corresponding distributions in Section 4.1 indicates the reproducibility of macro-level pore body and throat distributions, as characterised by the Euler characteristic.

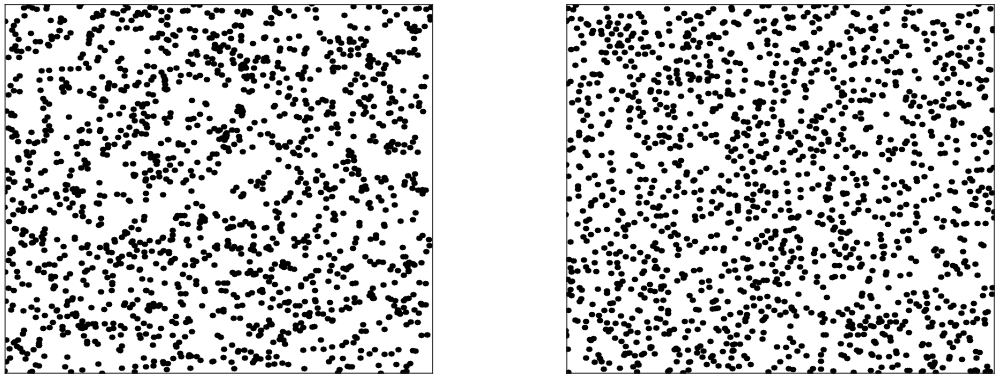

(a) (b)

Figure 5.1: Grain and pore space configurations of the artificially generated porous medium for in (a) structure 1, $\chi_0 = -680$ and in (b) structure 7, $\chi_0 = -930$.

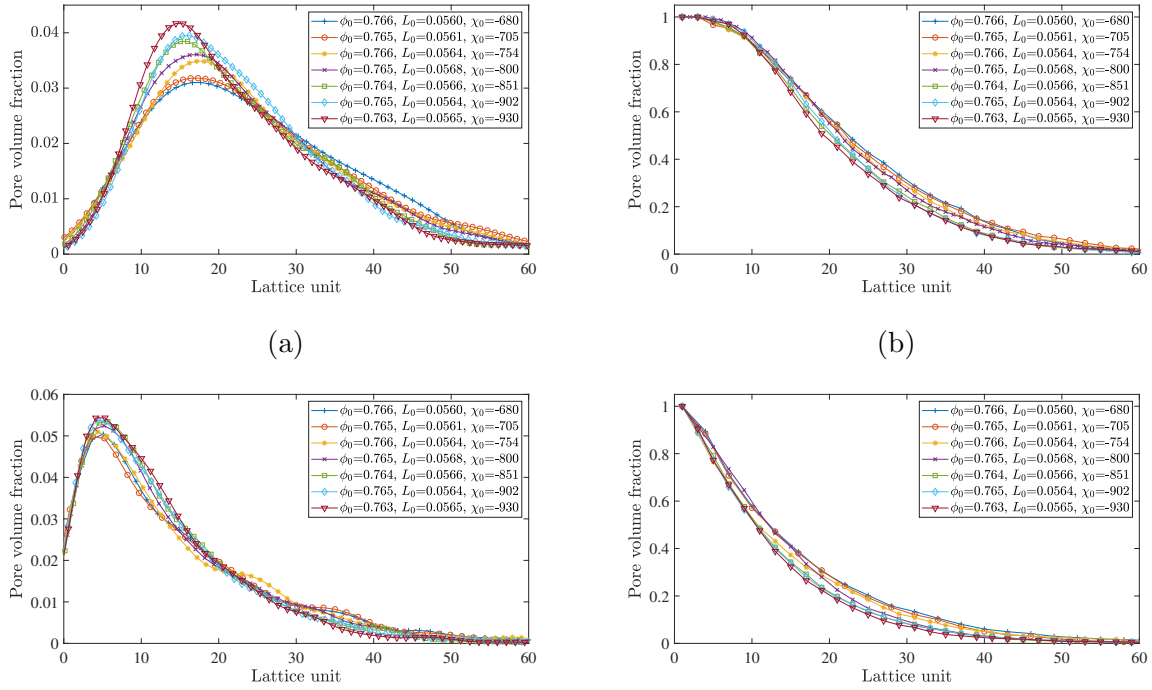

(a) (b)

(c) (d)

Figure 5.2: Pore size and pore throat distributions for the porous medium structures 1-7; (a) pore size distribution, (b) cumulative distribution of pore sizes, (c) pore throat distribution and (d) cumulative distribution of pore throats.

Table 5.1: The values of the effective Minkowski functionals (ϕ_0, L_0, $\bar{\chi}_0$), the average pore coordination number of the porous medium C_p, the hydraulic tortuosity T, the average pore size $\bar{d_P}$, and the average pore throat $\bar{d_T}$ for the seven artificial structures.

Structure	ϕ_0	L_0	$\bar{\chi}_0$ (χ_0)	C_p	T	$\bar{d_P}$	$\bar{d_T}$
1	0.766	0.0560	-0.00106 (-680)	3.425	1.208	24.76	12.59
2	0.765	0.0561	-0.00110 (-705)	3.449	1.218	24.88	12.57
3	0.766	0.0564	-0.00118 (-754)	3.482	1.211	24.24	12.34
4	0.765	0.0568	-0.00125 (-800)	3.513	1.234	23.70	12.27
5	0.764	0.0566	-0.00133 (-851)	3.475	1.195	23.50	11.92
6	0.765	0.0564	-0.00141 (-902)	3.473	1.201	22.64	11.81
7	0.763	0.0565	-0.00145 (-930)	3.466	1.212	22.22	11.65

5.2 Drainage and imbibition

Fig. 5.3 shows examples of the steady-state for structure 4 during drainage and imbibition at low ($S_w = 0.15$), medium ($S_w = 0.55$) and high ($S_w = 0.85$) wetting phase saturation (S_w) values. At $S_w = 0.15$, the non-wetting phase forms a fully connected path with the wetting phase only being present in isolated clusters. As the wetting phase saturation increases and transitions to a connected flow regime, the non-wetting phase becomes gradually disconnected, forming partially connected flow paths throughout the porous medium. Finally, at high S_w, the non-wetting phase exists in the form of disconnected ganglia whilst the wetting phase has formed a fully connected phase. By comparing intermediate saturation levels (for example, Figs. 5.3b and 5.3e), the steady-state immiscible displacement patterns between the two processes are significantly different. During imbibition (Fig. 5.3b), the non-wetting phase forms large connected fluid clusters in the domain with the non-wetting phase transported as distinct isolated loosely interconnected fluid streams. Instead, during the drainage process (Fig. 5.3e), the non-wetting phase flow highly bifurcates into secondary streams that tend to reconnect towards the outlet of the porous domain. Although the effect of the porous structure topology in the fluid invasion patterns is not studied in this chapter, its overall effect on the steady-state phase distribution results would appear to lead to interesting observations related to the hydrodynamic behaviour and fluid phase topology.

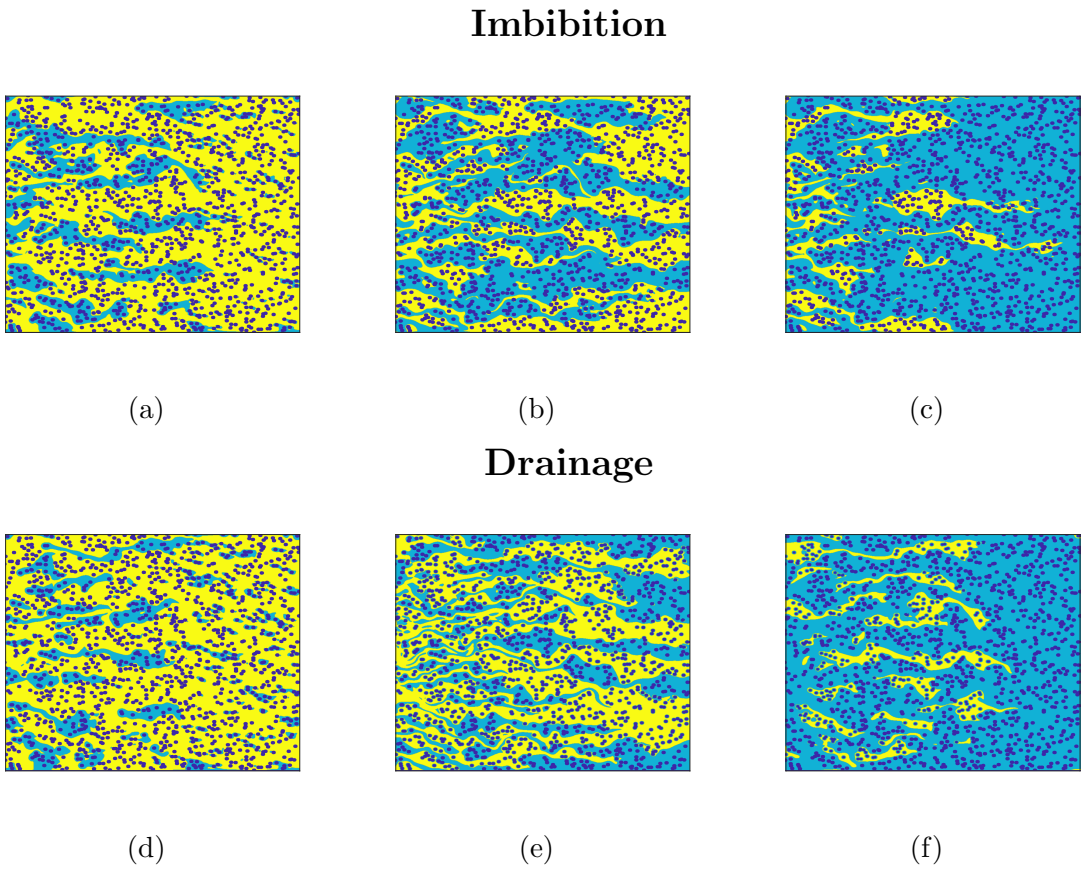

Figure 5.3: Predicted steady-state two-phase flow distribution patterns for imbibition on the top and drainage on the bottom for structure 4 and with $S_w = 0.15$ in (a) and (d), $S_w = 0.55$ in (b) and (e), and $S_w = 0.85$ in (c) and (f). The wetting phase is shown in blue, the non-wetting phase in yellow, and the solid phase in black.

Figs. 5.4 shows the relationship between relative permeability and S_w for drainage and imbibition, for 7 structures. The relative permeability of the κ^{th} phase is determined by the relation

$$k_{r,\kappa} = \frac{1}{N_{tot}} \frac{u_{x,\kappa} \nu_\kappa}{G\, k_\infty}, \tag{5.1}$$

where k_∞ is the absolute (or intrinsic) permeability of the porous medium, N_{tot} is the size (area) of the conducting phase (as determined by the LBM by summing the void space, that is, $N_w + N_{nw} + N_i$) and ν_κ and $u_{x,\kappa}$ represent the respective kinematic viscosity and x-direction component of the superficial velocity in the κ^{th} phase. The appropriate values for k_∞ were determined for oil and water independently and for each of the seven structures, by conducting appropriate single-phase simulations. Thus clearly k_∞ and $k_{r,\kappa}$ are all solid structure, phase and driving force dependent. The curves corresponding to the two

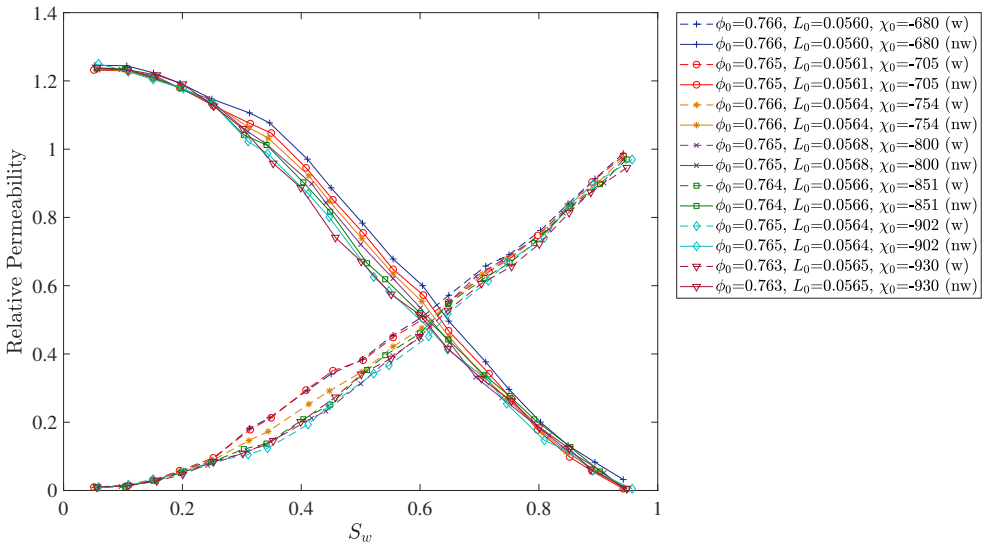

(a)

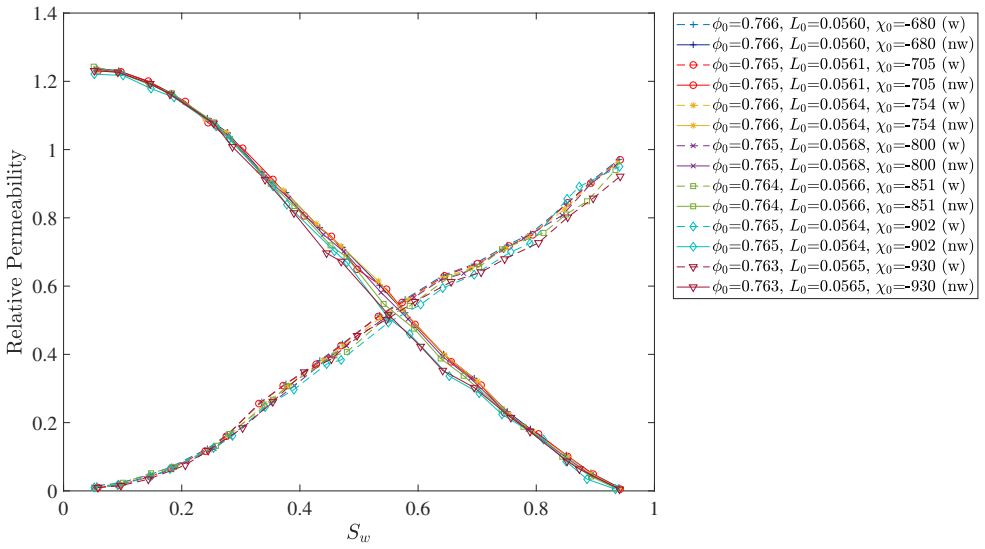

(b)

Figure 5.4: Variation of the steady-state relative permeability of the wetting phase (dashed lines) and the non-wetting phase (solid lines) with wetting phase saturation during (a) drainage and (b) imbibition.

processes appear to follow a similar pattern, but noticeable differences still exist in terms of the corresponding relative permeability magnitudes, at a given saturation. The relative permeability of wetting phase $k_{r,w}$ increases as S_w increases. The maximum value for both drainage and imbibition is around 1. The relative permeability of non-wetting phase $k_{r,nw}$ decrease as S_w increase from over 1.2 for both drainage and imbibition. The differences between the two processes are less noticeable at the extremes of the saturation range, i.e., $S_w < 0.25$ and $S_w > 0.75$. Because the contact angle has been set to 135^o, i.e., over 90^o, one would expect a negative normalized capillary height, indicating that an overpressure would be required to force the oil phase (i.e., non-wetting phase) into the pores. This could be the primary reason for the similar patterns observed from drainage and imbibition, which not only depend on the immiscible fluid system but also on the structures and the applied driving force. During drainage (Fig. 5.4a), it is evident that the pore space topology can have a noticeable and significant impact on both the wetting and non-wetting phase relative permeability values in the range $S_w = 0.25 - 0.75$. Conversely, it appears that the imbibition process is markedly less sensitive to the pore space connectivity as only minor differences are observed between the different structures, although any observed difference remains almost constant, for $S_w > 0.3$, for the wetting phase. It is also noticeable that for low $S_w \lessapprox 0.3$ the non-wetting phase relative permeability exceeds unity in both processes. This phenomenon becomes more intense in the pendular saturation region and is attributed to the "lubrication effect"; a result of the viscous coupling between the two-phases when the non-wetting to wetting phase viscosity ratio is greater than unity (Yiotis et al., 2007; Zhang et al., 2016). In general, both $k_{r,w}$ and $k_{r,nw}$ decrease with the reduction of the pore space χ_0 (i.e., a more negative Euler characteristic) at a given saturation. This can be attributed to the fact that more negative values of χ_0 correspond to a higher degree of uniformity of the grain distribution within the domain, which in turn leads to smaller average pore body and pore throat sizes. In contrast, it is observed that during a drainage process, structures with less negative values of χ_0 can more easily transmit the fluids, as the more intense solid phase clustering creates wider pathways for the different phases to move. However, this general observation does not entirely hold for the respective limits in the saturation range, that is, for $S_w < 0.25$ and $S_w > 0.75$, as all structures (with the possible exception of the wetting phase in the upper limit, where some minor differences are seen) seem to collapse to a single curve. This could be an indication that the pore space topology at the macroscale does not affect flow regimes dominated by pore-scale dynamics

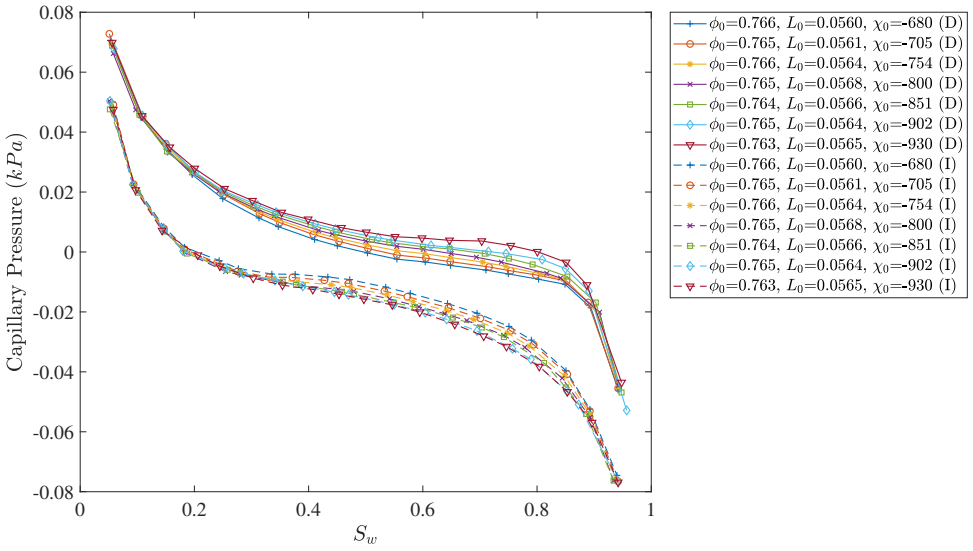

Figure 5.5: Steady state variation of the capillary pressure with wetting phase saturation during drainage (solid lines) and imbibition (dashed lines).

and is something that requires further systematic investigation.

The capillary pressure hysteresis curves are shown in Fig. 5.5. Pore space topology is seen to have a noticeable effect on both the drainage and imbibition processes, though in different directions. capillary pressure decrease as S_w increase for both process. During drainage, the capillary pressure curves become significantly distinct between $0.2 \lessapprox S_w \lessapprox 0.9$ with a more negative value of χ_0 resulting in a larger capillary pressure due to the higher homogeneity of the solid grain distribution and consequently smaller average pore throat size. Although the imbibition process is less affected by the variation of the pore space topology, a more negative χ_0 causes the reverse effect, that is, it decreases the capillary pressure for the same values of saturation. Hence it is reasonable to conclude that a higher uniformity of the solid grain distribution in the porous structure results in a lower average interfacial curvature as the affinity of the wetting phase to the closely spaced solid surfaces dampens the evolution of more highly curved interfaces. This observation is also in line with the previously described flow patterns shown in Figs. 5.3b and 5.3e.

In Figs. 5.6a and 5.6b the variation of the total length of the interface I_c between the wetting and non-wetting phases with S_w is shown as an non-dimensional quantity ζ, for the seven artificial porous structures. Since in two dimensions, the fluid-fluid interface

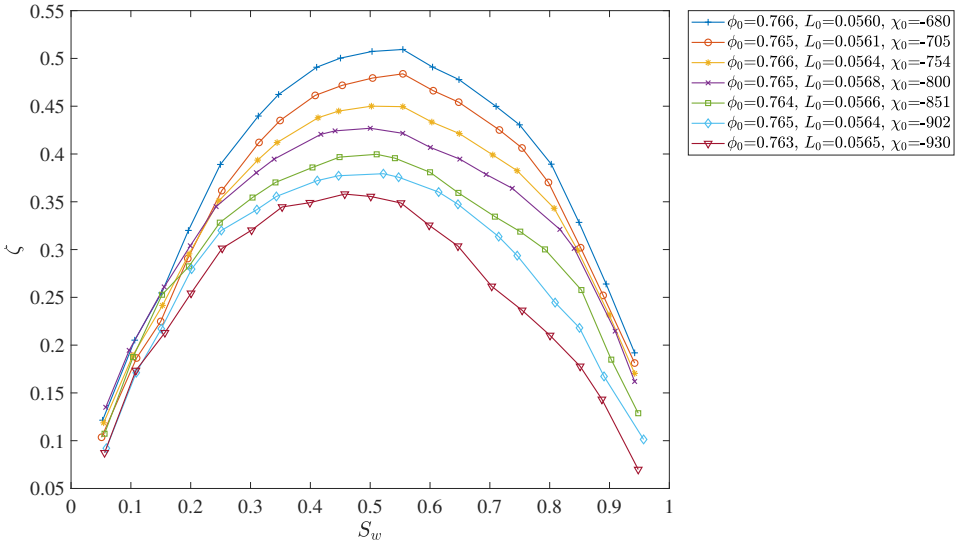

(a)

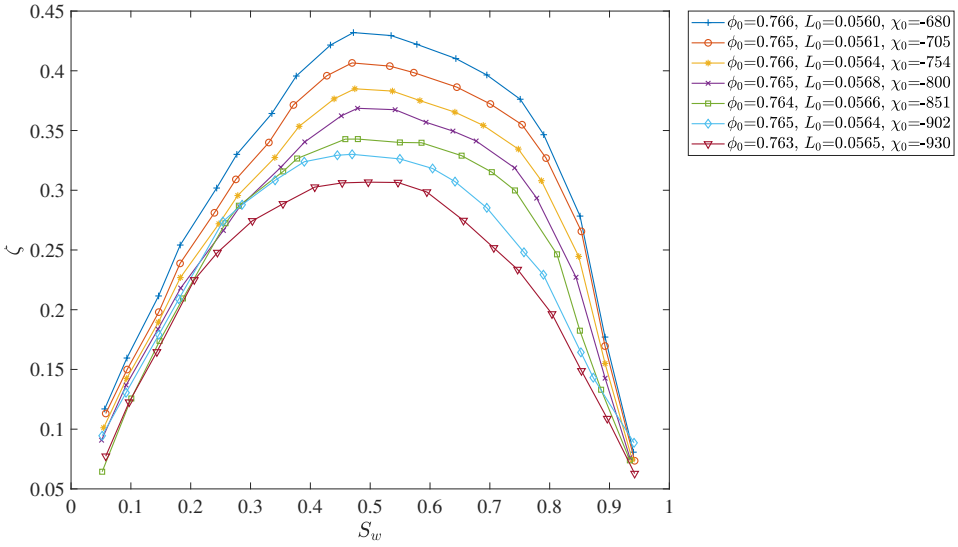

(b)

Figure 5.6: Variation at steady-state of the fluid-fluid interface length (as represented by the non-dimensional variable ζ) with wetting phase saturation during (a) drainage and in (b) imbibition.

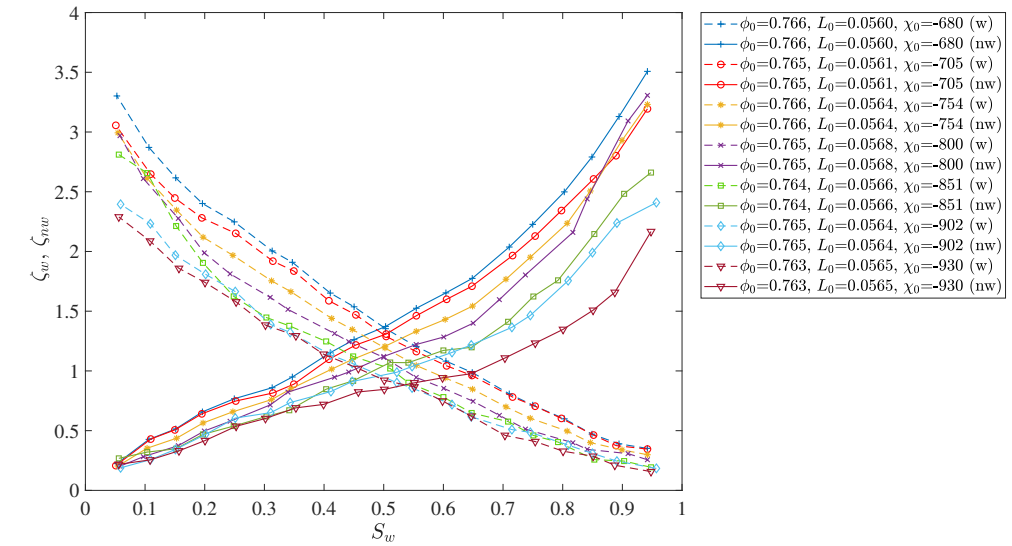

(a)

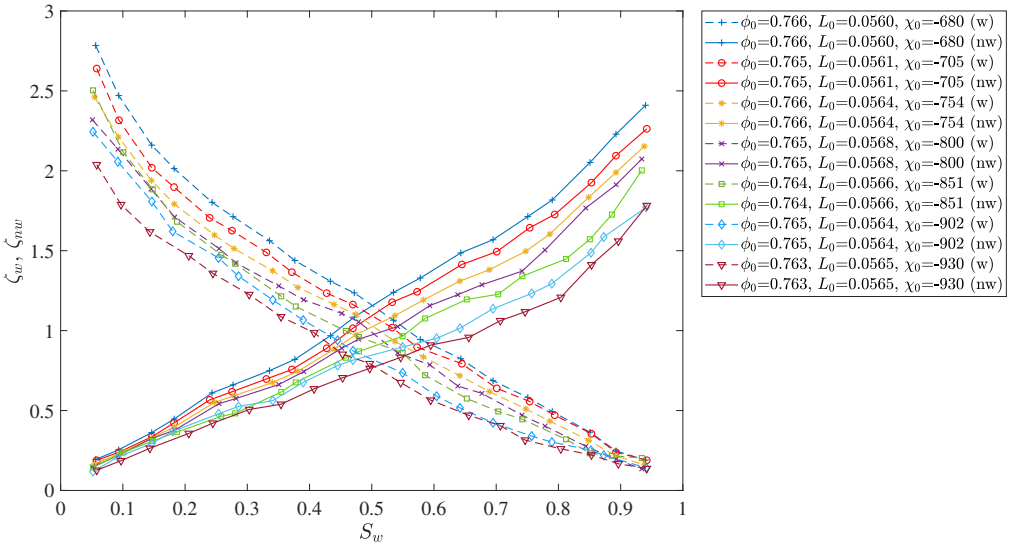

(b)

Figure 5.7: Variation at steady-state of ζ_w (solid lines) and ζ_{nw} (dashed lines) with wetting phase saturation during (a) drainage and (b) imbibition.

will either be one continuous curve or a set of curves, then in order to generate an appropriate non-dimensional quantity, the curves are defined as $\zeta = I_c\overline{d}_T/l^2$, where I_c is the (summed) total length of the interface curves, $\overline{d}_T$ is the average pore throat and l^2 is the area of the computational domain. For a given value of Euler characteristic, the general curve shape is similar in both the drainage and imbibition cases with ζ rising to a maximum as S_w increases before decreasing again in an approximately parabolic profile with small fluctuations. During drainage, as the pore space χ_0 increases, the interfacial length between the two-phase seems to increase significantly over most of the saturation range ($S_w \gtrapprox 0.2$) and the parabolic-like profile becomes increasingly asymmetric. Conversely, decreasing the pore space χ_0 further the interfacial length causes the parabolic-like profile to tend towards a high degree of symmetry over the entire range of the wetting phase saturation. The imbibition process generally follows a similar trend except at higher levels of the wetting phase saturation where the interfacial length is predicted to progressively collapse back to a single value, irrespective of the pore space χ_0 value. ζ decrease as χ_0 become more negative. Figs. 5.7a and 5.7b provide further evidence to support this observation that decreasing the pore space χ_0 further decreases the interfacial length. Fig.5.7 plot $\zeta_w = I_l\overline{d}_T/l_w^2$ and $\zeta_{nw} = I_l\overline{d}_T/l_{nw}^2$, respectively, against S_w, where the $\zeta_w\, v\, S_w$ curves are represented by dotted lines while the $\zeta_{nw}\, v\, S_w$ curves are represented by solid lines. This is a different way to analyse the interface length. The quantities l_w^2, l_{nw}^2 denote the respective wetting and non-wetting phase areas. For both drainage and imbibition, ζ_{nw} increase as S_w increase, and ζ_w decrease as S_w increase. At the same S_w value, both ζ_w and ζ_{nw} decrease as χ_0 gets more negative the same as ζ. However, at low saturations of the respective phases, the corresponding interfacial lengths, as characterised by either ζ_w or ζ_{nw}, converge to the same respective values, implying that in this limit the fluid-fluid interface length becomes increasingly less affected by the topology of the pore space. This is observed for both displacement processes although the convergence appears slower for the non-wetting phase in the case of drainage.

Based on the above general observations, it can be concluded that higher levels of solid grain clustering, i.e. a less negative porous medium χ_0, leads to a higher geometrical irregularity of the interface for a given S_w than that corresponding to lower levels of grain clustering, i.e. a lower porous medium χ_0.

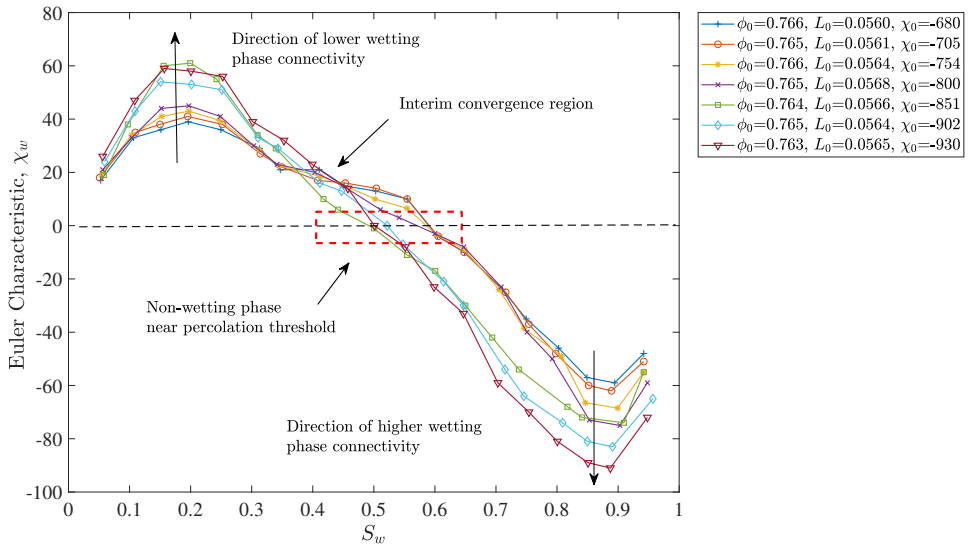

(a)

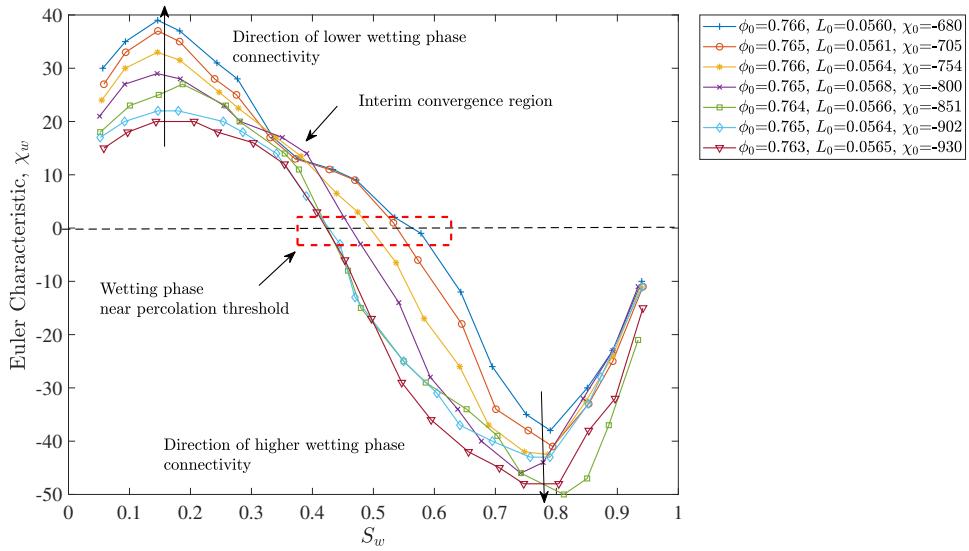

(b)

Figure 5.8: Variation at steady-state of the Euler characteristic of the wetting phase with wetting phase saturation during (a) drainage and (b) imbibition.

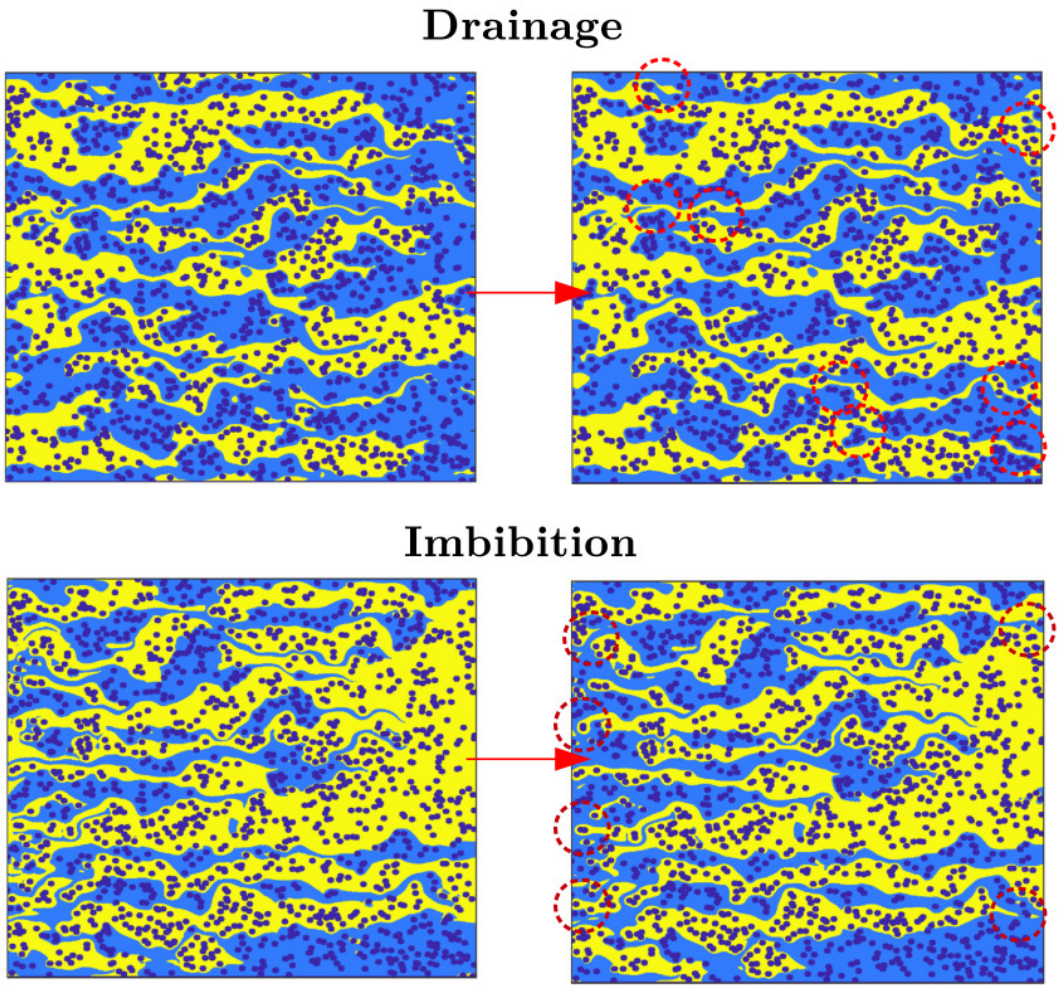

Figure 5.9: Major points of large cluster formation of non-wetting (upper - yellow colour) and wetting (lower - blue colour) phase clusters during the transient through $\chi_w = 0$, for structure 6.

Fig. 5.8 shows the evolution of the wetting phase Euler characteristic, χ_w, throughout its saturation range. For clarity, χ_w is plotted in its absolute form as opposed to the normalised form, χ_w/l^2, in order to provide a physical sense of the magnitude of the fluid phase topological variations in terms of the absolute number of the disconnected wetting phase blobs, at different saturation levels. The trends of both drainage and imbibition are similar. The χ_w first increase as S_w increase to the maximum point around $S_w = 0.2$, and then decrease across 0 points to the minimum value around $S_w = 0.8$, and increase again. Interestingly, and perhaps against typical expectation considering the observations of Figs. 5.6 and 5.7, decreasing the pore space χ_0 results in lower levels of wetting ($S_w \lessapprox 0.3$) and non-wetting phase ($S_w \gtrapprox 0.7$) connectivity at the corresponding ends of the saturation spectrum during drainage (Fig. 5.8a). One would expect that lower connectivity levels of the two-phase, which physically result in a greater number of isolated blobs in the domain would correspond to a greater total interfacial contact line, something that is not supported by the trends shown in Figs 5.6 and 5.7 (i.e. the lowest interfacial length occurs at the most negative χ_0 or $\bar{\chi_0}$). During drainage, a more homogeneous porous medium will tend to reduce the interfacial contact line between the two immiscible fluids. However, the fluid phase topology differs during imbibition, where a decreased pore space χ_0 results in higher wetting phase connectivity throughout the saturation spectrum. As was previously explained for the observed trends in the capillary pressure hysteresis curve (Fig. 5.5), this can be attributed to a more uniform wetting phase transmission pattern that retains its higher connectivity due to the increased affinity to a more uniformly, closely spaced solid phase in the porous structure. Consequently, at high wetting phase saturation levels, i.e., the ganglion dynamics regime, a decreased pore space χ_0, results in a highly connected wetting phase and subsequently a highly fragmented/disconnected non-wetting phase in the porous medium. It is worth noting that the two processes display two specific χ_w convergence points which are respectively at $S_w \approx 0.03$ and 0.46 for drainage and at $S_w \approx 0.35$ and 0.95 for imbibition. In the region of $S_w \approx 0.03$ for drainage and $S_w \approx 0.95$ for imbibition, it is not surprising that the non-wetting and wetting phases will respectively converge towards a unique topological state as they are about to fully saturate the porous medium.

The intermediate convergence points at $S_w \approx 0.46$ for drainage and $S_w \approx 0.35$ for imbibition are of more significant interest. By closely investigating the contour plots in the

proximity of these saturation values, it is observed that during drainage the interval around the convergence point corresponds to the saturation degree that the wetting phase almost becomes disconnected in the domain as the non-wetting phase saturation increases. In a similar fashion, during imbibition, the saturation levels close to the convergence point correspond to the instant that the first fully connected wetting phase path appears in the porous structure along the flow direction. Based on the above observations, it is reasonable to conclude that the initial formation of wetting phase connected pathways along the flow direction are not significantly dependent on the pore space topology but perhaps more strongly depends on fluid and hydrodynamic parameters, such as wetting conditions and saturation rate. However, a more systematic and general study would be required in the future to ensure that the grain size and shape are taken into account and that the rest of the morphological, fluid and hydrodynamic parameters are carefully monitored and precisely controlled. For example, structure 5 presents a small deviation from this general behaviour which could also be attributed to its lowest value of hydraulic tortuosity (i.e. in fully saturated single phase flow) among all structures. This deviation could also be linked to the diverging value of the resulting coordination number. The C_p value of structure 5 is almost identical to that for structure 6, indicating that the resulting grain configuration for this specific Euler characteristic has impacted the overall observed trend. It is inevitable that morphologically identical porous mediums will still present variations in their statistical, topological, geometrical and hydrodynamic parameters, such as mean pore body and throat sizes, mean coordination number, hydraulic tortuosity, etc. However, based on the randomized porous medium generation procedure and the overall consistency of the observations, the overall trends and underlying fluid transmission processes are still representative.

From a percolation theory point of view, a phase Euler characteristic of zero corresponds to a system operating near the percolation threshold. This is indicated in Figs. 5.8a and 5.8b with a dashed line across the plots at that level. Both plots in Fig. 5.8 show the effect of the pore space χ_0 on the transition from a positive wetting phase Euler characteristic to a negative one crossing through the zero point. Although the wetting phase first becomes connected or disconnected along the flow direction at lower saturation levels, a near-zero phase χ_w signifies the initiation of large fully connected clusters of the non-wetting and wetting phases that span the entirety of the domain (see Fig. 5.9 for an example in structure

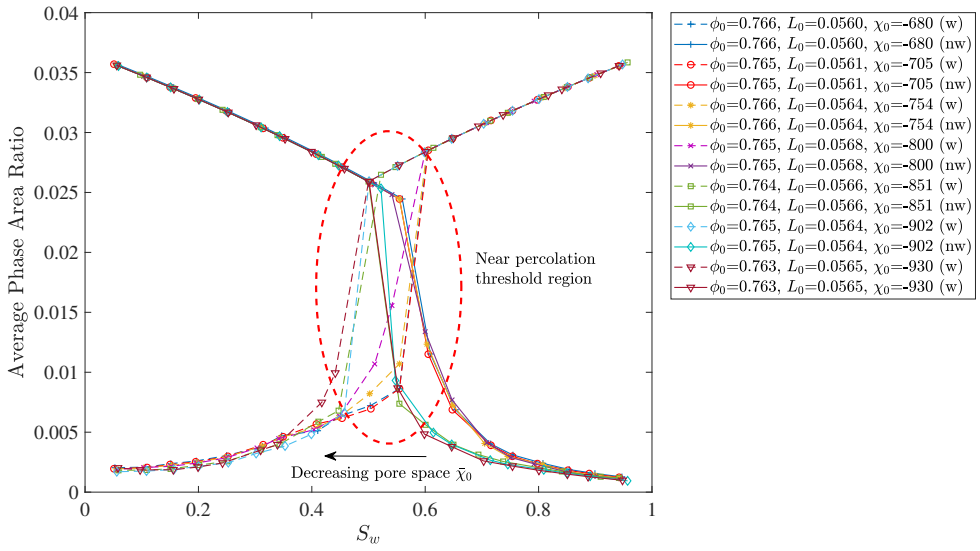

(a)

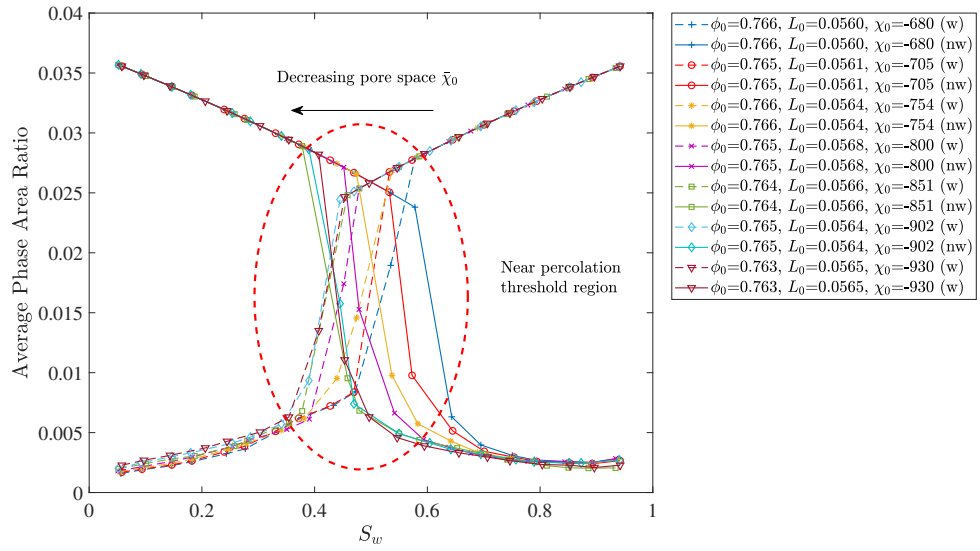

(b)

Figure 5.10: Variation at steady-state of the average pore size of the wetting phase (dotted lines) and the non-wetting phase (solid lines) against the wetting phase saturation during (a) drainage and (b) imbibition.

6). Fig. 5.10 shows the average size of the wetting and non-wetting phase clusters in the domain at different saturation levels for both drainage and imbibition. It can be clearly seen that as the value of the phase Euler characteristic χ_w passes through zero, distinct jumps in the average phase cluster sizes can be observed, in turn indicating a high degree of non-wetting and wetting phase connectivity in the computational domain. For both drainage and imbibition, the curves of the wetting and non-wetting phase both shift to the left as χ_0 decrease. It is evident from both Figs. 5.8 and 5.10 that as pore space χ_0 gets more negative, a lower saturation level at which this transition occurs for both processes. The direction of the black arrow on Figs. 5.10a and 5.10b indicate the resulting shift in the pore space connectivity level that corresponds to the transition through $\chi_w = 0$. Effectively, higher uniformity in the solid grain distribution in the porous structure seems to enhance the fluid phase connectivity for both drainage and imbibition. Additionally, outside this transient zone, the average phase cluster size follows an exponential growth behaviour for both processes and for all structures. The pore space χ_0 has a more obvious impact on the non-wetting phase clustering in this region, whereas the wetting phase remains largely unaffected. Following the jump, through the percolation threshold region, the cluster size growth becomes linear and independent of the displacement process and pore space χ_0.

5.3 Summary

To sum up, the steady-state study where the same body force G was applied to seven porous mediums with different χ_0. The flow properties such as relative permeability, capillary pressure, Euler characteristic, interface length, and average pore size at different saturation rates for drainage and imbibition were plotted and analyzed. It was shown that a more homogeneity pore structure, generally enhanced the relative permeability of the porous structure for $S_w = 0.25 - 0.75$, whereas outside this range the relative permeability progressively collapsed to a single curve during drainage. Also, the effect of pore space connectivity was more obvious for drainage than imbibition. The 'lubrication effect' due to a non-wetting/wetting phase viscosity ratio greater than unity was effectively captured in the pendular saturation region. The change in χ_0 was observed to affect both the drainage and imbibition capillary pressure curves, though in opposite ways. This could be attributed to a lower average interfacial curvature as a consequence of the affinity of the wetting phase to the closely spaced solid surfaces. The interface length was found to significantly increase

for both processes with an asymmetrical profile with respect to the S_w, for inhomogeneous structures. Additionally, the interface length was found to converge to the same value at low and high S_w, for drainage and imbibition respectively. It was concluded that at a given saturation rate, higher levels of grain clustering (i.e., higher χ_0) in the porous domain led to a greater geometrical irregularity of the interface between fluid phases. As for the topological state of the two-phase, during drainage, a decreasing χ_0 was found to result in lower levels of wetting and non-wetting phase connectivity at the corresponding ends of the saturation spectrum. A different behaviour was observed during imbibition where at low wetting phase saturation, more negative χ_0 resulted in higher wetting phase connectivity. χ_w was also found to pass through the zero point. At those levels, the average phase area was found to jump in an almost discontinuous way to higher magnitudes indicating the formation of large phase clusters that spanned the entire domain.

Chapter 6

Low driving forces study

This chapter presents a detailed analysis of immiscible two-phase flow at low driving forces. Including the results and discussions of both the drainage and imbibition process (the artificial porous medium and model set-up are the same as Chapter 4), which covers relative permeability, capillary number, Euler characteristic, and interface length.

6.1 Drainage

The aim of this study is to conduct a systematic determination of the impact of varying an externally applied driving pressure coupled with the impact of the pore space connectivity and topology on the transport of a two-phase displacement flow during drainage and imbibition. The focus of this study is characteristics with a series of plots showing the dependence of the relative permittivity, capillary pressure, the Euler characteristic and the interface length with the applied low driving force (per unit area) G and the structures Euler characteristic χ_0. Nearly all the presented curves have nonlinear, inflectional profiles. A further aim of the study is to elucidate what physical effects cause the observed nonlinearity and when/where the respective inflexion points occur. First, though, in Fig. 6.1 a sample of the predicted steady-state two-phase flow volume fraction contour plots of drainage process for structure 4 ($\chi_0 = -800$) at wetting phase saturation $S_w = 0.7$ and different values of the driving pressure G are displayed.

The four plots (Figs. 6.1a-6.1d) correspond to drainage where displacement of the existing wetting phase by the injected non-wetting phase is shown. To understand these plots, it

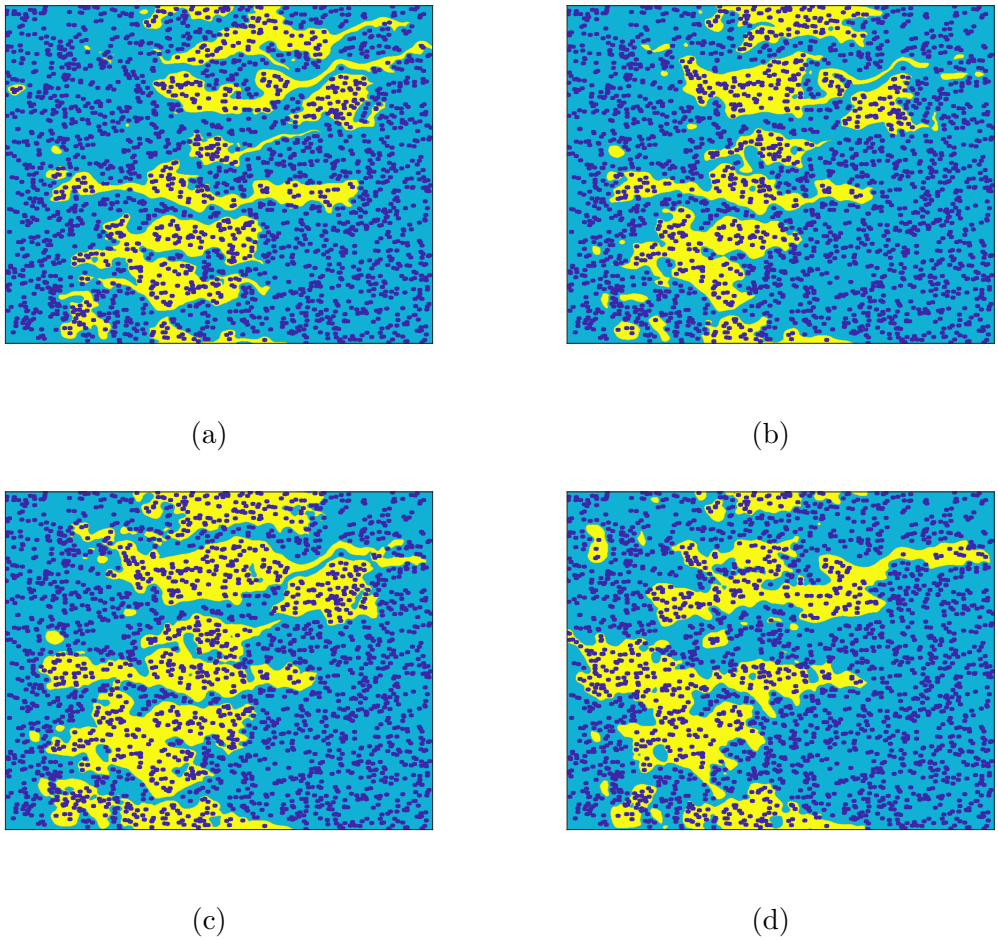

(a) (b)

(c) (d)

Figure 6.1: Predicted steady-state two-phase flow distribution patterns for drainage for structure 4 ($\chi_0 = 800$) at $S_w = 0.7$ and with a different driving force, $G = 5 \times 10^{-6}$ in (a), $G = 2 \times 10^{-6}$ in (b), $G = 1 \times 10^{-6}$ in (c), and $G = 5 \times 10^{-7}$ in (d). The wetting phase is shown in blue, the non-wetting phase in yellow, and the solid phase in black.

was noted that the wetting phases' affinity for the solid lattice of the pore structure whilst the non-wetting phase has a stronger preference for the conducting phase void space. In general, the wetting phase (blue) remains fully connected in Figs. 6.1a-6.1d as G is reduced though isolated blobs are visible in all four figures. Conversely, in all plots, the non-wetting phase (yellow) remains disconnected, but as G reduces, larger non-wetting phase blobs are observed with the expansion due to spreading in the normal direction to the applied driving force (per unit area).

Fig. 6.2 shows the dependence of the relative permeability of both the wetting (dashed lines) and non-wetting phase (solid lines) with the magnitude of the driving force (per unit area) G, for the seven considered porous structures and the five steady-state wetting phase saturation values $S_w = 0.91, 0.7, 0.49, 0.32, 0.2$. The relative permeability of the κ^{th} phase is determined by the relation $k_{r,\kappa} = \frac{1}{N_{tot}} \frac{u_{x,\kappa}\nu_\kappa}{G\, k_\infty}$, where k_∞ is the absolute (or intrinsic) permeability of the porous medium, N_{tot} is the size (area) of the conducting phase (as determined by the LBM by summing the void space, that is, $N_w + N_{nw} + N_i$) and ν_κ and $u_{x,\kappa}$ represent the respective kinematic viscosity and x-direction component of the superficial velocity in the κ^{th} phase. Fig. 6.2 reveals a nonlinear dependence between $k_{r,\kappa}$ and G, with the degree of nonlinearity being dependent on S_w, the phase and the pore topology. In general, as G decreases initially so do $k_{r,\kappa}$, though with ever decreasing gradients. For S_w=0.91, the relative permeability of the wetting phase is much larger than the non-wetting phase, and no clear nonlinear relationship can be seen. Because the fluid flow is dominated by the wetting phase and the non-wetting phase corresponds to the ganglion dynamics regime and indicates that higher non-wetting phase fragmentation exists across the domain. As G decrease, a small reduction can be seen for $k_{r,nw}$. As S_w decease, shown in Fig. 6.2b-6.2c, the non-wetting phase changes from ganglia dynamic to connected, the relative permeability of the non-wetting phase become larger than the wetting phase for higher G and remain smaller for lower G, For S_w=0.32 and 0.2, the non-wetting phase become fully connected, and the relative permeability of the non-wetting phase is much larger than the wetting phase for all G. In addition, as S_w decease (show in Fig. 6.2b-6.2e), the nonlinear correlation between $k_{r,\kappa}$ and G gets clearer. Inflectional profiles occur around $G = 2 \times 10^{-6}$ of structures with less negative χ_0 ($\chi_0 >= -750$) are more obvious compare to structures with more negative χ_0 ($\chi_0 <= -800$). During drainage, the non-wetting phase tends to follow preferential flow paths as G decrease, however, for more homoge-

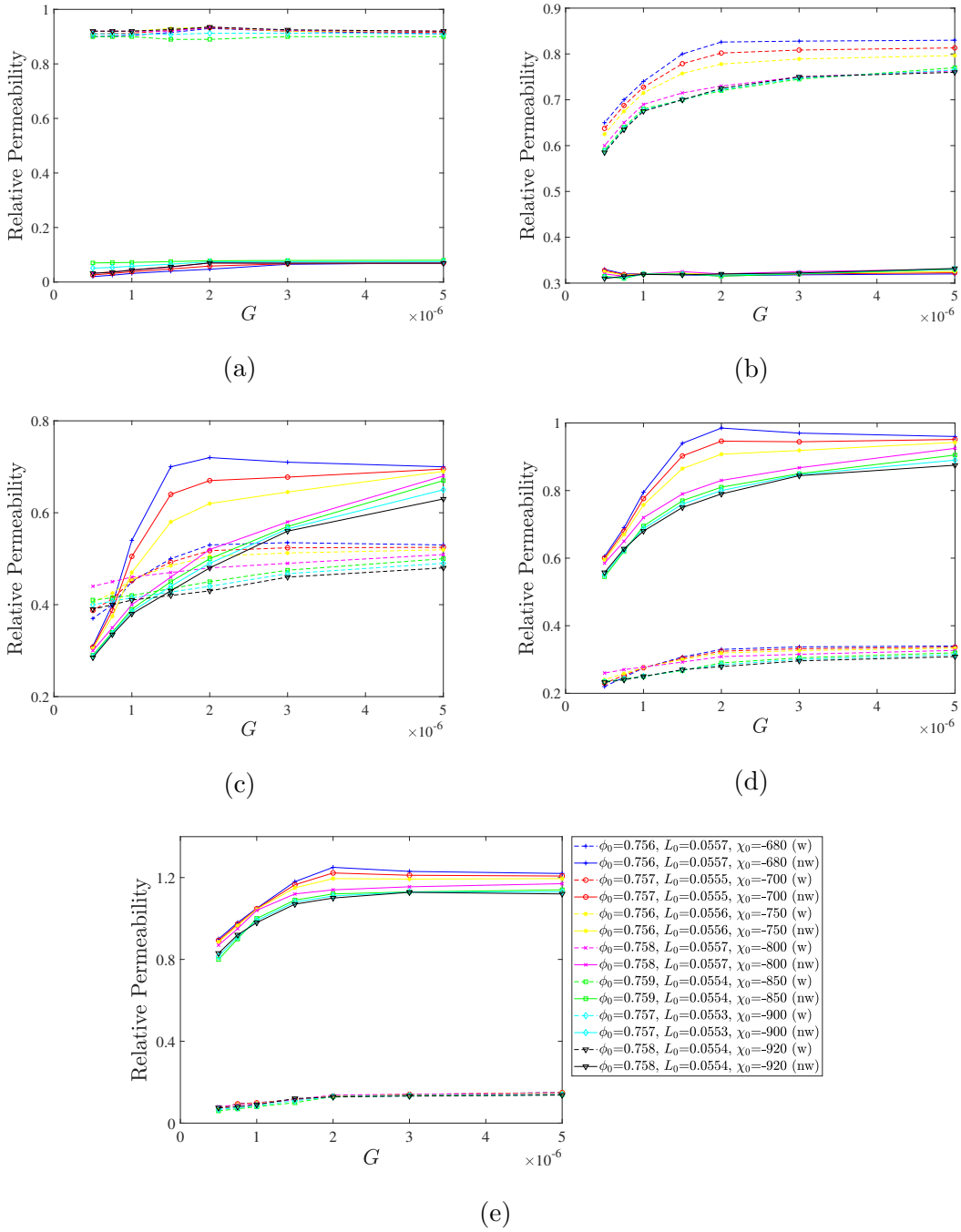

Figure 6.2: Variation of relative permeability of the wetting phase (dashed lines)and non-wetting phase (solid lines) with body force for the final constant values of in (a) S_w=0.91, in (b) S_w=0.7 in (c) S_w=0.49, in (d) S_w=0.32 in (e) S_w=0.2.

neous structures, the flow path spread more uniformly through the domain compared to inhomogeneous structures. Thus, the effect of G on homogeneous structures is less obvious. In addition, for most cases, structures with more negative χ_0 also result in lower $k_{r,\kappa}$. On account of the decreasing χ_0 having a negative effect on phase velocity, as χ_0 becomes more negative the superficial velocity of both phases decreases. Thus, structures with more negative χ_0 reach nonlinear regions at higher G compare to structures with less negative χ_0. In Chapter 5, for $G = 5 \times 10^{-6}$, it was shown that during drainage the topology of the pore space has a marked impact on $k_{r,w}$ and $k_{r,nw}$ in the range $0.25 \leq S_w \leq 0.75$ whilst outside this interval fewer differences are observed. Similar results can be seen in Fig. 6.2, the greatest spread between structures with different χ_0 occurring around $G = 2 \times 10^6$, and as G decrease the impact of pore space topology also decrease. For S_w=0.2, $k_{r,nw}$ during higher G exceeds unity due to viscous coupling, as G decrease, the $k_{r,nw}$ decrease below unity indicates that the "lubrication effect" does not occur at low driving forces.

Fig. 6.3 shows the log-log plot of the capillary number with G. The capillary number is defined as $Ca = \mu_{nw} u_{nw}/\sigma$, where μ_{nw} is the dynamic viscosity of non-wetting phase, u_{nw} is the average velocity of non-wetting phase in the x-direction, and σ is surface tension. The log-log plot is used here to emphasize the nonlinear relationship between Ca and G. For all structures, at all S_w, the Ca decrease as G decrease, due to the reduction of non-wetting phase velocity. Ca decrease as χ_0 become more negative. Similar to the effect of relative permeability, χ_0 has a negative effect on phase velocity. The nonlinear behaviours depend on χ_0 as well. For $S_w = 0.91$ and 0.7, the inflectional profiles appear as $G < 1 \times 10^{-6}$ for structures with less negative χ_0 and $G < 2 \times 10^{-6}$ for structures with more negative, shows in Fig.6.3a and 6.3b. However, in consideration of Ca the nonlinear behaviours of all structures appear as $Ca < 10^{-4}$. Because of the difference in χ_0, more homogeneous structures reach the low capillary region at higher G compared to inhomogeneous structures. As S_w decrease the nonlinear relationship becomes more clear for structures with more negative χ_0 and appear at higher Ca around 3×10^{-6}, which corresponds to the nonlinear relationship between $k_{r,nw}$ and G shows in Fig. 6.2c-6.2e. As discussed in Chapter 4, the non-wetting phase velocity strongly depends on S_w, as more non-wetting phase is injected into the pore structures, the superficial velocity increase as the non-wetting phase becomes more connected, and the low capillary region also changes. For the higher region of G, the Ca between each structure are quite small, but as G decrease and the nonlinear be-

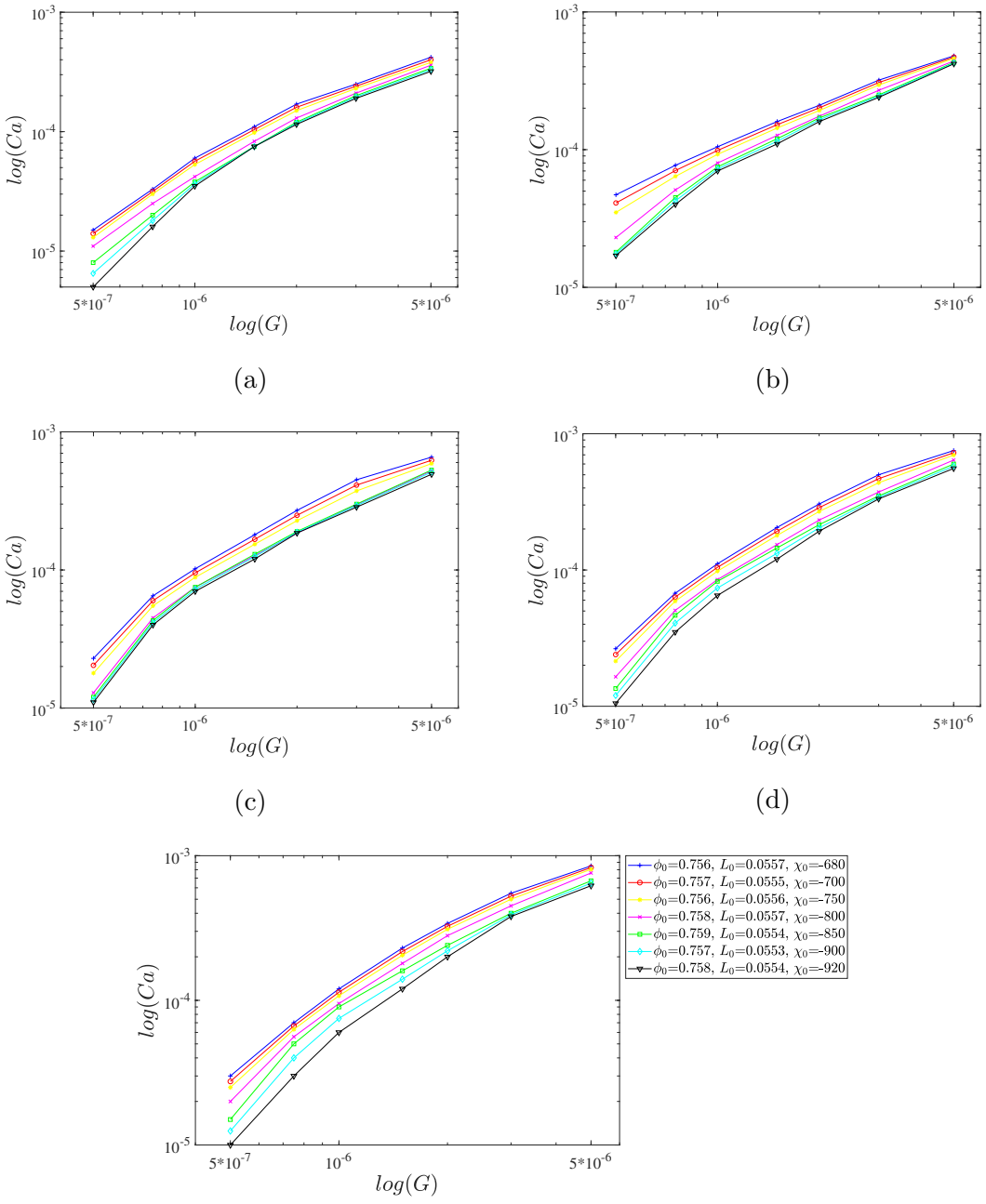

Figure 6.3: Variation of capillary number with body force for the final constant values of in (a) S_w=0.91, in (b) S_w=0.7 in (c) S_w=0.49, in (d) S_w=0.32 in (e) S_w=0.2.

haviour becomes more obvious, the difference becomes more visible for more homogeneous structures. Considering that more homogeneous structures also have smaller average pore throats shown in Table 5.1, which impact the capillary forces within the pore structures and shows more influence by G at low capillary number.

The dependence of the wetting phase Euler characteristic, χ_w, with G is shown in Fig. 6.4. For $S_w = 0.91, 0.7$, χ_w increases as G is decreased for all structures. However, how these increases are affected by the nature of the porous medium undergoes a transition in the range $2 \times 10^{-6} < G < 3 \times 10^{-6}$. For $G < 2 \times 10^{-6}$, as the grain distribution and pore space become more homogeneous, for a given value of G, χ_w becomes larger. For $G > 3 \times 10^{-6}$, there is some swapping in the relative value sizes. Between the different structures, convergence occurs in the curves in the interval $2 \times 10^{-6} < G < 3 \times 10^{-6}$, which corresponds to the inflectional profiles of both relative permeability and capillary number. At high S_w, the effect of G for more homogeneous is larger than for inhomogeneous structures. From percolation theory, a more negative χ_w indicates a higher degree of non-wetting phase fragmentation. The general increase of χ_w appears due to the non-wetting phase becoming more connected as G decrease, seen in Figs. 6.1, larger non-wetting phase blobs are observed at lower G. For $S_w = 0.91$ corresponds to the ganglion dynamics regime, structures with more negative χ_0 at low G shows lower non-wetting phase fragmentation. For $S_w = 0.7$, all χ_w increase from a negative value to around zero, indicating that the percolation threshold is reached at higher S_w at low driving force. For $S_w = 0.49$, χ_w increases from around zero to a positive value. The less spread of χ_w around 0 for $S_w = 0.7, 0.49$ is also evident that the changes in χ_0 are less influential close to the percolation threshold. For $S_w = 0.32, 0.2$ (Figs. 6.4d 6.4e), χ_w increases as G increases. Similar to higher S_w, the effect of G on more homogeneous structures is larger than on inhomogeneous structures. Beyond the percolation threshold, the non-wetting phase becomes fully connected and the decrease in χ_w is caused by the wetting phase becoming more connected as G decrease. In Fig. 6.4e, as χ_0 becomes more negative, χ_w increases for a given value of G. For inhomogeneous structures, the profiles are approximately linear but for homogeneous structures, the curves are more inflectional (nonlinear) in nature corresponding to the nonlinear profiles of both relative permeability and capillary number. In addition, as G gets smaller, the maximum and minimum value of χ_w also decreases. Meaning that higher connectivity levels of both the non-wetting phase at high S_w ($S_w = 0.91, 0.7$) and wetting phase at low

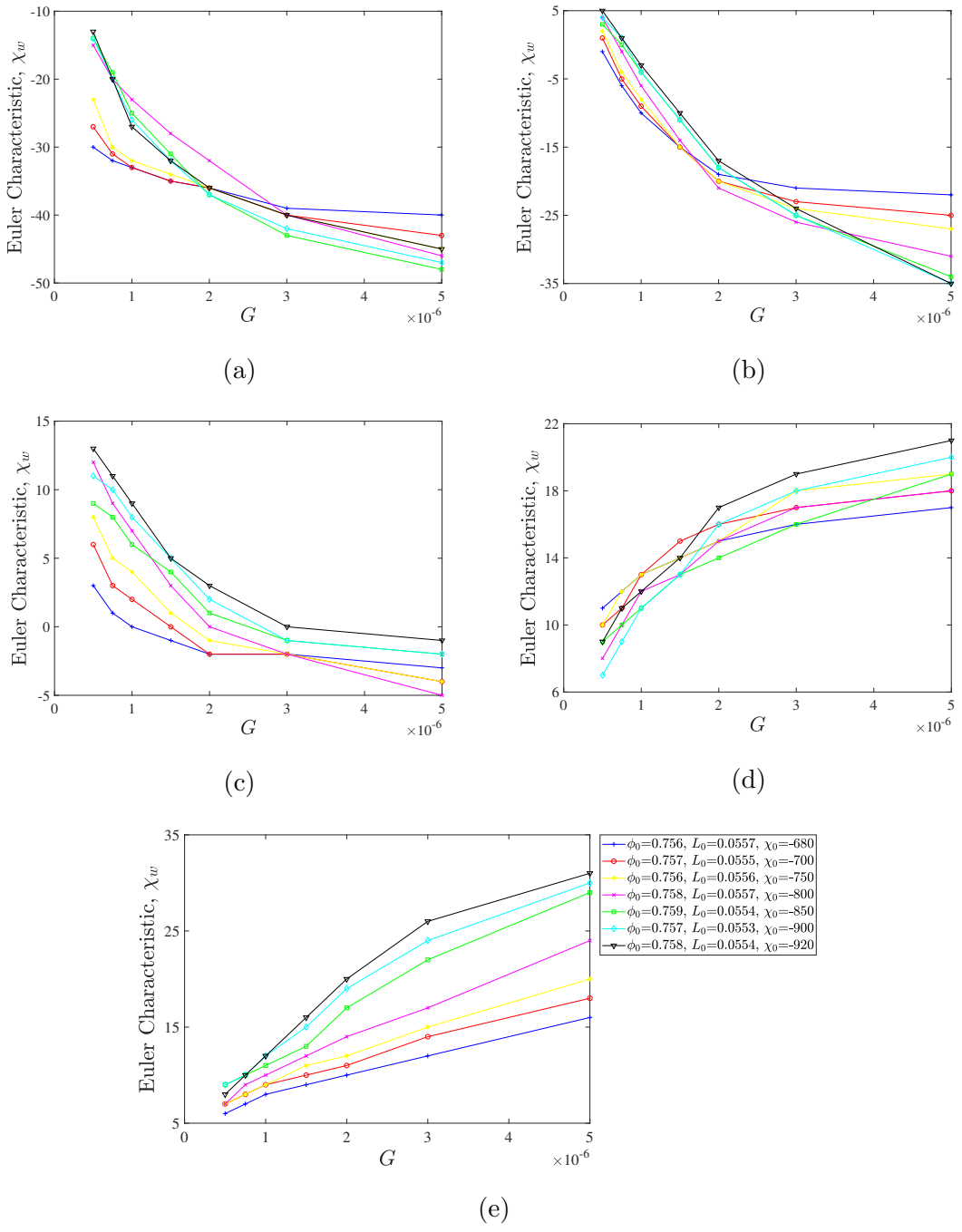

Figure 6.4: Variation of the Euler characteristic of the wetting phase χ_w with body force for the final constant values of in (a) S_w=0.91, in (b) S_w=0.7 in (c) S_w=0.49, in (d) S_w=0.32 in (e) S_w=0.2.

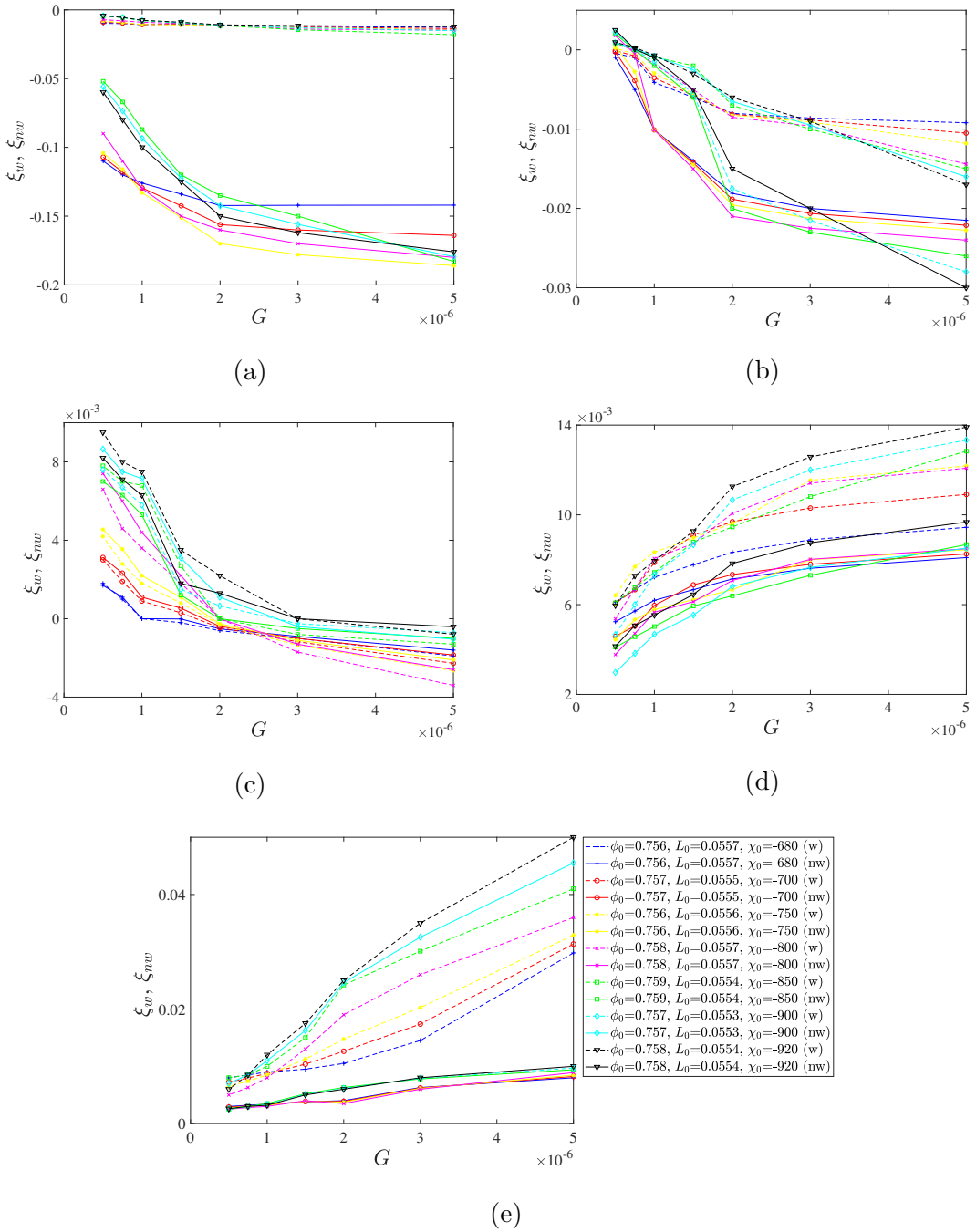

Figure 6.5: Variation of the Euler characteristic of the wetting and non-wetting phases per unit average grain, ξ_w and ξ_{nw} with body force for the final constant values of in (a) S_w=0.91, in (b) S_w=0.7 in (c) S_w=0.49, in (d) S_w=0.32 in (e) S_w=0.2.

S_w ($S_w = 0.32, 0.2$) are achieved, which result in less number of isolated blobs/droplets in the domain.

In Fig. 6.5, the dependence of the parameters ξ_w and ξ_{nw} with G are shown. For the κ^{th} phase, ξ_κ is defined as $\xi_\kappa = \chi_\kappa/\overline{N}_\kappa$, that is, the Euler characteristic of the κ-th phase per unit average grain surrounded by the κ^{th} phase. These parameters were also employed in the transient study shown in Chapter 4 where it was noted that they provide means of measuring the impact of the clustering of solid grains on the respective fluid phases ability to form blobs. In general, they provide a measure of the attraction of a given phase to the solid structure of a given porous medium during such events as coalescence or snap-off. An increase in ξ_κ would indicate, on average, that the κ^{th} phase surrounds a decreasing number of solid grains for a given pore space/solid structure network topology. For $S_w = 0.91, 0.7, 0.49$, ξ_w, ξ_{nw}, overall, increase while for the lower saturation values $S_w = 0.32, 0.2$ a reversal in behaviour is observed in that ξ_w, ξ_{nw} now decrease with decreasing G same as the χ_w plot shows in Fig. 6.4. The most variation is seen in the largest and smallest S_w values. In Fig. 6.5a, on the scale of the plot, the variations in ξ_w are much smaller than corresponding variations in ξ_{nw} due to the number of grains within the wetting phase is much higher than within non-wetting phase for all the considered structures. While all plots indicate an increase in the respective ξ_w, ξ_{nw} values as G decreases. The trend is similar to the observations made for Fig. 6.4a, the effect of the pore structure again transitions in the interval $2 \times 10^{-6} < G < 3 \times 10^{-6}$. For $S_w = 0.7$ (Fig. 6.5b) a number of curves in both ξ_w and ξ_{nw} display oscillations as they decrease around 0, near the non-wetting phase percolation threshold region. For $S_w = 0.49$ both ξ_w and ξ_{nw} increase from 0 as G decrease. Structures with more negative χ_0 result in a higher number of both ξ_w and ξ_{nw}. As the saturation levels become greater than the percolation threshold, at lower G, the non-wetting phase is largely fully connected resulting in a greater number of grains per phase blob. For the more homogeneous pore structures compare to the inhomogeneous pore structures, the wetting phase blobs would adhere to the solid grain clusters more intensively and result in a lower number of grains per blob. For $S_w = 0.32$ the wetting phase curves display more decrease than the corresponding non-wetting phase plots as G decrease. In Fig. 6.5e larger decreases are seen in ξ_w relative to ξ_{nw} with decreasing G, due to the saturation of non-wetting phase and the amount of grain within the non-wetting phase is much larger than the wetting phase. In the case of the wetting phase curves, the

inhomogeneous structures are concave upwards, as the χ_0 gets more negative the behaviour appears to be approximately linear. As ξ_w decrease, the difference between the wetting and non-wetting phase also decrease, indicating that the wetting phase blobs would adhere to the solid grain clusters more and more intensively as G decrease, resulting in a higher number of grain and lower ξ_w.

In Fig. 6.6 the dependence of the (total) interface length between the wetting and non-wetting phases, I_c, with G is shown in terms of the nondimensional variable ζ, where $\zeta = I_c\overline{d}_T/l^2$ and $\overline{d}_T$ denotes the average pore throat, while l^2 is the area of the computational region under consideration. For all S_w the ζ decrease as G decrease. Compare with Fig. 6.4, the decreasing G results in a lower absolute value of χ_w which represent a lower number of blobs/droplet and thus decreases the value of ζ. For all structures, nonlinear, inflectional curves are observed. In the case of $S_w = 0.91, 0.7, 0.49, 0, 32$, a number of curves display local oscillatory behaviour. The nonlinear region appear around $G = 2 \times 10^{-6}$ for structures with less negative χ_0. As χ_0 gets more negative, the inflexion point shifts right towards higher G. For structures with more negative χ_0 (χ_0=-900. -920), the profiles are almost linear for lower S_w (S_w=0.49, 0.32, 0.2), which is similar to the corresponds of $k_{r,\kappa}$, but different from χ_w. Indicate that, even though the effect of G on χ_w is larger for homogeneous structures compare to inhomogeneous structures, for interface length, the inhomogeneous structures remain larger at low capillary regions. For $S_w = 0.2$, the nonlinear region for inhomogeneous pore structures also increases to around $G = 3 \times 10^{-6}$, but the difference between structures becomes smaller the same as χ_w. For all plots, as χ_0 becomes less negative, the inflectional nature of the curves would appear to become more marked, implying that the degree of nonlinearity increases as the pore space/solid structure becomes progressively more inhomogeneous.

Another way of characterising I_c is shown in Fig. 6.7. Here plots of the nondimensional parameters $\zeta_{nw} = I_c\overline{d}_T/l_{nw}^2$ and $\zeta_w = I_c\overline{d}_T/l_w^2$ against G are displayed with l_κ^2 representing the area occupied by the κ^{th} fluid phase. Showed in Chapter 4, ζ_κ is a measure of interface length per unit wetting/non-wetting phase area. The same as ζ, both ζ_w and ζ_{nw} decrease as G decrease and nonlinear behavior appear at lower G region. For $S_w = 0.91$, on the scale of the plots, the profiles for the wetting phase look more linear but there is still inflectional behaviour as $G < 2 \times 10^{-6}$. It is also noted that the variations in ζ_w are much smaller than

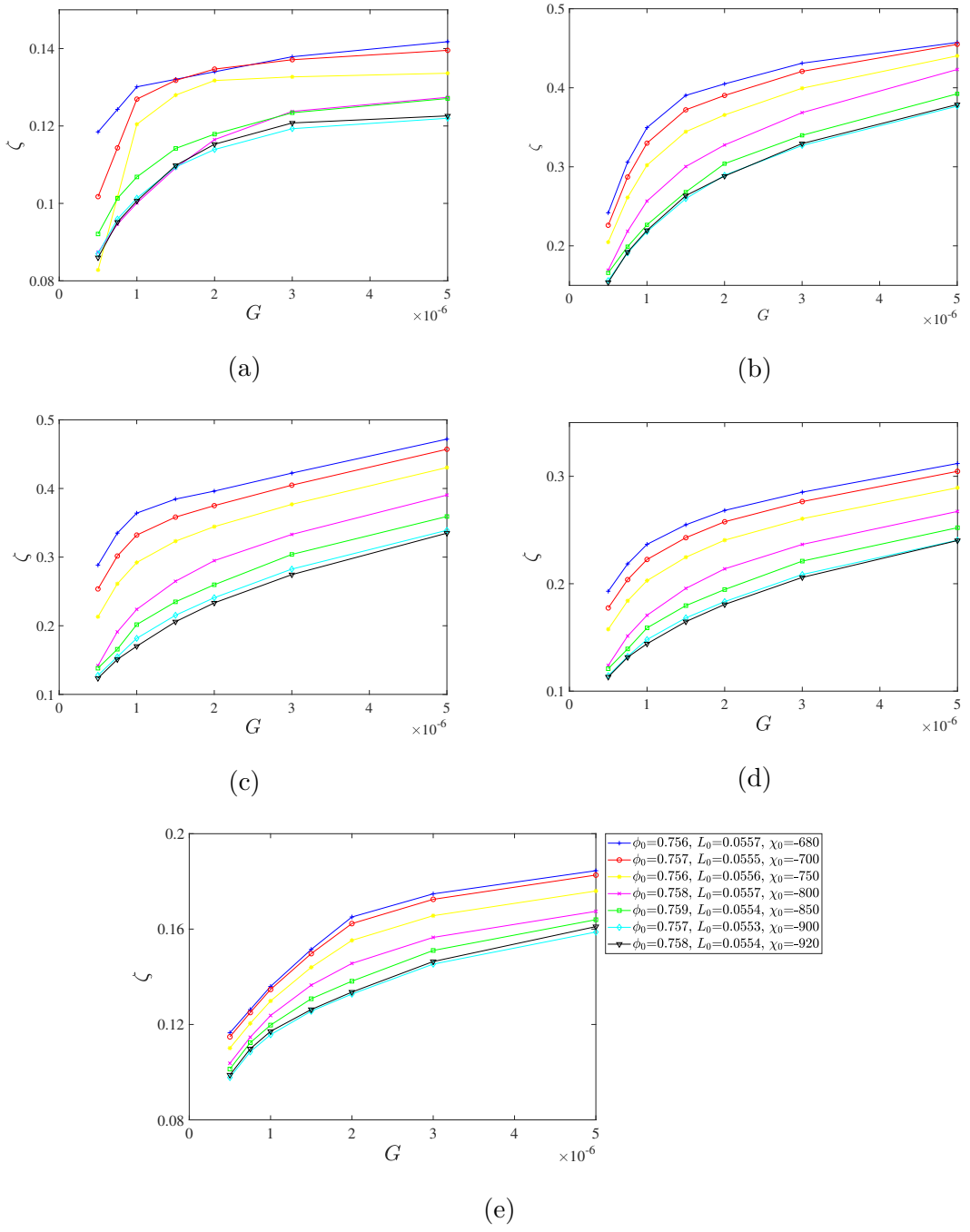

Figure 6.6: Variation of the interface length represented by the non-dimensional variable ζ with body force for the final constant values of in (a) S_w=0.91, in (b) S_w=0.7 in (c) S_w=0.49, in (d) S_w=0.32 in (e) S_w=0.2.

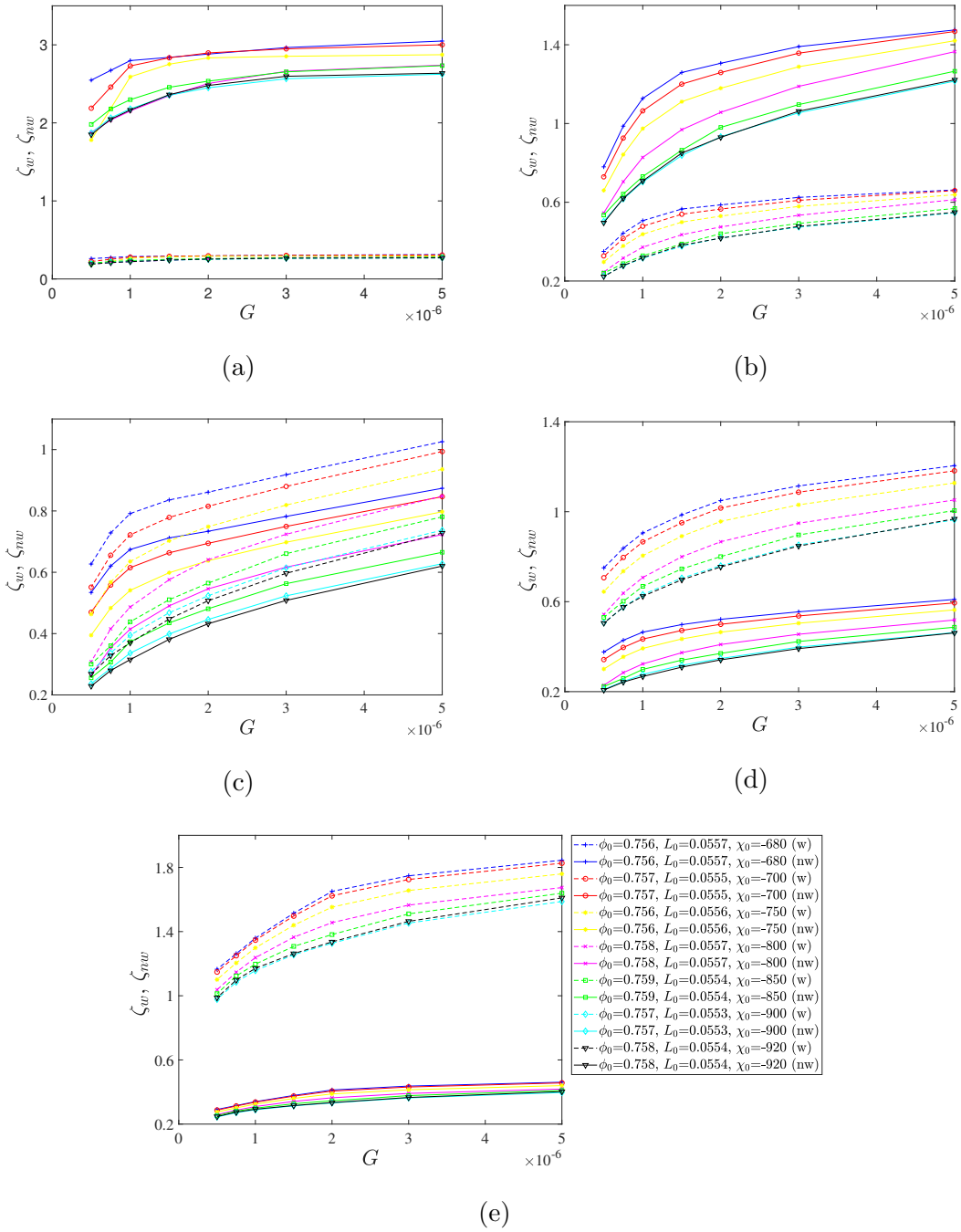

Figure 6.7: Variation of the interface length as represented by the non-dimensional variables ζ_w and ζ_{nw} with body force for the final constant values of in (a) S_w=0.91, in (b) S_w=0.7 in (c) S_w=0.49, in (d) S_w=0.32 in (e) S_w=0.2.

the corresponding changes in ζ_{nw} for all the considered structures due to the saturation of the wetting phase being much larger compare to the non-wetting phase. As S_w gets smaller, for $S_w = 0.7$, the trend of ζ_{nw} is similar as ζ shows in Fig. 6.6b. Whereas the changes in ζ_w are much smaller than ζ_{nw} because at this S_w, the wetting phase is fully connected and independent on the pore space topology. For $S_w = 0.49$, the difference between ζ_w and ζ_{nw} become smaller as G decrease. For the structure with the most negative χ_0, the profile of both the wetting and non-wetting phase is almost linear. For $S_w = 0.32, 0.2$, the ζ_w become larger than ζ_{nw}, and the non-linear behaviour is more clear for ζ_w compare to ζ_{nw}, again indicate that beyond the percolation threshold, the non-wetting phase become fully connected and the effect of χ_0 become smaller. Shows in both Fig. 6.6 and Fig. 6.7, the difference between each structure decreases as χ_o become more negative, especially structures with $\chi_0 = 900, 920$ collapses onto the same curve for all ζ, ζ_w, ζ_{nw}, indicate that the topology effect on interface length decrease as the porous medium become more homogeneous.

6.2 Imbibition

Figs. 6.8 shows the steady-state two-phase flow distribution for imbibition (displacement of the existing non-wetting phase by the injected wetting phase) of structure 4 ($\chi_0 = 800$) at $S_w = 0.3$ under different driving forces. For imbibition, compare to drainage (Figs. 6.1a-6.1d) reduction in G would appear to have less of an effect on the injected wetting phase with large wetting phase blobs occupying, in general, the central part of the computational domain in the x-direction. For the non-wetting phase, as G is reduced the potential for the formation of isolated blobs increases as seen, for example, in Fig 6.8d.

Fig. 6.9 reveals a nonlinear dependence between $k_{r,\kappa}$ and G of imbibition, similar to drainage. $k_{r,\kappa}$ of both phases decrease as G decrease, with increasing gradients. For $S_w = 0.09$, $k_{r,nw}$ are much larger than $k_{r,w}$, $k_{r,w}$ for all structures collapse onto the same curve, no significant effect can be detected for structures with different connectivity. $k_{r,nw}$ also collapse onto the same curve under high G ($G > 2 \times 10^{-6}$). As G reduce, the difference between structures increases. The topology effect on relative permeability becomes clearer at lower G. For this S_w the pore structures are dominated by the non-wetting phase, as G decreases, a decrease of $k_{r,nw}$ in the inhomogeneous structures are more obvi-

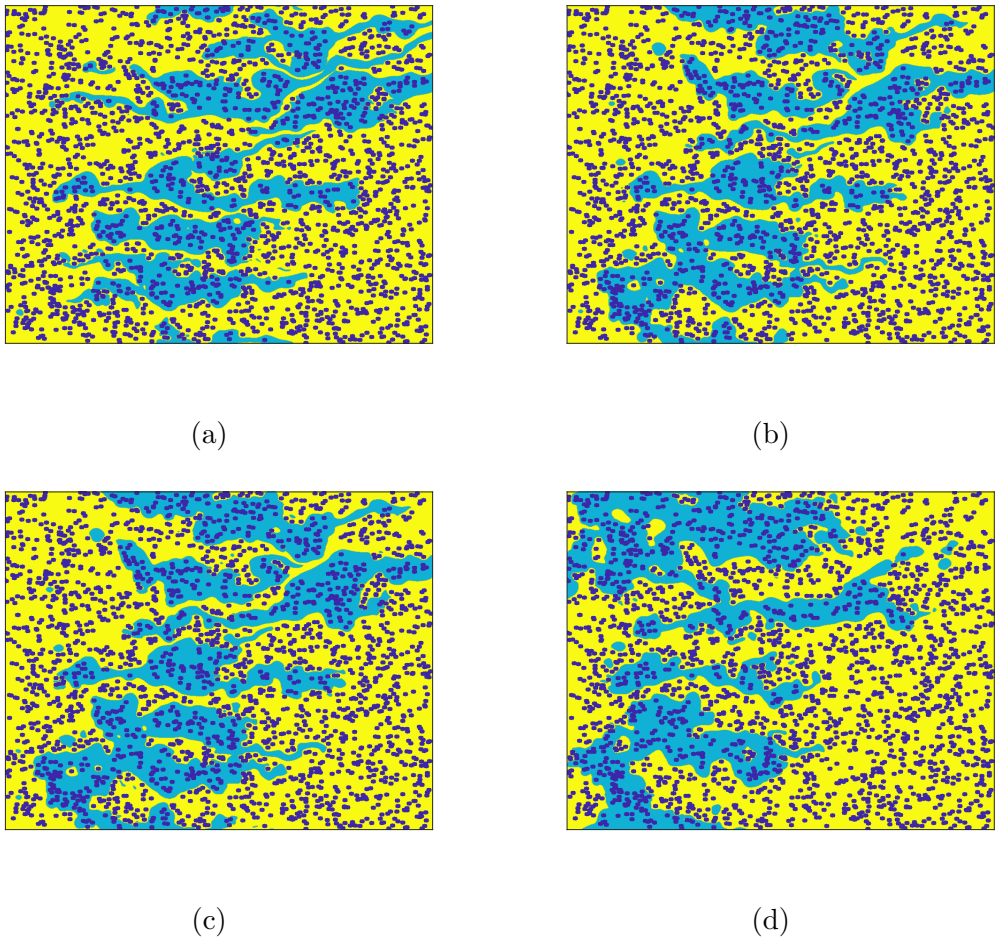

(a) (b)

(c) (d)

Figure 6.8: Predicted steady-state two-phase flow distribution patterns for imbibition for structure 4 ($\chi_0 = 800$) at $S_w = 0.3$ and with the different driving force, $G = 5 \times 10^{-6}$ in (a), $G = 2 \times 10^{-6}$ in (b), $G = 1 \times 10^{-6}$ in (c), and $G = 5 \times 10^{-7}$ in (d). The wetting phase is shown in blue, the non-wetting phase in yellow, and the solid phase in black.

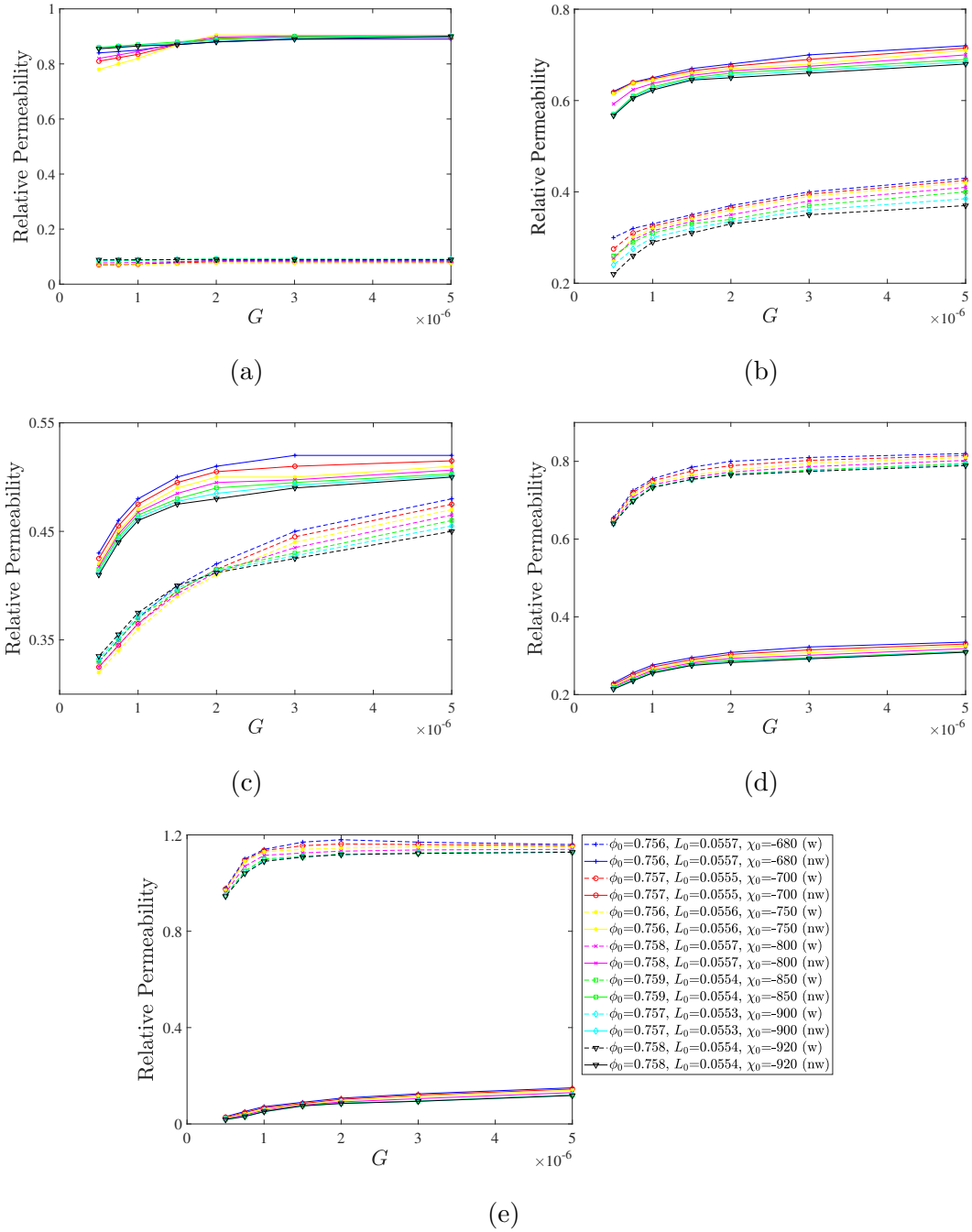

Figure 6.9: Variation of relative permeability of the wetting phase and non-wetting phase with body force for the final constant values of in (a) S_w=0.09, in (b) S_w=0.3 in (c) S_w=0.45, in (d) S_w=0.6 in (e) S_w=0.85.

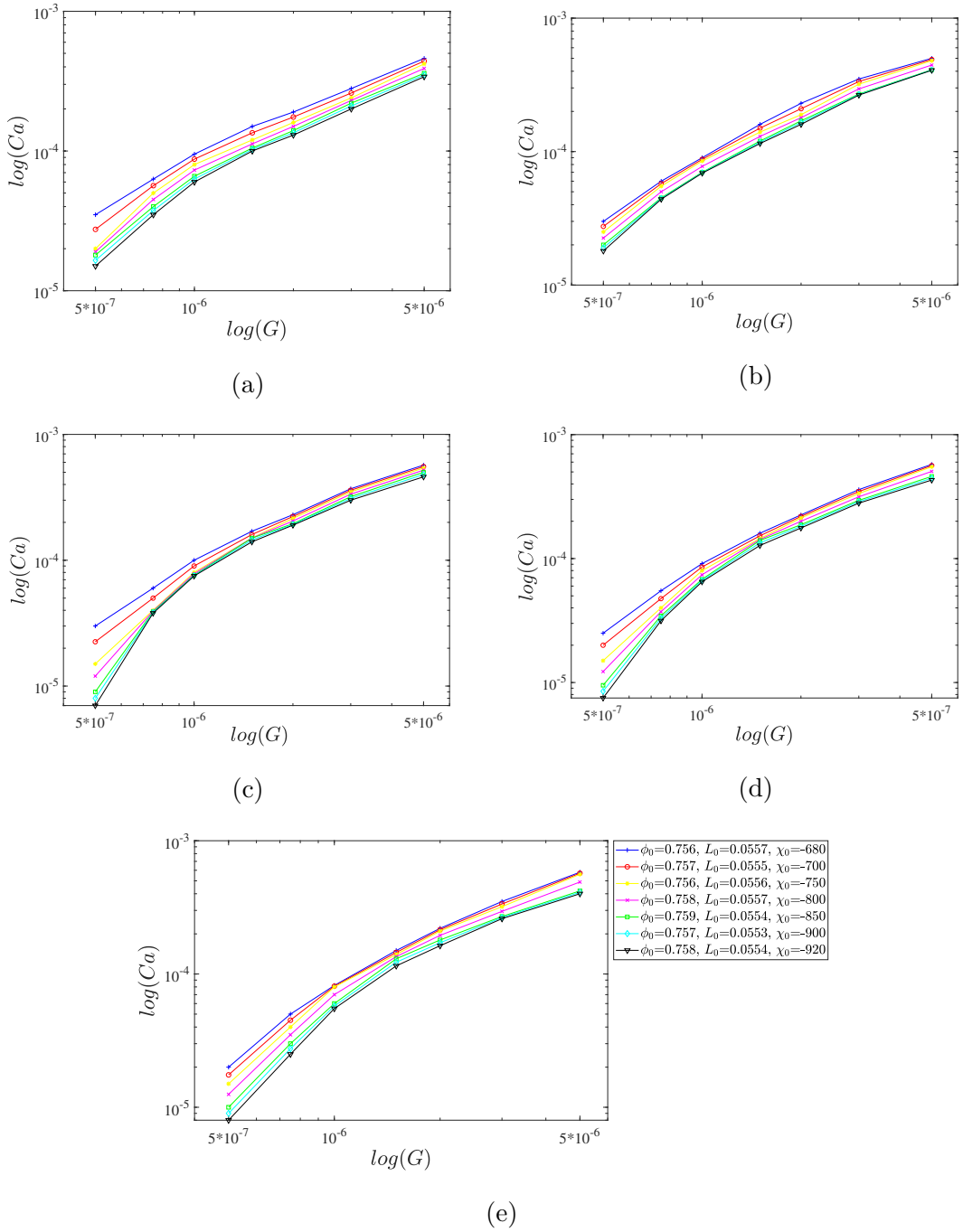

Figure 6.10: Variation of capillary number with body force (per unit area) for the final constant values of in (a) S_w=0.09, in (b) S_w=0.3, in (c) S_w=0.45, in (d) S_w=0.6 in (e) S_w=0.85.

ous because there are more preferential flow path exists in more inhomogeneous structures. For $S_w = 0.3, 0.45, 0.6, 0.85$, both wetting and non-wetting phase decrease as χ_0 get more negative. For $S_w = 0.3$, the nonlinear behaviour of both the wetting and non-wetting phase appears as G decrease to 1×10^{-6}, and the inflectional profiles of more homogeneous structures are clearer compare to inhomogeneous structures. In addition, structures with more negative χ_0 also result in lower relative permeability for both the wetting and non-wetting phase, due to the negative effect of χ_0 on phase velocity. Thus, the more homogeneous structures reach low capillary regions at higher G and result in a nonlinear behaviour, whereas the inhomogeneous structures stay almost linear. For $S_w = 0.45$, the nonlinear correlation is different between wetting and non-wetting. At high G, $k_{r,nw}$ stay almost constant the same as lower S_w, but $k_{r,w}$ decrease as G decrease. The nonlinear infliction point appears at G around $G = 2 \times 10^{-6}$ for both phases. At low G, the effect of pore topology decrease where $k_{r,w}$ of all structures collapsed onto a single curve. As S_w increase, the wetting phase changes from fragment to connected and the relative permeability of the wetting phase become larger than the non-wetting phase for all G. For $S_w = 0.6$ and 0.85, the difference between structures becomes smaller. The nonlinear profiles are similar for both the wetting and non-wetting phase, where the inflexion point appear around $G = 2 \times 10^{-6}$. Compare to drainage, the χ_0 shows less effect on $k_{r,\kappa}$ of all structures, where the biggest difference appears around $S_w = 0.45$. Similar results were shown in Chapter 5, where the topology of pore space has more impact on $k_{r,\kappa}$ during drainage for $G = 5 \times 10^{-6}$, the same impact continues as G decrease, indicating that the relative permeability of imbibition process is less sensitive to the pore space connectivity.

In Fig. 6.10, the dependence of the capillary number on the G is considered in the form of log-log plots where a clear monotonically increasing profile is seen in all cases. For all S_w, Ca decrease as G decrease, due to the decreasing non-wetting phase velocity the same as drainage. In addition, Ca decrease as χ_0 gets more negative, due to the lower velocity field in more homogeneous pore structures. For higher G regions, the profiles are almost linear and the difference between each structure is quite small. As G decreases, there is an observable spread in the capillary number for all values of S_w. Ca decrease as χ_0 becomes more negative, that is, as the pore space becomes more homogeneous. For $S_w = 0.09$, and 0.3 shows in Fig.6.10a and 6.10b, the nonlinear behaviour is not very clear, the curves are more parabolic than inflectional. Similar behaviour can be seen for relative permeability

shown in Fig. 6.9a and 6.9b, the nonlinear correlation is also not clear between $k_{r,nw}$ and G. At this S_w, the non-wetting phase is fully connected, and the topology effect at the low capillary region is limited. For $S_w = 0.45$, 0.6 and 0.85, as G decreases, the nonlinear relationship becomes clear, especially for structures with more negative χ_0. The inflexion point appears around $G = 1.5 \times 10^{-6}$ corresponds to the inflexion point of relative permeability. Different from drainage, as more wetting phase is injected into the pore structures, the non-wetting phase become more separated and the superficial velocity decrease as S_w increase, therefore the nonlinear behaviour become more obvious. Moreover, the nonlinear behaviour is more obvious for more homogeneous structures similar to drainage.

Fig 6.11 shows the relationship between wetting phase Euler characteristic, χ_w, with G. For $S_w = 0.09$, and 0.3 shown in Figs. 6.11a and 6.11b, χ_w decrease as G decrease in general with fluctuations because the wetting phase becomes more connected as G decrease. For $S_w = 0.09$, χ_w reduces as the structure becomes more homogeneous indicating that the connectivity of the wetting phase increase as χ_0 becomes more negative. The nonlinear behaviours are more obvious for inhomogeneous structures and almost linear for more homogeneous structures because the wetting phase tends to stay close to packed solid grains which exist more in inhomogeneous structures. For $S_w = 0.3$, the inhomogeneous structures appear to have a more smooth correlation between χ_w and G with the inflexion point appearing around $G = 2 \times 10^{-6}$. More homogeneous structures appear to have higher χ_w the same as $S_w = 0.09$. For $S_w = 0.45$, 0.6 and 0.85 (Figs. 6.11c 6.11e), χ_w increase as G decrease. For $S_w = 0.45$, as G decrease the difference between each structure get smaller. Under higher G ($G > 2 \times 10^{-6}$), structures with more negative χ_0 also have lower χ_w. As G reduce, the intersection region appear around $1 \times 10^{-6} < G < 2 \times 10^{-6}$, and the relationship reversed that structures with less negative χ_0 now have lower χ_w. Moreover, G have a greater impact on χ_w for more homogeneous structures compare to inhomogeneous structures the same as drainage. In addition, the χ_w increase from a negative value to a positive value indicates that as G decrease the wetting phase changes from fully connected to fragment and the percolation threshold is reached at higher S_w the same as drainage. A similar effect can be seen for $S_w = 0.6$, where χ_w increases toward 0 as G decreases. However, no clear intersection region can be observed. χ_w converge to the same value at the lowest G, due to the topology effect decrease close to the percolation threshold. For $S_w = 0.85$, χ_w increase as G decrease with increasing gradients. This S_w corresponds to

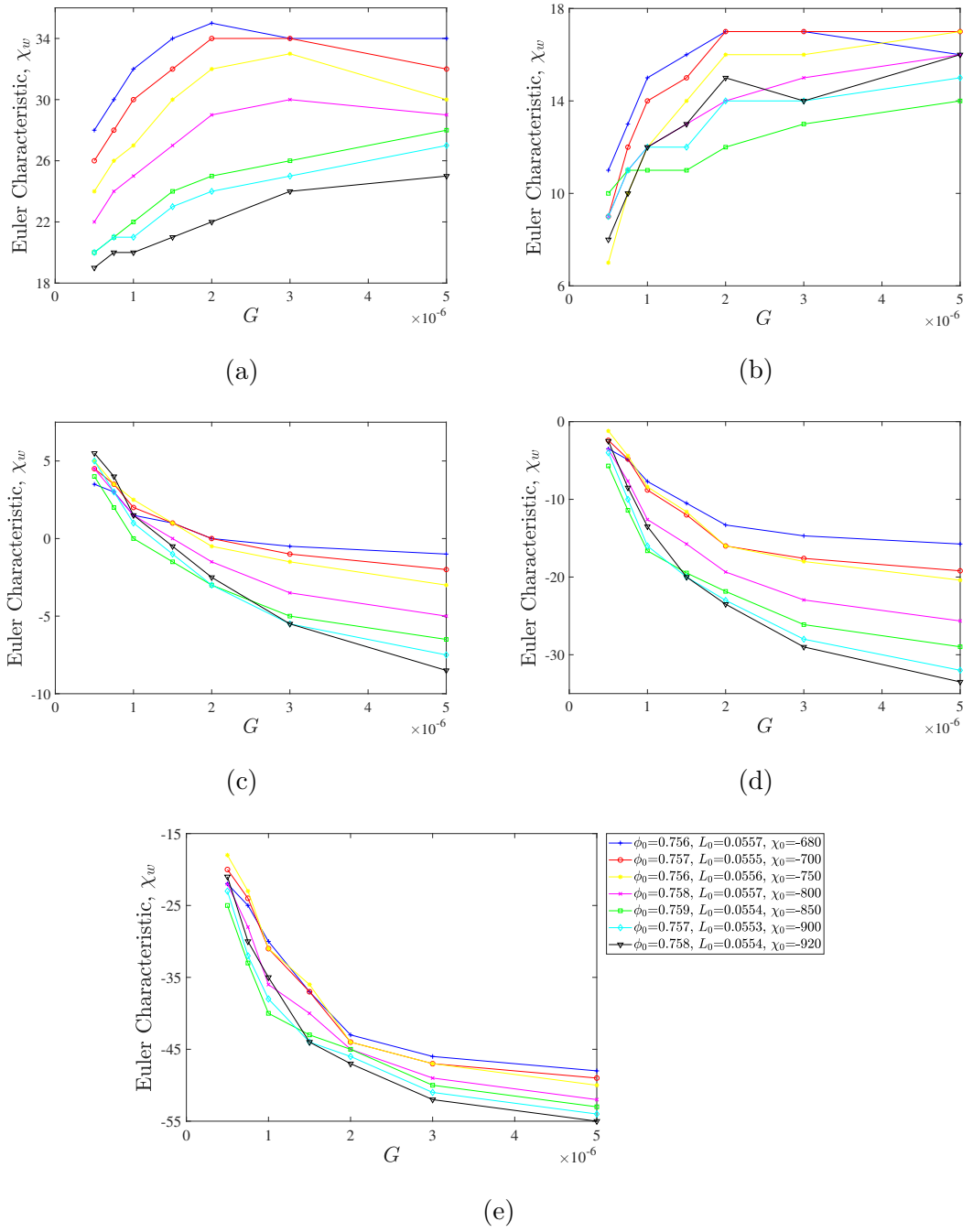

Figure 6.11: Variation of the Euler characteristic of the wetting phase χ_w with body force for the final constant values of in (a) S_w=0.09, in (b) S_w=0.3, in (c) S_w=0.45, in (d) S_w=0.6 in (e) S_w=0.85.

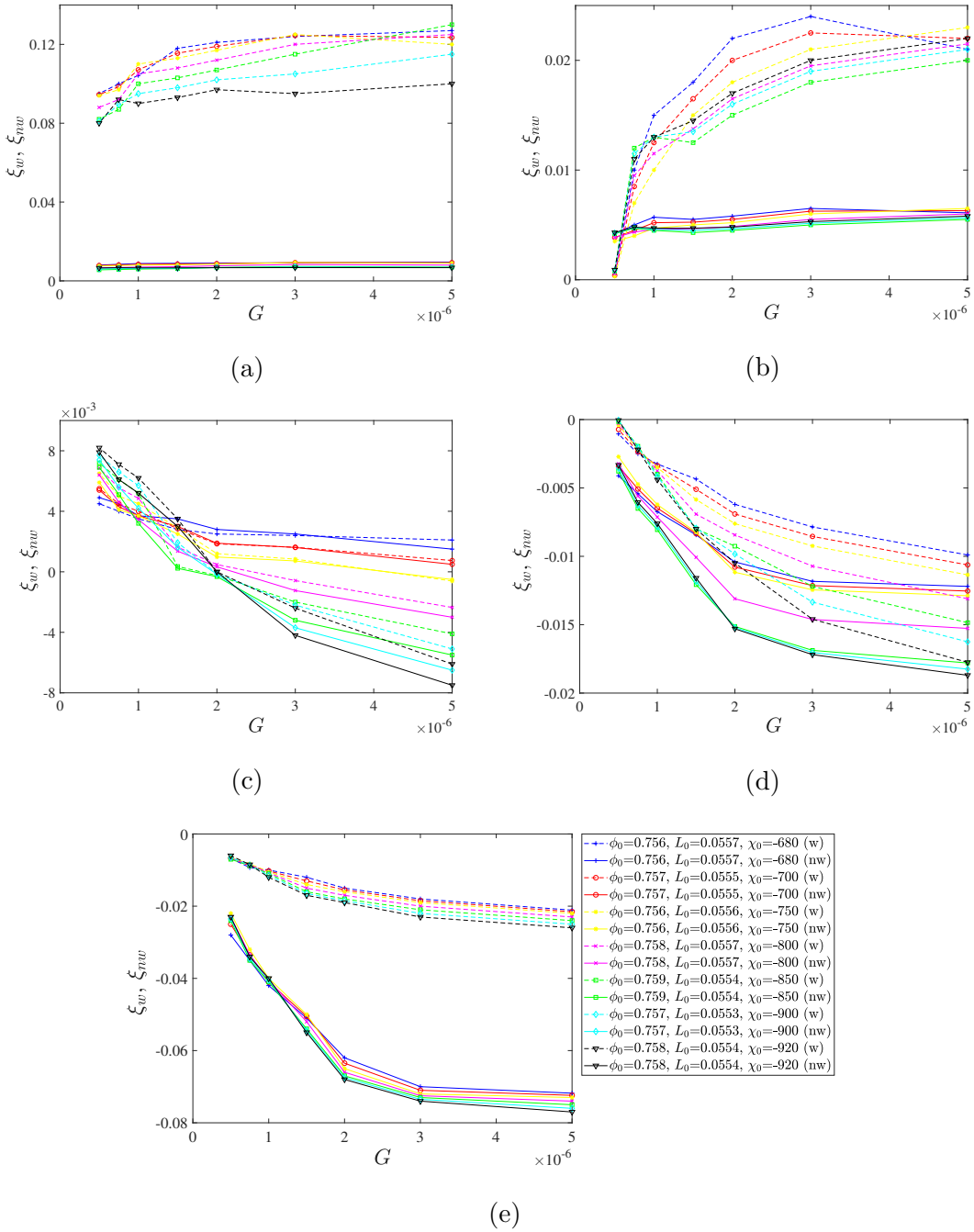

Figure 6.12: Variation of the Euler characteristic of the wetting and non-wetting phases per unit average grain, ξ_w and ξ_{nw} with body force for the final constant values of in (a) S_w=0.09, in (b) S_w=0.3, in (c) S_w=0.45, in (d) S_w=0.6 in (e) S_w=0.85.

the ganglion dynamics regime, and the increasing χ_w represents a higher non-wetting phase connection. The same as drainage, the maximum and minimum value of χ_w for a single structure decrease as G decrease.

Fig. 6.12 shows the relationship between the parameters ξ_w and ξ_{nw} with G. For $S_w = 0.09$, and 0.3, the trend of ξ_w is very similar to χ_w, which decrease as G decrease. The ξ_{nw} stay almost constant as G decrease, due to the fact that at low S_w, the non-wetting phase is fully connected, and the number of grains within the non-wetting phase is much larger than within the wetting phase. It is worth noticing that for $S_w = 0.3$, ξ_w become less than ξ_{nw} as $G < 7.5 \times 10^{-7}$, indicating that as G decrease, the wetting phase become more connected and result in a greater number of grain per phase blob compare to non-wetting phase. Moreover, the difference between each structure decreases as ξ_w decrease towards 0 further providing that the topology effect is less influential close to the percolation threshold. For $S_w = 0.45$, 0.6 and 0.85, both ξ_w and ξ_{nw} increase as G decrease. For $S_w = 0.45$, the tend of ξ_w and ξ_{nw} are quite similar. Under high G structures with less negative χ_0 appear to have higher values of ξ_w and ξ_{nw}. As G decreases, higher gradients are detected for more homogeneous structures, and ξ_κ of these structures become larger than inhomogeneous structures. This behaviour can also be seen in Fig. 6.11c, the effect on more homogeneous structures is more obvious than on inhomogeneous structures. For $S_w = 0.6$, ξ_{nw} become more negative than ξ_w and both ξ_κ increase toward 0 as G decrease. As the S_w increase and the wetting phase become fully connected, a greater number of grain per wetting phase blob appeared. For $S_w = 0.85$, ξ_{nw} is markedly more negative compare to ξ_w, and markedly more effected by G. For the same structure as the same S_w, the difference between ξ_w and ξ_{nw} get smaller as G decrease, indicating that both wetting and non-wetting phase results in larger blobs by surrounding more number of grain as G decrease, similar as drainage.

Fig. 6.13 shows the dependence of the (total) interface length between the wetting and non-wetting phases, I_c, with G in terms of the nondimensional variable ζ. In general, the ζ decrease as G decrease for all S_w. Showed in Fig. 6.11, the decreasing G results in a lower absolute value of χ_w which represent a lower number of blobs/droplet the same as drainage and therefore results in a lower value of ζ. In addition, a structure with less negative χ_0 appears to have larger ζ the same as drainage. For $S_w = 0.09$, the trend of ζ against G is almost linear, especially for more homogeneous structures which correspond to χ_w

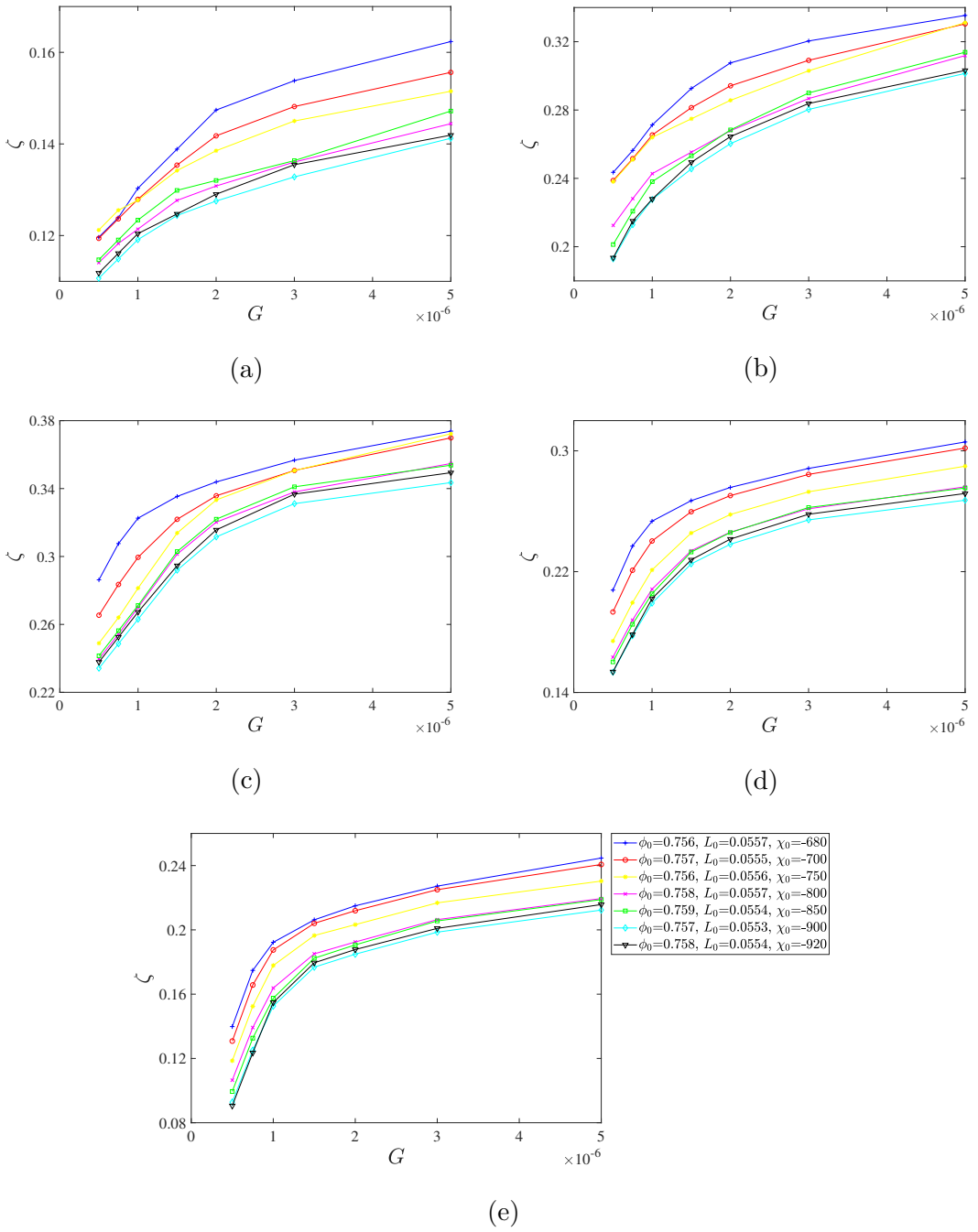

Figure 6.13: Variation of the interface length represented by the non-dimensional variable ζ with body force for the final constant values of in (a) S_w=0.09, in (b) S_w=0.3, in (c) S_w=0.45, in (d) S_w=0.6 in (e) S_w=0.85.

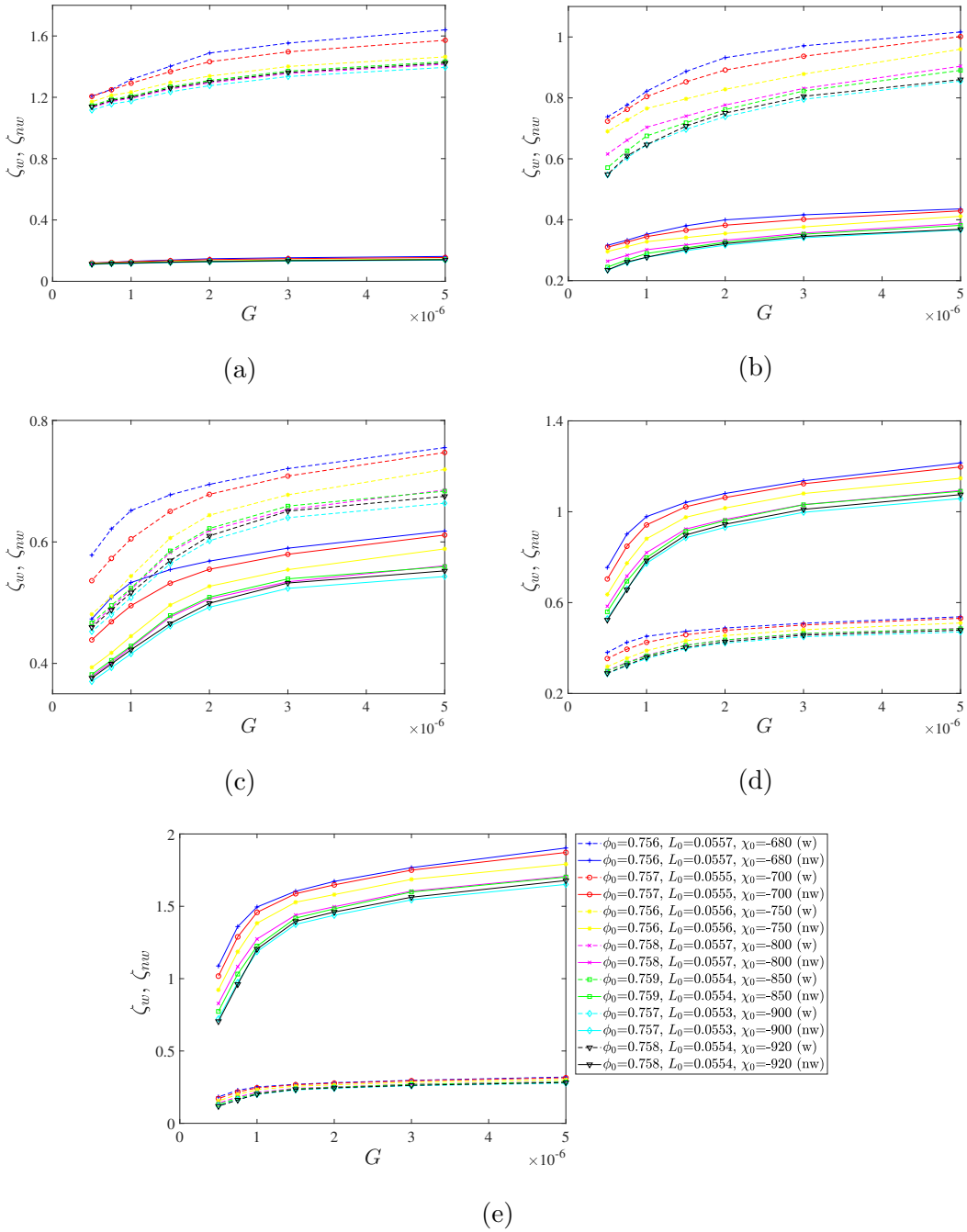

Figure 6.14: Variation of the interface length as represented by the non-dimensional variables ζ_w and ζ_{nw} with body force for the final constant values of in (a) S_w=0.09, in (b) S_w=0.3, in (c) S_w=0.45, in (d) S_w=0.6, in (e) S_w=0.85.

shown in Figs. 6.11a. The nonlinear relationship becomes more clear as S_w increases. For $S_w = 0.3$, the nonlinear profiles are more obvious than $S_w = 0.09$, without a clear inflexion point. For $S_w = 0.45$ and 0.6, the nonlinear correlation of structures with less negative χ_0 happens at lower G around $G = 1.5 \times 10^{-6}$. Whereas as χ_0 decreases, the inflexion point shift towards higher G. Similar behaviour can be seen for Ca, as more homogeneous structures reach low capillary regions at higher G compared to inhomogeneous structures. Similar to χ_w, G is more influential in more homogeneous structures than inhomogeneous structures. For $S_w = 0.85$, the effect of G become more uniform throughout all structures, the nonlinear region appears as G decrease to $G = 2 \times 10^{-6}$. Compare to drainage, the interface length between wetting and non-wetting phases is smaller for imbibition, as G decrease, the difference between drainage and imbibition becomes smaller.

Fig. 6.14 shows a different way of measuring I_c, where ζ_w and ζ_{nw} are plot separately. Similar to ζ, ζ_κ decrease as G decrease. For $S_w = 0.09$, the ζ_w is much larger than ζ_{nw}. The profile of ζ_w is similar to ζ, where structures with less negative χ_0 decrease more intensely compared to structures with more negative χ_0. The ζ_{nw} stays almost constant at all G at this S_w, and the content of the non-wetting phase is much larger than the wetting phase. For $S_w = 0.3$, the nonlinear behaviour of both the wetting and non-wetting phase becomes clear. The inflection point is more clear compare to ζ which appears around $G = 2 \times 10^{-6}$. In addition, the effect of G on ζ_{nw} is much smaller than ζ_w because the non-wetting phase is fully connected and independent of the structure topology. For $S_w = 0.45$, the ζ_w is still larger than ζ_{nw}, but the difference gets smaller as G decrease. The same as ζ, the inflexion profiles for more homogeneous structures appear at higher G compared to inhomogeneous pores medium. For $S_w = 0.6$ and 0.85, the ζ_{nw} become larger than ζ_w with more clear nonlinear trends appear around $G = 1.5 \times 10^{-6}$. The shifted inflexion point can also be seen in the ζ plot shown in Fig. 6.13d and 6.13e. As for ζ_w, even though the decreasing trends are less obvious than ζ_{nw}, the nonlinear correlation can be seen at lower G. Moreover, ζ_w for $S_w = 0.85$ of different structures overlap on the same curve, further providing that the effect of pore space topology decreases beyond percolation thresholds. Compare to drainage, the trends are very similar, as the structure becomes more homogeneous, and the difference between each structure decreases for all interface measurements. In addition, the interface lengths of imbibition are smaller than drainage at higher G regions, and the difference gets smaller as G decrease, indicating that the flow

pattern (drainage/imbibition) is less influential at low capillary regions.

6.3 Summary

To sum up, as different body force G was applied to seven porous mediums with different χ_0, the flow properties such as relative permeability, capillary number, Euler characteristic, and interface length, at different driving forces for drainage and imbibition, were plotted and analyzed. It was found that the nonlinear profile of relative permeability appears in low G. The inflectional profiles were clearer for more homogeneous structures because the flow path spread more uniformly through the domain compared to inhomogeneous structures. For imbibition, similar behaviour could be found with a smaller spread between structures the same as the results showed in chapter 5. As for the capillary number, Ca decreased as the pore structures become more homogeneous and the nonlinear behaviours can be seen for all structures. However, the inflectional profiles shifted to higher G as χ_0 decreased, because more homogeneous structures reached the low capillary region at higher G compared to inhomogeneous structures. During imbibition, the nonlinear behaviour was more obvious compared to drainage, due to the decreased non-wetting phase velocity as more wetting phases were injected into the pore structures. Higher connectivity of the wetting phase and non-wetting phase was reached in the low capillary region at low and high S_w, respectively. The number of isolated blobs/droplets decreased in the domain, which resulted in a lower absolute value of χ_w as G decreased. For both drainage and imbibition, the percolation threshold was reached at higher S_w at low driving forces. A less spread of χ_w could be seen around 0 indicating that the changes in pore space connectivity were less influential close to the percolation threshold. For drainage, the driving force had a greater impact on more homogeneous structures than the inhomogeneous structures. As for imbibition, the effect of G seemed more uniform for structures with different χ_w. The interface length decreased as G decreased, due to a lower absolute value of χ_w which represented a lower number of blobs/droplets. The nonlinear relationship could be seen in the low capillary region. The interface length of inhomogeneous structures remained higher as G decreased for both drainage and imbibition.

Chapter 7

Conclusion

7.1 Research summary

The motivation of this research was to study the effect of pore space connectivity, as expressed through the structure Euler characteristic (χ_0) on the two-dimensional, immiscible two-phase flows of a water wet, oil-water system during drainage and imbibition process. Three different states were investigated for this thesis: under transient state conditions, under steady-state conditions, and at low driving forces. The numerical simulations were performed using the MCMP lattice-Boltzmann model which was capable of simulating multi-phase flows in complex domains, due to its advantage in the treatment of interphase dynamics and complex boundaries condition. Seven different artificial pore structures were generated based on the random distribution of overlapping circles (Boolean model) with the same grain size and grain density. These artificial pore structures were set with specific predetermined values of Minkowski functionals, similar values of porosity and contour length, and different Euler characteristics, with the codes developed with MATLAB. Two sets of pore structures were generated, one used for the transient study and low driving forces study, and the other one used for the steady-state study. This research focused on analysing the relative permeability, interface length, Euler characteristic of the wetting and non-wetting phases, and the capillary pressure for different flow patterns at different saturation rates. The impact of structure topology on the average pore coordination number, pore size and pore throat distribution were also taken into account for a more complete geometrical and topological picture of the observed porous medium.

As discussed in Chapter 2, multiphase studies of immiscible two-phase flows in the porous medium had been done in both experimental and numerical on the macroscopic behaviour. However, most of these studies focused on the effect of properties of liquids, for instance, viscosity ratio, wetting angle, etc. rather than the impact of pore structures. To the best of the author's knowledge, there were no systematic investigations on the impact of the pore space morphology and more specifically connectivity. The impact of pore space connectivity on immiscible two-phase flows remained largely unexplored. However, understanding the effect of pore structures on the multi-phase flow was critically important in both nature and industrial fields, especially in petroleum related fields, groundwater treatment, geologic CO_2 sequestration, etc. In the current study, a two-dimensional MCMP LBM was used to study the impact of the topology properties of the porous medium on immiscible two-phase flows during the drainage and imbibition process, and the dependence of various fluid properties at different saturation rates was analysed under transient state condition, steady-state conditions, and low capillary number.

The transient study was shown in Chapter 4, where the same body force G was applied to seven porous mediums with different χ_0 during the drainage and imbibition process, and the flow properties such as saturation rate, velocity fields, capillary pressure, Euler characteristic, and interface length at different time steps from injection to steady-state were plotted and analyzed. It was found that the increasing levels of homogeneity in porous medium imposed greater flow restrictions which reduce the transmission velocities and extend the time interval needed to reach steady saturation. Capillary pressure decrease as the χ_0 becomes more negative. Euler characteristic of the fluid phases was used to show the phase fragmentation and connectivity patterns. For both drainage and imbibition, as S_w increases, the non-wetting phase transited from fully connected to ganglion dynamic through its percolation threshold. During drainage, the degree of phase fragmentation/connectivity depended on the wetting phase saturation level, Where for low S_w, more homogeneous structures resulted in a higher value of χ_w (higher wetting phase fragmentation), and for high S_w, more homogeneous structures resulted in lower value of χ_w (higher non-wetting phase fragmentation), whilst an indeterminate state was observed near the non-wetting phase percolation threshold. During imbibition, the wetting phase transited from a highly connected state to a less connected one for low S_w, and more homogeneous structures resulted in a lower value of χ_w for all S_w. In addition, the was shown

that the phase percolation threshold strongly relied on pore space topology. More homogeneous pore structures also resulted in higher levels of enclosed solid grains per phase blob for high S_w, and for low S_w the relationship inverted during drainage. As for imbibition, the wetting phase tended to enclose a higher number of solid grains, which resulted in a higher number of enclosed solid grains per phase blob for more homogeneous structures. For the interface length, it was shown that for both drainage and imbibition, it was higher for the inhomogeneous porous medium because of the higher degree of distortion of the corresponding blob geometries and flow channelisation.

The steady-state study was shown in Chapter 5, where the same body force G was applied to seven porous mediums with different χ_0. The flow properties such as relative permeability, capillary pressure, Euler characteristic, interface length, and average pore size at different saturation rates for drainage and imbibition were plotted and analyzed. It was shown that a more homogeneity pore structure, generally enhanced the relative permeability of the porous structure for $S_w = 0.25 - 0.75$, whereas outside this range the relative permeability progressively collapsed to a single curve during drainage. Also, the effect of pore space connectivity was more obvious for drainage than imbibition. The 'lubrication effect' due to a non-wetting/wetting phase viscosity ratio greater than unity was effectively captured in the pendular saturation region. The change in χ_0 was observed to affect both the drainage and imbibition capillary pressure curves, though in opposite ways. During drainage, as χ_0 became more negative the capillary pressure increased due to the higher homogeneity of the solid grain distribution. However, during imbibition, a more negative χ_0 resulted in lower capillary pressure. This could be attributed to a lower average interfacial curvature as a consequence of the affinity of the wetting phase to the closely spaced solid surfaces. The interface length between the two-phase was found to significantly increase for both processes with an asymmetrical profile with respect to the S_w, for inhomogeneous structures. Additionally, the interface length was found to converge to the same value at low and high S_w, for drainage and imbibition respectively. It was concluded that at a given saturation rate, higher levels of grain clustering (i.e., higher χ_0) in the porous domain led to a greater geometrical irregularity of the interface between fluid phases. As for the topological state of the two-phase, during drainage, a decreasing χ_0 was found to result in lower levels of wetting and non-wetting phase connectivity at the corresponding ends of the saturation spectrum. A different behaviour was observed dur-

ing imbibition where at low wetting phase saturation, more negative χ_0 resulted in higher wetting phase connectivity. χ_w was also found to pass through the zero point. At those levels, the average phase area was found to jump in an almost discontinuous way to higher magnitudes indicating the formation of large phase clusters that spanned the entire domain.

The low driving forces study was shown in Chapter 6, where different body force G was applied to seven porous mediums with different χ_0. The flow properties such as relative permeability, capillary number, Euler characteristic, and interface length, at different driving forces for drainage and imbibition, were plotted and analyzed. It was found that the nonlinear profile of relative permeability appears in low G. The nonlinear correlation between $k_{r,\kappa}$ and G got clearer as S_w decreased for drainage. The inflectional profiles were clearer for more homogeneous structures because the flow path spread more uniformly through the domain compared to inhomogeneous structures. For imbibition, similar behaviour could be found with a smaller spread between structures the same as the results showed in chapter 5. As for the capillary number, Ca decreased as the pore structures become more homogeneous and the nonlinear behaviours can be seen for all structures during both drainage and imbibition. However, the inflectional profiles shifted to higher G as χ_0 decreased, because more homogeneous structures reached the low capillary region at higher G compared to inhomogeneous structures. The nonlinear behaviours depended on S_w as well. During imbibition, the nonlinear behaviour was more obvious compared to drainage, due to the decreased non-wetting phase velocity as more wetting phases were injected into the pore structures. Higher connectivity of the wetting phase and non-wetting phase was reached in the low capillary region at low and high S_w, respectively. As G decreased, the number of isolated blobs/droplets also decreased in the domain, which resulted in a lower absolute value of χ_w. For both drainage and imbibition, the percolation threshold was reached at higher S_w at low driving forces. A less spread of χ_w could be seen around 0 indicating that the changes in pore space connectivity were less influential close to the percolation threshold. For drainage, the driving force had a greater impact on more homogeneous structures than the inhomogeneous structures. As for imbibition, the effect of G seemed more uniform for structures with different χ_w. As G decreased, the levels of enclosed solid grains per wetting and non-wetting phase blob also decreased, indicating that the wetting phase would adhere to the solid grain clusters more and more intensively resulting in a higher number of grain per phase blob as G decrease. The interface length

decreased as G decreased, due to a lower absolute value of χ_w which represented a lower number of blobs/droplets. The nonlinear relationship could be seen in the low capillary region. The interface length of inhomogeneous structures remained higher as G decreased for both drainage and imbibition.

7.2 Recommendations for future works

The current study is focused on the effect of pore space connectivity as expressed through the structure Euler characteristic (χ_0) on immiscible two-phase flows in two-dimension. However, due to the simulation time, a great amount of time was spent on running the simulation. A complete description of the morphological properties of porous medium effect in immiscible displacements can not be accomplished, and a large amount of work needs to be done. There are some recommendations for future work.

- The current study used a water-wet, oil-water system as the subject. It represents immiscible two-phase flows with a low viscosity ratio. Whereas in nature and industrial applications, high viscosity ratio two-phase flows are also common, for instance, in gas-liquid systems. Future works can force the effect of different viscosity ratios in the porous medium.

- In the case of two dimension pore structures, except for the Euler characteristic, there are also porosity and contour length. The geometrical properties of the porous medium are also important in immiscible two-phase flow developments. Studies can be performed to analyse the effect of these properties on the process of displacement (drainage/imbibition).

- This study is limited to 2-dimensional due to the long simulation time and computational cost, but 3-dimensional is also necessary. Not only because the reality is in 3-dimensional, but also because the impact of curvature which is the fourth Minkowski functional can only be studied in 3-dimensional. In order to extend the current study to 3-dimensional, the code of multiphase flow in porous medium needs to be further developed to speed up the simulations.

Bibliography

Afzali, S., Rezaei, N., Zendehboudi, S., and Chatzis, I. (2022). Computational fluid dynamic simulation of multi-phase flow in fractured porous media during water-alternating-gas injection process. *Journal of Hydrology*, 610:127852.

Aggelopoulos, C. and Tsakiroglou, C. (2008). The effect of micro-heterogeneity and capillary number on capillary pressure and relative permeability curves of soils. *Geoderma*, 148(1):25–34.

Aidun, C. K. and Clausen, J. R. (2010). Lattice-boltzmann method for complex flows. *Annu. Rev. Fluid Mech.*, 42:439–472.

Al-Tamimi, L., Farhat, H., and Hasan, W. F. (2021). Hybrid quasi-steady thermal lattice boltzmann model for investigating the effects of thermal, surfactants and contact angle on the flow characteristics of oil in water emulsions between two parallel plates. *J. Pet. Sci. Eng.*, 204:108572.

Arabjamaloei, R. and Ruth, D. (2017). Numerical study of inertial effects on permeability of porous media utilizing the lattice boltzmann method. *J.Nat. Gas. Sci. Eng*, 44:22–36.

Armstrong, R. T., McClure, J. E., Berrill, M. A., Rücker, M., Schlüter, S., and Berg, S. (2016). Beyond darcy's law: The role of phase topology and ganglion dynamics for two-fluid flow. *Phys. Rev. E*, 94:043113.

Armstrong, R. T., McClure, J. E., Robins, V., Liu, Z., Arns, C. H., Schlüter, S., and Berg, S. (2018). Porous media characterization using minkowski functionals: Theories, applications and future directions. *Transp. Porous Media*, pages 1–31.

Asai, A., Shioya, M., Hirasawa, S., and Okazaki, T. (1993). Impact of an ink drop on paper. *Journal of Imaging Science and Technology*, 37:205–207.

Ashgriz, N. (2011). Multiphase flow and spray systems laboratory (mussl). `https://mussl.mie.utoronto.ca/`.

Avraam, D. and Payatakes, A. (1995). Flow regimes and relative permeabilities during steady-state two-phase flow in porous media. *J. Fluid Mech.*, 293:207–236.

Aziz, R., Niasar, V., Erfani, H., and Martínez-Ferrer, P. J. (2020). Impact of pore morphology on two-phase flow dynamics under wettability alteration. *Fuel*, 268:117315.

Bachmat, Y. and Bear, J. (1986). Macroscopic modelling of transport phenomena in porous media. 1: The continuum approach. *Transp. Porous Media*, 1(3):213–240.

Bakhshian, S., Rabbani, H. S., Hosseini, S. A., and Shokri, N. (2020). New insights into complex interactions between heterogeneity and wettability influencing two-phase flow in porous media. *Geophysical Research Letters*, 47(14):e2020GL088187.

Bear, J. (2018). *Modeling phenomena of flow and transport in porous media*, volume 1. Springer.

Blackwell, R. (1975). Dynamics of fluids in porous media: J. bear. american elsevier, new york, n.y., 1972, 764 pp., dfl. 94.00. *Geoderma*, 14(2):173 – 175.

Blunt, M. J., Bijeljic, B., Dong, H., Gharbi, O., Iglauer, S., Mostaghimi, P., Paluszny, A., and Pentland, C. (2013). Pore-scale imaging and modelling. *Adv. Water Resour.*, 51:197–216.

Buckley, S. and Leverett, M. (1942). Mechanism of Fluid Displacement in Sands. *Transactions of the AIME*, 146(01):107–116.

Cai, J., You, L., Hu, X., Wang, J., and Peng, R. (2012). Prediction of effective permeability in porous media based on spontaneous imbibition effect. *Int. J. Mod. Phys. C*, 23:1250054.

Carman, P. C. (1937). Fluid flow through granular beds. *Trans. Inst. Chem. Eng.*, 15:150–166.

Chen, L., Kang, Q., Mu, Y., He, Y.-L., and Tao, W.-Q. (2014). A critical review of the pseudopotential multiphase lattice boltzmann model: Methods and applications. *International journal of heat and mass transfer*, 76:210–236.

Chen, S. and Doolen, G. D. (1998). Lattice boltzmann method for fluid flows. *Annu. Rev. Fluid Mech.*, 30(1):329–364.

COMSOL (2018). Using multiphase flow simulation to help design wastewater treatment plant. `http://cn.comsol.com/offers/cn-comsol-news-2018`.

Darcy, H. (1856). *Les fontaines publiques de la ville de Dijon: exposition et application...* Victor Dalmont.

Dou, Z. and Zhou, Z.-F. (2013). Numerical study of non-uniqueness of the factors influencing relative permeability in heterogeneous porous media by lattice boltzmann method. *Int. J. Heat Fluid Flow*, 42:23–32.

Ergun, S. (1952). Determination of geometric surface area of crushed porous solids. *Analytical Chemistry*, 24(2):388–393.

Erpelding, M., Sinha, S., Tallakstad, K. T., Hansen, A., Flekkøy, E. G., and Måløy, K. J. (2013). History independence of steady state in simultaneous two-phase flow through two-dimensional porous media. *Phys. Rev. E*, 88:053004.

Eshgarf, H., Nadooshan, A. A., and Raisi, A. (2023). A review of multi-phase and single-phase models in the numerical simulation of nanofluid flow in heat exchangers. *Engineering Analysis with Boundary Elements*, 146:910–927.

Farokhipour, A., Mansoori, Z., Saffar-Avval, M., and Ahmadi, G. (2020). 3d computational modeling of sand erosion in gas-liquid-particle multiphase annular flows in bends. *Wear*, 450-451:203241.

Feng, Y., Han, K., and Owen, D. (2007). Coupled lattice boltzmann method and discrete element modeling of particle transport in turbulent fluid flows: Computational issues. *Int. J. Numer. Meth. Eng.*, 72:1111 – 1134.

García-Salaberri, P. A., Zenyuk, I. V., Shum, A. D., Hwang, G., Vera, M., Weber, A. Z., and Gostick, J. T. (2018). Analysis of representative elementary volume and through-plane regional characteristics of carbon-fiber papers: diffusivity, permeability and electrical/thermal conductivity. *Int. J. Heat. Mass Trans.*, 127:687–703.

Ghassemi, A. and Pak, A. (2011). Numerical study of factors influencing relative permeabilities of two immiscible fluids flowing through porous media using lattice boltzmann method. *J. Pet. Sci. Eng*, 77(1):135–145.

Ghassemzadeh, J. and Sahimi, M. (2004). Pore network simulation of fluid imbibition into paper during coating: Ii. characterization of paper's morphology and computation of its effective permeability tensor. *Chem. Eng. Sci.*, 59(11):2265–2280.

Gong, S. and Cheng, P. (2012). Numerical investigation of droplet motion and coalescence by an improved lattice boltzmann model for phase transitions and multiphase flows. *Comput Fluids*, 53:93–104.

Gray, W. G. (1999). Thermodynamics and constitutive theory for multiphase porous-media flow considering internal geometric constraints. *Adv. Water Res.*, 22(5):521–547.

Gunstensen, A. K. and Rothman, D. H. (1993). Lattice-boltzmann studies of immiscible two-phase flow through porous media. *J. Geophys. Res. Solid Earth*, 98(B4):6431–6441.

Gunstensen, A. K., Rothman, D. H., Zaleski, S., and Zanetti, G. (1991). Lattice boltzmann model of immiscible fluids. *Physical Review A*, 43(8):4320.

Hatta, N., Fujimoto, H., Isobe, M., and Kang, J.-S. (1998). Theoretical analysis of flow characteristics of multiphase mixtures in a vertical pipe. *International Journal of Multiphase Flow*, 24(4):539–561.

Huinink, H. (2016). *Fluids in Porous Media*. 2053-2571. Morgan Claypool Publishers.

Hussain, F., Pinczewski, W. V., Cinar, Y., Arns, J.-Y., Arns, C., and Turner, M. (2014). Computation of relative permeability from imaged fluid distributions at the pore scale. *Transp. Porous Media.*, 104(1):91–107.

Inamuro, T., Ogata, T., Tajima, S., and Konishi, N. (2004). A lattice boltzmann method for incompressible two-phase flows with large density differences. *J. Comput. Phys.*, 198(2):628–644.

J. Kozeny, R. Acad Sci, V. (1927). Ueber kapillare leitung der wasser in boden. *Proc. Class I*, 136:271–306.

Joekar-Niasar, V., Hassanizadeh, S. M., and Dahle, H. (2010). Non-equilibrium effects in capillarity and interfacial area in two-phase flow: dynamic pore-network modelling. *J. Fluid Mech.*, 655:38–71.

Ju, Y., Gong, W., Chang, W., and Sun, M. (2020). Effects of pore characteristics on water-oil two-phase displacement in non-homogeneous pore structures: A pore-scale lattice boltzmann model considering various fluid density ratios. *International Journal of Engineering Science*, 154:103343.

Kalaydjian, F. (1990). Origin and quantification of coupling between relative permeabilities for two-phase flows in porous media. *Transp. Porous Media*, 5(3):215–229.

Katz, A. J. and Thompson, A. H. (1986). Quantitative prediction of permeability in porous rock. *Phys. Rev. B*, 34:8179–8181.

Khanamiri, H. H. and Torsæter, O. (2018). Fluid topology in pore scale two-phase flow imaged by synchrotron x-ray microtomography. *Water Resources Research*, 54(3):1905–1917.

Koponen, A., Kataja, M., and Timonen, J. (1997). Permeability and effective porosity of porous media. *Phys. Rev. E*, 56:3319–3325.

Kumar Singh, R. and Priyadarshini Nayak, N. (2023). Opportunities and challenges of nanotechnology in enhanced oil recovery: An overview. *Materials Today: Proceedings*.

Langaas, K. and Papatzacos, P. (2001). Numerical investigations of the steady state relative permeability of a simplified porous medium. *Transp. Porous Media.*, 45(2):241–266.

Lehmann, P., Berchtold, M., Ahrenholz, B., Tölke, J., Kaestner, A., Krafczyk, M., Flühler, H., and Künsch, H. (2008). Impact of geometrical properties on permeability and fluid phase distribution in porous media. *Adv. Water Resour.*, 31(9):1188–1204.

Li, H., Pan, C., and Miller, C. T. (2005). Pore-scale investigation of viscous coupling effects for two-phase flow in porous media. *Phys. Rev. E*, 72(2):026705.

Li, Y. (2014). Application and perspective of multiphase flow metering technologies for ocean oil and gas exploitation. *Qinghua Study Journal*, 51:88–96.

Li, Z., Galindo-Torres, S., Yan, G., Scheuermann, A., and Li, L. (2017). Pore-scale simulations of simultaneous steady-state two-phase flow dynamics using a lattice boltzmann model: Interfacial area, capillary pressure and relative permeability. *Transp. Porous Media.*, 129.

Li, Z., Galindo-Torres, S., Yan, G., Scheuermann, A., and Li, L. (2019). Pore-scale simulations of simultaneous steady-state two-phase flow dynamics using a lattice boltzmann model: Interfacial area, capillary pressure and relative permeability. *Transp. Porous Media.*, 129(1):295–320.

Liu, H. (2015). The thirteen-five environment technology funding meeting. `https://huanbao.bjx.com.cn/news/20151123/683929.shtml`.

Liu, H., Zhou, B., Yu, J., Liu, K., Han, X., and Zhang, G. (2023). Experimental investigation on the multiphase flow characteristics of oblique water entry of the hollow cylinders. *Ocean Engineering*, 272:113902.

Luo, L.-S. (1998). Unified theory of lattice boltzmann models for nonideal gases. *Phys. Rev. Lett.*, 81(8):1618.

Majid Hassanizadeh, S. and Gray, W. G. (1993). Toward an improved description of the physics of two-phase flow. *Adv. Water Resour.*, 16(1):53–67. Research Perspectives in Hydrology.

McClure, J., Ramstad, T., Li, Z., Armstrong, R., and Berg, S. (2020). Modeling geometric state for fluids in porous media: Evolution of the euler characteristic. *Transp. Porous Media.*, 133:229–250.

McWhorter, D. B. and Sunada, D. K. (1990). Exact integral solutions for two-phase flow. *Water Resources Research*, 26(3):399–413.

Mino, Y., Hasegawa, A., Shinto, H., and Matsuyama, H. (2018). Lattice-boltzmann flow simulation of an oil-in-water emulsion through a coalescing filter: Effects of filter structure. *Chem. Eng. Sci.*, 177:210–217.

Mohamad, A. (2011). *Lattice Boltzmann Method*, volume 70. Springer.

Morel-Seytoux, H. J. (1989). Unsaturated flow in hydrologic modeling. theory and practice.

Muskat, M. and Meres, M. W. (1936). The flow of heterogeneous fluids through porous media. *Physics*, 7(9):346–363.

Narváez, A. and Harting, J. (2010). A d3q19 lattice-boltzmann pore-list code with pressure boundary conditions for permeability calculations. *Adv. Appl. Math. Mech.*, 2:685.

Narváez, A., Zauner, T., Raischel, F., Hilfer, R., and Harting, J. (2010). Quantitative analysis of numerical estimates for the permeability of porous media from lattice-boltzmann simulations. *J. Stat. Mech: Theory Exp.*, 2010(11):P11026.

Nazeer, M., Hussain, F., Ghafar, M., and Javed, M. A. (2022). Investigation of electro-osmotic flow of hafnium particles mixed-up with casson fluid in convergent geometry: Theoretical study of multiphase flow. *Partial Differential Equations in Applied Mathematics*, 6:100448.

Nemer, M. N., Rao, P. R., and Schaefer, L. (2021). Coupled influence of wettability alteration and geometry on two-phase flow in porous media. *Advances in Water Resources*, 157:104055.

Nield, D. A., Bejan, A., et al. (2006). *Convection in porous media*, volume 3. Springer.

Oran, E. S. and Boris, J. P. (2002). Fluid dynamics. In Meyers, R. A., editor, *Encyclopedia of Physical Science and Technology (Third Edition)*, pages 31–43. Academic Press, New York, third edition edition.

Ott, H., Kharrat, A., Borji, M., and Arnold, P. (2020). Fluid-phase topology of complex displacements in porous media. *Phys. Rev. Research*, 2:023240.

Pasandideh-Fard, M., Qiao, Y. M., Chandra, S., and Mostaghimi, J. (1996). Capillary effects during droplet impact on a solid surface. *Physics of Fluids*, 8:650–659.

Paustian, R., Andersson, L., Helland, J. O., and Wildenschild, D. (2021). On the relationship between capillary pressure, saturation, and interfacial area for three-phase flow in water-wet porous media. *Adv. Water Resour.*, 151:103905.

Qian, Y.-H., d'Humières, D., and Lallemand, P. (1992). Lattice bgk models for navier-stokes equation. *Europhys. Lett.*, 17(6):479.

Rabbani, A., Jamshidi, S., and Salehi, S. (2014). An automated simple algorithm for realistic pore network extraction from micro-tomography images. *J. Pet. Sci. Eng*, 123:164 – 171.

Raghavan, R. (2009). A note on the theoretical foundations for multiphase pressure analysis for flow in porous media. *Journal of Petroleum Science and Engineering*, 68(1):81–88.

Ramstad, T., Idowu, N., Nardi, C., and Øren, P.-E. (2012). Relative permeability calculations from two-phase flow simulations directly on digital images of porous rocks. *Transp. Porous Media.*, 94(2):487–504.

Rücker, M., Berg, S., Armstrong, R. T., Georgiadis, A., Ott, H., Schwing, A., Neiteler, R., Brussee, N., Makurat, A., Leu, L., Wolf, M., Khan, F., Enzmann, F., and Kersten, M. (2015). From connected pathway flow to ganglion dynamics. *Geophys. Res. Lett.*, 42(10):3888–3894.

Sahimi, M. and Tsotsis, T. T. (1997). Transient diffusion and conduction in heterogeneous media: Beyond the classical effective-medium approximation. *Ind. Eng. Chem. Res.*, 36(8):3043–3052.

Santiago, C., Ghomeshi, S., Kryuchkov, S., and Kantzas, A. (2016). Pore level modeling of imbibition in heavy oil saturated media. *Journal of Petroleum Science and Engineering*, 140:108–118.

Scheller, B. L. and Bousfield, D. W. (1995). Newtonian drop impact with a solid surface. *Aiche Journal*, 41:1357–1367.

Scholz, C., Wirner, F., Götz, J., Rüde, U., Schröder-Turk, G. E., Mecke, K., and Bechinger, C. (2012a). Permeability of porous materials determined from the euler characteristic. *Phys. Rev. Lett.*, 109:264504.

Scholz, C., Wirner, F., Götz, J., Rüde, U., Schröder-Turk, G. E., Mecke, K., and Bechinger, C. (2012b). Permeability of porous materials determined from the euler characteristic. *Phys. Rev. Lett.*, 109(26).

Shan, X. and Chen, H. (1993). Lattice boltzmann model for simulating flows with multiple phases and components. *Phys. Rev. E*, 47(3):1815.

Shan, X. and Chen, H. (1994). Simulation of nonideal gases and liquid-gas phase transitions by the lattice boltzmann equation. *Physical Review E*, 49(4):2941.

Singh, A., Pandey, K. M., and Singh, Y. (2021). Cfd analysis of viscous fingering in hele-shaw cell for air-glycerin system. *Materials Today: Proceedings*, 45:6381–6385. International Conference on Mechanical, Electronics and Computer Engineering 2020: Materials Science.

Spanne, P., Thovert, J., Jacquin, C., Lindquist, W., Jones, K., and Adler, P. (1994). Synchrotron computed microtomography of porous media: topology and transports. *Phys. Rev. Lett.*, 73(14):2001.

Swift, M. R., Orlandini, E., Osborn, W., and Yeomans, J. (1996). Lattice boltzmann simulations of liquid-gas and binary fluid systems. *Physical Review E*, 54(5):5041.

Tanoh, D. A. (2016). The exploration and production life cycle of oil and gas. `http://www.reportingoilandgas.org/the-exploration-and-production-life-cycle-of-oil-and-gas/`.

Tsakiroglou, C., Theodoropoulou, M., and Karoutsos, V. (2003). Nonequilibrium capillary pressure and relative permeability curves of porous media. *AIChE J.*, 49(10):2472–2486.

Tsakiroglou, C., Theodoropoulou, M., Karoutsos, V., and Papanicolaou, D. (2005). Determination of the effective transport coefficients of pore networks from transient immiscible and miscible displacement experiments. *Water Resour. Res.*, 41(2).

Vogel, H. J. (2000). A numerical experiment on pore size, pore connectivity, water retention, permeability, and solute transport using network models. *Eur. J. Soil Sci*, 51(1):99–105.

Vogel, H.-J. and Roth, K. (2001). Quantitative morphology and network representation of soil pore structure. *Adv. Water. Res.*, 24(3):233 – 242.

Wang, C. (1998). Modeling multiphase flow and transport in porous media. In INGHAM, D. B. and POP, I., editors, *Transport Phenomena in Porous Media*, pages 383–410. Pergamon, Oxford.

Wang, Q. (2016). Review and application of multiphase pipe flow in petrochemical industry. *Contemporary Chemical Industry*, 45(2).

Wang, Y., Chen, J., and Han, X. (2010). Multiphase separating system for oil-containing wastewater treatment.

Wei, H., Zhu, X., Liu, X., Yang, H., Tao, W.-Q., and Chen, L. (2022). Pore-scale study of drainage processes in porous media with various structural heterogeneity. *International Communications in Heat and Mass Transfer*, 132:105914.

Whitaker, S. (1986). Flow in porous media i: A theoretical derivation of darcy's law. *Transp. Porous Media*, 1(1):3–25.

Xu, M. and Liu, H. (2018). Prediction of immiscible two-phase flow properties in a two-dimensional berea sandstone using the pore-scale lattice boltzmann simulation. *Eur. Phys. J. E*, 41(10):124.

Yadigaroglu, G. and Hewitt, G. F. (2017). *Introduction to multiphase flow: basic concepts, applications and modelling*. Springer.

Yang, P., Wen, Z., Dou, R., and Liu, X. (2017). Permeability in multi-sized structures of random packed porous media using three-dimensional lattice boltzmann method. *Int. J. Heat Mass Transfer*, 106:1368 – 1375.

Yang, W. and Zhang, D. (2022). Experimental study on multiphase flow in 3d-printed heterogeneous, filled vugs. *Journal of Petroleum Science and Engineering*, 208:109497.

Yang, Y., Jing, D., and Zhao, L. (2020). Computational fluid dynamics modeling of reactive multiphase flow for suspended photocatalytic water splitting of hydrogen production system. *Applied Thermal Engineering*, 173:115220.

Yiotis, A. G., Psihogios, J., Kainourgiakis, M. E., Papaioannou, A., and Stubos, A. K. (2007). A lattice boltzmann study of viscous coupling effects in immiscible two-phase flow in porous media. *Colloids Surf. A*, 300(1):35–49. Proceedings of the Fourth International TRI/Princeton Workshop "Characterization of Porous Materials: from Angstroms to Millimeters".

Yuan, P. and Schaefer, L. (2006). Equations of state in a lattice boltzmann model. *Phys. Fluids.*, 18(4):042101.

Zakirov, T. R. and Khramchenkov, M. G. (2020). Characterization of two-phase displacement mechanisms in porous media by capillary and viscous forces estimation using the lattice boltzmann simulations. *Journal of Petroleum Science and Engineering*, 184:106575.

Zhang, D., Papadikis, K., and Gu, S. (2016). A lattice boltzmann study on the impact of the geometrical properties of porous media on the steady state relative permeabilities on two-phase immiscible flows. *Adv. Water Resour.*, 95:61–79.

Zhang, J. (2011). Lattice boltzmann method for microfluidics: models and applications. *Microfluid. Nanofluid.*, 10(1):1–28.

Zhang, J., Cai, S., Zhu, H., and Zhang, Y. (2015). Experimental investigation of the flow at the entrance of a rotodynamic multiphase pump by visualization. *Journal of Petroleum Science and Engineering*, 126:254–261.

Zhang, W. (2021). The 2021 development of chinese water environment industry. `https://www.qianzhan.com/analyst/detail/220/210607-9ca6b5d9.html`.

Zhao, H., Ning, Z., Kang, Q., Chen, L., and Zhao, T. (2017). Relative permeability of two immiscible fluids flowing through porous media determined by lattice boltzmann method. *Int. Commun. Heat. Mass Transfer.*, 85:53–61.

Zou, Q. and He, X. (1997). On pressure and velocity boundary conditions for the lattice boltzmann bgk model. *Phys. Fluids*, 9(6):1591–1598.

Appendix A: Representative elementary volume

A representative elementary volume (REV) is the smallest volume scale over which measurements can make and/or parameters calculated that give representative values for the whole porous medium. Normally, a REV needs to be sufficiently large to achieve a meaningful volumetric average of the structure but sufficiently small to avoid any issues associated with large-scale heterogeneity of the pore structure (García-Salaberri et al. (2018)). Employing a REV also aids the computational process by reducing computational time and permitting the use of periodic boundary conditions where appropriate.

In the present work, we first note that since we constrain attention to two dimensions, the 'REV' we employ is actually a representative elementary area. In order to determine the appropriate dimensions for the REV, we note that typically it is sufficient to consider one morphological and one hydrodynamic factor, although consideration of other statistical quantities such as mean pore size can provide further validation. Here, the solid phase fraction and permeability were chosen as quantities to test. First, a 1500×1500 lu^2 porous medium was generated with a target porosity of 0.765. Then a set of smaller computational domains ranging from 100×100 lu^2 to 1400×1400 lu^2 were generated and the corresponding porosity and permeability of each structure were calculated. The resultant, respective, values are displayed in Fig. A1. For domains larger than 800×800 lu^2, the value of both the porosity and permeability is less than 5% of the respective target values. Therefore the domain 800×800 lu^2 is chosen as the REV for all results in this study.

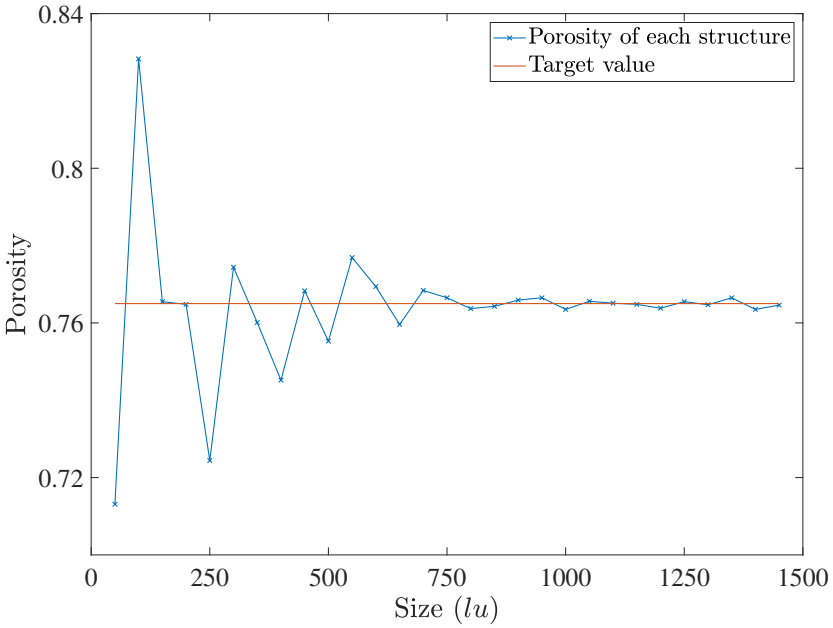

(a)

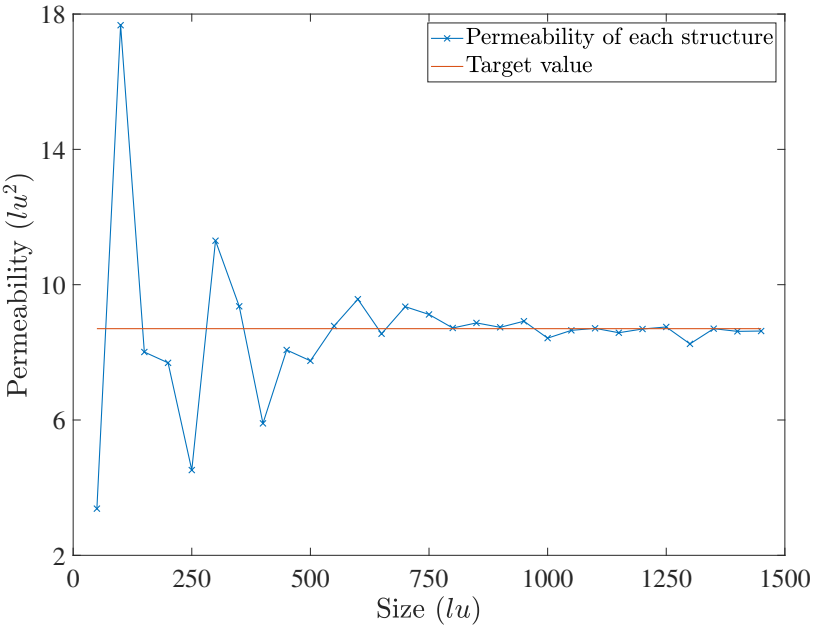

(b)

Figure A1: Representative elementary volume determination through testing (a) porosity and (b) permeability values.

Appendix B: Contour and vector plots for transient state study

In this appendix, volume fraction phase plots for $S_w = \{0.91, 0.49, 0.32, 0.2\}$ and an Euler characteristic of $\chi_0 = -800$ (structure 4) are shown respectively in Figs B1 - B4 for drainage, and for $S_w = \{0.09, 0.45, 0.6, 0.85\}$ in Figs B5 - B8 for imbibition. A velocity magnitude vector plot is also provided for flow illustration purposes in Fig. B9.

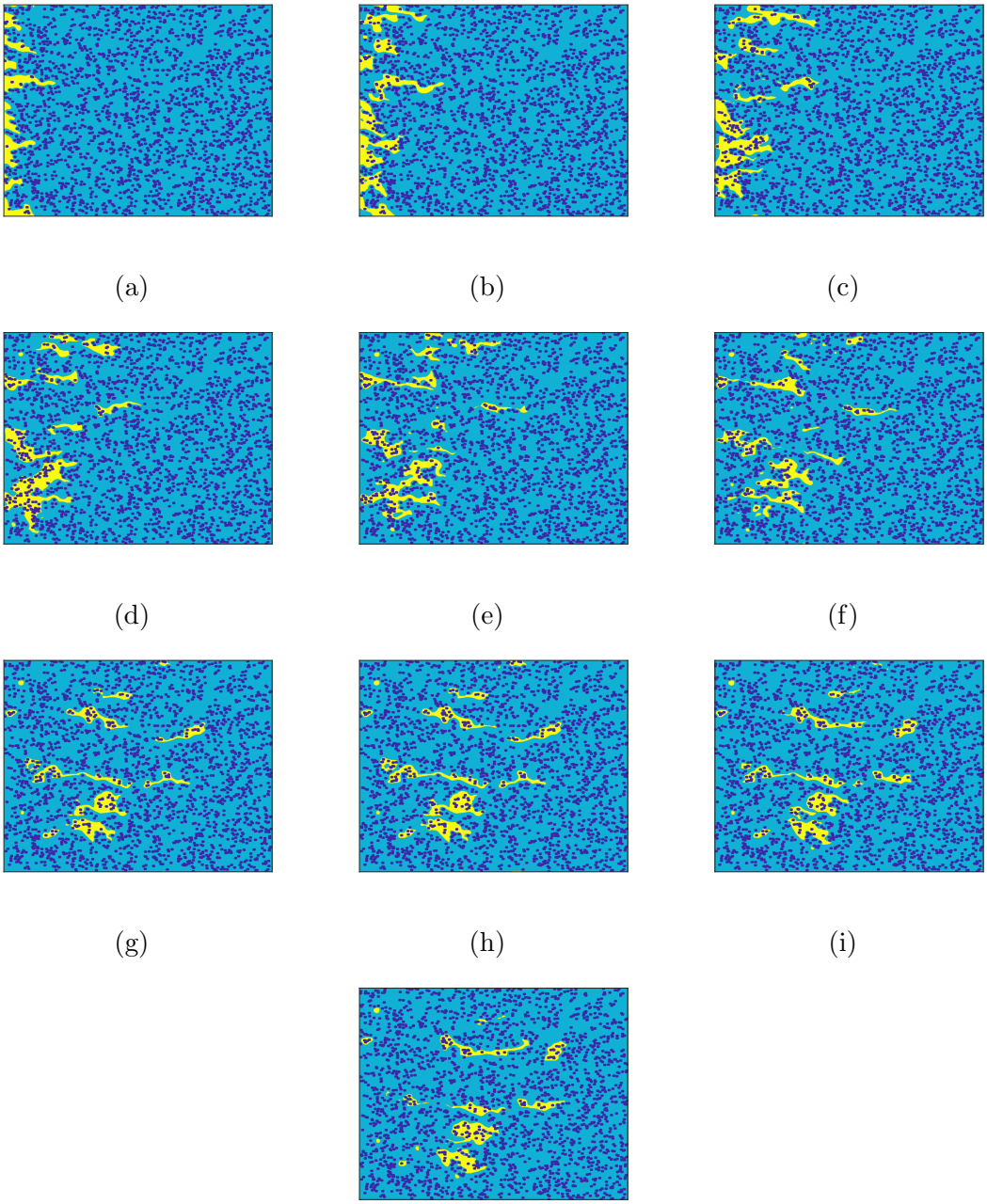

Figure B1: Volume fraction contour plots of the temporal evolution of the injection of the nonwetting phase (yellow) into the wetting phase (blue) for a steady state saturation rate of wetting phase of 0.91 and Euler characteristic $\chi_0 = -800$. In terms of lattice units $t = 5 \times 10^4$ in (a), $t = 1 \times 10^5$ in (b), $t = 1.5 \times 10^5$ in (c), $t = 2 \times 10^5$ in (d), $t = 2.5 \times 10^5$ in (e), $t = 3 \times 10^5$ in (f), $t = 3.5 \times 10^5$ in (g), $t = 4 \times 10^5$ in (h), $t = 4.5 \times 10^5$ in (i) and $t = 5 \times 10^5$ in (j).

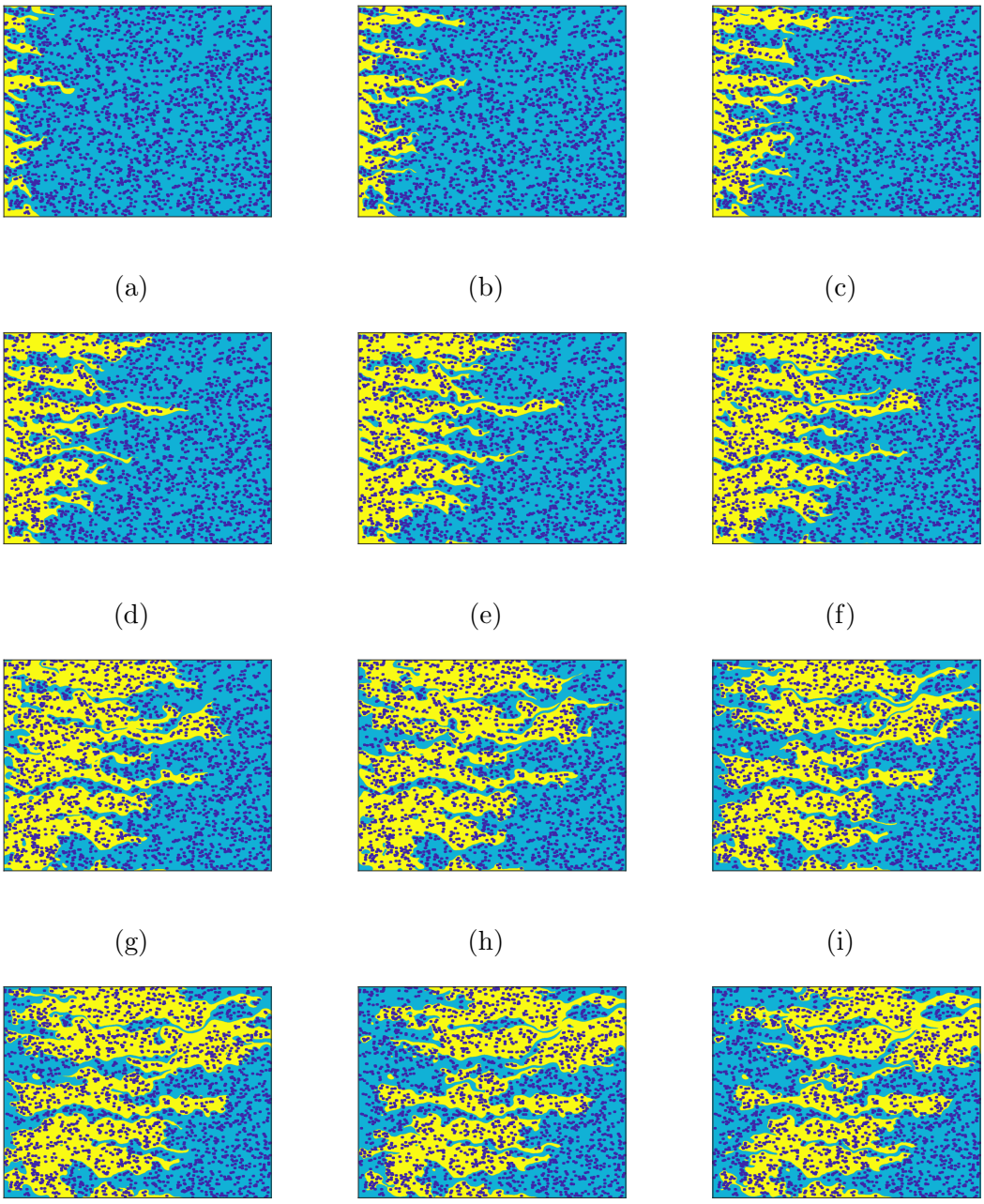

Figure B2: Volume fraction contour plots of the temporal evolution of the injection of the nonwetting phase (yellow) into the wetting phase for a steady state saturation rate of the wetting phase of 0.49 and Euler characteristic of $\chi_0 = -800$. In terms of lattice units $t = 6 \times 10^4$ in (a), $t = 1.2 \times 10^5$ in (b), $t = 1.8 \times 10^5$ in (c), $t = 2.4 \times 10^5$ in (d), $t = 3 \times 10^5$ in (e), $t = 3.6 \times 10^5$ in (f), $t = 4.2 \times 10^5$ in (g), $t = 4.8 \times 10^5$ in (h), $t = 5.4 \times 10^5$ in (i), $t = 6 \times 10^5$ in (j), $t = 6.6 \times 10^5$ in (k), $t = 7.2 \times 10^5$ in (l), $t = 7.8 \times 10^5$ in (m) and $t = 8.4 \times 10^5$ in (n).

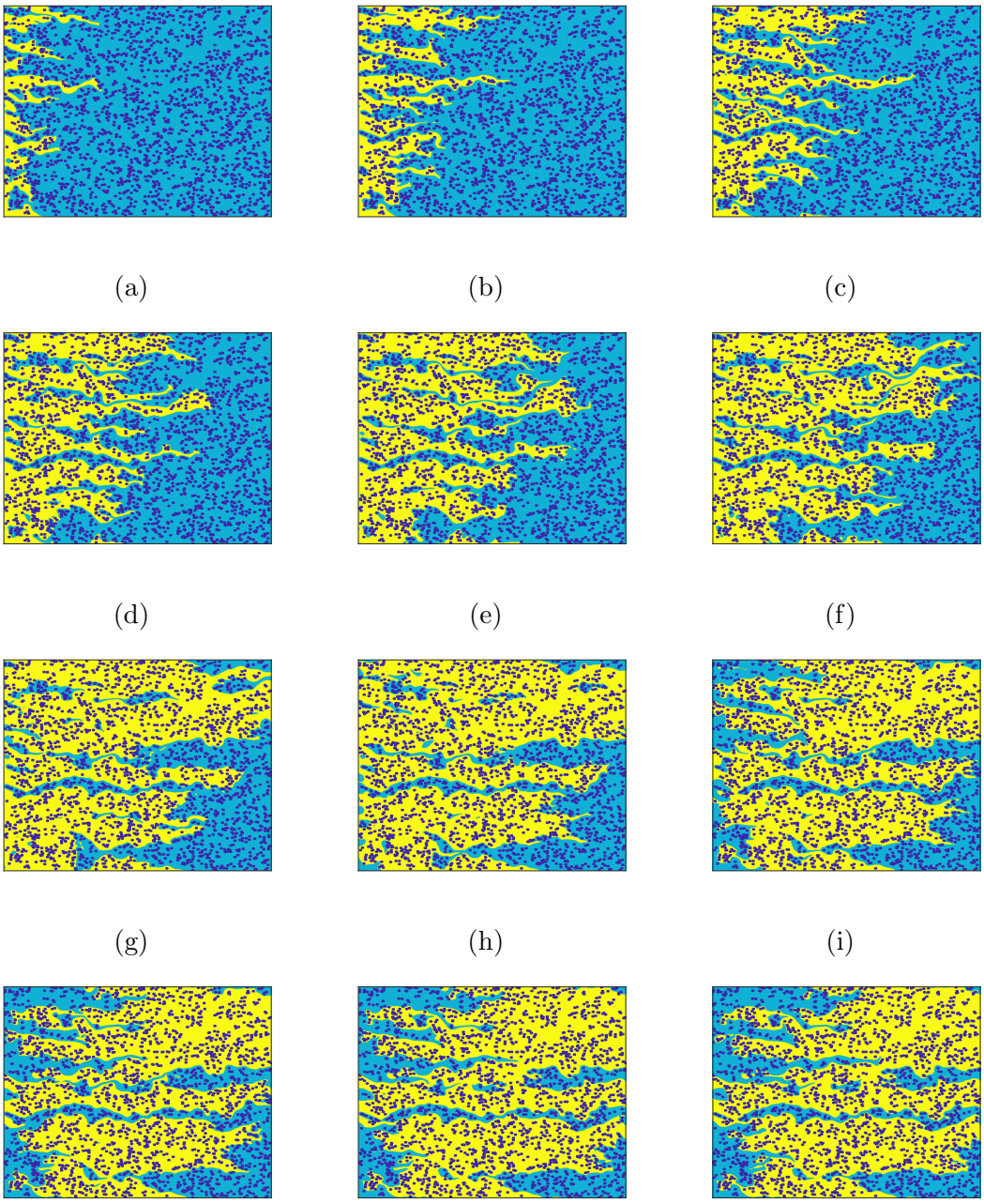

Figure B3: Volume fraction contour plots of the temporal evolution of the injection of the nonwetting phase (yellow) into the wetting phase (blue) for the steady saturation rate of the wetting phase of 0.32 and Euler characteristic of $\chi_0 = -800$. In terms of lattice units $t = 6 \times 10^4$ in (a), $t = 1.2 \times 10^5$ in (b), $t = 1.8 \times 10^5$ in (c), $t = 2.4 \times 10^5$ in (d), $t = 3 \times 10^5$ in (e), $t = 3.6 \times 10^5$ in (f), $t = 4.2 \times 10^5$ in (g), $t = 4.8 \times 10^5$ in (h), $t = 5.4 \times 10^5$ in (i), $t = 6 \times 10^5$ in (j), $t = 6.6 \times 10^5$ in (k), $t = 7.2 \times 10^5$ in (l), $t = 7.8 \times 10^5$ in (m) and $t = 8.4 \times 10^5$ in (n).

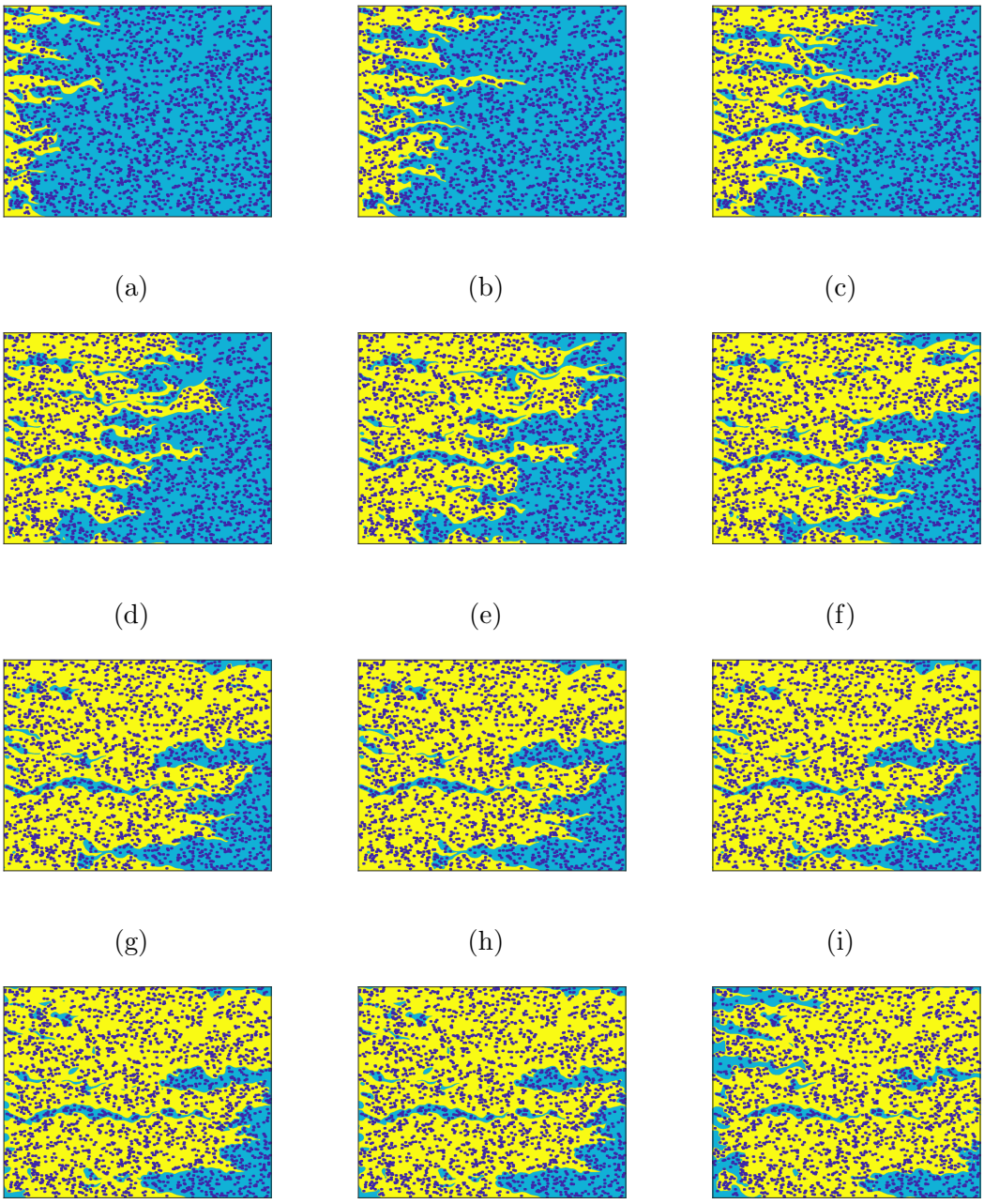

Figure B4: Volume fraction contour plots of the temporal evolution of the injection of the nonwetting phase (yellow) in the wetting phase (blue) for the steady saturation rate of the wetting phase of 0.2 and an Euler characteristic of $\chi_0 = -800$. In terms of lattice units $t = 7 \times 10^4$ in (a), $t = 1.4 \times 10^5$ in (b), $t = 2.1 \times 10^5$ in (c), $t = 2.8 \times 10^5$ in (d), $t = 3.5 \times 10^5$ in (e), $t = 4.2 \times 10^5$in (f), $t = 4.9 \times 10^5$ in (g), $t = 5.6 \times 10^5$ in (h), $t = 6.3 \times 10^5$ in (i), $t = 7 \times 10^5$ in (j), $t = 7.7 \times 10^5$ in (k), $t = 8.4 \times 10^5$ in (l), $t = 9.1 \times 10^5$ in (m) and $t = 9.8 \times 10^5$ in (n).

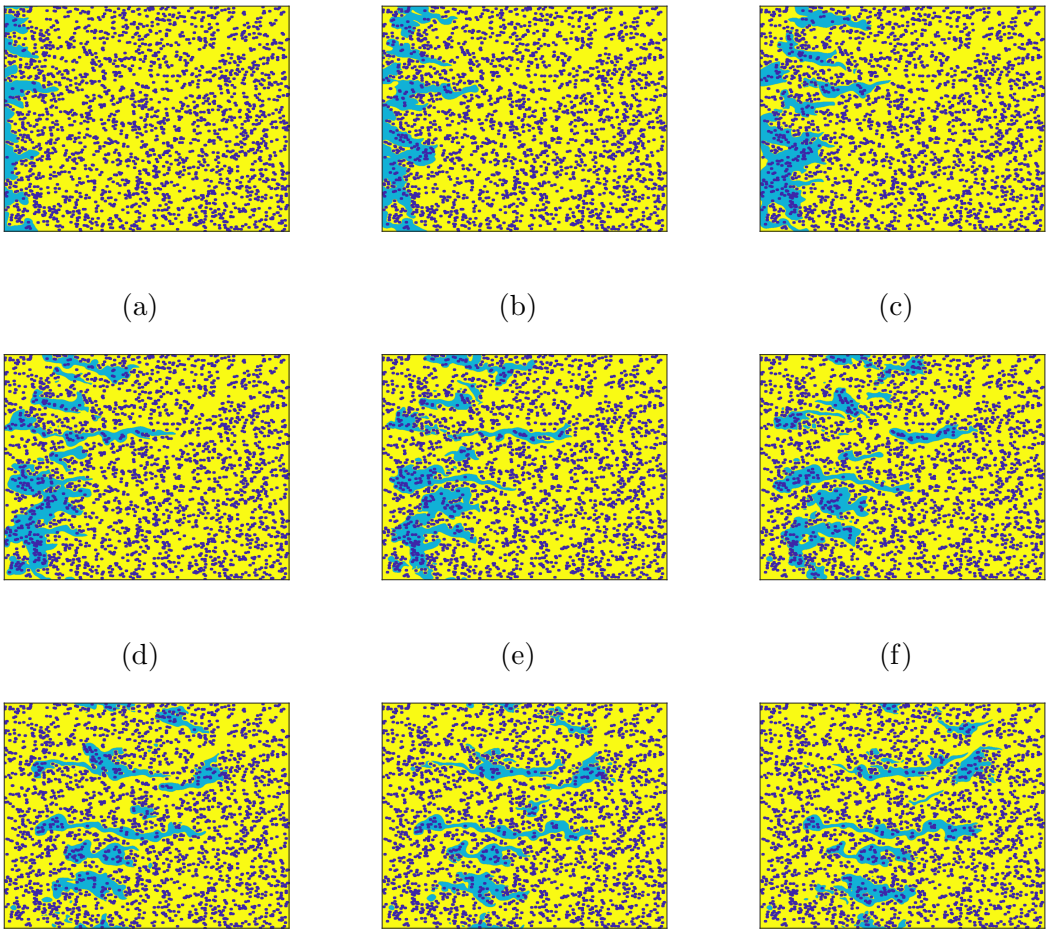

Figure B5: Volume fraction contour plots of the temporal evolution of the injection of the wetting phase (blue) into the non-wetting phase (yellow) for a steady state saturation rate of wetting phase of 0.09 and Euler characteristic $\chi_0 = -800$. In terms of lattice units $t = 5 \times 10^4$ in (a), $t = 1 \times 10^5$ in (b), $t = 1.5 \times 10^5$ in (c), $t = 2 \times 10^5$ in (d), $t = 2.5 \times 10^5$ in (e), $t = 3 \times 10^5$ in (f), $t = 4 \times 10^5$ in (g), $t = 4.5 \times 10^5$ in (h) and $t = 5 \times 10^5$ in (i).

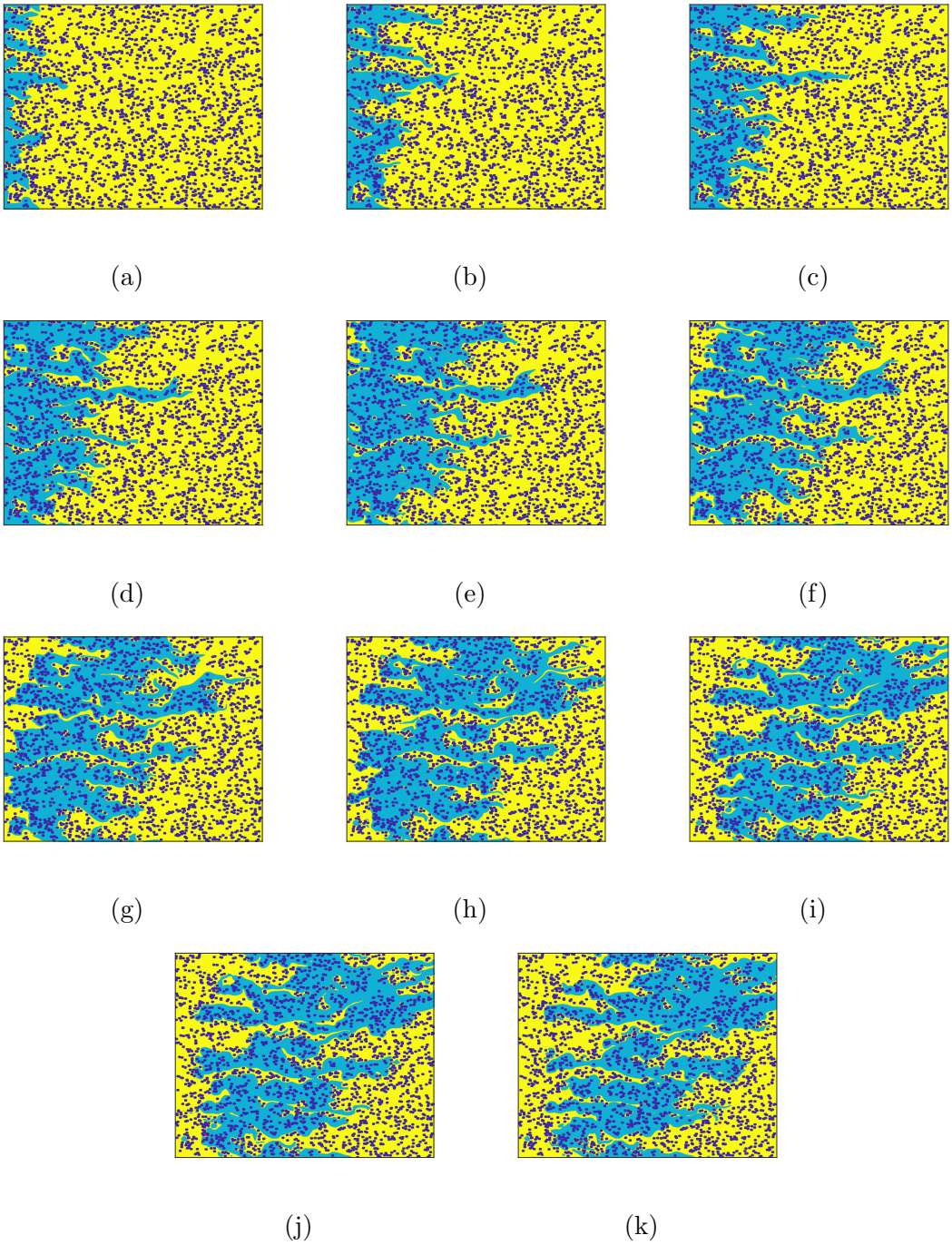

Figure B6: Volume fraction contour plots of the temporal evolution of the injection of the wetting phase (blue) into the non-wetting phase (yellow) for a steady state saturation rate of the wetting phase of 0.45 and Euler characteristic of $\chi_0 = -800$. In terms of lattice units $t = 7.2 \times 10^4$ in (a), $t = 1.44 \times 10^5$ in (b), $t = 2.16 \times 10^5$ in (c), $t = 2.88 \times 10^5$ in (d), $t = 3.6 \times 10^5$ in (e), $t = 4.32 \times 10^5$ in (f), $t = 5.04 \times 10^5$ in (g), $t = 5.76 \times 10^5$ in (h), $t = 6.48 \times 10^5$ in (i), $t = 7.2 \times 10^5$ in (j) and $t = 7.92 \times 10^5$ in (k).

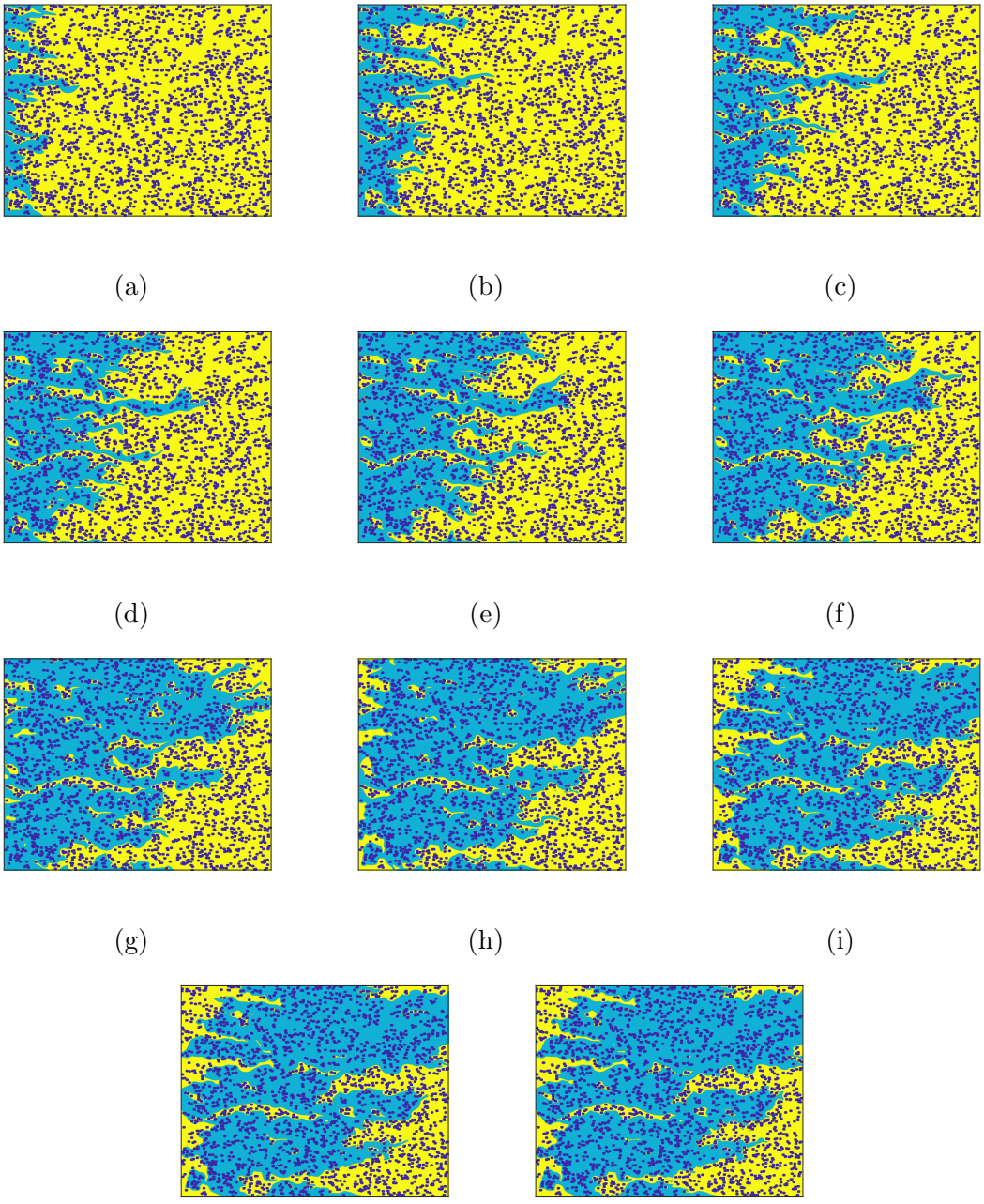

Figure B7: Volume fraction contour plots of the temporal evolution of the injection of the wetting phase (blue) into the non-wetting phase (yellow) for the steady saturation rate of the wetting phase of 0.6 and Euler characteristic of $\chi_0 = -800$. In terms of lattice units $t = 7.5 \times 10^4$ in (a), $t = 1.5 \times 10^5$ in (b), $t = 2.25 \times 10^5$ in (c), $t = 3 \times 10^5$ in (d), $t = 3.75 \times 10^5$ in (e), $t = 4.5 \times 10^5$ in (f), $t = 5.25 \times 10^5$ in (g), $t = 6 \times 10^5$ in (h), $t = 6.75 \times 10^5$ in (i), $t = 7.5 \times 10^5$ in (j) and $t = 8.25 \times 10^5$ in (k).

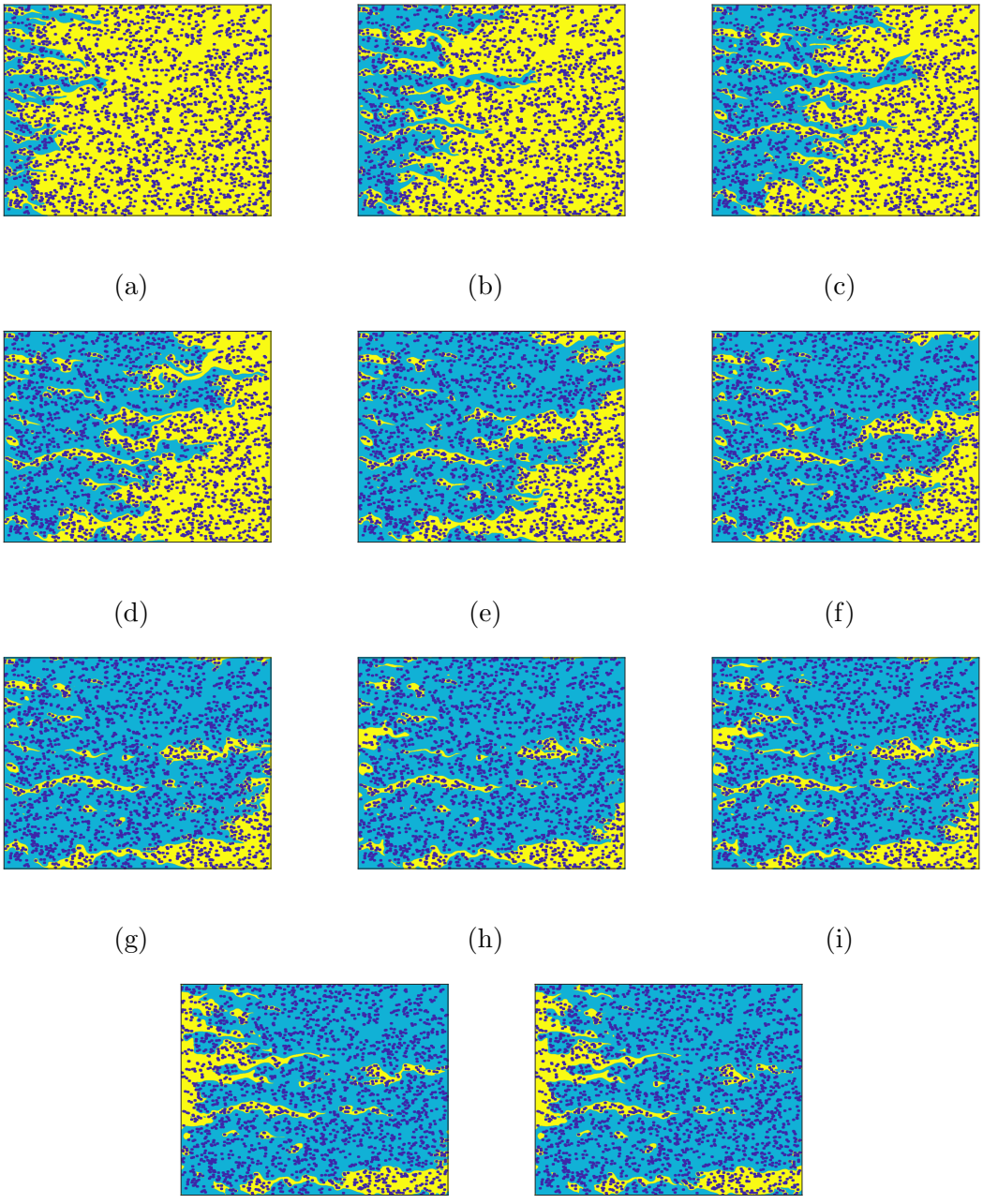

Figure B8: Volume fraction contour plots of the temporal evolution of the injection of the wetting phase (blue) in the non-wetting phase (yellow) for the steady saturation rate of the wetting phase of 0.85 and an Euler characteristic of $\chi_0 = -800$. In terms of lattice units $t = 8.5 \times 10^4$ in (a), $t = 1.7 \times 10^5$ in (b), $t = 2.55 \times 10^5$ in (c), $t = 3.4 \times 10^5$ in (d), $t = 4.25 \times 10^5$ in (e), $t = 5.1 \times 10^5$ in (f), $t = 5.95 \times 10^5$ in (g), $t = 6.8 \times 10^5$ in (h), $t = 7.65 \times 10^5$ in (i), $t = 8.5 \times 10^5$ in (j) and $t = 9.35 \times 10^5$ in (k).

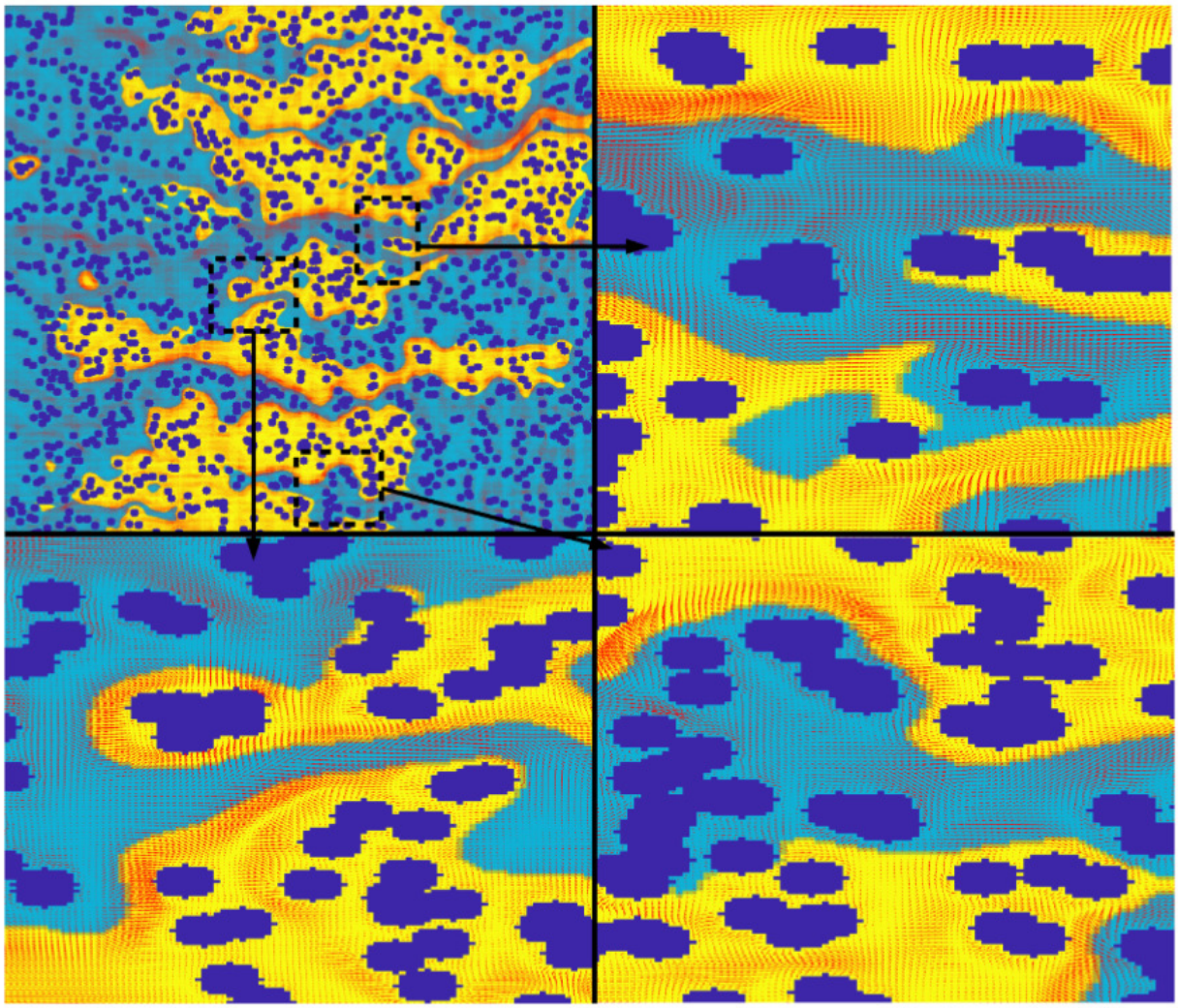

Figure B9: Velocity magnitude vector plot on selected areas (for flow demonstration purposes only).

This combined set of plots not only provides a visualisation of the transient development of this studied two-phase flow for $\chi_0 = -800$, for the five consider values of S_w but also enables me to more fully understand the presented macro-level ensemble plots. In all the volume fraction phase plots fingers of the non-wetting phase protruding into the wetting phase are clearly seen giving rise to the subsequent flow developments as the interaction of the displaced wetting phase and injected non-wetting phase bounded by the topology of the solid pore structure and morphology of the pore space shape the resultant two-phase flow. Two key features are the development of a number of blobs as a consequence of snap-off and at the micro-level phase development and transport is still seen, even though a macro-level steady state has been achieved.